UNIVERSITY OF CALIFORNIA, SAN DIEGO

Krypton and xenon in air trapped in polar ice cores: Paleo-atmospheric measurements for estimating past mean ocean temperature and summer snowmelt frequency

A Dissertation submitted in partial satisfaction of the
Requirements for the degree of Doctor of Philosophy

in

Earth Sciences

by

Melissa Anne Headly

Committee in Charge:

Professor Jeffery P. Severinghaus, Chair
Professor Christopher Charles
Professor Ralph Keeling
Professor Lynne Talley
Professor Mark Thiemens
Professor Ray Weiss

2008

This Dissertation of Melissa Anne Headly is approved and it is acceptable in quality and form for publication on microfilm:

_____

_____

_____

_____

_____

_____

Chair

University of California, San Diego

2008

TABLE OF CONTENTS

LIST OF TABLES

LIST OF FIGURES

ACKNOWLEDGEMENTS

I would like to thank Jeff Severinghaus for his support as my graduate advisor and committee chair. He has been a source of scientific ideas, advice, and support throughout my years here, and is one of the most creative and analytical thinkers I have ever met. I would also like to thank my thesis committee: Chris Charles, Ralph Keeling, Lynne Talley, Mark Thiemens, and Ray Weiss, whose breadth of knowledge and experience have helped to guide me and improve this work.

I want to thank all of the members of the Severinghaus lab through the years I have been here. Vasili Petrenko, Takuro Kobashi, and I all came to Scripps at the same time, and I am grateful to have had them as colleagues and friends. Takuro's visits to the lab were always welcome breaks, and his curiosity and positive nature made the lab a fun place to be. I also owe much thanks to Ross Beaudette, who has been an invaluable lab technician. Ross also created an efficient and supportive environment in the lab, which made my laboratory work much more enjoyable. Our newest addition to the lab, Anais Orsi, has been a delight to work with. I appreciate her insight and curiosity, both in matters of science and of life. I also thank the postdocs that have worked in our lab, who were great role models for me. Nicolas Caillon taught me the Ar ice core measurement technique, and provided much humor along the way. Roberta Hamme shared her knowledge of noble gases with me, and was always helpful and full of ideas when I wanted to discuss my research with her. She was also an inspiration to me as a successful female scientist. Finally, I thank Kenji Kawamura for teaching me his Kr and Xe measurement technique, and for our

collaboration on the Dome Fuji measurements. I appreciated his intelligence and patience as we worked together.

I would not have any ice cores to analyze if it were not for the people at NICL (the National Ice Core Lab): Eric Cravens, Geoffrey Hargreaves, Todd Hinkley, and Mark Twickler, who assisted with ice core sampling. I thank Eric and Ross for sampling the GISP2 and Vostok time series and the GISP2 LGM ice. I am also grateful to Eric for cutting the extra 8 samples for me this past spring, on very little notice. I would not have been able to develop my method without the use of large quantities of "practice ice:" partially melted ice or ice that would not be used for any other purposes. Jeff and Vas brought back several cores of ice from Summit, Greenland, which were essential to the development of the method outlined in Chapter 3. Much of the practice ice used in earlier development work was from Dye 3 and GISP2, and I thank Devendra Lal and Harmon Craig for sharing this ice with me.

Along the way, many others have helped me with this thesis work. Lynne Talley suggested that I use a detailed model of the ocean for the mass balance model described in Chapter 2, and Neil Gordon was extremely helpful in teaching me how to run this model in Matlab. Mark Thiemens also provided guidance and advice on my work dealing with the effects of CO_2 on the isotopes of oxygen.

One chapter in this dissertation has been published elsewhere. Chapter 2 was published previously as: Headly, M.A. and J.P. Severinghaus, A method to measure Kr/N_2 ratios in air bubbles trapped in ice cores and its application in reconstructing past mean ocean temperature, *Journal of Geophysical Research*, volume 112, D19105, doi:10.1029/2006JD008317, 2007.

Support for this work came from NSF grants ATM99-05241 and OPP05-38630, as well as the Scripps graduate office.

My classmates during the first year were intellectually and socially supportive, and I am so thankful for them. The climate curricular group (Heather, Vas, Takuro, Neil) made taking classes and studying for the departmental both hard work and a lot of fun ("low to the left!").

The friends I have made at Scripps have been the best in my life, and they have made this experience unforgettable. Heather Graven has been my officemate and a best friend since the first day I came to Scripps 7 years ago. I do not know what I would have done without her friendship, understanding, and support. Jenna Munson and Christine Whitcraft are also wonderful friends, and their love and support were invaluable to me. At girls nights and lunches at Pawka, we developed lifelong friendships and made great memories. Lydia Roach has made the last few years at Scripps so much fuller, and I am so grateful for her friendship. Evan Solomon was my roommate for several years, and made hanging out at home both interesting and fun. Other friends who I'd like to thank for making my years at Scripps better ones are Mike Vardaro, Roberta Hansman, Travis Meador, Jenna Hill, Julie Robidart, Greg Dick, Roman deJesus, Wendy Strangman, Katherine Maloney, Patrick Rafter, Andrew King, Genevieve Boisvert, Neil Gordon, and Vas Petrenko.

Finally, I want to thank my family for their unconditional love and support during graduate school. I thank my mom, whom I talk to almost every day, for being a friend and constant supporter. I could not have done this without her. I thank my dad, who has always encouraged me to take the difficult and challenging path, and

whom I credit for inspiring me to pursue a graduate degree. I am also thankful to my brother, who has always been a best friend, and came out for frequent visits towards the end of graduate school, when I needed a friend around. I am so grateful to my grandparents for being source of strength and support to me. Lastly, I want to thank my boyfriend Brian Hopkinson. He has been my friend and partner, and is a daily inspiration to me. I am so grateful for his love, understanding, and support.

VITA

2001	Bachelor of Arts, Cum Laude, Northwestern University
2002	Teaching Assistant, Department of Earth Sciences University of California, San Diego
2001-2008	Research Assistant, University of California, San Diego
2008	Doctor of Philosophy, University of California, San Diego

PUBLICATIONS

Headly, M.A. and J.P. Severinghaus, A method to measure Kr/N_2 ratios in air bubbles trapped in ice cores and its application in reconstructing past mean ocean temperature, *Journal of Geophysical Research*, volume 112, D19105, doi:10.1029/2006JD008317, 2007.

FIELD OF STUDY

Major Field: Earth Sciences

Studies in Paleoclimatology
Professors Jeffrey Severinghaus and Christopher Charles

Studies in Oceanography
Professor Lynne Talley

ABSTRACT OF THE DISSERTATION

Krypton and xenon in air trapped in polar ice cores: Paleo-atmospheric measurements for estimating past mean ocean temperature and summer snowmelt frequency

by

Melissa Anne Headly

Doctor of Philosophy in Earth Sciences

University of California, San Diego, 2008

Professor Jeffrey P. Severinghaus, Chair

Krypton and xenon are highly soluble noble gases. Because they are inert, they do not react biologically or chemically, and therefore can trace purely physical processes. By taking advantage of both the inert nature of these gases and their high

solubilities, krypton and xenon can be used to reconstruct past ocean temperature variations and summer snow melt frequency.

Ocean temperature is a fundamental parameter of the climate system. It plays a vital role in the transport and storage of heat, and may play a role in regulating atmospheric CO_2, but its past variations are poorly constrained. This is due to the ambiguous nature of the benthic $\delta^{18}O$ record in ocean sediments, which reflects both deep water temperature and the $\delta^{18}O$ of the water itself (which depends on the extent of ice sheets on land). Recent studies have better constrained localized ocean temperature, but there is still need for global mean ocean temperature reconstructions.

Krypton (Kr) and xenon (Xe) are highly soluble and more soluble in colder water. The total amount of Kr and Xe in the atmosphere and ocean together are essentially constant through time, so variations in mean ocean temperature would therefore modulate atmospheric Kr and Xe abundances. Kr and Xe, measured as ratios to nitrogen (N_2), are measured in air bubbles in ice cores to reconstruct atmospheric Kr/N_2 and Xe/N_2 histories, which can then be interpreted in terms of past mean ocean temperature. These Kr/N_2 and Xe/N_2 data and their derived mean ocean temperature (noble gas temperature index, NGTI) reconstructions are presented in Chapters 2 and 3. In Chapter 2, the initial Kr/N_2 data from the LGM indicate that mean ocean temperatures were ~2.7ºC colder at that time, which is consistent with other estimates of local deep ocean temperatures. In Chapter 3, $\delta Kr/N_2$ and $\delta Xe/N_2$ time series during the last glacial termination and inception are presented. The reconstructed mean ocean temperatures (NGTI's) are consistent with our earlier

measurement and those of other studies. Additionally, these mean ocean temperature reconstructions appear to vary in step with atmospheric CO_2.

Because Kr and Xe are highly soluble, they can also be used as an indicator of ice that has melted and refrozen. Visual identification of melt layers is been used as a proxy for exceptionally warm summers temperatures, but this type of melt layer identification becomes difficult as air bubbles form air clathrates at deeper depths. The use of Kr and Xe, measured as ratios to argon (Ar), is examined in Chapter 4. Seasononality may play a role in climate change, so a proxy of summer temperatures may prove to be a powerful constraint on climate change mechanisms that invoke seasonality.

Chapter 1

Introduction

Ice cores contain information that has allowed scientists to learn much about the earth's past climate. The isotopes of the oxygen and hydrogen of the ice itself ($\delta^{18}O$, δD) have been used to reconstruct past surface temperature (Dansgaard, 1954; Dansgaard et al., 1969; Cuffey and Clow, 1997; Petit et al., 1999). Gases, such as carbon dioxide (CO_2) and methane (CH_4), in the air bubbles trapped in ice cores have also been measured to reconstruct paleo-concentrations (Petit et al., 1999; Blunier and Brook, 2001; among others). In recent years, measurements of noble gases and their isotopes in the air bubbles in ice cores have added to our knowledge about abrupt climate change (Severinghaus et al., 1998; Severinghaus and Brook, 1999; Grachev and Severinghaus, 2003a and 2003b; Kobashi et al., 2007). Because noble gases are inert, they move throughout the earth's systems without reacting, and can therefore record physical processes.

In this thesis, the first measurements of paleo-atmospheric $\delta Kr/N_2$ and $\delta Xe/N_2$ are contributed to the ice core literature. We have taken advantage of the relationship between the solubility of Kr and Xe and the temperature of the water in which it is dissolved to discern past variations in the global mean ocean temperature. We have also used the solubilities of Kr and Xe to identify melt layers in ice cores, which are indicative of warm summers.

Ocean Temperature Reconstructions

It was originally thought that deep ocean temperature did not change significantly between cold glacial and warm interglacial periods. The $\delta^{18}O$ of the $CaCO_3$ of benthic foraminifera ($\delta^{18}O_{benthic}$) recorded in ocean sediments reflects both

ocean temperature and the $\delta^{18}O$ of the water itself (which depends on ice volume) (Shackleton, 2000). Early studies proposed that the glacial-interglacial oscillations in the $\delta^{18}O_{benthic}$ record mainly reflect changes in ice volume (Shackleton, 1967; Duplessy et al., 1970). Subsequent work by Schrag and others (1996) allowed for more direct measurement of the $\delta^{18}O$ in sea water. They measured the $\delta^{18}O$ in sediment pore fluids and modeled the attenuation from the last glacial maximum (LGM, 20,000 years ago) to reconstruct the LGM value of sea water $\delta^{18}O$ ($\delta^{18}O_{sw}$). By subtracting their pore fluid-derived $\delta^{18}O_{sw}$ from $\delta^{18}O_{benthic}$, Schrag et al. (1996) could isolate the $\delta^{18}O$ change due to deep ocean temperature change. They found that deep waters were ~4ºC colder during the LGM. Adkins et al. (2002) continued this work, measuring pore fluid $\delta^{18}O$ in more geographically diverse sediment cores, and also adding pore fluid chlorinity measurements. Their results supported the earlier work by Schrag et al. (1996), finding that the LGM deep ocean was ~4ºC colder, and ~1 psu saltier than today. Another interesting conclusion from this study was that the Southern Ocean appeared to be the saltiest water mass during the LGM, as opposed to North Atlantic Deep Water, which is more saline than other deep waters today. Based on their reconstructed deep water temperatures and salinities, Adkins et al. (2002) concluded that the deep ocean was flooded with cold, salty water most likely formed in the Southern Ocean.

Other investigators have used regressions between coral-derived relative sea level (RSL) and $\delta^{18}O_{benthic}$ to identify the $\delta^{18}O$ due to sea level, and then isolate the $\delta^{18}O$ due to ocean temperature (Waelbroeck et al., 2002; Cutler et al., 2003). Using

this method, Waelbroeck et al. (2002) found that the deep North Atlantic, Southern Indian, and Pacific Oceans were ~4ºC, 3ºC, and 2ºC colder than today during the LGM. Cutler et al. (2003) found similar results, reconstructing deep ocean temperatures that were ~2ºC colder in the deep Pacific, and ~4ºC colder in the deep Atlantic during the LGM. Martin et al. (2002) produced consistent deep ocean temperature estimates during the LGM using Mg/Ca ratios in benthic foraminifera, finding that the LGM Pacific deep ocean was ~2.5ºC colder than today. Using a nearby core in a subsequent study, Martin et al. (2005) found that the deep ocean may have been ~4ºC colder during the LGM. Bintanja et al. (2005) used a coupled model of ocean temperature and Northern Hemisphere ice sheets, forced to match a stacked $\delta^{18}O_{benthic}$ record, to separate out the ice volume and temperature effects from the benthic $\delta^{18}O$ record. They found that deep ocean temperatures decreased rapidly by 2-2.5ºC at the glacial inception, cooling to ~ $\leq$3ºC by the end of the glacial period.

Glacial-interglacial cycles and carbon dioxide

The $\delta^{18}O_{benthic}$ curves described above show fluctuations between longer cold periods (glacial periods) and shorter, warmer periods (interglacial periods). From ~3 million – 800,000 years before present (B.P.), glacial-interglacial cycles appeared to have shorter periods of ~40,000 years (40 kyr), after which time (at ~800-750 kyr) they switched from 40-kyr to 100-kyr oscillations (Raymo, 1997). These 100-kyr glacial-interglacial cycles are well documented in the ice cores (Petit et al., 1999; Jouzel et al., 2007). Milankovitch theory holds that that these glacial-interglacial oscillations may be modulated by variations in isolation (Hays et al., 1976), the three

main variations being precession, obliquity, and eccentricity, with timescales of ~23-kyr, 41-kyr, and 100-kyr, respectively. The cause of the shift to 100-kyr glaciations at ~800 kyr B.P. is puzzling in that the eccentricity insolation forcing (with ~100-kyr periods) needs amplification to cause the observed changes in climate (Hays et al., 1976; Imbrie and Imbrie, 1980). Some have suggested that ice sheet dynamics or the carbon cycle may be part of the explanation for the 100-kyr cycles observed in the climate record (Imbrie and Imbrie, 1980; Shackleton, 2000).

Measurements of temperature ($\delta^{18}O$, δD) and CO_2 in ice cores show that both of these climate parameters varied on 100-kyr glacial-interglacial cycles and appear to be well correlated (Petit et al., 1999; Jouzel et al., 2007; Lüthi et al., 2008). There are a variety of explanations for these glacial-interglacial CO_2 oscillations. A small portion of the CO_2 drawdown during glacial periods is likely due to the increased solubility of CO_2 in colder glacial ocean waters. There is evidence that the ocean was more stratified during glacial periods (Francois et al., 1997; Adkins et al., 2002; Sigman et al., 2004), which may have allowed for CO_2 to be sequestered in the deep ocean, preventing it from coming in contact with the atmosphere. This increase in ocean stratification may have been related to a shift in the importance of temperature versus salinity in the equation of state of seawater. As the ocean cooled during glacial times, seawater density became less dependent on temperature and more sensitive to changes in salinity. Pore water evidence indicates that the Southern Ocean was saltier than the North Atlantic (today's most saline water mass), and that Southern-source deep water may have flooded of the deep ocean in both the Atlantic and Pacific (Adkins et al., 2002). Brine rejection during sea ice formation is a likely candidate to

explain this increase in Southern Ocean salinity. As further evidence for increased ocean stratification during glacial periods, a modeling study by de Boer et al. (2007) shows that as the mean ocean temperature cools (as in a glacial period), overturning decreases, enhancing stratification. Additionally, Antarctic westerlies may have migrated equatorward during glacials, reducing the associated Southern Ocean upwelling (Toggweiler et al., 2006).

Sigman et al. (2007) and Toggweiler et al. (2006) suggest that this enhanced stratification allowed for CO_2 to remain in the deep ocean, preventing it from reaching the atmosphere. Toggweiler (2006) calls for a deep ocean stratification, though, while Sigman et al. (2007) suggest a near-surface stratification. Keeling and Stephens (2001) have postulated that Southern Ocean waters, near the freezing point, flooded the deep ocean during the glacial period. Keeling and Stephens (2001) also proposed that the Southern Ocean water would be relatively salty, as later found by Adkins et al. (2002). Because this water was near the freezing point, permanent sea ice may have formed during the winter (with stratification present in the summer), preventing CO_2 exchange with the atmosphere and causing the atmospheric decrease in CO_2. Our estimates of mean ocean temperature presented in this dissertation may help to constrain these theories, elucidating the connection between the ocean and atmospheric CO_2.

Organization of the dissertation

Conceptual model of $\delta Kr/N_2$ and $\delta Xe/N_2$ and ocean temperature

In Chapter 2, we present a model of $\delta Kr/N_2$ and $\delta Xe/N_2$ that result from changing average ocean temperature. Assuming mass balance, the total amount of Kr, Xe, and N_2 in the atmosphere and ocean together should remain constant. Krypton and xenon are more soluble in colder water (Figure 1.1). Therefore, as the ocean cools, more Kr and Xe (and to a much lesser extent, N_2) will be dissolved in the ocean. Because the total amount of these gases in the atmosphere-ocean system is constant, an increase in oceanic gas concentrations in a cooler world would cause a resultant decrease in atmospheric abundances. We calculate the expected change in atmospheric $\delta Kr/N_2$ and $\delta Xe/N_2$, and then compare the modeled values to our measurements of the paleo-atmospheric $\delta Kr/N_2$ and $\delta Xe/N_2$ from ice cores.

In order to estimate the Kr, Xe, and N_2 oceanic inventories, we use the potential temperature and density data from Levitus (1994), and the Kr, N_2, and Xe solubilities of Weiss and Kyser (1978), Weiss (1970), and Wood and Caputi (1966), respectively. We then subtract (or add) temperatures uniformly to simulate cooling (or warming) to calculate past inventories. This model assumes that gases are in equilibrium with the atmosphere, which is not necessarily the case. It is possible that gases are super-saturated in the deep waters due to rapid cooling at the surface followed by sinking (Hamme and Severinghaus, 2007), or that they are super-saturated owing to bubble injection (Hamme and Emerson, 2002). Another possibility is that geothermal heating of a stagnant deep water mass could increase ocean temperature without changing the Kr and Xe (in contrast to a surface warming) (Adkins et al., 2005). These caveats should not significantly affect our estimates, and will be discussed in detail in Chapter 2.

Initial LGM $\delta Kr/N_2$ and $\delta Xe/N_2$ data

In addition to the model description, the initial $\delta Kr/N_2$ and $\delta Xe/N_2$ data during LGM are shown and discussed in Chapter 2. The measurement method development is detailed as well. The $\delta Kr/N_2$ measured in GISP2 ice from the late Holocene are within error of 0‰, as expected, and the mean LGM $\delta Kr/N_2$ is -1.34‰ ± 0.37‰, corresponding to a 2.7 ± 0.6ºC temperature change. There was too much scatter in this initial $\delta Xe/N_2$ data to interpret it in terms of ocean temperature change. The $\delta Kr/N_2$-derived LGM mean ocean temperature estimate (~2.7ºC colder than today) is consistent with other estimates of LGM deep ocean temperature. Schrag et al. (1996) and Adkins et al. (2002) use pore fluid measurements to reach an estimate of LGM cooling of ~4ºC, while Cutler et al. (2003) and Waelbroeck et al. (2002) used coral-derived RSL-$\delta^{18}O_{benthic}$ regressions to find LGM deep ocean temperatures ranging from ~2ºC (Pacific) to 4ºC (Atlantic) colder than today.

$\delta Kr/N_2$ and $\delta Xe/N_2$ during the last glacial termination and inception

In Chapter 3, records of $\delta Kr/N_2$ and $\delta Xe/N_2$ spanning the last glacial termination (~24-14 kyr B.P.) and inception (~123-104 kyr B.P.) are presented. The measurement procedure, which differs from that of Headly and Severinghaus (2007) in Chapter 2, and its development are also described in this chapter. This method called for a 10-fold increase in sample size, allowing for better $\delta Kr/N_2$ and $\delta Xe/N_2$ precision, as well as making the measurement of $\delta^{86}Kr$ possible. For clarity, we refer

to the gravitationally and thermally corrected $\delta Kr/N_2$ and $\delta Xe/N_2$ data presented in Chapter 3 as Kr* and Xe*. Reconstructed mean ocean temperatures based on Kr* and Xe* are solubility-weighted mean ocean temperatures, so we define this temperature estimate as Noble Gas Temperature Index (NGTI). NGTI's appear to vary in step with atmospheric CO_2, rising at ~18 kyr B.P. during deglaciation, and falling at ~115 kyr B.P. at the glacial inception. These findings may have climate change implications in terms of the connection between ocean temperature and CO_2, and may place constraints on proposed mechanisms of climate change.

δKr/Ar and δXe/Ar as indicators of melt layers

In Chapter 4, the use of δKr/Ar and δXe/Ar as indicators of melt layers is discussed. In addition to signifying past variations in ocean temperature, Kr and Xe measurements in ice cores can act as a proxy for summer warmth. Melt layers in ice cores form when temperatures are anomalously warm (T > 1ºC) (Das and Alley, 2005). Scientists have used melt layer frequency as an indicator of warm summers. Typically, melt layer analyses have been limited to visual identification and counting of melt layers. Visual identification of melt layers becomes impossible as air bubbles in ice form air clathrates at deeper depths in the ice core (~800-1200m) (Miller, 1969). We have found that δKr/Ar and δXe/Ar are strongly elevated and have a unique signature in melt layers. Kr and Xe are highly soluble gases, and are more soluble than Ar (Figure 1.1). We propose that these differences in solubilities cause elevated δKr/Ar and δXe/Ar in melt layers. Also, δXe/Ar and δKr/Ar have unique relationship

in melt layers: δXe/Ar tends to be ~3 times as enriched as δKr/Ar, which is consistent with theoretical predictions. We have modeled the effects of melt, gravitational settling, and gas loss on δKr/Ar, δXe/Ar, and δ^{40}Ar to better understand the mechanisms affecting these gas ratios.

References

Adkins, J. F., K. McIntyre, and D. P. Schrag (2002), The salinity, temperature, and $\delta^{18}O$ of the glacial deep ocean, *Science*, *298*, 1769-1773.

Adkins, J. F., A. P. Ingersoll, C. Pasquero (2005), Rapid climate change and conditional instability of the glacial deep ocean from the thermobaric effect and geothermal heating, *Quaternary Science Reviews*, *24*, 581-594.

Blunier, T. and E.J. Brook (2001), Timing of millennial-scale climate change in Antarctica and Greenland during the last glacial period, *Science*, *291*, 109-112.

Cuffey, K.M., and G.D. Clow (1997), Temperature, accumulation, and ice sheet elevation in central Greenland through the last deglacial transition, *Journal of Geophysical Research*, 102:26383-26396.

Cutler, K. B., R. L. Edwards, F. W. Taylor, H. Cheng, J. Adkins, C. D. Gallup, P. M. Cutler, G. S. Burr, and A. L. Bloom (2003), Rapid sea-level fall and deep-ocean temperature change since the last interglacial period, *Earth Planet. Sci. Lett.*, *206*, 253-271.

Dansgaard, W. (1954), The O18-abundance in fresh water, *Geochim. et Cosmochim. Acta, 6*, 241.

Dansgaard, W., S.J. Johnsen, J. Møller, and C.C. Langway, Jr. (1969), One thousand centuries of climatic record from Camp Century on the Greenland Ice Sheet, *Science*, *166*(3903), 377-381.

Das, S.B. and R.B. Alley (2005), Characterization and formation of melt layers in polar snow: observations and experiments from West Antarctica, *Journal of Glaciology*, *51*(173), 307-312.

de Boer, A.M., D.M. Sigman, J.R. Toggweiler, J.L. Russel (2007), Effect of global ocean temperature change on deep ocean ventilation, *Paleoceanography*, *22*, PA2210, doi: 10.1029/2005PA001242.

Duplessy, J.C., C. Lalou, and A.C. Vinot (1970), Differential isotopic fractionation in benthic foraminifera and paleotemperatures reassessed, *Science*, *168*, 250-251.

Francois, R., M.A. Altabet, E.-F. Yu, D.M. Sigman, M.P. Bacon, M. Frank, G. Bohrmann, G. Bareille, and L.D. Labeyrie (1997), Contribution of Southern Ocean surface-water stratification to low atmosphere CO_2 concentrations during the last glacial period, *Nature*, *389,* 929-935.

Grachev, A.M. and J.P. Severinghaus (2003a), Laboratory determination of thermal diffusion constants for $^{29}N_2/^{28}N_2$ in air at temperatures from -60 to 0ºC for reconstruction of magnitudes of abrupt climate changes using the ice core fossil-air paleothermometer, *Geochimica et Cosmochimica Acta*, *67*(3), 345-360.

Grachev, A.M. and J.P. Severinghaus (2003b), Determining the thermal diffusion factor for 40Ar/36Ar in air to aid paleoreconstruction of abrupt climate change, *Journal of Physical Chemistry A*, *107*, 4636-4642.

Hays, J.D., J. Imbrie, and N.J. Shackleton (1976), Variations in the earth's orbit: Pacemaker of the ice ages, *Science*, *194*(4270), 1121-1132.

Hamme, R. C., and S. R. Emerson (2002), Mechanisms controlling the global oceanic distribution of inert gases argon, nitrogen, and neon, *Geophys. Res. Lett.*, *29*(23), 2120, doi:10.1029/2002GL015273.

Hamme, R. C., and J. P. Severinghaus (2007), Trace gas disequilibria during deep-water formation, *Deep-Sea Research Part I, 54*, 939-950.

Headly, M.A. and J.P. Severinghaus (2007), A method to measure Kr/N_2 ratios in air bubbles trapped in ice cores and its application in reconstructing past mean ocean temperature, *Journal of Geophysical Research*, *112*, D19105, doi:10.1029/2006JD008317,.

Imbrie, J. and J.Z. Imbrie (1980), Modeling the climatic response to orbital variations, *Science*, *207*(4434), 943-953.

Jouzel, J., V. Masson-Delmotte, O. Cattani, G. Dreyfus, S. Falourd, G. Hoffmann, B. Minster, J. Nouet, J.M. Barnola, J. Chappellaz, H. Fischer, J.C. Gallet, S. Johnsen, M. Leuenberger, L. Loulergue, D. Luethi, H. Oerter, F. Parrenin, G. Raisbeck, D. Raynaud, A. Schilt, J. Schwander, E. Selmo, R. Souchez, R. Spahni, B. Stauffer, J.P. Steffensen, B. Stenni, T.F. Stocker, J.L. Tison, M. Werner, and E.W. Wolff (2007), Orbital and millennial Antarctic climate variability over the past 800,000 years, *Science*, *317*, 793-797.

Kobashi, T., J.P. Severinghaus, E.J. Brook, J.-M. Barnola, A. Grachev (2007), Precise timing and characterization of abrupt climate change 8,200 years ago from air trapped in polar ice, *Quaternary Science Reviews*, *26*, 1212-1222.

Levitus, S. (1994), World Ocean Atlas, NOAA, Washington D.C.

Martin, P. M., D. W. Lea, Y. Rosenthal, N. J. Shackleton, M. Sarnthein, and T. Papenfuss (2002), Quaternary deep sea temperature histories derived from benthic foraminiferal Mg/Ca, *Earth Planet. Sci. Lett.*, *198*, 193-209.

Martin, P., D. Archer, D.W. Lea (2005), Role of deep sea temperature in the carbon cycle during the last glacial, *Paleoceanography*, *20*, PA2015, doi:10.1029/2003PA000914

Miller, S.L. (1969), Clathrate Hydrates of Air in Antarctic Ice, *Science*, *165*(3892), 489-490.

Petit, J.R., J. Jouzel, D. Raynaud, N.I. Barkov, J.-M. Barnola, I. Basile, M. Benders, J. Chappellaz, M. Davis, G. Delayque, M. Delmotte, V.M. Kotlyakov, M. Legrand, V.Y. Lipenkov, C. Lorius, L. Pépin, C. Ritz, E. Saltzman, and M. Stievenard (1999), Climate and atmospheric history of the past 420,000 years from the Vostok ice core, Antarctica, *Nature*, *399*, 429-436.

Schrag, D. P., G. Hampt, and D. W. Murray (1996), Pore Fluid Constraints on the Temperature and Oxygen Isotopic Composition of the Glacial Ocean, *Science*, *272*, 1930-1932.

Shackleton, N. (1967), Oxygen isotope analyses and Pleistocene temperatures re-assessed, *Nature, 215*, 15-17.

Shackleton, N. (2000), The 100,000-year ice-age cycle identified and found to lag temperature, carbon dioxide, and orbital eccentricity, *Science, 289*(5486), 1897-1902.

Severinghaus, J.P. and E.J. Brook (1999), Abrupt climate change at the end of the last glacial period inferred from trapped air in polar ice, *Science, 286*, 930-934.

Severinghaus, J.P., T. Sowers, E.J. Brook, R.B. Alley, M.L. Bender (1998), Timing of abrupt climate change at the end of the Younger Dryas interval from thermally fractionated gases in polar ice, *Nature*, *391*, 141-146.

Sigman, D.M., S.L. Jaccard, G.H. Haug (2004), Polar ocean stratification in a cold climate, *Nature*, *428*, 59-63.

Sigman, D.M., A.M. de Boer, G.H. Haug (2007), Antarctic stratification, atmospheric water vapor, and Heinrich events: a hypothesis for late Pleistocene deglaciations, *Ocean Circulation: Mechanisms and Impacts*, Geophysical Monograph Series 173, 10.1029/172GM21.

Toggweiler, J.R., J.L Russel, and S.R. Carson (2006), Midlatitude westerlies, atmospheric CO_2, and climate change during the ice ages, *Paleoceanography*, *21*, PA2005, doi:10.1029/2005PA001154.

Waelbroeck, C., L. Labeyrie, E. Michel, J. C. Duplessy, J. F. McManus, K. Lambeck, E. Balbon, and M. Labracherie (2002), Sea-level and deep water temperature changes

derived from benthic foraminifera isotopic records, *Quaternary Science Reviews*, *21*, 295-305.

Weiss, R. F. (1970), The solubility of nitrogen, oxygen and argon in water and sea water, *Deep Sea Research*, *17*, 721-735.

Weiss, R.F. and T. K. Kyser (1978), Solubility of krypton in water and seawater, *J. Chem. Eng. Data*, *23*(1), 69-72.

Wood, D. and R. Caputi (1966), Solubilities of Kr and Xe in fresh and seawater, *Tech. rep.*, U. S. Naval Radiological Defense Laboratory, San Francisco, CA.

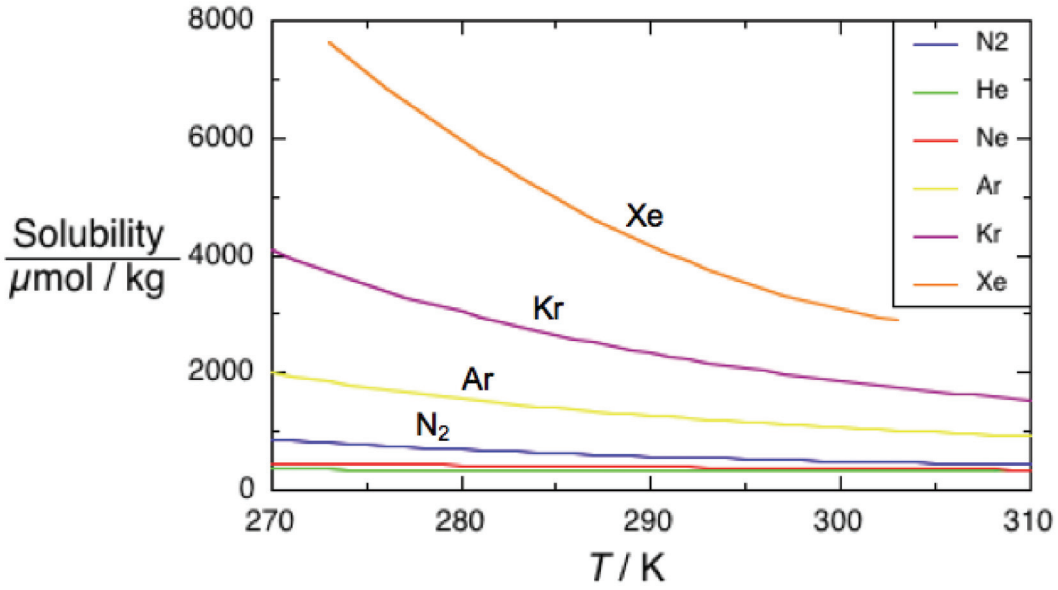

Figure 1.1. Solubility (µmol/kg) for Xe (orange), Kr (purple), Ar (yellow), N_2 (blue), Ne (red), and He (green) vs. water temperature (K).

Chapter 2

A Method to Measure Kr/N_2 Ratios in Air Bubbles Trapped in Ice Cores, and its Application in Reconstructing Past Mean Ocean Temperature

Abstract

We describe a new method for precise measurement of Kr/N_2 ratios in air bubbles trapped in ice cores, and a reconstruction of atmospheric Kr/N_2 during the last glacial maximum (LGM) ~20,000 years ago. After gravitational correction, the Kr/N_2 record in ice cores should represent the atmospheric ratio, which in turn should reflect past ocean temperature change due to the dependence of gas solubility on temperature. The increase in krypton inventory in the glacial ocean due to higher gas solubility in colder water causes a decrease in the atmospheric inventory of krypton. Assuming Kr and N_2 inventories in the ocean-atmosphere system are conserved, we use a mass balance model to estimate a mean ocean temperature change between the LGM and today. We measured Kr/N_2 in air bubbles in Greenland (GISP2) ice from the late Holocene and LGM, using the present atmosphere as a standard. The late Holocene $\delta Kr/N_2$ means from two sets of measurements are not different from zero (+0.07 ± 0.30‰ and –0.14 ± 0.93‰), as expected from the relatively constant climate of the last millennium. The mean $\delta Kr/N_2$ in air bubbles from the LGM is –1.34 ± 0.37‰. Using the mass balance model, we estimate that the mean temperature change between the LGM ocean and today's ocean was 2.7 ± 0.6°C. Although this error is large compared to the observed change, this finding is consistent with most previous estimates of LGM deep ocean temperature based on foraminiferal $\delta^{18}O$ and sediment pore water $\delta^{18}O$ and chlorinity.

Introduction

Deep ocean temperature is a fundamental parameter of the climate system, but its past variations remain poorly known despite decades of research. This is due mainly to the inherent ambiguity of oxygen isotope ($\delta^{18}O$) records from benthic foraminifera, which are affected by both temperature and ice volume (Shackleton, 2000). In an effort to separate the temperature from the ice volume signal in the benthic $\delta^{18}O$ record, Schrag et al. (1996) measured the $\delta^{18}O$ in sediment pore waters. These pore water studies provided single estimates of deep ocean cooling at the last glacial maximum (LGM) at several different core sites. Their conclusion was that the deep ocean temperature was ~4°C cooler during the LGM than it is today, near the freezing point of seawater (Schrag et al., 1996). However, this result only applies to the local temperature at the sediment core sites. Changes in local hydrography can obscure the global signal (Adkins and Schrag, 2001). The deep ocean is heterogeneous from place to place, limiting the representativeness of these sites. Others have also tried to reconstruct deep ocean temperature by using benthic Mg/Ca ratios (Martin et al., 2002) and regressions of benthic $\delta^{18}O_{calcite}$ vs. reconstructed relative sea level from fossil corals (Waelbroeck et al., 2002, Cutler et al., 2003). Like Schrag et al.'s study, these are estimates of local deep ocean temperature. Furthermore, Mg/Ca ratios in benthic foraminifera can be affected by diagenesis, in addition to temperature (Martin et al., 2002).

We use $\delta Kr/N_2$ measured in air bubbles in ice cores as a new proxy for past ocean temperature variations. The dissolved concentration of krypton in seawater

varies with ocean temperature, causing a complementary shift in its atmospheric abundance (Craig and Weins, 1996). Krypton is measured as a ratio to nitrogen concentration because nitrogen does not respond as sensitively to ocean temperature due to its low solubility in water, and direct measurement of the absolute krypton inventory is impractical. Molecular weight primarily governs the solubility of gases in solution, so krypton is more soluble than the lighter gases. Solubility for gases increases with lower water temperatures, and its dependence on temperature becomes more pronounced at lower temperatures. The relative fractions of krypton in the present day atmosphere and ocean are approximately 98% and 2%, respectively, and 99.5% and 0.5% for nitrogen (Schlesinger, 1997, Weiss and Kyser, 1978, Weiss, 1970).

The $\delta Kr/N_2$ measurements should provide an estimate of whole-ocean average temperature change because Kr and N_2 are well mixed in the atmosphere. These atmospheric gases integrate global solubility-driven air-sea fluxes. Additionally, $\delta Kr/N_2$ measurements in ice cores have the potential to resolve a time series of ocean temperature change because they provide discrete samples of the past atmosphere, in contrast to the pore water studies which are limited to a single (LGM) point.

Hypothesis and Conceptual Model

In order to interpret the $\delta Kr/N_2$ measured in ice cores as a proxy of past mean ocean temperature, we calculate expected paleo-atmospheric concentrations of Kr and N_2 using a conceptual model of the ocean-atmosphere system. A mass balance

approach is used, conserving the total inventory of Kr and N_2 in the ocean-atmosphere system between the LGM and today, as shown in (2.1) and (2.2) below.

$$Kr_{\text{present ocean}} + Kr_{\text{present atmosphere}} = Kr_{\text{total}} = Kr_{\text{LGM ocean}} + Kr_{\text{LGM atmosphere}} \quad (2.1)$$

$$N_{2\text{present ocean}} + N_{2\text{present atmosphere}} = N_{2\text{total}} = N_{2\text{LGM ocean}} + N_{2\text{LGM atmosphere}} \quad (2.2)$$

By conservation of mass, the difference between the LGM ocean inventory and today's inventories must have been taken up by the LGM atmosphere, as these gases are inert or nearly so, and sources and sinks to the ocean-atmosphere system are negligible on the timescale of interest. We assume that nitrogen fixation and denitrification have a negligible effect on the total N_2 inventory. This assumption is supported by the observation that the entire denitrifiable inventory of nitrogen represents less than 0.01% of the atmospheric inventory (Schlesinger, 1997).

For clarity, we note that gas content and heat content in the ocean are set at the surface outcrop where air-sea equilibration occurs (Hamme and Emerson, 2002). As a water parcel moves through the ocean, these quantities are conserved. There is no time lag of one versus the other. Therefore, the amount of Kr and N_2 in the ocean is indicative of the average temperature of the ocean at any point in time, making the consideration of ocean mixing time in our calculation unnecessary.

The current oceanic Kr and N_2 inventories ($Kr_{\text{present ocean}}$ and $N_{2\text{present ocean}}$, respectively) are estimated by using a multi-box model of the ocean that incorporates the distribution of observed temperatures. The ocean is divided into 1°-latitude x 1°-longitude boxes with varying depth segments (ocean depth is divided into 33 depth

intervals). $Kr_{present\ ocean}$ and $N_{2present\ ocean}$ are calculated using the krypton solubility algorithms of Weiss and Kyser (1978), and those for nitrogen of Weiss (1970). Dissolved gases in the ocean are assumed to be at equilibrium with the atmosphere. This assumption may not be strictly correct (Hamme and Severinghaus, 2007), but it will not affect our calculation substantially. Ocean temperature data used in our calculations are given as the mean temperature of each grid box used in the model (Levitus, 1994). Salinity is assumed to be 35 psu in all boxes.

The Kr and N_2 solubilities (in mol/μg) are multiplied by the mass of the ocean in each grid box in order to convert them to Kr and N_2 inventories in moles, as shown in (2.3) and (2.4). The Levitus density data (ρ) are multiplied by the grid box's volume (V) to calculate the mass of each grid box. The model does not include bottom topography, and therefore does not take into account varying bottom depths in calculating ocean volume. Rather, data taken at depths deviating from the 33 standard depth levels are interpolated from the observed depth to a standard depth. The standard depths are then used in calculating ocean volume. The inventories of Kr ($Kr_{present\ ocean}$) and N_2 ($N_{2present\ ocean}$) for n grid boxes are calculated as shown below.

$$Kr_{present\ ocean} = \sum_{i=1}^{n} [G]_{Kr}(T,S) \times \rho \times V \qquad (2.3)$$

$$N_{2present\ ocean} = \sum_{i=1}^{n} [G]_{N_2}(T,S) \times \rho \times V \qquad (2.4)$$

The Kr and N_2 in each box are summed to obtain a whole-ocean inventory of Kr and N_2 in today's ocean ($Kr_{present\ ocean}$ and $N_{2present\ ocean}$), which are used in equations (2.1) and (2.2). We find $Kr_{present\ ocean}$ and $N_{2present\ ocean}$ to be 4.35×10^{12} moles and 6.52×10^{17} moles, respectively.

The second terms in equations (2.1) and (2.2), $Kr_{present\ atmosphere}$ and $N_{2present\ atmosphere}$, are calculated by multiplying the known mole fraction of these gases in today's atmosphere by the total moles of air, 1.77×10^{20} moles (calculated using the mass of the atmosphere and the molecular weight of dry air from Schlesinger, 1997). The calculated atmospheric Kr and N_2 inventories are 2.02×10^{14} moles and 1.38×10^{20} moles, respectively.

The first terms on the right side of equations (2.1) and (2.2), $Kr_{LGM\ ocean}$ and $N_{2LGM\ ocean}$, are calculated using the ocean box model described above. The temperature variable used to calculate the present oceanic inventories is reduced by 0.5°C to 6.0°C to simulate a wide range of mean ocean temperature changes between the LGM and today. Higher salinity of the LGM ocean is also included in the model, assuming an LGM salinity of 36 psu (Adkins and Schrag, 2001). The LGM ocean model also accounts for the reduction in sea level (and thus ocean volume) at that time. Measurements from past coral terraces indicate that sea level was ~120m lower during the LGM (Fairbanks, 1989), which corresponds to a 3% decrease in ocean volume. Another expected consequence of lower sea level during the LGM is an increase in sea level barometric pressure. This pressure increase is due to the displacement of water from the ocean and onto land in the form of ice sheets, decreasing surface pressure over land, and increasing it over the lower sea level. We

estimate the increase in sea level pressure resulting from a 120m-decrease in sea level as follows:

$$p/p_o = e^{-z/H} \qquad (2.5).$$

The scale height of the atmosphere (H) is assumed to be 7600m in deep water formation regions, and sea level height (z) at the LGM is –120m (in reference to today's sea level). This yields 1.0159 for p/p_o, the ratio of LGM sea level pressure (at z = -120m), to the pressure at sea level today (at z = 0). Henry's law states that partial pressure and dissolved concentration of a gas are directly proportional, so the Kr and N_2 oceanic inventories would increase by 1.59% due to higher sea level pressure during the LGM. This calculation neglects the fact that ice sheets displace air at slightly higher elevations (and thus lower air densities) than does seawater, although this fact is largely compensated by the lower density of ice than water. This calculation also neglects possible synoptic changes in sea level barometric pressure, which are currently unknown.

Other potential factors that could influence the amount of Kr and N_2 in the LGM ocean include changes in wind patterns and diapycnal mixing. It is widely accepted that winds were stronger during the LGM, as suggested by increased dust deposits in ice cores (Crowley and North, 1991). Stronger winds or changes in wind patterns during the LGM could alter the amount of bubble entrainment, or injection, into ocean waters. Hamme and Emerson (2002) have shown that air bubble injection preferentially increases the abundance of less soluble gases (including N_2) in the

ocean. Therefore, an increase in bubble injection would cause our measurements to be biased towards lower $\delta Kr/N_2$ values, and an underestimation of ocean temperature change. Bubble injection is unlikely to have a significant influence on our measurements. The effect of doubling bubble injection would change $\delta Kr/N_2$ by ~0.2‰, which is less than measurement error (0.37‰) (Hamme and Severinghaus, 2007). Likewise, although diapycnal mixing is suggested to have changed between the LGM and today (Watson and Naveira, 2006, Egbert et al., 2004), it is unlikely to affect our measurements significantly. Diapycnal mixing within the ocean, isolated from the surface, would have no affect on atmospheric $\delta Kr/N_2$ because we are concerned with Kr and N_2 abundances, rather than their saturation state. In a case where diapycnal mixing creates an intermediate depth water parcel that outcrops at the surface, the effect on $\delta Kr/N_2$ values should only be ~0.1-0.2‰ at most, which is within our measurement error.

The last terms in equations (2.1) and (2.2), $Kr_{LGM\ atmosphere}$ and $N_{2LGM\ atmosphere}$, are measured in the air bubbles in ice from the LGM as the ratio, Kr/N_2. $Kr_{LGM\ atmosphere}$ and $N_{2LGM\ atmosphere}$, are also modeled using the mass balance ocean-atmosphere model, and compared to the measurements to interpret the results. The total amount of Kr and N_2 in the ocean and atmosphere together are constant on these time scales, so the increase in LGM ocean inventories due to ocean temperature change must cause a resultant decrease in LGM atmospheric inventories. Therefore, it follows from (2.1) and (2.2) that

$$Kr_{LGM\ atmosphere} = Kr_{total} - Kr_{LGM\ ocean} \qquad (2.6)$$

$$N_{2LGM\ atmosphere} = N_{2total} - N_{2LGM\ ocean} \qquad (2.7)$$

where Kr_{total} and N_{2total} are the sum of today's atmosphere and ocean inventories of each gas. The modeled Kr and N_2 in the LGM atmosphere vary with mean ocean temperature change (Figure 2.1). In this study, the Kr/N_2 ratio is expressed in the customary delta notation, which describes the deviation of the sample Kr/N_2 from a standard Kr/N_2 ratio:

$$\delta Kr/N_2 = \left[\left(Kr/N_{2sample} / Kr/N_{2standard}\right) - 1\right] \times 10^3‰ \qquad (2.8)$$

The standard used is the ratio of Kr/N_2 present in today's atmosphere (from samples taken on the SIO pier in La Jolla, CA).

Analytical technique

The analytical approach used in this study is based primarily on the techniques outlined by Severinghaus et al. (2003) and Sowers et al. (1989). Ice samples of approximately 50-60 grams are cut using a band saw in a walk-in freezer, kept at –20°C. Edges (5mm) of the ice sample are removed using a band saw to expose fresh ice surfaces. The long axis of the sample is parallel to the ice core, so that each sample is typically an average of several annual layers. The piece is then cut into 2-4 smaller pieces to fit into the extraction vessel. The extraction vessel is a custom-made 400-cm^3 glass vessel. The ice sample and two glass-covered magnetic

stir bars are lowered into the extraction vessel with chilled tongs. Two stir bars were found to be more effective than one in extracting krypton during the transfer of gas from the extraction vessel to the sample dip tube (Figure 2.2).

The extraction vessel is then attached to the vacuum line using a gold-plated copper conflat gasket, and the ambient air is pumped out of the vessel for 40 minutes. The extraction vessel is kept in an ethanol dewar at -20°C during the pump down. Sublimation and subsequent water vapor flow during pumping effectively remove any gases adsorbed onto the ice (Severinghaus et al., 2003). The total pressure is measured to monitor outgassing at 5 minutes and at the end of the 40 minutes of pumping, at which point the pressure should reduce to the vapor pressure of water over ice at -20ºC. After 40 minutes, the extraction vessel is sealed, and the ice sample is melted using a warm bath, releasing the trapped gas in the ice. The trapped gas is transferred for 20 minutes through a -100°C glass water trap. The gas transfer is accomplished by freezing the sample at 4K in a dip tube that has been lowered into a tank of liquid helium. Connections are made using Ultratorr fittings with Viton O-rings. During transfer, two stir bars are used to agitate the melted ice to ensure complete extraction of krypton, which is difficult to degas because of its high solubility. The residual pressure after the 20-minute transfer is checked to ensure complete transfer. The gas in the dip tube comprises approximately 4 standard cm^3.

We have modified the gas extraction method outlined in Severinghaus et al., 2003 to ensure complete extraction of krypton. We varied several parameters to determine the optimal gas extraction and transfer conditions. These parameters include transfer time through the water trap into the sample tube in liquid He, the

number of magnetic stir bars used, and temperature of the glass vessel (which is maintained with a warm bath during the transfer). We interpret the degree of Kr extracted in terms of the δKr/Ar of late Holocene ice in reference to the current atmosphere. Ideally, the δKr/Ar measurement should be 0‰ because neither krypton nor argon's atmospheric abundance should have changed significantly during the late Holocene. Because of potential Ar gas loss out of the ice, we expected the actual δKr/Ar measured in Holocene ice to be slightly higher than 0‰ (Severinghaus et al., 2003 found +4‰). Kr/N_2 measurement (which apparently is not affected by gas loss; Severinghaus and Battle, 2006) was not yet possible at the time of this method development.

The δKr/Ar results from the gas extraction tests are shown in Figure 2.2. The most complete extraction of krypton from the melted ice occurred with longer transfer times and the use of two stir bars. A transfer time of at least 20 minutes resulted in higher measured δKr/Ar values, which are indicative of a more complete krypton extraction. An additional stir bar (two stir bars total), used to increase the agitation of the melt water and encourage outgassing, likewise appeared to increase the δKr/Ar values. We also tested the addition of a warm bath surrounding the glass vessel containing the ice during transfer, which raised the temperature of the melted ice and therefore lowered krypton's solubility in the melt water. The presence of the warm bath did not noticeably increase the observed δKr/Ar; however, it is possible that gas occlusion in the water trap (discussed below) may mask enhanced extraction due to increased flow of water vapor.

Another consideration is the possibility that Kr might be unintentionally trapped in the water trap during gas transfer by gas occlusion. Previous work has shown that when a large amount of water vapor is transferred through a water trap, a gas can become trapped by occlusion under the freezing water vapor (W. Jenkins, personal communication). Our control data from ice from the late Holocene shows no change in $\delta Kr/N_2$ within error (Figure 2.6), so it is unlikely that occlusion preferentially affects either Kr or N_2. Nevertheless, we have tested for the presence of this effect by heating up the water trap after gas extraction and transfer. The occluded gas subsequently released from the water trap (~0.005% of the total sample pressure) was then transferred to the dip tube (already containing the original sample) through a second water trap. Gas occlusion in the water trap in this second transfer is less likely due to lower water vapor flow than in the original transfer. $\delta Kr/N_2$ results from this "test" sample of late Holocene ice showed no significant difference from the rest of our data set from the late Holocene ($\delta Kr/N_2$ values were within error of 0‰). Therefore, it appears that gas occlusion is not significantly affecting our measurements.

After the gas extraction, the dip tube is removed from the liquid He tank. It then warms to room temperature and is allowed to homogenize before mass spectrometry. Sample tube homogenization time was estimated in a separate experiment by transferring an aliquot of an air standard gas of ~4 cm^3 into a sample dip tube, letting it homogenize for various amounts of time after removal from the liquid He tank, and then running it against the standard gas itself on a Finnigan Delta Plus XP mass spectrometer. Tested homogenization times ranged from 30 minutes to

18 hours. The measured $\delta^{15}N$, $\delta^{18}O$, $\delta O_2/N_2$, and $\delta Ar/N_2$ all approached 0‰ (the expected value for the standard gas versus itself) at 2 hours homogenization time (Figure 2.3). We therefore chose 2 hours to be the minimum homogenization time for a sample after it is removed from liquid He. This homogenization time applies to the sample tube containing ~4 cm^3 of air extracted from the ice samples.

After at least 2 hours of homogenization, the gas in the sample dip tube is analyzed on a Finnigan Delta Plus XP mass spectrometer to determine the $\delta^{15}N$, $\delta^{18}O$, $\delta O_2/N_2$, and $\delta Ar/N_2$ of the sample. The standard gas, dry La Jolla air from a laboratory tank at approximately 50 psig, is expanded into a 1-cm^3 aliquot volume for 6 minutes. Then both sample and standard gas aliquots are expanded into their respective bellows for 6 minutes. The mass spectrometer measures the delta values in blocks of 16 cycles consisting of 16 s integrations. We use 2 blocks of measurements, giving a total of 32 measurements per sample. The $\delta Ar/N_2$ measurement is used later to directly calculate the $\delta Kr/N_2$ value:

$$\delta Kr/N_2 = \left\{ \left[\frac{\left(\frac{\delta\, {}^{84}Kr/{}^{36}Ar}{10^3} + 1 \right)}{\left(\frac{\delta\, {}^{40}Ar/{}^{36}Ar}{10^3} + 1 \right)} \times \left(\frac{\delta\, {}^{40}Ar/{}^{28}N_2}{10^3} + 1 \right) \right] - 1 \right\} \times 10^3 ‰ \qquad (2.9)$$

The $\delta^{15}N$ of N_2 is used as an additional indicator of gravitational fractionation (the other being $\delta^{40}Ar/^{36}Ar$), and to identify thermal fractionation (Severinghaus and Brook, 1999). The $\delta^{18}O$ of O_2 may be used for chronological purposes (Sowers and

Bender, 1995), and the $\delta O_2/N_2$ is used to indicate gas loss and to correct for an artifact known as the "chemical slope" (Severinghaus et al., 2003), which is described in next section. Typical standard deviations of the reported values for the $\delta^{15}N$, $\delta^{18}O$, $\delta O_2/N_2$, and $\delta Ar/N_2$ measurements in ice cores are 0.008‰, 0.014‰, 0.50‰, and 0.40‰, respectively. CO_2 and water vapor in the sample and standard gases are monitored for possible isobaric interference (Sowers, et al., 1989).

The sample gas is then recovered from the Delta XP mass spectrometer for noble gas measurements on the Finnigan MAT 252 mass spectrometer. Remaining gas in the inlet and the sample bellows of the Delta XP mass spectrometer is quantitatively refrozen into another dip tube in liquid helium. We have tested this "refreezing" step to determine if any significant fractionation occurs in the subsequent noble gas measurements. We measured two sets of samples: one consisting of gas samples that were "refrozen" from the mass spectrometer, and one set that were "blanks," identical gas samples that were not subject to the refreezing step. The gas used for these tests was a laboratory standard tank filled with dry La Jolla air at 50 psig. Both sets of samples were measured on the Finnigan MAT 252 for $\delta^{40}Ar/^{36}Ar$ (hereafter referred to as $\delta^{40}Ar$) and $\delta Kr/Ar$. The "blanks" and refrozen samples were run alternately. Using a Student t-test, measured values of $\delta^{40}Ar$ and $\delta Kr/Ar$ in the two sets of data were compared to each other.

The first set of tests, done in September 2003, showed a marginally significant difference at the 95% confidence level in the $\delta Kr/Ar$ measurement between the "blanks" and refrozen samples ($t = 2.170$), but no significant difference

in the δ^{40}Ar measurements (t = 1.340). The mean and standard deviations for δKr/Ar "blanks" and refrozen samples were 29.97 ± 0.25‰ and 30.19 ± 0.25‰, respectively, and those of δ^{40}Ar were 1.907 ± 0.020‰ and 1.915 ± 0.011‰, respectively. A subsequent set of testing in May 2004 revealed that this difference had been caused by a leaky valve in the Delta XP mass spectrometer. When the sample gases were not exposed to this valve, the two sets of measurements were not significantly different at the 95% confidence level (t = 0.046 and 0.496 for δKr/Ar and δ^{40}Ar, respectively). The means and standard deviations of "blanks" and refrozen samples were 29.30 ± 0.40‰ and 29.32 ± 0.84‰, respectively, for δKr/Ar, and 1.885 ± 0.036‰ and 1.869 ± 0.064‰ for δ^{40}Ar.

During the May analysis, two samples were excluded owing to anomalously low δ^{40}Ar values. These δ^{40}Ar values were both measured on May 3, 2004. The first sample measured that day had a δ^{40}Ar value of 1.189‰, with subsequent sample δ^{40}Ar values climbing steadily throughout the day, until reaching a typical δ^{40}Ar value (~1.8-1.9‰) on the following day. The cause of the low δ^{40}Ar values therefore appeared to be linked to a problem with the mass spectrometer, possibly a small contamination that occurred before starting measurements on May 3, and then reduced in intensity throughout the day due to pumping of the mass spectrometer source and inlet.

After the sample is recovered by this refreezing step, the sample gas is exposed to a Zr/Al getter at 900°C to remove the N_2, O_2, and other reactive gases, following Severinghaus et al. (2003). The remaining noble gases are frozen into a

dip tube at 4K for 3 minutes. Ultrahigh purity tank N_2 equal to 10× the noble gas pressure in the vacuum line (precision of 0.001 torr) is added to the sample to add bulk, which is necessary to maintain pressure for viscous flow during mass spectrometry. The N_2 is frozen into the same dip tube at 4K for 3 minutes. The accuracy of the N_2 addition is evaluated by measuring sample N_2/Ar versus the N_2/Ar in the working standard (which also has a N_2/Ar ratio of 10). The average δN_2/Ar values in this dataset were ~2‰. After 40 minutes of homogenization, δ^{40}Ar, δKr/Ar, and δXe/Ar in the sample are measured on a Finnigan MAT 252 mass spectrometer, with respect to the working standard. The δ^{40}Ar, δKr/Ar, and δXe/Ar are analyzed on the mass spectrometer as described in Severinghaus et al., 2003. Typical standard deviations of δ^{40}Ar, δKr/Ar, and δXe/Ar in replicate ice core measurements at a given depth are 0.020‰, 0.70‰, and 3.5‰, respectively.

The $\delta Kr/N_2$ is calculated using the δKr/Ar and δ^{40}Ar measured on the MAT 252, and the $\delta Ar/N_2$ measured on the Delta XP (equation 2.9). The δ^{40}Ar measurement is also used to correct for gravitational settling, as described in a subsequent section.

Corrections

The sample and standard gases are not necessarily the same size when expanded into the mass spectrometer bellows. During mass spectrometry, the pressure of a smaller gas sample typically falls faster than that of a bigger sample. This pressure imbalance can artifactually affect the measured values because of

machine nonlinearity. To minimize this effect, we start the smaller sample at a higher pressure than the bigger sample at the beginning of the mass spectrometer run. We also make a correction for the actual pressure difference between sample and standard gases by scaling the pressure difference by the empirically determined Pressure Imbalance Sensitivity (PIS) (equations 2.10 and 2.11), as described in Severinghaus et al., 2003.

$$\delta_{corrected} = \delta_{measured} - PIS\Delta_{pressure} \qquad (2.10)$$

$$\Delta_{pressure} = {}^{36}Ar_{sample} / {}^{36}Ar_{standard} - 1 \quad (MAT\ 252) \qquad (2.11a)$$

$$\Delta_{pressure} = {}^{28}N_{2\,sample} - {}^{28}N_{2\,standard} \quad (Delta\ XP)\ (volts) \qquad (2.11b)$$

Another correction is made for the sensitivity of the measured isotopic ratios, $\delta^{40}Ar$, $\delta^{15}N$, and $\delta^{18}O$, to certain elemental ratios. We call this the "chemical slope" correction (Severinghaus et al., 2003). The $\delta^{40}Ar$ measurement is sensitive to changes in the N_2/Ar ratio because the relative ionization efficiencies of ^{40}Ar and ^{36}Ar are affected by differences in N_2/Ar between the sample and standard gases. This effect is probably due to ion-molecule reactions in the mass spectrometer source, but is not well understood. We make this correction empirically following Severinghaus et al., 2003. Varying amounts of ultrapure N_2 are added to an aliquot of the working standard gas, and then it is run on the mass spectrometer versus the standard gas. The pressure-corrected $\delta^{40}Ar$ of the standard vs. itself should be 0‰, so any deviation from that value can be attributed to the chemical slope. The correction for the chemical slope is calculated as follows:

$$\delta^{40}Ar/^{36}Ar_{\text{slope corrected}} = \delta^{40}Ar/^{36}Ar_{\text{pressure corrected}} - [\text{chemical slope}] \times \delta N_2/Ar_{\text{measured}} \quad (2.12)$$

The chemical slope is usually calculated at the beginning of a set of measurements. The chemical slope used in this study was y = 0.000446x (R^2 = 0.97). The chemical slope corrections to the δ^{40}Ar measurements were <0.005‰, which are small compared to the signal size (~1.200-1.800‰) and measurement error (0.020‰). The mass spectrometer used for our measurements is tuned to optimize linearity, and thus minimize chemical slope (Severinghaus et al., 2003). The chemical slope does not change more than 20% over time and during the source filament lifetime, which limits the possible error under the most extreme scenario to 0.001‰.

A chemical slope correction is also made to the δ^{15}N measurement, which can be affected by the $\delta O_2/N_2$ and the δCO_2 values. A difference between the sample and standard CO_2 abundance can cause differential isobaric interference of CO^+ with N_2^+ (Sowers, et al., 1989). The ion $^{13}CO^+$ has a mass of 29, which is the same as the mass measured for the δ^{15}N of N_2 ($^{15}N^{14}N$). The δ^{18}O measurement is also corrected for differences in $\delta N_2/O_2$. All chemical slope corrections are made as described above for δ^{40}Ar.

Normalization to atmosphere

Ice core $\delta Kr/N_2$ values are measured on the mass spectrometer in reference to working standards made from commercially available gases or dry air from the SIO pier (Severinghaus et al., 2003). Because the isotopic values of the working standards may be arbitrary, we normalize the ice core measurements to the atmosphere. We measure air from the SIO pier in La Jolla, CA (which we call La Jolla air) in reference to the working standards while attempting to mimic the ice core analysis to the extent possible. La Jolla air is collected following Severinghaus et al. (2003), which broadly follows Keeling et al. (1998). We have modified this method by including an additional pump, which pulls air into a large intake tube, concentrically enclosing a smaller tube that captures the air to be measured. This type of aspirated intake set-up was designed to increase air flow into the intake tubes, thereby reducing possible fractionation associated with the initial capture of air (Blaine, PhD thesis, 2005). The smaller tube, and the tubing used in this air collection method is ¼" OD Synflex polyethylene-aluminum composite tubing. Connections are made using Ultratorr fittings with Viton O-rings. The air is then pumped at 4 L min^{-1} through two glass water traps at –100ºC to remove the water vapor. After it is dried, the air is pumped through ~2m of tubing to a series of three stainless steel 4-cm^3 volumes, followed by a 2-m tail of tubing to prevent the ambient air from entering the 4-cm^3 volumes. Air is pumped through this set-up for 10 minutes to attain a steady state with respect to possible fractionation. The pump is then stopped abruptly, and after waiting 5 seconds for air flow to stop, we close the valves on the 4-cm^3 sample volumes.

La Jolla air samples are analyzed by the same procedure used for ice analysis, with the exception of air extraction from the ice. Air from the 4-cm^3 sample volume is transferred into a dip tube, which is then run on the Finnigan Delta Plus XP mass spectrometer to measure $\delta^{15}N$, $\delta^{18}O$, $\delta O_2/N_2$, and $\delta Ar/N_2$. After mass spectrometry, air in the sample bellows is refrozen into another dip tube at 4K. The air in the dip tube is then gettered, enriched with ultrapure N_2, and measured on the Finnigan MAT 252 mass spectrometer to determine the $\delta^{40}Ar$, $\delta Kr/Ar$, and $\delta Xe/Ar$.

La Jolla air is measured regularly throughout a set of ice core measurements, approximately once every two weeks. After they are measured, the La Jolla air values are used to normalize ice core measurements until the next time La Jolla air is measured. The La Jolla air values were relatively constant through the duration of these measurements (Figure 2.4), with a standard deviation among the $\delta Kr/N_2$ means of 0.22‰ (the standard deviation of the entire dataset taken together is 0.44‰). We typically measure La Jolla air in triplicate, using three 4-cm^3 volumes, as described above. We use the mean La Jolla air $\delta Kr/N_2$ value of the three replicates, corrected for pressure imbalance and chemical slope effects, to normalize the $\delta Kr/N_2$ ice core measurements to the atmosphere:

$$\delta \mathrm{Kr/N_2} = \left\{ \left[\frac{\left(\delta \mathrm{Kr/N_{2\,measured,corrected}}\right)/10^3 + 1}{\left(\delta \mathrm{Kr/N_{2\,La\ Jolla\ air}}\right)/10^3 + 1} \right] - 1 \right\} \times 10^3 ‰ \qquad (2.13)$$

This normalization allows us to refer to ice core $\delta Kr/N_2$ in terms of deviation from today's atmosphere.

Sources of fractionation within the firn

The top ~50-100m of an ice sheet is composed of a porous snow layer, called the firn. Air in the firn mixes with the atmosphere mainly through diffusion, and sometimes through convection (Schwander et al., 1993, Battle et al., 1996). At the bottom of the firn, air is trapped in bubbles, and the firn becomes ice. Processes occurring within the firn can affect the $\delta Kr/N_2$, as well as other gases, and the trapped air reflects these effects.

Gravitational fractionation

Gravitational fractionation is one such process that can obscure the accurate representation of the paleo-atmosphere. Gravitational settling causes the air in firn and in bubbles that form at the firn/ice transition to preferentially include heavier isotopes. Gravitational fractionation is described by the barometric equation modified for a gas pair (Craig et al., 1988):

$$R/R_o = \mathrm{e}^{gz\Delta m/R^*T} \qquad (2.14)$$

where R is the isotope or gas ratio measured, R_o is the same ratio in the free atmosphere, g is the local gravitational acceleration, z is the thickness of the firn, Δm

is the mass difference between the two isotopes, R^* is the gas constant, and T is the isothermal temperature of the column.

Gravitational fractionation varies in accordance with mass difference, so $\delta^{84}Kr/^{28}N_2$ is 14 times more affected by gravity than $\delta^{40}Ar$ (mass difference of 56 amu compared to a difference of 4 amu) (Figure 2.5). The measured $\delta^{40}Ar$ value is used to correct $\delta Kr/N_2$ for gravitational fractionation as follows:

$$\delta \mathrm{Kr}/\mathrm{N}_{2\,\mathrm{gravcorr}} = \delta \mathrm{Kr}/\mathrm{N}_{2\,\mathrm{measured}} - \delta^{40}\mathrm{Ar} \times \Delta m/4 \qquad (2.15)$$

In this case, Δm is the mass difference between ^{84}Kr and $^{28}N_2$, which is 56 amu.

Gas loss fractionation

Bender et al. (1995) noted another form of fractionation in ice cores, which they refer to as "configurational" fractionation. After correcting for gravitational fractionation, they found that the elemental ratios O_2/N_2 and Ar/N_2 were significantly lower than atmospheric values. They concluded that gases must have been escaping through small cracks created in the ice cores during drilling and retrieval. Bender et al. found that the mode of gas transport through these cracks could be what they refer to as configurational fractionation, where molecular diameter controls relative rates of gas loss. According to their analysis, smaller gas molecules were preferentially able to escape through small cracks in the ice.

Further studies have found that gases may also escape from the ice naturally during bubble close-off, causing a similar type of size-dependent fractionation (Severinghaus and Battle, 2006; Bender, 2002). Severinghaus and Battle measured Ar/N_2, Ne/N_2, O_2/N_2, Kr/N_2, and Xe/N_2 in firn air from Siple Dome and South Pole, Antarctica. They found enrichments in firn air Ar/N_2, Ne/N_2, O_2/N_2, while the Kr/N_2 and Xe/N_2 data show no enrichment. The O_2/N_2 measured in bubble ice show a complementary depletion, which suggests a process by which smaller molecules preferentially escape from the air bubble as it closes off (Severinghaus and Battle, 2006).

This finding may indicate the existence of a threshold molecular size, in which molecules of greater size than the threshold value are not affected by this "close-off" fractionation. The Siple Dome and South Pole firn air data show that the extent of close-off fractionation decreases with increasing molecular diameter, from Ne to O_2 to Ar. Kr and Xe, on the other hand, do not show any enrichment in the firn air. The effective diameter of Kr is 3.64Å, while Ar has a diameter of 3.54Å, suggesting a threshold diameter of ~3.6Å (Severinghaus and Battle, 2006).

Kr and N_2 are both larger than this "threshold size," so $\delta Kr/N_2$ measured in air bubbles should not be affected by gas loss fractionation, and hence should represent the abundance of these gases in the paleo-atmosphere. However, some ice cores do show variations in Kr/N_2 that correlate with extreme gas loss (deep Byrd core, Severinghaus, unpublished). In this case, $\delta O_2/N_2$ is about –200‰, in contrast to typical values of –5 to –10‰ for well-preserved ice samples (Bender et al., 1995).

Ice having undergone this extreme level of gas loss should not be considered as reliably recording atmospheric Kr/N_2.

Results

Ice from the late Holocene part of the GISP2 ice core (gas age ~230 years before present) was analyzed for $\delta Kr/N_2$ as a control test. The mean ocean temperature has not changed substantially between the late Holocene and today, so $\delta Kr/N_2$ measured in air bubbles in ice from the late Holocene should be within error of 0‰ if it is primarily reflecting ocean temperature change. The measured $\delta Kr/N_2$ from this late Holocene ice is +0.07 ± 0.30‰ (n = 16, from 9 depths) for one set of measurements (~146m), and –0.14 ± 0.93‰ (n = 17, from 6 depths) for another set of measurements (~140.5-142m) (Figure 2.6). Here, measurement error is reported as the pooled standard deviation (equation 16) divided by the square root of the number of replicates. These error calculations are described in detail below. These Holocene $\delta Kr/N_2$ data are all within measurement error of 0‰. The technique thus passes this first-order test.

The $\delta Kr/N_2$ measured in air bubbles from the LGM portion of the GISP2 ice core show a negative shift in their values (Figure 2.6). The measured $\delta Kr/N_2$ from the LGM is –1.34 ± 0.37‰, which corresponds to a modeled mean ocean temperature change of 2.7 ± 0.6ºC between the LGM and today (Figure 2.1). GISP2 ice core depth for these LGM samples ranged from 1930.00m to 1932.36m, which correlates to a ~100 year time span from 20,386 – 20,487 years before 1950 (B.P.) (Meese et

al., 1997). Assuming the gas age-ice age difference is ~860 years (Severinghaus and Brook, 1999), the gas ages span the interval 19,500 – 19,600 yr. B.P.

We also measured $\delta Xe/N_2$ simultaneously with $\delta Kr/N_2$ in the late Holocene and LGM ice samples. $\delta Xe/N_2$ precision is much poorer than that of $\delta Kr/N_2$. In the late Holocene ice samples (the same as those in which we measured $\delta Kr/N_2$), $\delta Xe/N_2$ values were -0.29 ± 1.71‰ (n = 16, from 9 depths) at ~146m, and -2.29 ± 3.49‰ (n = 17, from 6 depths) at ~140.5-142m (Figure 2.7). $\delta Xe/N_2$ error is calculated in the same way as that of $\delta Kr/N_2$. $\delta Xe/N_2$ measured in ice from the LGM was -6.93 ± 1.83‰, which corresponds to a 4.5 ± 1.0ºC temperature change between the LGM and today (Figure 2.7). We compute this temperature estimate in the same way as for $\delta Kr/N_2$, but using the Xe mole fraction in the atmosphere to estimate $Xe_{present\ atmosphere}$, and Xe solubilities (Wood and Caputi, 1966, Hamme and Severinghaus, 2007) to estimate $Xe_{present\ ocean}$ and $Xe_{LGM\ ocean}$. The large error in the $\delta Xe/N_2$ Holocene and LGM measurements, as well as the apparent overestimate of temperature change indicated by LGM $\delta Xe/N_2$, are possibly due to analytical problems that are not yet understood. It is also possible that processes such as adsorption/desorption of Xe onto boreal soils could affect the $\delta Xe/N_2$ results. This effect is discussed in the next section. We do not yet understand these $\delta Xe/N_2$ measurements, but with improved precision, they may serve as an additional, independent indicator of ocean temperature change, or they may elucidate other processes affecting the $\delta Kr/N_2$ measurements.

Standard error is calculated using the pooled standard deviation. As defined in

Severinghaus et al. (2003), pooled standard deviation, s_{pooled}, is the square root of the summed squared deviations of replicates δ_i from their respective means, δ_{jmean}, divided by the degrees of freedom (the number of samples n minus the number of reported means m):

$$s_{pooled} \equiv \left(\frac{\sum_{i,j=1}^{n,m} \left(\delta_i - \overline{\delta_j}\right)^2}{n-m} \right)^{0.5} \qquad (2.16)$$

Ice samples are measured in duplicate or triplicate, so this calculation is useful because it includes the deviation between replicates from the same depth to compute the overall deviation of the data set. Each depth is typically measured in triplicate, so the standard error is calculated as the pooled standard deviation divided by the square root of the number of replicates (in this case, 3).

As can be seen in Figures 2.6 and 2.7, the scatter in the data is large compared to the expected signal. This limits the current utility of the method for paleoclimatic application. However, future improvements in precision are anticipated, and the current work serves as an indication of the method's potential.

Discussion

Processes affecting $\delta Kr/N_2$ interpretation

Geothermal heating is one source of heat to the ocean that would not be calculable using atmospheric $\delta Kr/N_2$. $\delta Kr/N_2$ can only record inputs of heat from the surface, whereas geothermal heat enters the ocean at the sea floor. Geothermal heat input (0.05 W/m^2) is generally expected to have a negligible effect on ocean heat content, as its input is much smaller than solar heat flux into the ocean (~200 W/m^2). However, this may not be the case if the ocean were extremely stagnant in the past, allowing heat to build up in the deep ocean (Adkins et al., 2005). It is believed that the deep ocean was more stagnant in the LGM, as compared to today (Adkins et al., 2002). If the ocean were stagnant long enough for a substantial amount of geothermal heat to accumulate in the deep ocean, then our $\delta Kr/N_2$ method would overestimate ocean temperature change. Assuming a heat flux of 0.05 W/m^2, we find that the deep ocean would need to be stagnant (or at least to avoid contact with the atmosphere) for 2,500 years for mean ocean temperature to increase by 0.3ºC (Joyce et al., 1986). The temperature change due to geothermal heating in this extreme case is still below the detection limit of the $\delta Kr/N_2$ method presented in this study (0.6ºC error). There is no evidence for deep ocean stagnation of such an extent during the LGM, so we conclude that geothermal heating would not bias our LGM ocean temperature estimate significantly.

One last caveat in interpreting atmospheric $\delta Kr/N_2$ as solely reflecting ocean temperature change is the possibility that "sticky" gases like krypton are affected by adsorption/desorption onto boreal soils. This effect would be even more extreme for xenon, which we have measured simultaneously with krypton. Our xenon results have more uncertainty (~2‰), with $\delta Xe/N_2$ shifted to more negative values for both

Holocene and LGM measurements (Figure 2.7). Taking into account this unexplained negative bias, there is still an excess change in $\delta Xe/N_2$ that exceeds the change expected based on the $\delta Kr/N_2$-derived LGM temperature change (Figure 2.7). It is possible that this difference is caused by net desorption of xenon from cold boreal soils through time from the LGM to the present. Krypton would be less affected than xenon, as xenon is a more adsorptive gas, but it may be affected nonetheless. If this is the case, our temperature change estimate using $\delta Kr/N_2$ may be an upper estimate. We expect to be able to better constrain a possible effect of boreal soils with improved $\delta Xe/N_2$ measurement precision.

Comparison with other deep ocean temperature estimates

The modeled temperature change presented in this paper can be compared with other estimates of deep ocean temperature. Schrag et al.'s (1996) pore fluid data from a limited number of sites suggested a deep ocean temperature change of ~4ºC, while Martin et al. (2002) found a smaller change of ~2.5ºC using Mg/Ca of benthic foraminifera. Waelbroeck et al. (2002) and Cutler et al. (2003) have used a combination of benthic $\delta^{18}O$ ($\delta^{18}O_b$) measurements and coral-based sea level estimates to estimate deep ocean temperatures. In comparing $^{18}O_b$ and coral-derived relative sea level (RSL), Waelbroeck et al. (2002) identified two different regression "regimes": one during glaciation, and the other during deglaciation. They used these regressions between RSL and $\delta^{18}O_b$ to estimate deep ocean temperature, assuming a

global mean $\Delta\delta^{18}O$ due to ice volume change of 1.1‰. They found that the LGM deep ocean was ~4ºC, 3ºC, and 2ºC colder than today in the North Atlantic, Southern Indian, and Pacific Ocean, respectively, with larger temperature changes possible if $\Delta\delta^{18}O$ due to ice volume is less than 1.1‰. Using a similar method to Waelbroeck et al., (2002), Cutler et al. (2003) found deep ocean temperature changes of 2°C in the Pacific and 4°C in the Atlantic, using a combination of $\delta^{18}O_b$ and sea level estimates from the Huon Peninsula, Papua New Guinea, and Barbados corals. In comparison to these local estimates of deep ocean temperature change, the mean ocean temperature change of 2.7 ± 0.6ºC that we present in this paper appears to be at least a consistent estimate.

This estimate of the mean ocean temperature change between the LGM and today may provide some insight into the change in deep ocean temperature during this time period, which could help constrain previously proposed mechanisms of climate change. Keeling and Stephens (2001) propose a mechanism for Pleistocene climate instability that requires for its operation the cooling of deep ocean waters to virtually the freezing point. The mean ocean temperature change of 2.7 ± 0.6ºC that we present here implies that the deep ocean may have been near the freezing point of seawater, but a more precise estimate would place tighter constraints on this hypothesis.

This chapter has been published elsewhere. Chapter 2 was published previously as: Headly, M.A. and J.P. Severinghaus, A method to measure Kr/N_2 ratios in air bubbles trapped in ice cores and its application in reconstructing past

mean ocean temperature, *Journal of Geophysical Research*, volume 112, D19105, doi:10.1029/2006JD008317, 2007.

Acknowledgments: We thank R. Keeling for suggesting the idea that atmospheric Kr would reflect ocean temperature change, and we thank W. Jenkins, R. Hamme, and K. Kawamura for helpful discussions. R. Beaudette assisted in the laboratory. We thank the staff of the National Ice Core Laboratory for assistance in ice sample handling. This work was supported by NSF grants ATM99-05241and OPP05-38630.

References

Adkins, J. F., and D. P. Schrag (2001), Pore fluid constraints on deep ocean temperature and salinity during the last glacial maximum, *Geophys. Res. Lett.*, *28*(5), 771-774.

Adkins, J. F., A. P. Ingersoll, C. Pasquero (2005), Rapid climate change and conditional instability of the glacial deep ocean from the thermobaric effect and geothermal heating, *Quaternary Science Reviews*, *24*, 581-594.

Adkins, J. F., K. McIntyre, and D. P. Schrag (2002), The salinity, temperature, and $\delta^{18}O$ of the glacial deep ocean, *Science*, *298*, 1769-1773.

Battle, M., M. Bender, T. Sowers, P. P. Tans, J. H. Butler, J. W. Elkins, J. T. Ellis, T. Conway, N. Zhang, P. Lang, and A.D. Clarke (1996), Atmospheric gas concentrations over the past century measured in air from firn at the South Pole, *Nature, 383*, 231-235.

Bender, M., T. Sowers, and V. Lipenkov (1995), On concentrations of O_2, N_2, and Ar in trapped gases from ice cores, *J. Geophys. Res.*, *100*, 18,651-18,660.

Blaine, T. W. (2005), Continuous measurements of atmospheric argon/nitrogen as a tracer or air-sea heat flux: models, method, and data, Ph.D. thesis, University of California, San Diego, La Jolla, California.

Craig, H., and R. C. Weins (1996), Gravitational enrichment of $^{84}Kr/^{36}Ar$ ratios in polar ice caps: a measure of firn thickness and accumulation temperature, *Science*, *271*, 1708-1711.

Craig, H., Y. Horibe, and T. Sowers (1988), Gravitational separation of gases and isotopes in polar ice caps, *Science*, *242*, 1675-1678.

Crowley, T. J. and G. R. North (1991), *Paleoclimatology*, Oxford, New York.

Cutler, K. B., R. L. Edwards, F. W. Taylor, H. Cheng, J. Adkins, C. D. Gallup, P. M. Cutler, G. S. Burr, and A. L. Bloom (2003), Rapid sea-level fall and deep-ocean temperature change since the last interglacial period, *Earth Planet. Sci. Lett.*, *206*, 253-271.

Egbert, G. D., R. D. Ray, and B. G. Bills (2004), Numerical modeling of global semidiurnal tide in the present day and in the last glacial maximum, *J. Geophys. Res*, *109*, C03003, doi:10.1029/2003JC001973.

Fairbanks, R. G (1989), A 17,000-year glacio-eustatic sea level record; influence of glacial melting rates on the Younger Dryas event and deep-ocean circulation, *Nature*, *342*, 637-642.

Hamme, R. C., and S. R. Emerson (2002), Mechanisms controlling the global oceanic distribution of inert gases argon, nitrogen, and neon, *Geophys. Res. Lett.*, *29*(23), 2120, doi:10.1029/2002GL015273.

Hamme, R. C., and J. P. Severinghaus (2007), Trace gas disequilibria during deep-water formation, *Deep-Sea Research Part I, 54*, 939-950.

Joyce, T. M., B. A. Warren, and L. D. Talley (1986), The geothermal heating of the abyssal subarctic Pacific Ocean, *Deep Sea Research Part A. Oceanographic Research Papers*, *33*(8), 1003-1015.

Keeling, R. F., and B. B. Stephens (2001), Antarctic sea ice and the control of Pleistocene climate Instability, *Paleoceanography*, *16*, 112-131.

Keeling, R. F., A. C. Manning, E. M. McEvoy, and S. R. Shertz (1998), Methods for measuring changes in atmospheric O_2 concentration and their application in southern hemisphere air, *J. Geophys. Res.*, *103*(D3), 3381-3397.

Levitus, S. (1994), World Ocean Atlas, NOAA, Washington D.C.

Martin, P. M., D. W. Lea, Y. Rosenthal, N. J. Shackleton, M. Sarnthein, and T. Papenfuss (2002), Quaternary deep sea temperature histories derived from benthic foraminiferal Mg/Ca, *Earth Planet. Sci. Lett.*, *198*, 193-209.

Meese, D. A., A. J. Gow, R. B. Alley, G. A. Zielinski, P. M. Grootes, M. Ram, K. C. Taylor, P. A. Mayewski, and J. F. Bolzan (1997), The Greenland Ice Sheet Project 2 depth-age scale: Methods and results, *J. Geophys. Res.*, *102*, 26411-26423.

Munk, W. H., and C. Wunsch (1998), Abyssal Recipes: II. Energetics of tidal and wind mixing, *Deep Sea Res.*, *45*, 1977-2010.

Pilson, Michael E. Q. (1998), *An Introduction to the Chemistry of the Sea*, Prentice-Hall, Inc., Upper Saddle River, New Jersey.

Schlesinger, W. H. (1997), *Biogeochemistry, An Analysis of Global Change*, 2nd ed., Academic Press, San Diego, CA.

Schrag, D. P., G. Hampt, and D. W. Murray (1996), Pore Fluid Constraints on the Temperature and Oxygen Isotopic Composition of the Glacial Ocean, *Science*, *272*, 1930-1932.

Schwander, J., J.-M. Barnola, C. Andrie, M. Leuenberger, A. Ludin, D. Raynaud, and B. Stauffer (1993), The Age of the Air in the Firn and the Ice at Summit, Greenland, *J. Geophys. Res., 98*, 2831-2838.

Severinghaus, J.P., and Battle, M. (2006), Fractionation of gases in polar ice during bubble close-off: new constraints from firn air Ne, Kr, and Xe observations, *Earth Planet Sci. Lett. 244*, 474-500.

Severinghaus, J. P., and E. J. Brook (1999), Abrupt climate change at the end of the last glacial period inferred from trapped air in polar ice, *Science*, *286*, 930-934.

Severinghaus, J. P., B. Luz, and N. Caillon (2003), A method for precise measurement of argon 40/36 and krypton/argon ratios in trapped air in polar ice with applications to past firn thickness and abrupt climate change in Greenland and at Siple Dome, Antarctica, *Geochim. Cosmochim. Acta*, *67*(3), 325-343.

Shackleton, N. J. (2000), The 100,000 year ice-age cycle identified and found to lag temperature, carbon dioxide, and orbital eccentricity, *Science*, *289*, 1897-1902.

Sowers, T., and M. L. Bender (1995), Climate records covering the last deglaciation, *Science*, *269*, 210-214.

Sowers, T., M. L. Bender, and D. Raynaud (1989), Elemental and isotopic composition of occluded O_2 and N_2 in polar ice, *J. Geophys. Res.*, *94*, 5137-5150.

Waelbroeck, C., L. Labeyrie, E. Michel, J. C. Duplessy, J. F. McManus, K. Lambeck, E. Balbon, and M. Labracherie (2002), Sea-level and deep water temperature changes derived from benthic foraminifera isotopic records, *Quaternary Science Reviews*, *21*, 295-305.

Watson, A. J., and A. C. Naveira Garbato (2006), The role of Southern Ocean mixing and upwelling in glacial-interglacial atmospheric CO_2 change, *Tellus*, *58B*, 73-87.

Weiss, R. F. (1970), The solubility of nitrogen, oxygen and argon in water and sea water, *Deep Sea Research*, *17*, 721-735.

Weiss, R.F. and T. K. Kyser (1978), Solubility of krypton in water and seawater, *J. Chem. Eng. Data*, *23*(1), 69-72.

Wood, D. and R. Caputi (1966), Solubilities of Kr and Xe in fresh and seawater, *Tech. rep.*, U. S. Naval Radiological Defense Laboratory, San Francisco, CA.

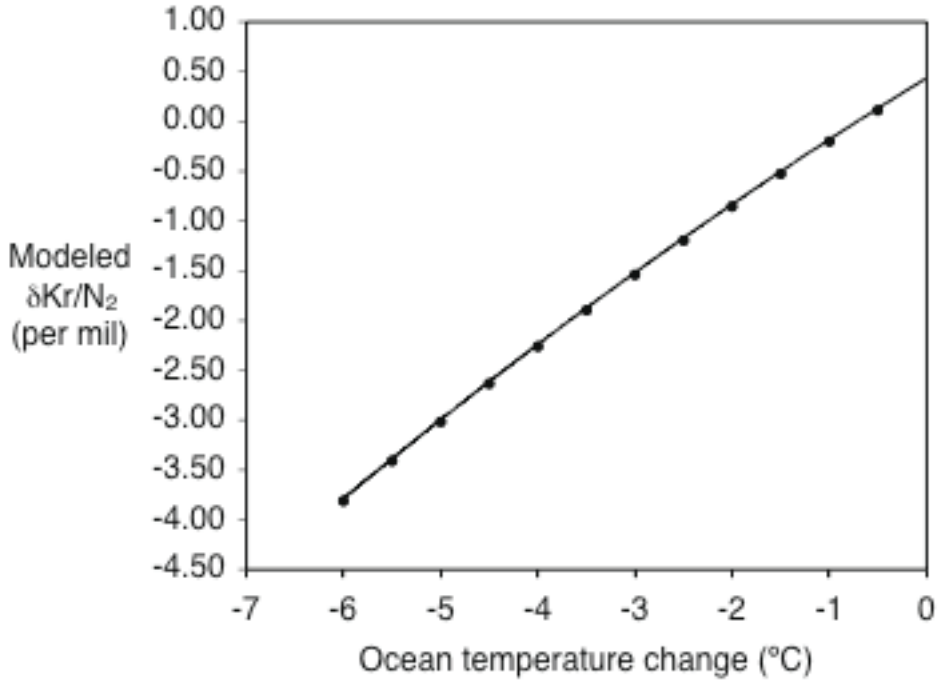

Figure 2.1. Modeled $\delta Kr/N_2$ vs. ocean temperature change between now and the LGM. Modeled $\delta Kr/N_2$ is positive at –0.5ºC because of smaller ocean volume during the LGM. Second order polynomial fit to points: $y = -0.0175x^2 + 0.5989x + 0.4146$.

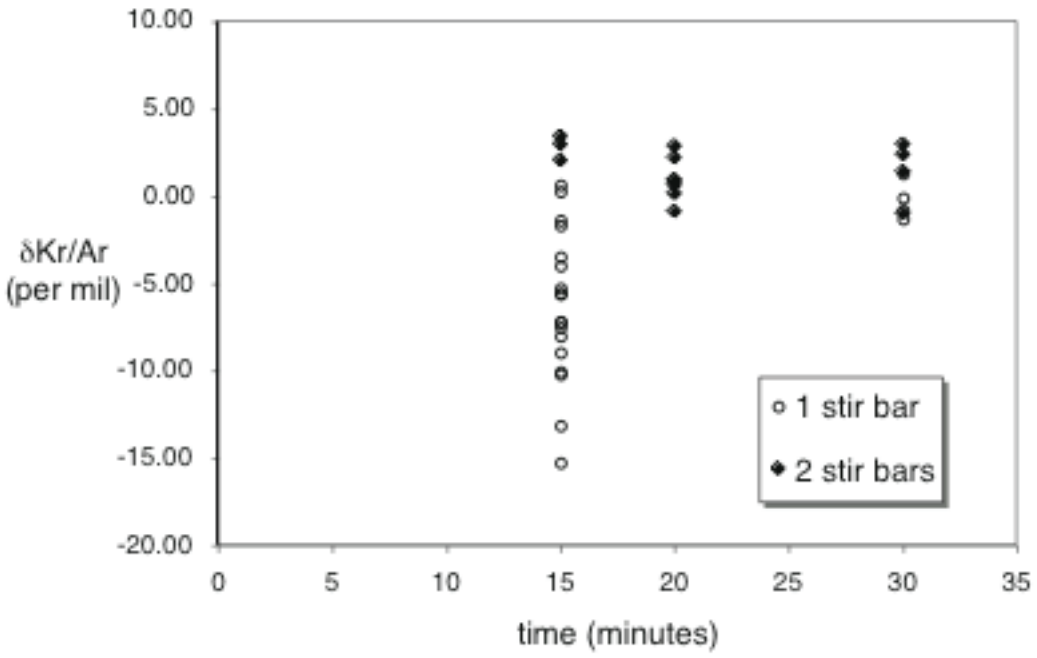

Figure 2.2. Test results from development of gas transfer technique for δKr/Ar. δKr/Ar is plotted vs. time. The number of stir bars used to agitate the melt water during gas transfer is indicated.

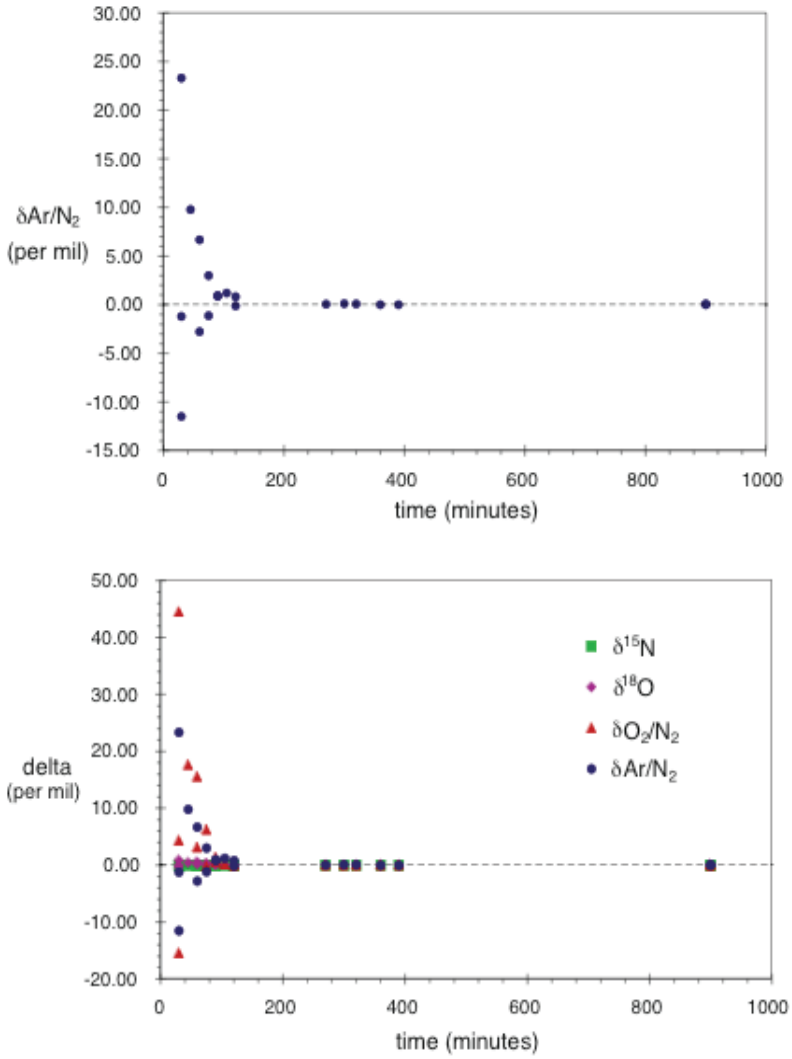

Figure 2.3. (Top) Measured $\delta Ar/N_2$ plotted vs. homogenization time. (Bottom) All measured gases on the Delta XP ($\delta^{15}N$, $\delta^{18}O$, $\delta Ar/N_2$, and $\delta O_2/N_2$) vs. homogenization time. Note that all gases approach 0‰ (their expected value) after 2 hours.

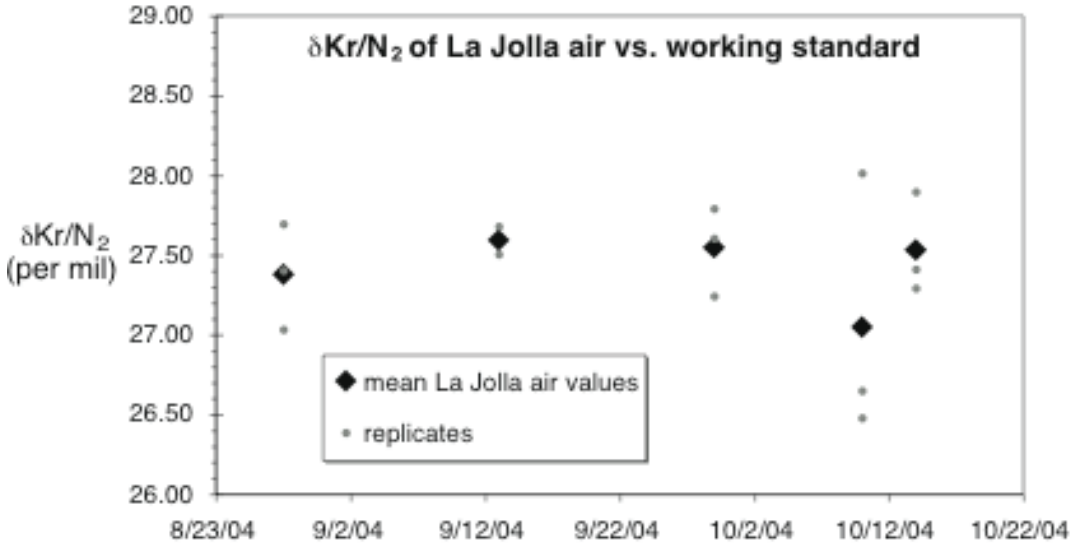

Figure 2.4. $\delta Kr/N_2$ of La Jolla air (sampled from the SIO pier in La Jolla, CA) measured vs. the working standard, over a two-month period. $\delta Kr/N_2$ is calculated using measured $\delta Kr/Ar$, $\delta^{40}Ar$, and $\delta Ar/N_2$ in La Jolla air. La Jolla air is typically measured in triplicate. The small dots in the figure represent the individual replicates, and the bigger diamonds are the mean value for each set of replicates. The standard deviation of the mean values from each set of three replicates is ± 0.22‰. The standard deviation of all of the replicates from the entire dataset is 0.45‰.

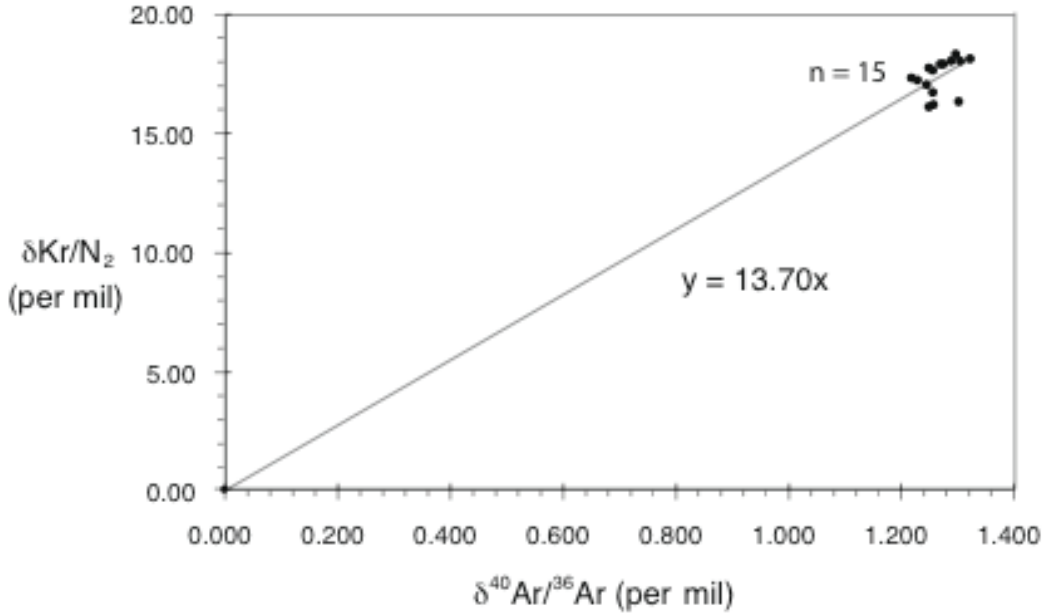

Figure 2.5. $\delta Kr/N_2$ plotted vs. $\delta^{40}Ar/^{36}Ar$ in GISP2 late Holocene ice (140-142m), n = 15. $\delta Kr/N_2$ is ~14 times $\delta^{40}Ar/^{36}Ar$, as expected due to gravitational fractionation.

Figure 2.6. GISP2 ice core depth plotted vs. $\delta Kr/N_2$. Vertical axis is not to scale. Long vertical line in gray denotes $\delta Kr/N_2 = 0‰$. Small gray circles are individual replicates at each depth, and bold black diamonds are the mean values for each depth. Late Holocene $\delta Kr/N_2$ are shown for depths ~140-142m and ~146-147m. Means are $+0.07 \pm 0.30‰$ (n = 16) for one set of measurements (~146m), and $-0.14 \pm 0.93‰$ (n = 17) for another set of measurements (~140.5-142m). Both measurements are within error of 0‰. Measurement error is reported as the pooled standard deviation (equation 16) divided by the square root of the number of replicates. LGM $\delta Kr/N_2$ measurements are shown in the bottom portion of the figure (at 1930-1933m depths). The mean $\delta Kr/N_2$ at in this depth range is $-1.34 \pm 0.37‰$. Short vertical lines are the modeled $\delta Kr/N_2$ resulting from a 2º, 3º, and 4ºC ΔT mean ocean temperature change.

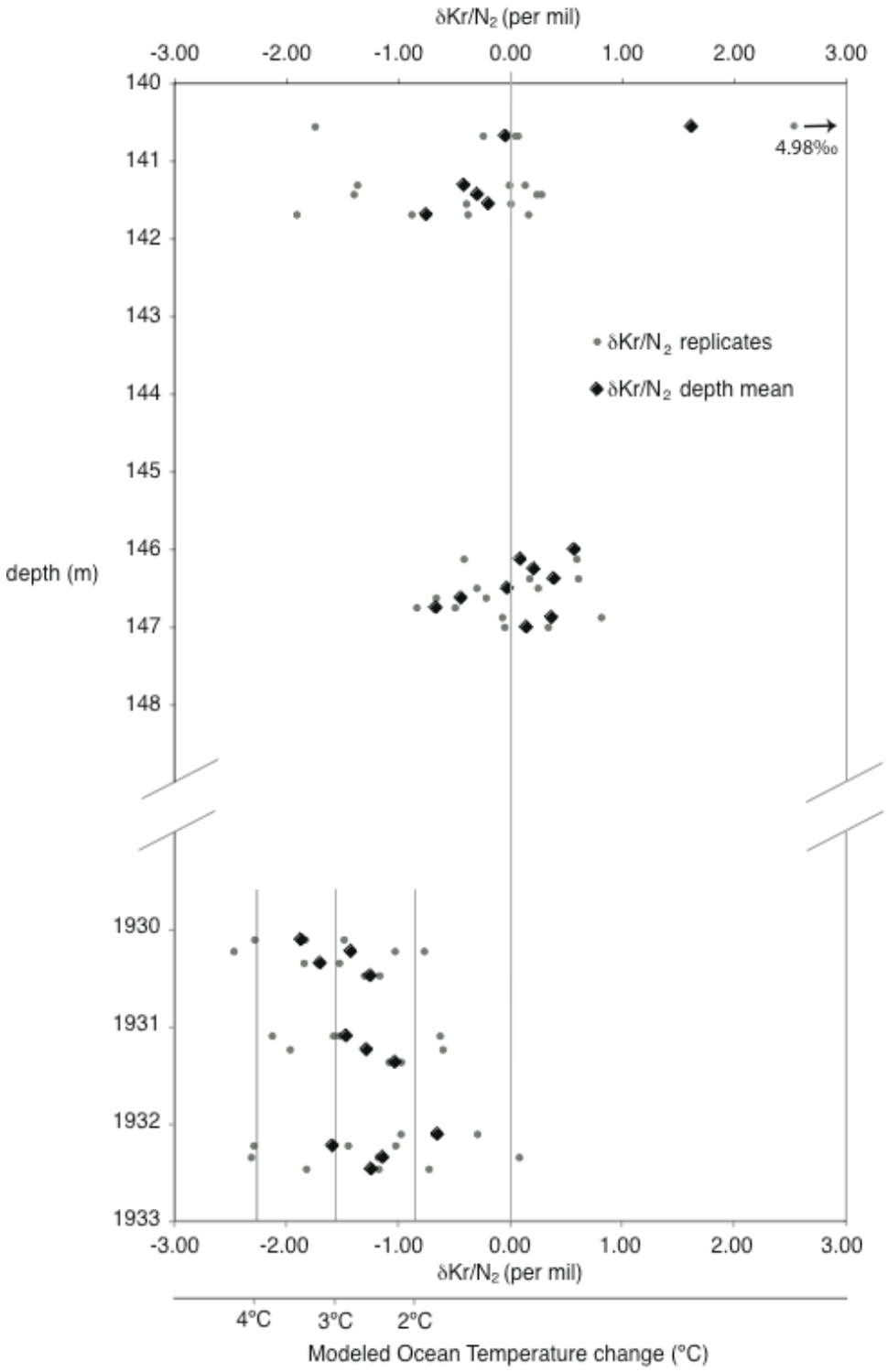
δKr/N2 (per mil)
-3.00
-2.00
-1.00
0.00
1.00
2.00
3.00
140
141
142
143
144
145
146
147
148
4.98‰
δKr/N2 replicates
δKr/N2 depth mean
depth (m)
1930
1931
1932
1933
δKr/N2 (per mil)
4°C
3°C
2°C
Modeled Ocean Temperature change (°C)

Figure 2.7. GISP2 ice core depth plotted vs. $\delta Xe/N_2$. Vertical axis is not to scale. Long vertical line in gray denotes $\delta Xe/N_2 = 0‰$. Small gray circles are individual replicates at each depth, and bold black diamonds are the mean values for each depth. Late Holocene $\delta Xe/N_2$ means are -0.29 ± 1.71‰ (n = 16) at ~146m, and -2.29 ± 3.49‰ (n = 17) at ~140.5-142m. Measurement error is reported as the pooled standard deviation (equation 16) divided by the square root of the number of replicates (3 replicates at each depth). The LGM $\delta Xe/N_2$ mean is –6.93 ± 1.83‰ (shown in the bottom portion of the figure at 1930-1933m depths). Short vertical lines are the modeled $\delta Xe/N_2$ resulting from a 2º, 3º, 4ºC, and 5ºC ΔT mean ocean temperature change.

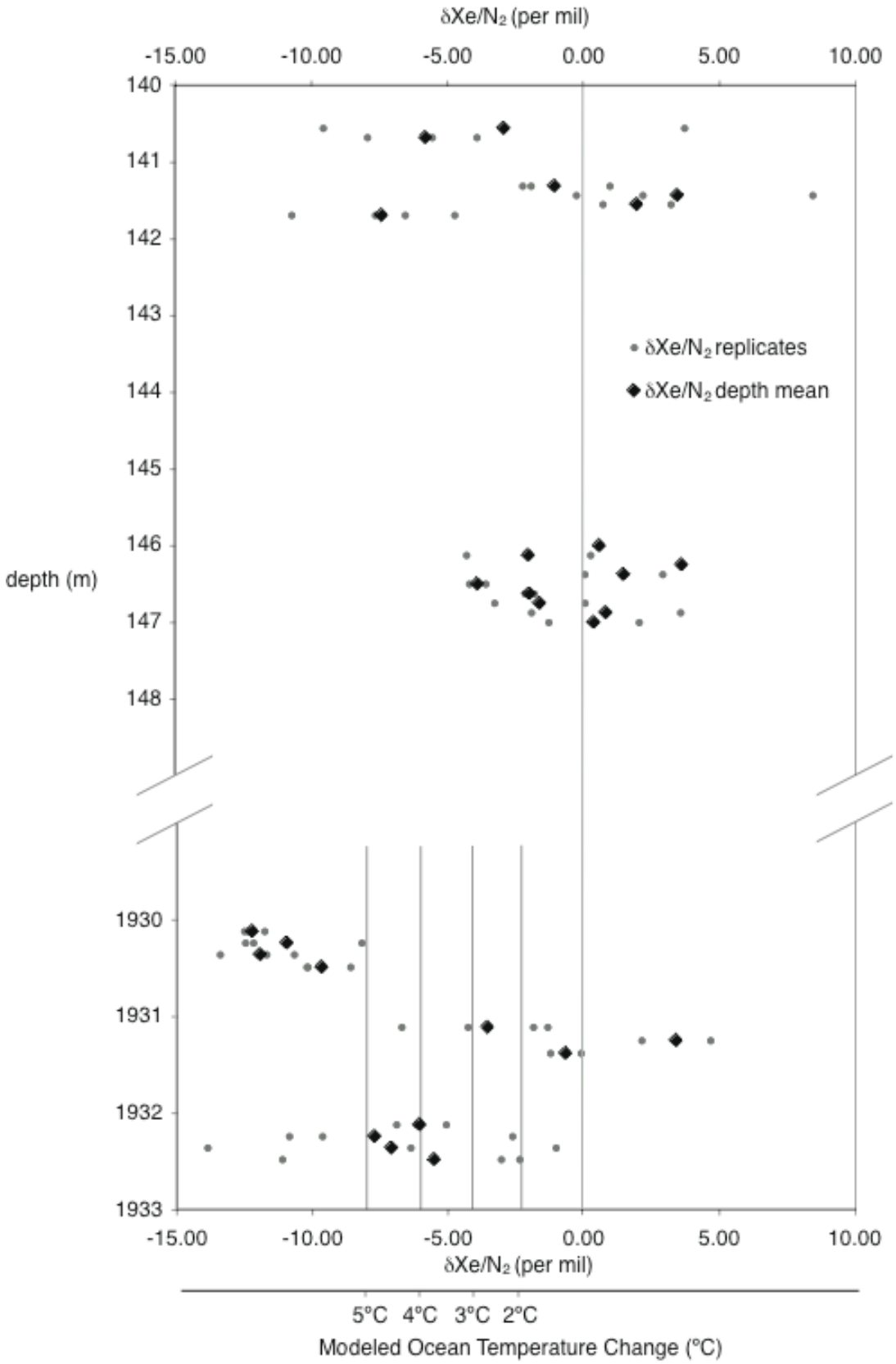
δXe/N2 (per mil)
-15.00
-10.00
-5.00
0.00
5.00
10.00
140
141
142
143
144
145
146
147
148
depth (m)
δXe/N2 replicates
δXe/N2 depth mean
1930
1931
1932
1933
-15.00
-10.00
-5.00
0.00
5.00
10.00
δXe/N2 (per mil)
5°C 4°C 3°C 2°C
Modeled Ocean Temperature Change (°C)

Chapter 3

Mean ocean temperature change during last glacial inception and termination based on $\delta Kr/N_2$ and $\delta Xe/N_2$ ice core measurements from Vostok and GISP2

Abstract

We present a record of $\delta Kr/N_2$ and $\delta Xe/N_2$ measured in air bubbles in ice cores during the last glacial termination and inception. Changes in the atmospheric ratios of Kr/N_2 and Xe/N_2 should reflect changes in mean ocean temperature, due to the strong dependence of Kr and Xe solubilities on temperature. Assuming conservation of Xe, Kr, and N_2 in the atmosphere and ocean system, we use a mass balance model to interpret the $\delta Kr/N_2$ and $\delta Xe/N_2$ data in terms of ocean temperature. We find that the $\delta Kr/N_2$- and $\delta Xe/N_2$-derived ocean temperature (Noble Gas Temperature Index, NGTI) curves appear to correlate with CO_2 during both the last glacial termination and inception. Furthermore, they indicate that mean ocean temperature was 2.0-2.2 ±0.6ºC colder during the LGM, which is consistent with reconstructed Pacific temperatures during the LGM.

Introduction

Glacial/interglacial cycles are evident as 100,000-year oscillations of temperature and ice volume, as well as CO_2, over the last ~750,000-1 million years (Petit et al., 1999, Jouzel et al., 2007, Lüthi et al., 2008). Figure 3.1 shows the fluctuations in temperature and CO_2 over the last 800,000 years. Before 750,000-800,000 years before present (750-800 kyr B.P.), glacial cycles may have occurred on shorter timescales of ~40,000-years (Raymo, 1997). These glacial-interglacial cycles are fundamental aspect of the climate record, yet we still do not entirely understand their causes. Studying climate changes that occur during glacial inceptions and

terminations may elucidate the mechanisms and/or causes of these dramatic climate transitions.

Much like temperature and ice volume, atmospheric CO_2 oscillated between high levels (~280 ppm) during interglacial warm periods and low levels (~180 ppm) during glacial periods (Figure 3.1). The cause of these oscillations is not completely understood. Variations in ocean temperature are likely only part of the explanation, as colder ocean temperatures during the glacial period would likely cause only ~20% or less of the observed CO_2 drop during glacial periods due to enhanced solubility (Martin et al., 2005). As can be seen in Figure 3.1, atmospheric CO_2 concentrations tend to correlate with Antarctic surface temperatures over the last several glacial cycles. During the last deglaciation, CO_2 and Antarctic temperature rose at approximately the same time (~18,000 years before present). During the last glacial inception, CO_2 and Antarctic temperature appeared to have been decoupled, with surface temperature falling several thousand years before CO_2 began to fall. The reason for this decoupling remains unclear. Some have hypothesized that ocean stratification (Toggweiler, 1999, Sigman et al., 2004, Sigman, 2007), sea ice (Keeling and Stephens, 2001), or pH of the ocean (Marchitto et al., 2005) may have played a role in the atmospheric CO_2 drawdown into the last glacial period, and the decoupling might be explained in the context of these mechanisms if deep ocean processes lag Antarctic temperature by several thousand years.

The ocean plays a major role in storing and transporting heat, so investigating the timing and extent of global mean ocean temperature change may help to explain why climate cooled into the last glacial period (~120 kyr B.P.) and then warmed into

the current warm period (Holocene), and may shed light onto fundamental causes of glaciations and deglaciations. Mean ocean temperature can provide insight into deep ocean temperature, which has been somewhat of an enigma due the ambiguity of the benthic foraminiferal $\delta^{18}O$ record. The $\delta^{18}O$ of benthic foraminifera ($\delta^{18}O_{benthic}$) in ocean sediment cores is affected by both sea level and deep ocean temperature. Recent work has tried to decouple these effects on $\delta^{18}O_{benthic}$ through pore water studies (Schrag et al., 1996, Adkins et al., 2002), regressions with coral-derived relative sea level (Cutler et al., 2003, Waelbroeck et al., 2002) and isotope models of ice sheets and ocean temperature influences on $\delta^{18}O_{benthic}$ (Bintanja et al., 2007). While many of these methods have been effective at describing local deep water temperature at the sediment core site, there is a lack of information about global and deep ocean mean temperatures due to the spatial heterogeneity of the deep ocean. Furthermore, the pore-water approach only provides a single value for the last glacial period, hence there is a need for a time series that can illuminate the temporal evolution of ocean temperature at a resolution comparable to the CO_2 record.

In this study, we present a time series of $\delta Kr/N_2$ and $\delta Xe/N_2$ in ice cores during the last glacial termination (~24-14 kyr B.P.) and the last glacial inception (~123-105 kyr B.P.) from the GISP2 and Vostok ice cores, respectively. We have found that $\delta Kr/N_2$ measured in ice cores reflects past mean ocean temperature due to changes in ocean solubility with temperature (Headly and Severinghaus, 2007). In that earlier study, we measured $\delta Kr/N_2$ in GISP2 ice from the Last Glacial Maximum. Using a mass balance model, we calculated the expected $\delta Kr/N_2$ for varying degrees

of globally mean ocean temperature change. We found that the $\delta Kr/N_2$ from the LGM was -1.34‰, in reference to today's atmosphere, which reflects a 2.7ºC mean ocean temperature change. Because Xe is also a soluble gas (in fact, more soluble that Kr), its abundance in the atmosphere should be more strongly affected by changes in ocean temperature than Kr. We attempted to measure $\delta Xe/N_2$ in the LGM as well (Headly and Severinghaus, 2007), but our precision was too low to make any conclusions about how $\delta Xe/N_2$ may have changed though time. In the present study, we have increased the sample size by 10-fold and changed our analytical procedure from that used in Headly and Severinghaus (2007) in order to improve the $\delta Kr/N_2$ and $\delta Xe/N_2$ precision.

We have produced estimates of mean ocean temperature during the last glacial termination and inception based on our $\delta Kr/N_2$ and $\delta Xe/N_2$ measurements. For clarity, we refer to the fully corrected $\delta Kr/N_2$ and $\delta Xe/N_2$ data (corrected for gravitational and thermal effects) as Kr* and Xe*, to differentiate between these corrected data and the raw data. The ocean temperatures reconstructed using Kr* and Xe* are solubility-weigted mean ocean temperatures, meaning that a given change in ocean temperature at colder temperatures corresponds to a larger Kr* and Xe* change than a change in ocean tempreature at higher temperatures. This is due to the higher sensitivity (i.e. steeper slope) of Kr and Xe solubilities at low temperatures versus high temperatures (Figure 3.2). We define this solubility-weighted mean ocean temperature derived by Kr* and Xe* as the Noble Gas Temperature Index, or NGTI, which also has units of ºC.

The relationship between these reconstructed temperature (NGTI) curves and other climate parameters during these transitions may have implications for possible climate change hypotheses. We show that there appears to be a correlation between NGTI and CO_2, and that this relationship may constrain proposed mechanisms of climate change (e.g., Toggweiler, 1999, Sigman et al., 2004, Keeling and Stephens, 2001, Sigman, 2007). Furthermore, deep ocean temperature during the last glacial inception is poorly constrained due to a dearth of sea level reconstructions during this transition. The NGTI curves generated in this study may help to disentangle the temperature and sea level influences on the $\delta^{18}O$ foraminiferal record in both the inception and termination of the last glacial period.

Conceptual Model

In Headly and Severinghaus (2007), we have described in detail a conceptual model used to interpret $\delta Kr/N_2$ measurements in terms of average ocean temperature change. We use the same approach to interpret the Kr* and Xe* data presented in this study. Using the solubilities of Weiss and Kyser (1978), Weiss (1970), and Wood and Caputi (1966) for Kr, N_2, and Xe, respectively, we use a mass balance approach to estimate the change in oceanic and atmospheric inventories resulting from varying degrees of average ocean temperature change. We assume that the total amounts of Kr and Xe in the atmosphere and ocean are conserved as shown in Equations (3.1) and (3.2). We assume that atmospheric nitrogen is essentially conserved as well, as the denitrifiable inventory of nitrogen comprises ~0.01% of the atmospheric inventory (Schlesinger, 2007).

$$\mathrm{Kr}_{present\ atmosphere} + \mathrm{Kr}_{present\ ocean} = \mathrm{Kr}_{total} = \mathrm{Kr}_{past\ atmosphere} + \mathrm{Kr}_{past\ ocean} \quad (3.1)$$

$$\mathrm{Xe}_{present\ atmosphere} + \mathrm{Xe}_{present\ ocean} = \mathrm{Xe}_{total} = \mathrm{Xe}_{past\ atmosphere} + \mathrm{Xe}_{past\ ocean} \quad (3.2)$$

We calculate present and past oceanic inventories using gas solubilities, and the Levitus potential temperature and density database (Levitus, 1994). Solubilities are calculated for each temperature and density point in the database; every 1º-latitude by 1º-longtitude, at 33 depth intervals. For the glacial termination dataset using the GISP2 ice core, we take into account sea level rise during the deglaciation (Fairbanks, 1992, Cutler et al., 2003). Lower sea levels during the glacial period result in both reduced overall oceanic volume and increased sea level barometric pressure (due to the displacement of water from the ocean onto land, in the form of ice sheets). For the Vostok glacial inception data, the modern sea level is used, as sea level reconstructions during this time period are sparse (Cutler et al., 2003), and sea level after cooling began was likely ≤ 40 m lower than that of today. This introduces a bias of ≤ ~0.13‰ and ~0.33‰ for the modeled $\delta Kr/N_2$ and $\delta Xe/N_2$ towards higher values in the Vostok glacial inception (age < ~115 kyr). This bias is significantly smaller than the measurement precision (~0.42‰ and 0.78‰ for Kr* and Xe*, respectively). Present atmospheric inventories are calculated using known mole fractions (Schlesinger, 1997). We then solve for the past atmospheric inventories. The resultant atmospheric $\delta Kr/N_2$ and $\delta Xe/N_2$ curves versus ocean temperature change (Figures 3.2(a) and 3.2(b)) can be used to interpret the Kr* and Xe* data from GISP2 termination and Vostok inception datasets.

Method

The experimental procedure used for each sample in this ice core analysis consisted of several consecutive steps. Ice samples were stored in a -25ºC freezer. For both the Vostok and GISP2 ice, samples were typically ~20cm long (along the depth axis), with a diameter of ~8cm. While still in the freezer, 1-2mm of ice was trimmed from all surfaces with a band saw. Samples were 600-700 g after the 1-2mm surface removal. Once a sample was prepared in the -25ºC freezer, it was transported to the laboratory in a cooler, also chilled to -25ºC.

1) Extraction

The ice sample and a large stir bar are then placed in a stainless steel extraction vessel, which is kept at -25ºC in a large freezer in the laboratory. We designed the vessel as a replicate of that used by Kawamura and others (2003) in the analysis of Dome Fuji paleo-atmospheric gases and during subsequent noble gas analyses at Scripps Institution of Oceanography (Kawamura, personal communication). The extraction vessel, which is sealed with a copper gasket, is then attached to the vacuum line and immersed in a bath of -25ºC ethanol. Ambient air in the vessel is evacuated during 40-min of pumping via the vacuum line and turbomolecular pump (as in Severinghaus et al., 2003 and Headly and Severinghaus, 2007). The 40-minute pump down also allows for some sublimation of ice off the surface of the sample, further cleaning the surface of any adhered gases. After 40 minutes of pumping, the valve to the pump is closed, and the vapor pressure over ice

is recorded. Then the extraction vessel is sealed by closing the valve leading to the vacuum line.

The extraction procedure is based on the method used by Kawamura and others (2003), with modifications to ensure complete gas extraction of the soluble gases, krypton and xenon. A water vapor trap and an evacuated dip tube are attached to the vacuum line. The vacuum line is then pumped on for 30 minutes, after which we check for a leak in the water trap and the dip tube connection. Then, the valve between the extraction vessel and the line is opened, and we test for a leak in vessel connection to the line using a liquid N_2 trap. Once a vacuum is established, the valve to the pump is closed and we begin the transfer of extracted air into the dip tube. The -25ºC ethanol dewar surrounding the extraction vessel is removed, and replaced with a hot water bath covering the bottom surface of the vessel. As the ice begins to melt, the air that had been trapped in the air bubbles within the ice is released and immediately frozen into the dip tube in liquid Helium at 4K. During this transfer to the dip tube, the air is passed through an ethanol/liquid N_2 water vapor trap at ~-80ºC. As indicated in Headly and Severinghaus (2007), it is unlikely that gas occlusion by the rapid freezing of water vapor in the water trap is measurably affecting our samples.

Pressure, as recorded by a baratron pressure gauge, is usually ~2 torr during the portion of the sample transfer in which the ice is still melting. The ice sample typically melts in $\leq$ 20 minutes, at which time pressure stabilizes at 0.050 torr. At this point, the hot water bath surrounding the extraction vessel is removed. A magnetic stir base is then placed under the vessel to agitate the meltwater for the remainder of

the transfer. Following Kawamura (personal communication), when the pressure in the vacuum line stabilizes at $p \leq 0.001$ torr after 1 hour, the transfer is terminated by closing the valve to the dip tube.

2) *Overnight equilibration/Splitting*

The dip tube containing the extracted air is then removed from the liquid He and hooked up to a series of stainless steel volumes: a 180-cm^3 and a 4-cm^3 volume, which are attached to a vacuum line (Figure 3.3). These are contained in a large isothermal bath, filled with 6 gallons of water at room temperature. Both volumes are evacuated for 1 hour, after which we ensure that there is no leak in the volumes or connections. Next, we close the valve between the 4-cm^3 volume and the rest of the line (valve 3), and open the sample dip tube (valve 1) to allow the gas to expand into both volumes. We allow the sample to "equilibrate" among the 180-cm^3 and 4-cm^3 volumes overnight (~15 hours). After the overnight equilibration, the valve separating the 4-cm^3 and 180-cm^3 volumes (valve 2) is closed, splitting the sample into two samples to be analyzed separately. The sample in the 4-cm^3 volume is passed through a liquid N_2 U-trap to remove CO_2 and frozen into a dip tube in liquid He at 4K for 5 minutes. That sample is measured on the Finnigan Delta XP mass spectrometer for $\delta^{15}N$, $\delta^{18}O$, $\delta O_2/N_2$, and $\delta Ar/N_2$. The larger sample in the 180-cm^3 volume is then frozen into another dip tube in liquid He for 25 minutes. That sample is ultimately measured on the Finnigan MAT 252 for $\delta^{40/36}Ar$, $\delta^{86/82}Kr$ (hereafter $\delta^{40}Ar$ and $\delta^{86}Kr$), $\delta Kr/Ar$, and $\delta Xe/Ar$.

We tested this "splitting" step by measuring all isotopic and element ratios for "split" samples and those that have not been subjected to the splitting step, which we will refer to as "blanks". The blanks were 80-cm^3 or 1.4-cm^3 volumes (for measurement on the MAT 252 or Delta XP, respectively) filled with dry air collected from the Scripps pier. The 1.4-cm^3 sample was attached to the vacuum line, transferred through a liquid N_2 trap into a dip tube in liquid He, and then measured on the Delta XP for $\delta^{15}N$, $\delta^{18}O$, $\delta O_2/N_2$, and $\delta Ar/N_2$. The 80-cm^3 volume was gettered to isolate the noble gases (as described in the following section) and then transferred to a dip tube in liquid He to be measured on the MAT 252 for $\delta^{40}Ar$, $\delta^{86}Kr$, $\delta Kr/Ar$, and $\delta Xe/Ar$.

The samples subject to the splitting step were collected in the same manner as that of the "blanks." An 80-cm^3 volume was filled with dry air from the SIO pier, and attached to the vacuum line. It was then frozen into a dip tube in liquid He for 25 minutes. After the transfer, the dip tube was attached to 180-cm^3 and 4-cm^3 volumes in water bath (as in Figure 3.3). As detailed in an earlier section, the volumes were evacuated for an hour, after which the sample was expanded into them to equilibrate overnight (~15 hours). After overnight equilibration, the sample was treated as described above for the ice core samples: the valve separating the 180-cm^3 and 4-cm^3 volumes was closed, and each portion of the sample was transferred into a dip tube in liquid He. The smaller sample in the 4-cm^3 volume was passed through a liquid N_2 trap before being frozen into a dip tube in liquid He for 5 minutes, while the larger 180-cm^3 sample was frozen directly into a dip tube for 25 minutes. The smaller sample was then run on the Delta XP for $\delta^{15}N$, $\delta^{18}O$, $\delta O_2/N_2$, and $\delta Ar/N_2$ analysis.

Before analyzing the larger sample, it was gettered to remove reactive gases (a process described in the following section) and frozen into a dip tube in liquid He. Then it was analyzed for $\delta^{40}Ar$, $\delta^{86}Kr$, $\delta Kr/Ar$, and $\delta Xe/Ar$.

Overnight equilibration times of 12 hours or more did not appear to affect the isotope or element ratio measurements. Shorter equilibration times were found to systematically fractionate the $\delta^{15}N$ measurements (values were typically ~ -0.020‰). Once an overnight equilibration of ≥12 hours was established, we did a series of tests to ensure that the splitting method did not cause any fractionation in any of the measured values. A student's t-test was performed to determine whether a significant difference existed between the measurements of the blanks and the split samples. There were no significant differences between the blanks and split samples at the 95% confidence level for any of the measurements, with the exception of $\delta Ar/N_2$. $\delta Ar/N_2$ measured in the blanks is different from that of the split samples at $p < 0.005$, by a mean value of 0.06‰. Nevertheless, our $\delta Ar/N_2$ precision among ice core samples (typically up to an order of magnitude larger) is not good enough to make this difference significant.

4) *Gettering*

The larger portion of the ice core sample (split into the 180-cm^3 volume) must be gettered in order to isolate the noble gases for analysis. The sample gas sample is exposed to a heated Zr/Al getter, which removes all gases but the noble gases. Our gettering process follows that of Kawamura et al., (in prep) and is similar to that of Severinghaus et al. (2003). The sample (in a dip tube) is attached to a vacuum line

adjacent to the quartz tube getter oven and an 80-cm^3 volume (Figure 3.4). The 80-cm^3 volume aids in drawing gas out of the dip tube during gettering. We use 30 Zr/Al getter sheets in a 1/2-in diameter quartz tube oven. The getter is activated for 10 minutes at 100ºC, and then 10 minutes at 900ºC. Following activation, the getter is allowed to cool for 3 minutes, after which we leak test the volume and connections. Then we close the valve separating the getter oven/dip tube/80-cm^3 volume from the rest of the vacuum line (valve 1), turn the getter oven to 900ºC, and open the dip tube (valve 2) to begin gettering. After 10 minutes, we close the valve to the dip tube (valve 2), and continue gettering the sample that remains in the getter oven and 80-cm^3 volume for 10 more minutes at 900ºC, and then 5 minutes at 300ºC to absorb H_2. The getter oven is turned off, and the sample is then frozen into another dip tube in liquid He for 5 minutes. After this transfer, we repeat this gettering procedure for any sample remaining in the dip tube, closing the valve to the getter area (valve 1), opening the dip tube valve (valve 2), gettering the sample at 900ºC for 20 minutes, and 300ºC for 5 minutes. Then the remaining sample is combined with the first portion by transfer to the dip tube in liquid He (the same dip tube into which the first portion of the sample was frozen) for 5 minutes. We getter the sample in two steps as described here due to the large sample size, which otherwise prohibits rapid gettering due to the requirement that reactive gas diffuse through a substantial pressure of argon.

5) *Mass Spectrometry*

We analyze the smaller portion of the sample (split into the 4-cm^3 volume) on the Finnigan Delta XP mass spectrometer. Mass spectrometry analysis on the Delta XP follows that of Headly and Severinghaus (2007). The sample is measured against a working standard (Air 20). The working standard gas, a laboratory tank of dry air collected from the SIO pier at ~20 psig, is expanded into a 1-cm^3 aliquot and allowed to equilibrate for 3 minutes. Then the sample gas and standard aliquot are expanded into the mass spectrometer bellows for 3 minutes. The mass spectrometry measurement method (air_method), is the same as that used in Headly and Severinghaus (2007), and makes 16 cycles of measurements in each block. We run 25 blocks (of 16 cycles each) in this study, as opposed to 4 blocks in our previous study. Delta XP mass spectrometry produces $\delta^{15}N$, $\delta^{18}O$, $\delta O_2/N_2$, and $\delta Ar/N_2$ for each ice core sample. Typical external precisions or reproducibilities (1 standard deviation) for mass spectrometry of each sample are 0.004‰, 0.010‰, 0.011‰, and 0.013‰.

We also monitored CO_2 and H_2O after each set of 25 blocks. CO_2 can potentially interfere with both $\delta^{15}N$ and $\delta^{18}O$ measurements due to isobaric interference between ^{13}CO and $^{15}N^{14}N$ (Sowers et al., 1989, Headly and Severinghaus, 2007), and possible ion-molecule reactions between CO_2 and O_2 resulting in enhanced $\delta^{18}O$ with increasing CO_2 abundance (Headly et al., in prep, Appendix). Corrections for these interactions are made to $\delta^{15}N$ as described in a subsequent section and in Severinghaus et al. (2003) and Headly and Severinghaus (2007).

We measure $\delta^{40}Ar$, $\delta^{86}Kr$, $\delta Kr/Ar$, and $\delta Xe/Ar$ on a Finnigan MAT 252 mass spectrometer. $\delta Kr/Ar$ and $\delta Xe/Ar$ were analyzed by peak jumping. The working standard gas is a laboratory tank of Ar, Kr, and Xe, in which the relative partial pressures of the gases closely resemble their atmospheric proportions. As in the Delta XP procedure, the standard gas (~8 psig) is expanded into a 1-cm^3 aliquot for 3 minutes, after which the sample and standard gases are expanded into the bellows for 3 minutes. The $\delta^{40}Ar$, $\delta Kr/Ar$, and $\delta Xe/Ar$ measurement methods on the mass spectrometer are the same as in Headly and Severinghaus, 2007, with an additional 3 blocks added to the $\delta^{40}Ar$ measurement, producing a total of 5 blocks of 16 $\delta^{40}Ar$ measurements. We doubled the number of $\delta Kr/Ar$ and $\delta Xe/Ar$ measurements, producing 4 of each. For each sample, we also measured the background voltages on the Kr, Xe, and Ar cups for the peak jumping measurements. Measurement of $\delta^{86}Kr$ was possible for this dataset (unlike the earlier work of Headly and Severinghaus, 2007) because we have increased the sample size by 10-fold, as compared to that study. Six blocks of 24 cycles each were run for $\delta^{86}Kr$ analysis. Typical mass spectrometry external precisions (standard deviations) of $\delta^{40}Ar$, $\delta^{86}Kr$, $\delta Kr/Ar$, and $\delta Xe/Ar$ for each sample were 0.007‰, 0.050‰, 0.30‰, and 0.75‰. Details of mass spectrometry on the MAT 252 are given in Table 3.1.

$\delta Kr/N_2$ and $\delta Xe/N_2$ are not measured directly. Rather, they are calculated using measured $\delta Kr/Ar$, $\delta Xe/Ar$, $\delta Ar/N_2$, and $\delta^{40}Ar$, as shown in Equation 3.3 below:

$$\delta Kr/N_2 = \left\{ \left[\frac{\left(\frac{\delta\,^{84}Kr/^{36}Ar}{10^3} + 1 \right)}{\left(\frac{\delta\,^{40}Ar/^{36}Ar}{10^3} + 1 \right)} \times \left(\frac{\delta\,^{40}Ar/^{28}N_2}{10^3} + 1 \right) \right] - 1 \right\} \times 10^3‰ \qquad (3.3)$$

Corrections

In the case of a pressure imbalance between the sample and standard during mass spectrometry, the pressure of the smaller sample falls faster than that of the larger one. This pressure difference can impart an artifact on the measured values due to machine non-linearity. Pressure imbalance corrections for measurements on both the Delta XP and the Finnigan MAT 252 mass spectrometers are made as in Severinghaus et al. (2003) and Headly and Severinghaus (2007), and as shown in Equations 3.4 and 3.5. All isotope and element ratios are corrected for pressure imbalance as are $\delta^{86}Kr$ and $\delta^{15}N$ below. A new Pressure Imbalance Sensitivity (PIS) (Equations 3.4 and 3.5) is determined every 1-2 weeks.

$$\delta_{corrected} = \delta_{measured} - PIS\Delta_{pressure} \qquad (3.4)$$

$$\Delta_{pressure} = {}^{86}Kr_{sample}/{}^{86}Kr_{standard} - 1 \quad (\text{MAT 252}) \qquad (3.5a)$$

$$\Delta_{pressure} = {}^{28}N_{2\,sample} - {}^{28}N_{2\,standard} \quad (\text{Delta XP}) \text{ (volts)} \qquad (3.5b)$$

A second correction is made to account for the "chemical slope", the fact that differences in the amount of O_2, N_2, CO_2, and Ar between sample and standard can affect measured isotopic ratios. An imbalance of O_2 or N_2 can affect $\delta^{15}N$ or $\delta^{18}O$, respectively, while differences in CO_2 between sample and standard can affect both

$\delta^{15}N$ and $\delta^{18}O$ (Headly et al., in prep, Appendix). Furthermore, excess Ar in the sample or standard can affect $\delta^{86}Kr$ measurements on the Finnigan MAT 252 (Figure 3.5). These effects are corrected for using a chemical slope correction outlined in Severinghaus et al. (2003) and Headly and Severinghaus (2007). In the case of $\delta^{86}Kr$, we correct for difference in $\delta Ar/Kr$ as shown in Equation 3.6. All other chemical slope corrections are done in a similar fashion. The chemical slopes were experimentally determined at the beginning of these measurements.

$$\delta^{86}Kr/^{82}Kr_{\text{chemical slope corrected}} = \delta^{86}Kr/^{82}Kr_{\text{pressure corrected}} - [\text{chemical slope}] \times \delta Ar/Kr_{\text{measured}} \qquad (3.6)$$

Normalization to Pier Air

The modern atmosphere is our ultimate reference gas for these measurements. The working standards we use during mass spectrometry are taken from a laboratory tank, and may differ from the atmosphere and change through time as they are used. In order to make a meaningful standardization of the ice core measurements, we measure present-day air collected from the end of the Scripps Pier in La Jolla, CA (pier air), and measure that air against the working standard. Then the ice core measurements are standardized to the measured pier air (Equation 3.7). By using pier air as the ultimate standard, the ice core measurements reflect a change relative to the present atmosphere.

$$\delta Kr/N_{2\,normalized} = \left(\left(\frac{\delta Kr/N_{2\,ice\ core}}{1000} + 1\right) \Big/ \left(\frac{\delta Kr/N_{2\,pierair}}{1000} + 1\right) - 1\right) \times 1000 \qquad (3.7)$$

The method used to collect pier air follows Headly and Severinghaus, 2007, with a modification that air is collected into one 2-L flask, rather than 4-cm^3 pipettes. Air is pumped through an aspirated intake, passing through two -100ºC ethanol/liquid N_2 water traps, into the 2-L flask for 10 minutes. The air is pumped through ¼-inch Synflex tubing before the water trap, and before and after it reaches 2-L flask, as in Headly and Severinghaus (2007).

One 2-L flask can be used to make ~7 individual pier air measurements. We analyzed pier air samples at least once per month. For each measurement, an 80-cm^3 aliquot of air is taken from the 2-L flask, and is then frozen into a dip tube in liquid He for 25 minutes. The air sample in the dip tube is then handled in the same way as an ice sample. It is expanded into the 180-cm^3 and 4-cm^3 volumes and allowed to equilibrate overnight (Figure 3.3). The sample is then split into two sub-samples by closing the valve between the 180- and 4-cm^3 volumes. The smaller sample is transferred through a liquid N_2 trap, frozen into a dip tube, and analyzed on the Delta XP for $\delta^{15}N$, $\delta^{18}O$, $\delta O_2/N_2$, and $\delta Ar/N_2$. The larger sample is transferred into a dip tube, and then gettered using the same procedure described in an earlier section. The larger, gettered sample is analyzed on the Finnigan MAT 252 for $\delta^{40}Ar$, $\delta^{86}Kr$, $\delta Kr/Ar$, and $\delta Xe/Ar$. Error associated with gas handling is therefore reduced when the ice core samples are normalized to the pier air samples, since both are subject to the same experimental procedure.

Typically, the pier air values used to normalize ice core measurements are the mean of all pier air measurements made during the duration of the ice core analysis (in this case, October-December 2007 and January-March 2008). The $\delta Kr/N_2$ and $\delta Xe/N_2$ measured in pier air during these time periods are shown in Figures 3.6 (a) and (b). The $\delta^{15}N$ and $\delta^{86}Kr$, which are used in ice core measurements to correct for gravitational settling and thermal diffusion, in pier air are shown in Figure 3.6 (c) and (d). Average pier air values and standard deviations of $\delta Kr/N_2$, $\delta Xe/N_2$, $\delta^{86}Kr$, and $\delta^{15}N$ used to normalize the Vostok and GISP2 measurements, along with other measured values, are given in Table 3.2.

With the exception of $\delta^{86}Kr$, all of the pier air measurements were stable during the duration of the measurements. $\delta^{86}Kr$ is stable during the Vostok measurements, but it appears to shift to higher values during the course of the GISP2 measurements. We fit a linear trend to the pier air $\delta^{86}Kr$ data measured during the GISP2 measurements (January –March 2008), and use this linear trend to normalize the ice data, as done for $\delta^{40}Ar$ by Severinghaus et al, 2003. The fit to the data is shown in Figure 3.6(c). The x-axis in Figure 3.6(c) is the day number on which the sample is measured, which is then used to calculate the pier air $\delta^{86}Kr$ using the linear trend ($y = 0.0009x + 1.1935$).

Corrections for sources of fractionation within the firn

We also make corrections for processes that can fractionate gases within the firn, a porous snow layer comprising the top 50-100m of an ice sheet.

1) Gravitational settling

Gravitational settling in the firn, which causes heavier isotopes to be enriched in air bubbles that form at the firn/ice interface, is the largest of these corrections (Severinghaus et al., 2003, Headly and Severinghaus, 2007). This enrichment is proportional to the mass difference between the two isotopes measured, as shown in the barometric equation modified for a gas pair (Craig et al., 1988):

$$R/R_o = e^{gz\Delta M/R^*T} \qquad (3.8)$$

where R is the isotope or gas ratio measured, R_o is the same ratio in the atmosphere (our standard gas), g is the local gravitational acceleration, z is the thickness of the firn, Δm is the mass difference between the two isotopes, R^* is the gas constant, and T is the isothermal temperature of the column.

Because gravitational settling fractionates only according to mass difference, in principle correction for gravitational settling should be possible with the product of the Kr-N_2 mass difference and an isotope pair only affected by gravitational settling. In fact, no such isotope pair exists, but δ^{86}Kr approaches this ideal closely because of its very weak thermal diffusion sensitivity. We experimented with several different approaches. In one approach, we use δ^{86}Kr measured in each sample to correct for gravitational settling as shown in Equations 3.9 and 3.10:

$$\delta \mathrm{Kr}/\mathrm{N}_{2gravcorr} = \delta \mathrm{Kr}/\mathrm{N}_{2\,measured} - \Delta m_{\mathrm{Kr-N_2}} \times \delta^{86/82}\mathrm{Kr}/4 \qquad (3.9)$$

$$\delta \mathrm{Xe}/\mathrm{N}_{2gravcorr} = \delta \mathrm{Xe}/\mathrm{N}_{2\,measured} - \Delta m_{\mathrm{Xe-N_2}} \times \delta^{86/82}\mathrm{Kr}/4 \qquad (3.10)$$

The $\delta^{86/82}$Kr/4 is the gravitational settling effect per mass unit, which is then multiplied by the mass difference between the two gases in the desired element ratio (i.e. $\Delta m_{Kr\text{-}N2} \sim 56$ and $\Delta m_{Xe\text{-}N2} \sim 106$).

2. Thermal diffusion

Gases are also affected by temperature gradients within the firn, and in a second approach, we correct for thermal diffusion (Grew and Ibbs, 1952) explicitly in addition to gravitational settling. Severinghaus et al. (1998) found that thermal diffusion within firn, which is then imparted to the air bubbles in ice cores, can be identified using a combination of δ^{15}N and δ^{40}Ar measurements. They then used the extent of thermal diffusion in the firn to infer the temperature difference between the top and bottom of the diffusive part of the firn ΔT, from which they determined the magnitude of abrupt temperature changes at the surface, as did others in subsequent work (Severinghaus and Brook, 1999, Grachev and Severinghaus 2005, Kobashi et al., 2007).

We use δ^{86}Kr, as opposed to δ^{40}Ar (which was used in Severinghaus et al., 1998, and subsequent studies), as representative of gravitational settling. We have found that δ^{40}Ar may be artifactually enriched by gas loss, and may not be representative of a pure gravitational effect (the effect of gas loss on δ^{40}Ar is

discussed in a subsequent section in this paper, and also in Severinghaus et al. (2003)). A drawback of using the $\delta^{86}Kr$ as representative of gravitational settling is that $\delta^{86}Kr$ may be fractionated when a deep convection zone is present at the top of the firn. This effect is likely to only affect our Vostok data, and will be discussed further in the following section.

We attribute the measured excess of $\delta^{15}N$ over $\delta^{86}Kr/4$ to thermal diffusion, and use it as a parameter analogous to the $\delta^{15}N_{excess}$ of Severinghaus and Brook (1999) that is only sensitive to thermal diffusion. ($\delta^{86}Kr$ is divided by 4 to scale to one mass unit.) The implied temperature gradient within the firn (ΔT) is calculated as shown in Equation 3.11. Thermal diffusion sensitivities, Ω, used for ^{15}N and ^{86}Kr are from Grachev and Severinghaus (2003a) and Kawamura et al. (in prep), respectively.

$$\Delta T = \left(\Omega(^{15}\mathrm{N}) - \Omega(^{86}\mathrm{Kr})/4\right) \Big/ \left(\delta^{15}\mathrm{N} - \delta^{86}\mathrm{Kr}/4\right) \qquad (3.11)$$

The thermal diffusion sensitivities (Ω) of $\delta Kr/Ar$, $\delta Xe/Ar$, $\delta Ar/N_2$, and $\delta^{40}Ar$ are known, so we calculate thermally corrected $\delta Kr/N_2$ and $\delta Xe/N_2$ as shown in Equations 3.12 and 3.13 below (Nemzer and Severinghaus, in prep). The values of the thermal diffusion sensitivities (Ω) and thermal diffusion factors (α), which are a function of temperature, are shown in Table 3.3. We use ΔT to calculate the gravitational component of the $\delta^{86}Kr$, which is used to correct for gravitational settling (Equations 3.12 and 3.13). Also explicitly defined in Equations 3.12 and 3.13

are Kr* and Xe*, which are the gravitationally and thermally corrected $\delta Kr/N_2$ and $\delta Xe/N_2$ data, representing paleo-atmospheric $\delta Kr/N_2$ and $\delta Xe/N_2$.

$$Kr^* = \delta Kr/N_{2\,gravthermcorr} = \delta Kr/N_{2raw} - \left(\Delta m_{Kr-N_2} \times \left(\delta^{86}Kr/4 - \Delta T \times \Omega(^{86}Kr)/4\right)\right) - \left(\Omega(Kr/N_2) \times \Delta T\right) \qquad (3.12)$$

$$Xe^* = \delta Xe/N_{2\,gravthermcorr} = \delta Xe/N_{2raw} - \left(\Delta m_{Xe-N_2} \times \left(\delta^{86}Kr/4 - \Delta T \times \Omega(^{86}Kr)/4\right)\right) - \left(\Omega(Xe/N_2) \times \Delta T\right) \qquad (3.13)$$

$\Omega(Kr/N_2)$ and $\Omega(Xe/N_2)$ have not been measured directly. Because they are defined in terms of a natural logarithm of the gas ratios, we calculate them as follows:

$$\Omega(Kr/N_2) = \Omega(Kr/Ar) - \Omega(^{40}Ar) + \Omega(Ar/N_2) \qquad (3.14)$$

$$\Omega(Xe/N_2) = \Omega(Xe/Ar) - \Omega(^{40}Ar) + \Omega(Ar/N_2) \qquad (3.15)$$

The calculated values of ΔT from both the GISP2 glacial termination and the Vostok glacial inception are plausible (Figure 3.7a and b). In the GISP2 glacial termination data, the warming associated with the Bolling-Allerod and interstadial 2 are ~10 and 4ºC, respectively, while the remaining ΔT estimates are within error of 0ºC: -0.34ºC ± 1.58ºC (Figure 3.7a). The ΔT values calculated in the Vostok glacial inception data are also within error of 0ºC, but tend to be slightly more positive: 0.57ºC ± 1.12ºC (Figure 3.7b).

3. *Convective mixing in the firn*

The presence of a convection zone is another potential source of fractionation. A convection zone can be present in the upper portion of firn, where convective mixing (typically due to strong winds) (Colbeck, 1989) eliminates any thermal or gravitational signal imparted on the isotope or gas ratios (Sowers et al., 1992). In the presence of a convection zone, fractionation of gases with low molecular diffusivities may be reduced relative to fast-diffusing gases. This greater disequilibrium of slow-diffusing gases may be thought of as a form of kinetic fractionation. This effect is confirmed by the observation that as gases return to equilibrium below the zone of convective mixing, gases with lower molecular diffusivities (i.e. Kr and Xe) do not reach equilibrium as fast as gases with higher diffusivities (like N_2) (Kawamura et al., in prep.). The presence of a convection zone can therefore potentially cause an underestimation of $\delta^{86}Kr$ (used in our gravitational and thermal corrections) relative to $\delta^{15}N$, and of $\delta Kr/N_2$ and $\delta Xe/N_2$, owing to the slower diffusivities of Xe and Kr, relative to N_2 (Kawamura et al., in prep).

It is unclear whether our samples from either Vostok or GISP2 have been affected by convective mixing within the firn. Based on reconstructed conditions of the GISP2 core site during deglaciation (Cuffey and Clow, 1997), as well as the consistency between $\delta^{15}N$ measurements and firn densification models (Landais et al., 2006), it is unlikely that a significant convection zone existed at GISP2 during the last deglaciation. Vostok, in contrast, may have had a deep convection zone in the past, as convection zones of ~10 m have been found today at Vostok, and Dome F (Bender et al., 1994, Kawamura et al., 2006) and as much as 20-25 m at Megadunes, which is

near Vostok (Kawamura et al., in prep). A convection zone at Vostok during the glacial inception could have an effect on our measurements as described above. We are not be able to make an ideal correction for convection at this time, but improved methods to measure other Kr isotopes, as well as Xe isotopes will make this correction possible (Kawamura et al., in prep). The slightly positive ΔT in the Vostok data (Figure 3.7(b)) may be indiciative of a small convective zone in the early portion of the data (age > 110 kyr B.P.).

4. *Gas loss*

It has been observed that some gases leak out of the air bubbles in ice cores during the natural bubble close-off at the base of the firn (Severinghaus and Battle, 2006, Bender et al., 2002), as well as during storage (Bender et al., 1995). Kr, Xe, and N_2 appear to be intact in air bubbles in ice cores, while Ar appears to be depleted in air bubbles (Bender et al., 1995, Severinghaus et al., 2003, Severinghaus and Battle, 2006). For this reason, we measure Kr and Xe as ratios to N_2, rather than Ar. Ar isotopes may also be affected by gas loss (Severinghaus et al., 2003), with higher $\delta^{40}Ar$ corresponding to increased gas loss. For this reason, we have chosen to use $\delta^{86}Kr$ to correct for gravitational fractionation as opposed to $\delta^{40}Ar$. By using the isotopic measurements of $\delta^{40}Ar$ and $\delta^{86}Kr$ in this work, we may have been able to isolate the signal in $\delta^{40}Ar$ that is due to gas loss. To calculate the $\delta^{40}Ar$ enrichment due to gas loss ($\delta^{40}Ar_{\text{gas loss residual}}$), we subtract $\delta^{86}Kr_{grav}$ ($\delta^{86}Kr_{\text{observed}} - \Omega(^{86}Kr)/4\times\Delta T$) and $\delta^{40}Ar_{therm}$ ($\Omega(^{40}Ar)\times\Delta T$) from $\delta^{40}Ar_{observed}$ (Equation 3.14a-c).

$$\delta^{40}\mathrm{Ar}_{gas\ loss\ residual} = \delta^{40}\mathrm{Ar}_{observed} - \delta^{86}\mathrm{K}r_{grav} - \delta^{40}\mathrm{Ar}_{therm} \quad (3.16a)$$

$$\delta^{86}\mathrm{K}r_{grav} = \delta^{86}\mathrm{Kr}_{observed} - \Omega(^{86}\mathrm{Kr}) \times \Delta T \quad (3.16b)$$

$$\delta^{40}\mathrm{Ar}_{therm} = \Omega(^{40}\mathrm{Ar}) \times \Delta T \quad (3.16c)$$

If δ^{40}Ar were only affected by gravitational fractionation and thermal fractionation, the expected value of $\delta^{40}\mathrm{Ar}_{\text{gas loss residual}}$ is zero. Yet, in this data set, the average $\delta^{40}\mathrm{Ar}_{\text{gas loss residual}}$ is 0.017 ± 0.009‰. Plotted against δKr/Ar, it produces a slope of 0.003 (Figure 3.8), which is broadly comparable to an earlier published relationship of 0.007‰ δ^{40}Ar per 1‰ δKr/Ar (Severinghaus et al., 2003). The value of $\delta^{40}\mathrm{Ar}_{\text{gas loss residual}}$ should not be constant in different ice cores and/or at different depths than those presented in this data set, because the $\delta^{40}\mathrm{Ar}_{\text{gas loss residual}}$ depends on the degree of gas loss. It is unclear whether the relationship between δKr/Ar and $\delta^{40}\mathrm{Ar}_{\text{gas loss residual}}$ is a constant one in different ice cores. Nevertheless, the $\delta^{40}\mathrm{Ar}_{\text{gas loss residual}}$ calculated here may be used to isolate the gas loss effect in other studies of δ^{40}Ar in GISP2 ice during this time period from the last termination.

5. Kinetic Fractionation Correction

In addition to convection, a slight disequilibrium can be caused by rapid snow accumulation. Based on evidence from the West Antarctic Ice Sheet (WAIS) divide core in Antarctica, at high accumulation sites, slower diffusing Kr isotopes are depleted as compared to δ^{15}N, which has a higher molecular diffusivity. It is thought that this effect arises when the firn deepens faster than the slowly diffusing Kr

isotopes can gravitationally equilibrate, causing $\delta^{86}Kr$ to be lower than would be expected due to gravitational settling (Severinghaus, personal communication). At WAIS divide, $\delta^{86}Kr$ was typically ~10 per meg lower than the expected gravitational settling enrichment in $\delta^{86}Kr$ (Severinghaus, personal communication), and a firn gas transport model reproduced this value. Because conditions at GISP2 are similar to that of WAIS divide, we use the 10 per meg value to correct the GISP2 $\delta^{86}Kr$ data, adding 10 per meg to the $\delta^{86}Kr$ measurements from that core. We have not used this correction at Vostok, due to differences in accumulation from the WAIS site, as well as the possibility of a deep convection zone at Vostok.

Testing the method with late Holocene ice

We analyzed late Holocene ice (~1000 yr B.P.) from GISP2 and a shallow core recently drilled at Greenland Summit to test to integrity of our method. The mean ocean temperature, and hence, $\delta Kr/N_2$ and $\delta Xe/N_2$ in the atmosphere, should not have changed during the last ~1000 years. Therefore, we would expect to find values of 0‰ for both $\delta Kr/N_2$ and $\delta Xe/N_2$ in late Holocene ice, using today's atmosphere as a standard.

The results from these measurements are shown in Figure 3.9. The four shallowest points in the Summit data were measured in collaboration with Kenji Kawamura. Both $\delta Kr/N_2$ and $\delta Xe/N_2$ are shown using $\delta^{86}Kr$ to correct for gravitational fractionation. The $\delta Kr/N_2$ from GISP2 and Summit are 0.26 ± 0.78 ‰ and 0.08 ± 0.38 ‰, respectively. The typical standard deviation of $\delta Kr/N_2$ between

replicates at the same depth from GISP2 and Summit are ±0.14‰ and ±0.31‰, respectively. Replicates were obtained by cutting a large sample in half lengthwise, yielding two ~600-700g samples of ice from one depth interval. The $\delta Xe/N_2$ from GISP2 and Summit are 0.87 ± 1.34 ‰ and 0.76 ± 0.75 ‰, respectively, with standard deviations between replicates of ±0.59‰ and ±0.57‰. Also shown in Figure 3.9 are the isotopic ratios, $\delta^{40}Ar$, $\delta^{86}Kr$, and $\delta^{15}N$, shown per unit mass difference. The GISP2 samples, which often had significant internal fractures, were older and not as pristine as the Summit samples (which had been drilled only months before this analysis). We attribute the higher standard deviation among the GISP2 samples to this difference in the condition of the ice cores.

The other data measured (in addition to $\delta Kr/N_2$ and $\delta Xe/N_2$) show greater standard deviations in the GISP2 shallow data, as compared to the Summit data, as well. From the shallow GISP2 dataset as a whole, the standard deviations of $\delta^{40}Ar/4$, $\delta^{86}Kr/4$, $\delta Kr/Ar$, $\delta Xe/Ar$, $\delta^{15}N$, $\delta^{18}O$, $\delta O_2/N_2$, and $\delta Ar/N_2$ were as follows: ±0.007‰, ±0.014‰, ±1.28‰, ±1.37‰, ±0.008‰, ±0.159‰, ±6.83‰, and ±0.86‰. The high error in the $\delta Kr/Ar$, $\delta Xe/Ar$, $\delta O_2/N_2$, $\delta Ar/N_2$ are likely due to gas loss, since some samples had significant internal fractures. The typical standard deviation between replicates is substantially lower. We analyzed 4 sets of replicates, out of 11 total samples in our GISP2 late Holocene dataset. Replicate standard deviations are as follows: $\delta^{40}Ar/4$: ±0.002‰, $\delta^{86}Kr/4$: ±0.002‰, $\delta Kr/Ar$: ±0.14‰, $\delta Xe/Ar$: ±0.52‰, $\delta^{15}N$: ±0.001‰, $\delta^{18}O$: ±0.015‰, $\delta O_2/N_2$: ±0.32‰, $\delta Ar/N_2$: 0.08‰.

The standard deviations of the entire Summit dataset (n = 16) for each measured value are as follows: $\delta^{40}Ar/4$: ±0.004‰, $\delta^{86}Kr/4$: ±0.006‰, δKr/Ar: ±0.62‰, δXe/Ar: ±0.64‰, $\delta^{15}N$: ±0.004‰, $\delta^{18}O$: ±0.009‰, $\delta O_2/N_2$: ±1.25‰, $\delta Ar/N_2$: 0.64‰. Typical standard deviations between the five sets of depth replicates in the Summit data are $\delta^{40}Ar/4$: ±0.002‰, $\delta^{86}Kr/4$: ±0.005‰, δKr/Ar: ±0.08, δXe/Ar: ±0.23‰, $\delta^{15}N$: ±0.003‰, $\delta^{18}O$: ±0.004‰, $\delta O_2/N_2$: ±0.16‰, and $\delta Ar/N_2$: 0.04‰. Despite the difference in ice quality between the two sets of late Holocene ice, the precision between replicates of the same depth from both datasets are quite similar.

The isotope pattern in the bottom two plots in Figure 3.9 is also worthy of mention. The $\delta^{40}Ar$ values are generally elevated in comparison to $\delta^{15}N$ and $\delta^{86}Kr$ values. This pattern of elevated $\delta^{40}Ar$ is likely due to gas loss, as we have shown in a previous section (positive values of $\delta^{40}Ar_{gaslosscorr}$ are found in the GISP2 glacial termination data).

Results

GISP2 deglaciation $\delta Kr/N_2$ and $\delta Xe/N_2$ record

One dataset presented here spans the last glacial termination (24,000-14,000 years before present) and was sampled from the GISP2 ice core in Greenland. Plotted in Figure 3.10(a) are $\delta^{15}N$ data (from this work, Severinghaus and Brook, 1999, and Severinghaus, personal communication) and the $\delta^{18}O_{ice}$ record (Stuiver and Grootes, 1995) versus ice core depth during the last deglaciation. The Bølling-Allerød warming, expressed as the peaks in $\delta^{15}N$ and $\delta^{18}O_{ice}$, is prominent in both records at

~1800m depth, and the Younger Dryas cooling following the Bølling-Allerød is seen in the $\delta^{18}O_{ice}$ record as well. The peaks in $\delta^{15}N$ and $\delta^{18}O$ do not occur at the same depths in Figure 3.10(a), yet they both represent the abrupt warming into the Bølling-Allerød. This depth "mis-match" in features in the ice versus those of the trapped gas is due to the well-known gas age-ice age difference (Severinghaus and Brook, 1999). This difference arises owing to the mixing of relatively younger air into the older firn. When air bubbles form at the base of the firn, the air trapped in the ice is younger than the ice that encloses the air bubble. The gas age-ice age difference in Figure 3.10(a) is evident in the offset between the $\delta^{15}N$ peak and the rise in $\delta^{18}O$. By producing a high-resolution record of $\delta^{15}N$, Severinghaus and Brook (1999) were able to compare the timing of the abrupt increase in $\delta^{15}N$ with the layer-counted age of the shift in $\delta^{18}O_{ice}$. They found the gas age-ice age difference at the Bølling-Allerød was ~863 years.

We use this gas age-ice age difference at ~14,600 years before present (14.6 kyr B.P) to constrain the timescale we use for the data presented here. The Bølling-Allerød warming and the warming at Interstadial 2 (~2000m) bound our data. The $\delta^{15}N$-derived gas age-ice age difference at Interstadial 2 is ~1063 years (Severinghaus, personal communication). In order to estimate the gas age-ice age difference between these two end-points, we assume a constant linear relationship between gas age-ice age difference and surface temperature (derived from the $\delta^{18}O_{ice}$ record, Alley, 2000, Cuffey and Clow, 1997). Figure 3.10(b) shows the $\delta^{15}N$ and $\delta^{18}O_{ice}$ data from Figure 3.10(a) plotted on our age scale. Note that the Bølling-Allerød and Interstadial 2

warmings, as represented by the peaks in $\delta^{18}O_{ice}$ and $\delta^{15}N$, occur simultaneously on this timescale, as expected.

Shown in Figure 3.11 are the raw $\delta Kr/N_2$ and $\delta Xe/N_2$ results (solid symbols) from the GISP2 deglaciation dataset, ~24-14 kyr B.P. The timescale used is our corrected timescale described above. The raw $\delta Kr/N_2$ and $\delta Xe/N_2$ data, normalized to pier air $\delta Kr/N_2$ and $\delta Xe/N_2$, are shown in pink and blue solid symbols, respectively. The open symbols in Figure 3.11 are the gravitational components of the $\delta Kr/N_2$ and $\delta Xe/N_2$ data, calculated by multiplying the $\delta^{86}Kr/4$ data (shown in Figure 3.11) times the mass difference between Kr and N_2 (~56) for $\delta Kr/N_2$, and multiplying $\delta^{86}Kr/4$ by 106 (the mass difference between Xe and N_2) for the $\delta Xe/N_2$ gravitational component.

Isotope data from the deglaciation measured concurrently with $\delta Kr/N_2$ and $\delta Xe/N_2$ are shown in Figure 3.12. The $\delta^{15}N$ data shown here are the same as those plotted as solid green triangles in Figure 3.10. These values of $\delta^{86}Kr$ and $\delta^{15}N$ are used in the gravitational and thermal corrections of the $\delta Kr/N_2$ and $\delta Xe/N_2$ data. The $\delta^{40}Ar$ data are elevated throughout most of this dataset. This enrichment in $\delta^{40}Ar$ is likely due to gas loss, as addressed in a previous section. The warming associated with the Bølling-Allerød is clearly seen in the spike in $\delta^{15}N$ and $\delta^{40}Ar$ at ~14 kyr B.P. $\delta^{86}Kr$ is less affected by the warming due to its lower thermal diffusion sensitivity (Table 3.3). $\delta^{86}Kr$ does begin to increase after the rise in $\delta^{15}N$ and $\delta^{40}Ar$, consistent with a deepening of the firn (due to an increase in accumulation) that followed the initiation of the warming (Severinghaus and Brook, 1999).

The gravitationally corrected (by $\delta^{86}Kr$), and thermally corrected (by $\delta^{86}Kr$ and $\delta^{15}N$) $\delta Kr/N_2$ and $\delta Xe/N_2$ data are shown in Figure 3.13. The gravitationally corrected data ($\delta Kr/N_{2gravcorr}$ and $\delta Xe/N_{2gravcorr}$) are shown in open symbols. The data that are corrected for both thermal diffusion and gravitational settling (Kr* and Xe*, or $\delta Kr/N_{2gravthermcorr}$ and $\delta Xe/N_{2gravthermcorr}$) are represented by solid symbols. The thermal correction is most dramatic at ~14 kyr B.P. during the Bølling-Allerød-associated warming. Kr* and Xe* approach 0‰ (equivalent to present-day $\delta Kr/N_2$ and $\delta Xe/N_2$) at ~16-14 kyr B.P. This observation is puzzling, as it suggests that mean ocean temperature at that time is the same as today. It is possible that some unaccounted-for bias in our corrections explains this.

A summary of Kr*, Xe*, $\delta Kr/N_{2gravcorr}$, and $\delta Xe/N_{2gravcorr}$, as well as the isotopes measured in the GISP2 glacial termination sequence is shown in Figure 3.14. Note the high $\delta^{15}N$ values associated with the Bølling warming and Interstadial 2, and the associated large thermal fractionation corrections in the $\delta Kr/N_2$ and $\delta Xe/N_2$ at ~14 and 24 kyr B.P. This observation is consistent with the laboratory-measured values of thermal diffusion sensitivities, which are larger (on a per-mass-unit basis) for the element ratios than for krypton isotopes (Grachev and Severinghaus, 2003b; Nemzer and Severinghaus, in prep.; Kawamura et al., in prep.).

We have converted Kr* and Xe* to a solubility-weighted mean ocean temperature, or Noble Gas Temperature Index (NGTI), by inputting the Kr* and Xe* data into our modeled ocean temperature curve for the deglaciation (Figure 3.2(a)). Plotted in Figure 3.15 are the NGTI curves derived from Kr* and Xe*. The Kr* and

Xe* data produce similar NGTI values, lending confidence to our measurements and their interpretation.

An immediate observation of the NGTI curves is that at ~18 kyr B.P. (or possibly slightly before that at ~17.7 kyr B.P.), both records begin to warm to near-present day temperatures (ocean temperature change near 0ºC) within a few thousand years. Additionally, before 18 kyr B.P., both curves indicate that NGTI was relatively stable at ~2.0-2.2ºC from 24-18 kyr B.P. The NGTI between 24-18 kyr B.P. was 2.0 ± 0.6 ºC and 2.2 ± 0.5 ºC colder than the present ocean based on Kr* and Xe*, respectively.

Vostok glacial inception data

Plotted in Figure 3.16 are the raw $\delta Kr/N_2$ and $\delta Xe/N_2$ data from the Vostok core, spanning ~123 – 105 kyr B.P. The timescale used is the GT4 timescale (Petit et al., 1999). Also shown in Figure 3.16, in open symbols, are the gravitational components of the $\delta Kr/N_2$ and $\delta Xe/N_2$ data (calculated using $\delta^{86}Kr$ as described for the GISP2 data). For much of the data, there is an apparent excess of raw $\delta Kr/N_2$ and $\delta Xe/N_2$ over their gravitational components. Part of this excess is likely to be a thermal effect, and much of it may also be due to the presence of a deep convection zone at Vostok (this possibility is addressed later in this section). We cannot rule out the possibility of a true atmospheric excess caused by a warmer ocean, though, as we discuss below.

The isotope data ($\delta^{86}Kr$, $\delta^{15}N$, and $\delta^{40}Ar$) measured in the Vostok core concurrently with $\delta Kr/N_2$ and $\delta Xe/N_2$ are shown in Figure 3.17. As in the GISP2 deglacial data (Figure 3.12), $\delta^{40}Ar$ is generally elevated above the other data. Also notable in Figure 3.17 is that $\delta^{86}Kr$ values tend to be lower than those of $\delta^{15}N$ during ~115-123 kyr B,P., possibly indicating the presence of a deep convection zone. The $\delta^{15}N$-$\delta^{86}Kr$ difference may also be due in part to thermal gradients within the firn.

The corrected $\delta Kr/N_2$ and $\delta Xe/N_2$ data are plotted in Figure 3.18. Gravitationally corrected data are shown in open symbols, while both thermally and gravitationally corrected data, Kr* and Xe*, are shown in solid symbols. The thermal correction is generally minimal, with the exception of possible surface warming at ~116 and ~121 kyr B.P., as evidenced in the $\delta^{15}N_{excess}$ at those times. A summary of the Vostok glacial inception data (the isotope measurements and the corrected $\delta Kr/N_2$ and $\delta Xe/N_2$ data) is shown in Figure 3.19.

NGTI curves for the glacial inception (Figure 3.20) are derived by inputting the Kr* and Xe* data into the modeled ocean temperature curve for this time period (from Figure 3.2(b)). Although there is some scatter, both NGTI curves appear to begin to decrease at ~115 kyr B.P. There is possibly an initial dip in both NGTI's beginning at ~120 kyr B.P., but there are few data points during this interval, and it is difficult to ascertain whether this is a real decrease in ocean temperature or simply scatter in the data. One of these Kr* and Xe* low points (at 119 kyr B.P.) may be due to an abnormally high $\delta^{86}Kr$ value measured at that depth, which is in turn used to correct for gravity (Figure 3.19).

Also notable is that the both NGTI curves, generated by the Kr* and Xe* records, show the same basic structure: warmer temperatures during the Eemian (the last interglacial warm period), a possible dip in temperatures at ~120 kyr B.P., and then cooling into the glacial period at ~115 kyr B.P. The two NGTI curves are generally within error of each other, but the Kr* data appear to produce lower temperatures than that of Xe* at certain times during the record (123-120, 114-112, and 109-107 kyr B.P.). This excess Xe* may be related to the excess $\delta Xe/N_2$ found by a firn air study at the base of the firn at South Pole (Severinghaus and Battle, 2006). Severinghaus and Battle (2006) speculated that the excess $\delta Xe/N_2$ (beyond that expected due gravitational settling of Xe relative to N_2) may be caused by the formation of a Xe-H_2O complex, which has a higher mass, and therefore greater gravitational settling. Perhaps the formation of Xe-H_2O complexes may explain some of the excess Xe*-derived NGTI, relative to that of Kr*.

Another observation of the Kr*- and Xe*-derived NGTI curves (Figure 3.20) is that they indicate relatively warmer ocean temperatures during the Eemian, as compared to today's ocean. The NGTI's between 123-115 kyr B.P. in Figure 3.20 show ocean temperature averaging ~2ºC warmer than today's ocean. There is no evidence of such an extent of deep ocean warming during the Eemian (Cutler et al., 2003; Waelbroeck et al., 2002), so the mean ocean temperature reconstruction in Figure 3.20 is likely to be an overestimate of ocean temperature. The high Kr* and Xe* in this dataset may be result of an underestimation of the gravitational settling correction due to deep convection. The presence of a deep convection zone in the firn causes lower $\delta^{86}Kr/4$ than $\delta^{15}N$, which then leads to an underestimation of firn depth,

and hence, gravitational settling (Kawamura et al., in prep). Using such $\delta^{86}Kr$ values to correct for gravitational settling would cause gravitationally corrected $\delta Kr/N_2$ and $\delta Xe/N_2$ to be biased towards higher values. Therefore, the presence of a deep convection zone at Vostok may explain the high Kr* and Xe* values that we find in the Vostok glacial inception ice. The effect of deep convection on Xe/N_2 and Kr/N_2 ratios (due to differential molecular diffusivities of Xe, Kr, and N_2, increasing in that order) would somewhat counteract the impact of the low $\delta^{86}Kr$ gravitational correction, though. For a convective zone of 20m (likely an upper limit), the elemental effect (effect of deep convection on the element ratios) would cause $\delta Kr/N_2$ and $\delta Xe/N_2$ to be lowered by ~0.008‰ and ~0.012‰, respectively (Kawamura et al., in prep). The isotope effect would be much stronger on the corrected $\delta Kr/N_2$ and $\delta Xe/N_2$. A 20m convective zone would underestimate $\delta^{86}Kr$ by ~0.009‰, which would cause $\delta Kr/N_2$ and $\delta Xe/N_2$ to be ~0.50‰ and ~1.30‰ higher after gravitational correction (Kawamura et al., in prep).

Despite the potential fractionation introduced by a deep convection zone at Vostok, it remains a possibility that the $\delta Kr/N_2$ and $\delta Xe/N_2$ atmospheric ratios were higher than today's values. If this were the case, then part of the excess Kr* and Xe* during the Eemian may be reflecting warmer mean ocean temperatures than the present-day ocean.

Error calculations

Due to the large size of each sample (~600 g), we were unable to run samples in duplicate. We attempt to estimate the error in $\delta Kr/N_2$ and $\delta Xe/N_2$ in this section. One way to estimate error is to use the standard deviation among the late Holocene Summit $\delta Kr/N_{2gravcorr}$ and $\delta Xe/N_{2gravcorr}$ data (from the previous section), 0.38‰ and 0.75‰ respectively. These standard deviations in $\delta Kr/N_{2gravcorr}$ and $\delta Xe/N_{2gravcorr}$ correspond to standard deviations in the NGTI estimate of ±0.57ºC and ±0.42ºC, respectively. Error may also be introduced in the gravitational and thermal corrections made to the $\delta Kr/N_2$ and $\delta Xe/N_2$. We have quantified the error introduced by the gravitational correction (in which $\delta^{86}Kr$ is used) by using the standard deviations of the raw $\delta Kr/N_2$ (0.21‰), raw $\delta Xe/N_2$ (0.51‰) and $\delta^{86}Kr$ (0.020‰) in late Holocene Summit data as follows:

$$Error\,\mathrm{Kr/N}_{2\,gravcorr} = \sqrt{\left(\sigma\,\delta\mathrm{Kr/N}_{2\,raw}{}^{2} + \left(\sigma\,\delta^{86}\mathrm{Kr}/4 \times \Delta m\right)^{2}\right)} \qquad (3.17)$$

$$Error\,\mathrm{Xe/N}_{2\,gravcorr} = \sqrt{\left(\sigma\,\delta\mathrm{Xe/N}_{2\,raw}{}^{2} + \left(\sigma\,\delta^{86}\mathrm{Kr}/4 \times \Delta m\right)^{2}\right)} \qquad (3.18)$$

These error calculations give errors of ±0.35‰ and ±0.73‰ for $\delta Kr/N_{2gravcorr}$ and $\delta Xe/N_{2gravcorr}$, respectively, which are similar to the standard deviations of gravitiationally corrected $\delta Kr/N_2$ and $\delta Xe/N_2$ values in the Summit data (±0.38‰ and ±0.75‰, respectively). Accounting for error introduced by the thermal diffusion correction is less straightforward. We use the $\delta^{15}N$ excess ($\delta^{15}N$-$\delta^{86}Kr/4$) to make the thermal correction. Using the standard deviation of $\delta^{15}N$ (σ = 0.003‰) and $\delta^{86}Kr/4$

(σ =0.005) in the Summit data, we calculate the root mean square error of the $\delta^{15}N$ excess as 0.0058‰. This error in the $\delta^{15}N$ excess causes 0.5ºC error in the calculated ΔT in the firn column, which in turn imparts an error ($\sigma\delta Kr/N_{2therm}$ and $\sigma\delta Xe/N_{2therm}$) of ~0.24‰ in both the in the thermally corrected $\delta Kr/N_2$ and $\delta Xe/N_2$. Taking into consideration both the error introduced by the gravitational and thermal corrections, we find that the error in the corrected $\delta Kr/N_2$ and $\delta Xe/N_2$ data, Kr* and Xe*, is ±0.42‰ and ±0.78‰, respectively (Equations 3.19 and 3.20).

$$Error\ \mathrm{Kr}^* = \sqrt{\left(\sigma\delta \mathrm{Kr}/\mathrm{N}_{2\,raw}{}^2 + \left(\sigma\delta^{86}\mathrm{Kr}/4 \times \Delta m\right)^2\right) + \sigma\delta \mathrm{Kr}/\mathrm{N}_{2\,therm}{}^2} \quad (3.19)$$

$$Error\ \mathrm{Xe}^* = \sqrt{\left(\sigma\delta \mathrm{Xe}/\mathrm{N}_{2\,raw}{}^2 + \left(\sigma\delta^{86}\mathrm{Kr}/4 \times \Delta m\right)^2\right) + \sigma\delta \mathrm{Xe}/\mathrm{N}_{2\,therm}{}^2} \quad (3.20)$$

These errors in Kr* and Xe* equate to NGTI errors of ~ ±0.64ºC and ±0.46ºC, respectively, in the GISP2 termination data, and ±0.68ºC and ±0.49ºC, respectively, in the Vostok glacial inception data. Error bars in Figures 3.13 and 3.18, as well as 3.15 and 3.20, reflect these calculated errors.

Another method to analyze the error in these datasets is to fit a curve to the data, and then determine the fluctuation from that curve. We have measured $\delta Kr/N_2$ and $\delta Xe/N_2$ every ~250-500 years, during which time the global ocean temperature should not be able to change significantly, given an ocean mixing time of >1000 years. We fit a moving average curve to the Kr* and Xe* data from the glacial termination and inception, averaged over 4 samples (~1000 years) (Figures 3.21 and

3.22). The deviation from the moving average (Equations 3.21 and 3.22, where n = number data points and m = 4, the number of data points averaged for each point on the moving average) in the GISP2 deglaciation data is 0.77‰ for Kr* and 2.05‰ for Xe*, corresponding to NGTI deviations of 1.06ºC (using $\delta Kr/N_2$) and 1.18ºC (using $\delta Xe/N_2$). The deviations from the moving average in the Vostok data are 0.87‰ for Kr* and 1.46‰ for Xe*, which correspond to 1.39ºC and 0.90ºC, respectively.

$$Kr^*_{deviation} = \sqrt{\frac{\sum_{i=1}^{n}\left(Kr^*_{n} - Kr^*_{moving\ average}\right)^2}{n/m}} \qquad (3.21)$$

$$Xe^*_{deviation} = \sqrt{\frac{\sum_{i=1}^{n}\left(Xe^*_{n} - Xe^*_{moving\ average}\right)^2}{n/m}} \qquad (3.22)$$

These deviations ($Kr^*_{deviation}$ and $Xe^*_{deviation}$) from both the GISP2 deglaciation data and Vostok glacial inception data are higher than those found by calculating the propagation of errors in each correction, as described above (Equations 3.19 and 3.20). It is possible that ocean temperature did change on relatively shorter timescales (250-500 years), so these error estimates may serve as an upper bound on the error. For this reason, we use the error calculated by propagating errors (as in Equations 3.19 and 3.20) as the measure of error of Kr*, Xe*, and their inferred mean ocean temperatures.

Relationship between $\delta Kr/N_2$ and $\delta Xe/N_2$

Kr* and Xe* appear to covary to some extent in both the GISP2 deglaciation record and the Vostok glacial inception record (Figures 3.13 and 3.18). We investigate the relationship between $\delta Kr/N_2$ and $\delta Xe/N_2$ variations in order to determine whether this correlation represents real natural variation in ocean temperature, or an experimental artifact imparted on both $\delta Kr/N_2$ and $\delta Xe/N_2$. We have plotted $\delta Xe/N_2$ vs. $\delta Kr/N_2$ in the glacial termination (GISP2) and inception (Vostok) data in Figure 3.23. Xe* vs. Kr* show a slope of ~2.1 and 2.0 in GISP2 and Vostok, respectively (Figure 3.23(a)), likely reflecting ocean temperature effects (solubility slope = 2.6). Another process or processes may explain why the slopes of the data are less than the expected solubility slope. The effects of gravitational settling and thermal fractionation on the Xe*/Kr* slope are shown in the vectors on the left side of the plot in Figure 3.23(a). Both the gravity and thermal slopes are lower than the solubility slope (gravity: m=1.9, thermal: m=1.1), so these processes may not be completely corrected for, and hence may contribute to the lower slope of 2.0-2.1 in Figure 3.23(a). Another possibility is the presence of a convection zone, which would cause Xe to be depleted relative to N_2 and slightly more depleted than Kr due to differences in their molecular diffusivities (Kawamura et al., in prep). This scenario is unlikely in the GISP2 data, though, as there is no evidence of a large convective zone at GISP2 (Landais et al., 2006). It remains a possibility at Vostok, though, as there may have been a convective zone at that site (Caillon et al., 2003). This overall effect would depend on whether the convective zone deepened or shoaled as the ocean cooled.

Plotted in Figure 3.23(b) and 3.23(c) are the gravitationally corrected $\delta Xe/N_2$ vs. $\delta Kr/N_2$ (no thermal correction) and the raw data (no corrections). Both show lower slopes than the fully corrected data in Figure 3.23(a), with slopes ranging from 1.5-1.9. The Vostok glacial inception raw data, with and $\delta Xe/N_2/\delta Kr/N_2$ slope of 1.9, primarily reflect gravitational settling (which produces a slope of ~1.9), while the gravitationally corrected data (m~1.75) reflects a mix of thermal effects and solubility effects. The GISP2 glacial termination gravitationally corrected and raw data (Figures 3.23(b) and 3.23(c)) show slightly lower slopes (~1.5-1.6) than those of the Vostok data. The GISP2 data may depict more of a thermal diffusion signature due to the presence of the Bølling-Allerød warm period in our record. The enriched end-members in the GISP2 data in plots 3.23(b) and 3.23(c) are enriched due to thermal fractionation during this warm period (this enrichment is also visible in Figures 3.11 and 3.13).

We have investigated the relationship between Xe* and Kr* in both their low- and high-frequency variability in the glacial termination and inception data. We analyze the low frequency variability in Xe* and Kr* by plotting the moving average values (from Figures 3.21 and 3.22) of Xe* versus those of Kr* (Figure 3.24). It is evident in Figure 3.24 that the correlation between the low frequency variability in Xe* and Kr* is very high (R^2 = 0.90-0.93). Also, the slope of Xe* vs. Kr* (m=2.3-2.4) in Figure 3.24 is closer to the solubility relationship (~2.6). The high correlation and near-solubility slope between the Xe* and Kr* in this plot suggest that the low frequency variability in Kr* and Xe* primarily reflects ocean temperature change, as expected. Other observations of Figure 3.24 are that the glacial termination data

generally consist of two end-member groups, whereas the Vostok data show more of a complete trend (individual points lie along the trend). This may indicate that the ocean temperature shift at the termination was more abrupt, resembling a step function, while the glacial inception cooling may have been a more gradual transition. These patterns are somewhat clear in the NGTI reconstructions in Figures 3.15 and 3.20. Another conclusion from this low-frequency analysis is that the slope in Figure 3.24 is higher than that of Kr* and Xe* in Figure 3.23(a). It may be that the lower slopes (m=2.0-2.1) in Figure 3.23(a) are due to high frequency variability that is not related to ocean temperature. This is discussed further in the next paragraph.

Comparing the deviation in Kr* and Xe* from the moving average curves in both the glacial termination and inception data (Figures 3.21 and 3.22) can help isolate the cause of the high frequency variability in Kr* and Xe*. There appears to be slight correlation between the Kr* and Xe* deviations from the moving average (Figure 3.25), yet this correlation is relatively weak (R^2 = 0.3-0.4) in both datasets. The slope of the GISP2 termination data in Figure 3.25 is 1.67, which falls between the thermal fractionation slope (m~1.1) and gravitational fractionation (m~1.9). Therefore, it is possible that a combination of these effects is causing the variability. Another possibility is that the Kr* and Xe* values shifted slightly through time as the measurements were made. Plotted in Figure 3.26(a) are the Termination 1 (GISP2) Kr* and Xe* deviations from the moving average versus the order in which they were run. There appears to be a slight trend towards decreasing values as the samples were run. We do not feel that the correlation with sample order is high enough to make a correction for this potential downward trend. The correlation with sample order may

nevertheless help explain some of the high frequency correlation between the Xe* and Kr*. The glacial inception (Vostok) Kr* and Xe* deviations from the moving average do not show this dependence on sample order (Figure 3.26(b)), yet they also show a slight high frequency correlation (Figure 3.25). Hence, there may be another unexplained mechanism causing high frequency correlation. It is also possible that they are reflecting ocean temperature variation, but this is highly unlikely given the speed of the fluctuations and the oceanic mixing time of >1,000 years.

Discussion

Data comparisons

We have compared our data to other records from the same ice core or time period. The isotopic measurements, $\delta^{15}N$ and $\delta^{40}Ar$, measured in GISP2 during the deglaciation can be directly compared to prior isotopic measurements from the GISP2 core. In Figure 3.10 (and 3.27(a), in more detail), the $\delta^{15}N$ data is compared to earlier $\delta^{15}N$ measurements during the Bølling-Allerød warm period (Severinghaus and Brook, 1999) and Interstadial 2 (Severinghaus, personal communication). We also compare the $\delta^{40}Ar/4$ data from this work and that of Severinghaus and Brook (1999) (Figure 3.27(b)). Both the $\delta^{15}N$ and $\delta^{40}Ar$ are consistent with previous measurements. The Vostok glacial inception $\delta^{15}N$ can also be compared to unpublished data analyzed at our laboratory at SIO (Kawamura, personal communication) (Figure 3.28). These $\delta^{15}N$ data generally agree as well.

Our GISP2 deglaciation Kr* and Xe* data also are in reasonable agreement with Kr* and Xe* measured in Dome Fuji ice (Kawamura, personal communication) as shown in Figure 3.29. Per our definition of Kr* and Xe*, the $\delta Kr/N_2$ and $\delta Xe/N_2$ data from both Dome Fuji and GISP2 (Figure 3.29) are corrected for gravitational and thermal fractionation. Both the Kr* and the Xe* from Dome Fuji tend to be more depleted than the GISP2 data, but they are generally within error of each other. The mean of the Dome Fuji Kr* and Xe* data between ~18-24 kyr B.P. are -1.27 ± 0.29‰ and -4.04 ± 0.72‰, respectively, and the means of the GISP2 data presented here during this time period are -0.86 ± 0.40‰ and -2.75 ± 1.02‰, respectively. Another interesting observation is that the Dome Fuji Kr* and Xe* appear to initiate their increase at the same time as does these data in GISP2: ~18 kyr B.P.

The values of Kr* during ~18-24 kyr B.P. in our data can be compared to our earlier measurements of $\delta Kr/N_2$ in GISP2 at the LGM (~20 kyr B.P) in Headly and Severinghaus, 2007. The LGM $\delta Kr/N_2$, in reference to today's atmosphere, reported in Headly and Severinghaus was -1.34 ± 0.37‰. This is likely an overestimate of the change in $\delta Kr/N_2$ and therefore, ocean temperature, because we used $\delta^{40}Ar$ to correct the $\delta Kr/N_2$ for gravitational settling in this prior study. As we have shown in a previous section, $\delta^{40}Ar$ is likely elevated in air bubbles in ice cores (including in the GISP2 core) due to Ar gas loss. Therefore, using elevated $\delta^{40}Ar$ values to correct for gravity would produce lower $\delta Kr/N_2$ results than that which reflects the true atmospheric value. If we correct our $\delta Kr/N_2$ data presented in this study using $\delta^{40}Ar$,

we find a mean $\delta Kr/N_2$ value (~18-24 kyr B.P.) of -1.58 ± 0.40‰, which is quite consistent with that of Headly and Severinghaus (2007).

$\delta Kr/N_2$ and $\delta Xe/N_2$: Deep ocean temperature?

Most of the ocean volume and dissolved gases are contained in the deep ocean, so changes in $\delta Kr/N_2$ and $\delta Xe/N_2$ predominantly indicate deep ocean temperature change. Our Levitus-based model has 80% of the ocean with potential temperature less than 4 ˚C, and slightly more than 80% of the ocean's Kr atoms are in this temperature class. In order to demonstrate the role of deep ocean cooling on our LGM Kr* and Xe* data, we have run the LGM ocean temperature model keeping the deep ocean temperature constant (the deep ocean is conservatively defined as potential temperature (θ) < 4ºC). To produce the observed values of Kr* and Xe* in the LGM portion of the GISP2 data, the intermediate and surface ocean (θ > 4ºC) would have had to cool by 12ºC, a cooling that is extremely unlikely and one that has not been observed in paleoclimate records. Therefore, we assume that our NGTI's also have implications for deep ocean temperature change.

Comparisons with other ocean temperature estimates

Our mean ocean temperature estimates based on Kr* and Xe* can be compared to other estimates of deep ocean temperature and/or mean ocean temperature. Many studies have estimated deep ocean temperature during the LGM (~20 kyr B.P.). Pore fluid measurements (Schrag et al., 1996, Adkins and Schrag, 2001) have produced deep ocean temperature estimates during the LGM of ~4ºC

colder waters than today. Others have used benthic Mg/Ca to estimate deep ocean temperature during the LGM, finding that the deep ocean was ~2.5ºC colder (Martin et al., 2002). Subsequent benthic Mg/Ca studies by Martin et al. (2005) have found that the deep ocean may have been colder than their original estimates, closer to Schrag et al.'s (1996) estimate of 4ºC.

Others have used a regression between coral-derived relative sea level and the benthic $\delta^{18}O$ record ($\delta^{18}O_{benthic}$) to produce a time series of deep ocean temperature and sea level during the last glacial period (Cutler et al., 2003 (Figure 3.30), Waelbroeck et al., 2002). Waelbroeck et al. found that the deep ocean during the LGM was ~4ºC, 3ºC, and 2ºC colder than today in the North Atlantic, Southern Indian, and Pacific Ocean, respectively. Cutler et al. found that the deep Atlantic and Pacific were ~4ºC and 2ºC colder during the LGM. Averaging our estimates of mean ocean temperature change between 24-18 kyr B.P. produces values of 2.0 ± 0.6ºC and 2.2 ± 0.5ºC colder average ocean temperature (using $\delta Kr/N_2$ and $\delta Xe/N_2$, respectively). These values are on the lower end of the range of deep ocean temperature change estimates during the LGM presented previously (i.e., ΔT=2-4ºC), suggesting that possibly intermediate and/or non-polar surface waters did not cool as much as the deep ocean during the LGM. This scenario is unlikely, as the maximum cooling of deep waters was constrained by the freezing point. Another possibility is that the mean ocean temperature was primarily influenced by the Pacific and Southern Oceans during the LGM as North Atlantic Deep Water formation may have weakened, which is consistent with water mass reconstructions of southern source-

water filling the deep ocean basins at that time (Schrag et al., 1996, Adkins and Schrag, 2001, Curry and Oppo, 2005).

We compare our Kr*- and Xe*-derived NGTI time series during the last glacial inception and termination with those of Cutler et al. (2003) for the Pacific deep ocean (Carnegie Ridge) and the Atlantic deep ocean (Ceara Rise) during the last glacial period (~130 kyr B.P. – present) (Figures 3.30 and 3.31). Upon close inspection in Figures 3.31 (a) and (b), we can compare the timing and magnitude of the temperature change for each record. During the last glacial termination (Figure 3.31(a)), NGTI's during ~24 – 18 kyr B.P. (before warming began) were similar to Pacific temperatures (2ºC colder than today). The timing of the initiation of NGTI warming generally agrees with that of both deep ocean temperature reconstructions. The deep Atlantic and the deep Pacific appear to begin warming at ~20 and 18 kyr B.P., respectively, and our data show a mean ocean temperature warming that begins at ~18 kyr B.P. A difference between these two sets of temperature reconstructions are that the NGTI curves appear to rise to almost present-day levels relatively quickly (in a few 1000 years), while the deep ocean temperatures do not reach present-day levels until 10 kyr B.P. If this in fact occurred, it is possible that other ocean water masses (intermediate and surface waters) warmed faster than the deep ocean, though this is unlikely given current evidence of the timing of tropical (Stott et al., 2007) and mid-latitudinal warming (Kiefer and Kiensast, 2005). Another possibility is that the two cores analyzed by Cutler et al. are not representative of the global deep ocean, and that more $\delta^{18}O$ curves need to be examined to give a more thorough picture of deep ocean warming.

During the glacial inception (Figure 3.31(b)), it is apparent that the Kr*- and Xe*-derived NGTI's are warmer than deep ocean temperatures. We have discussed that our data may be artifactually enriched due to possible deep convection at Vostok. The NGTI during the Eemian is ~2ºC higher than that of the Cutler et al. reconstructions. Nevertheless, the magnitude of the cooling (~2-2.5ºC) may be similar to the deep ocean cooling reconstructed from both $\delta^{18}O$ records (2-2.5ºC). In terms of the timing of ocean cooling during the glacial inception, NGTI cooling into the glacial period may lag both deep Atlantic and Pacific cooling. The deep ocean temperatures appear to initiate glacial cooling at ~120 kyr B.P., while the Kr*- and Xe*-derived NGTI's begin to decrease at ~115 kyr, although there is some cooling before 115 kyr. The initial possible dip in Kr* and Xe* at ~120 kyr B.P. (addressed in the Vostok results section) may be more in step with the deep ocean cooling, but we cannot conclude whether this is a real drop in Kr* and Xe* or simply scatter in the data due to the lack of high resolution data points during this time period. It is also possible that the mismatch in timing may be a function of a mismatch between the timescales used for each record.

Implications for climate change

Identifying the extent and timing of mean ocean temperature change during the last glacial termination and inception has important implications for climate change. It also allows for a comparison with other parameters of the climate system, such as CO_2. In Figures 3.32 (a) and (b), we have plotted Kr*- and Xe*-derived NGTI along with CO_2 during the last glacial termination and inception. We observe

that CO_2 and NGTI vary in step through these glacial-interglacial transitions. They appear to be strongly correlated, with a glacial termination rise in both CO_2 and NGTI beginning at ~18 kyr B.P (Figure 3.32(a)). During the glacial inception (Figure 3.32(b)), NGTI and CO_2 both appear to remain elevated at interglacial values until 115 kyr B.P., at which point they begin to decrease. Researchers have been puzzled as to the persistence of high CO_2 values from the Eemian until 115 kyr, while Antarctic surface temperatures dropped at ~120 kyr, well before 115 kyr (Figure 3.33). A correlation between the drop in CO_2 and mean ocean cooling may help to explain the aforementioned discrepancy. These relationships will be discussed further at the end of this section.

Figure 3.34 shows the complete Dome Fuji record of Kr* and Xe* (from Figure 3.29) (Kawamura, personal communication), our GISP2 Kr* and Xe* data, and Dome Fuji CO_2. It is notable in Figure 3.34 that Dome Fuji Kr* and Xe* continue to track CO_2 after the initial rise (18-15 kyr), stabilizing during the Antarctic cold reversal (15-13 kyr), as does CO_2, and then continuing to rise afterwards (13-11 kyr). Another interesting observation from this data is that the Kr* and Xe* values are positive during the early Holocene, which may indicate that the ocean was slightly warmer during this time. This is consistent with findings of early Holocene warmth that may be due to stronger northern summer insolation during this time period (Ciais, 1992). Another possibility is that stronger summer insolation may have triggered snow melting at the GISP2 core site, which would elevate Kr and Xe levels in the ice rather than the air (Headly and Severinghaus, in prep, Chapter 4). Melt layers were

not visible in these samples, though, so it is unlikely that there was significant melting-induced Kr and Xe enrichment.

We have shown that atmospheric pCO_2 and Kr*- and Xe*-derived NGTI have varied in step with each other through the transitions into and out of the last glacial period. In order to investigate the nature of this relationship between ocean temperature and CO_2, we have used a simple mass balance model, with considerations for carbonate chemistry (Dickson, 2001), to calculate the effect of mean ocean temperature change on the pCO_2 in the atmosphere. This model is similar to the one used to calculate changes in $\delta Kr/N_2$ and $\delta Xe/N_2$ due to ocean temperature change, but with only one-box to describe the ocean to simplify carbonate chemistry calculations. Using this model, we have simulated mean ocean temperatures ranging from 3ºC (today's approximate mean ocean temperature) to -2ºC (the lower temperature limit, slightly below the freezing point of seawater). We calculate that the atmospheric pCO_2 sensitivity to mean ocean temperature change is ~8µatm/ºC, which is consistent with Martin et al.'s (2005) modeled temperature sensitivity of 6-10 µatm/ºC. These calculations indicate that part of the correlation between Kr* and Xe* and the CO_2 record (Figure 3.32) is likely due to the solubility effect on the CO_2 record. In the GISP2 deglaciation data, CO_2 increases by ~50µatm, and Kr* and Xe* indicate a ~2.1ºC NGTI warming, while the Vostok data show a ~50µatm drop in CO_2 and a ~2.4ºC cooling. Our data show a pCO_2-NGTI relationship of 20-25µatm/ºC. Thus, the solubility effect of mean ocean temperature on CO_2 may explain only ~1/3 of the total change in atmospheric CO_2 during both of these transitions.

Perhaps a more significant cause for the CO_2 oscillations between glacial and interglacial periods may have to do with ocean stratification, which may also be associated with deep ocean temperature. There is increasing evidence that the ocean was more stratified during glacial periods (Francois et al., 1997, Adkins et al., 2002, Sigman et al., 2004, Adkins et al., 2005, de Boer et al., 2007). Considerations of the equation of state of seawater may help explain ocean stratification during glacial periods. At colder water temperatures, near the freezing point, the dependence of seawater density on temperature ($\partial\rho/\partial T$) decreases to near zero, causing density to be more sensitive to salinity. Therefore, it has been suggested that ocean overturning may have been more sensitive to the salinity structure of the ocean, rather than that of temperature, during glacial periods (Adkins et al., 2002, Adkins et al., 2005, de Boer et al., 2007). In today's ocean, the North Atlantic is more saline than the relatively fresh Southern and Pacific Oceans. This salinity organization may have changed during the glacial period, with more saline waters in Southern Ocean (due to brine rejection during sea ice formation), rather than in the North Atlantic (Keeling and Stephens, 2001, Adkins et al., 2002). Keeling and Stephens have posited that the entire deep ocean was filled with Southern source water that was both cold and salty, relative to the North Atlantic waters. Benthic foraminiferal $\delta^{13}C$ data support this glacial water mass structure, indicating that southern source water penetrated the North Atlantic as far north as ~60ºN at $\geq$ 2000m-depth (Curry and Oppo, 2005). There is also modeling evidence that lower mean ocean temperatures cause global mean overturning to decrease as well, causing enhanced stratification, especially in the Southern and Pacific Oceans (de Boer et al., 2007, Sigman et al., 2007).

Furthermore, Antarctic westerlies are thought to have migrated equatorward during the last glacial period, causing reduced Southern Ocean upwelling, thus enhancing deep ocean stratification (Toggweiler et al., 2006, Toggweiler and Samuels, 1995). The stratification argued for by Toggweiler (2006) is a deep ocean stratification, while that of Sigman et al. (2007) and Francois et al. (1997) is a near-surface ocean stratification. One caveat that must be made to this stratification discussion is that if salt was accumulating in the deep ocean from brine rejection, then there must have been some high latitude region where the glacial ocean was less stratified than today.

If the ocean were more stratified during the glacial period, the CO_2- and nutrient-rich deep ocean may have been cut off from the atmosphere, restricting CO_2 outgassing and thus sequestering CO_2 in the deep ocean. There is evidence that CO_2 may have been drawn down by increased stratification (Francois et al., 1997), and further drawn down by compensation due to decreases in CO_3^{-2} in the deep ocean during glacial periods (Toggweiler, 1999, Marchitto et al., 2005). There are also arguments that increased iron deposition during the glacial periods (Wolff et al., 2006), combined with southern ocean stratification, allowed for enhanced nutrient utilization and entrapment of CO_2 in the deep ocean (Sigman, 2000).

Assuming the ocean was more stratified during the last glacial period, as deglaciation proceeded, ocean stratification may have weakened, allowing for increased overturning. Stronger ventilation of the deep ocean during deglaciation would potentially correlate with ocean warming, as warmer surface waters from the polar regions were entrained into the deep, thus linking temperature with stratification. Furthermore, as North Atlantic Deep Water (NADW) strengthened and

flooded much of the deep Atlantic (~14 kyr), the ocean would warm further. During the glacial inception, as ocean waters cooled in the polar regions and sea ice formed, the deep ocean may have flooded with cold, salty waters, thus strengthening stratification. In this way, ocean temperature, stratification, and CO_2 may be correlated.

During the last glacial termination, many climate parameters appear to shift at ~18 kyr B.P., coincident with the increase in Kr* and Xe* (and their derived NGTI's) presented here. As already discussed, atmospheric CO_2 began to rise at ~18 kyr B.P. (Figure 3.32). Antarctica (Jouzel et al., 2007) (Figure 3.35) and the Southern Ocean (Sachs et al., 2001, Stott et al., 2007) also appear to have begun warming at ~18 kyr, and the warming of the southern source regions for deep water began at ~19 kyr, perhaps leading CO_2 rise by ~1000 years (Stott et al., 2007). Also occurring at ~18 kyr B.P. was Heinrich Event 1, an event in which large amounts of icebergs were discharged into the North Atlantic, recorded as ice rafted debris in sediment cores (Bond et al., 1992), potentially stalling/slowing NADW formation (McManus et al., 2004). It is believed that the freshwater input to the North Atlantic during Heinrich Event 1 may have stabilized the water column in the North Atlantic, with freshwater at the surface preventing deep water formation (Vidal et al., 1997, McManus et al., 2004). Marchitto et al. (2007) found sediment $\Delta^{14}C$ evidence of very old waters in the intermediate Pacific at ~18 kyr B.P., suggesting that extremely old water from the deep Pacific had upwelled at that time, possibly releasing CO_2. The existence of a poorly ventilated deep water mass is also supported by Galbraith et al. (2007), but they find no evidence for an increase in overturning until ~14.6 kyr B.P.

Sigman et al. (2007) have postulated a connection between some of these events. They hypothesize that (1) an increase insolation may have triggered Heinrich 1, which (2) caused NADW to stall/slow due to freshwater input, causing (3) Southern Ocean overturning to strengthen due to buoyancy constraints (de Boer et al., 2007) and a predisposition to instability due to decreased atmospheric freshwater transport as climate cooled into the LGM. The invigoration of Southern Ocean overturning then allowed for (4) CO_2 trapped in the deep ocean to be released into the atmosphere, which further warmed the deep ocean. Martin et al. (2005) have modeled this greenhouse warming of the deep ocean due to increased CO_2, and found that it would produce a slope of ~25µatm/ºC. This relationship is similar to what we observe in our data in Figure 3.31 (20-25µatm/ºC). The timing of mean ocean warming that we find here (~18 kyr B.P.) appears consistent with the deglaciation hypothesis put forward by Sigman et al. (2007).

Our reconstructed NGTI records are also consistent with the sea ice hypothesis of Keeling and Stephens (2001). In their model, Keeling and Stephens do not call for Southern ocean to be continuously stratified during the glacial period (although the ocean basins to the north are stratified with a cold salty layer underlying fresher surface and intermediate waters). Rather, the formation of sea ice in the Southern Ocean blocks CO_2 exchange with atmosphere during the winter, while there may have been a stratified surface layer during the summer. Our Kr* and Xe* data indicate that NGTI's were 2.0-2.2ºC colder during the LGM. This cooling may have brought much of the deep ocean (Southern and Pacific deep waters) to temperatures near the freezing point. Furthermore, mean ocean warming would likely go hand in hand with

the melting of sea ice, causing CO_2 to be released into the atmosphere. In the reconfigured "glacial" modes in Keeling and Stephens model, the deep ocean needs to be near the freezing point of seawater to permit abrupt climate events (Dansgaard/Oeschger, or D/O events). It is difficult to determine from our glacial inception Kr* and Xe* data whether ocean temperatures reached near-freezing temperatures at the beginning of the glacial period, as necessitated for the occurrence of D/O events. The change in temperature (~2-2.5ºC) is similar to that of the termination (2-2.0ºC), but the absolute values are higher than expected, and therefore do not indicate near-freezing point temperatures. As discussed in the results section these Kr* and Xe* values are possibly elevated due to convective processes occurring within the firn.

Our glacial inception data may shed light on the cause of the CO_2 drawdown at this time. Unlike the last glacial termination, during the glacial initiation, there is a disconnect between surface temperature recorded in Antarctic ice cores, which begin to fall at~120 kyr B.P., and CO_2 and NGTI (which begin to decrease at later, at ~115 kyr B.P.) (Figure 3.33). The correlation between CO_2 and NGTI suggests that the ocean was either acting to draw down CO_2 or responding to it by greenhouse cooling. Since ice core surface temperatures cool first, perhaps the lag in ocean temperatures is simply a surface signal (cooling) penetrating down into the ocean. As colder waters filled the deep ocean, they may have caused enhanced stratification, as a result of brine rejection (Keeling and Stephens, 2001, Adkins et al., 2002) or due to buoyancy constraints (de Boer et al., 2007, Sigman et al., 2007). CO_2 may have been drawn down as well, sequestered in the cold, deep ocean. The increase CO_2 in the deep

ocean would have reduced deep ocean CO_3^{-2}, which has been observed in CO_3^{-2} proxy, Zn/Ca, data (Marchitto et al., 2005). Carbonate compensation could further draw down atmospheric CO_2 during glaciation, with both stratification and carbonate compensation playing major roles in lowering CO_2 values during the glacial period (Toggweiler, 1999). Our data make it difficult to state that ocean chemistry, and thus, carbonate compensation, were the initial drivers of CO_2 change into the glacial period, as there is no obvious reason for NGTI to remain correlated to CO_2 in that scenario. Rather, ocean chemistry may have amplified the CO_2 drawdown due to changes in ocean circulation, as described above.

Our data point to a connection between the NGTI (and likely, deep ocean temperature) with CO_2 during both transitions into and out of the last glacial period. During the last termination, NGTI is linked to Antarctic temperature as well, while they are decoupled during the glacial inception. It may be that the ocean is responding to cooling imposed at the surface during the inception, and that the ocean is more of a driver of climate change during the glacial termination.

References

Adkins, J. F., and D. P. Schrag (2001), Pore fluid constraints on deep ocean temperature and salinity during the last glacial maximum, *Geophys. Res. Lett.*, *28*(5), 771-774.

Adkins, J.F., K. McIntyre, D.P. Schrag (2002), The salinity, temperature, and $\delta^{18}O$ of the glacial deep ocean, *Science*, *298*, 1769-1772.

Adkins, J.F., A.P. Ingersoll, C. Pasquero (2005), Rapid climate change and conditional instability of the glacial deep ocean from the thermobaric effect and geothermal heating, *Quaternary Science Reviews*, *24*, 581-294.

Alley, R.B. (2000), The Younger Dryas cold interval as viewed from central Greenland. *Quaternary Science Reviews, 19*. 213-226.

Bender, M. L., T. Sowers, J.-M. Barnola, and J. Chappellaz (1994), Changes in the O_2/N_2 ratio of the atmosphere during recent decades reflected in the composition of air in the firn at Vostok Station, Antarctica, *Geophys. Res. Lett.*, *21*(3), 189–192.

Bender, M., T. Sowers, and V. Lipenkov (1995), On concentrations of O_2, N_2, and Ar in trapped gases from ice cores, *J. Geophys. Res.*, *100*, 18,651-18,660.

Bender, M. L. (2002) Orbital tuning chronology for the Vostok climate record supported by trapped gas composition, *Earth and Planetary Science Letters*, *204*, 275-289.

Bintanja, R., R.S.W. van de Wal, and J. Oerlemans (2005), A new method to estimate ice age temperatures, *Climate Dynamics*, *24*, 197-211, doi: 10.1007/s00382-004-0486-x.

Bond, G. H. Heinrich, W. Broecker, L. Labeyrie, F. McManus, J. Andrews, S. Huon, R. Jantschik, S. Clasen, C. Simet, K. Tedesco, M. Klas, G. Bonani, S. Ivy (1992), Evidence for massive discharges of icebergs into the North Atlantic ocean during the last glacial period, *Nature*, *360*, 245-249.

Caillon, N., J.P. Severinghaus, J. Jouzel, J.-M. Barnola, J. Kang, and V.Y. Lipenkov (2003), Timing of atmospheric CO_2 and Antarctic temperature changes across Termination-III, *Science, 299*, 1728-1731.

Ciais, P., J.R. Petit, J. Jouzel, C. Lorius, N.I.Barkov, V. Lipenkov, and V. Nicolaiev (1992), Evidence for an early Holocene climatic optimum in the Antarctic deep ice-core record, *Climate Dynamics*, *6*(3-4), 160-177.

Colbeck, S.C. (1989), Air movement in snow due to windpumping, *Journal of Glaciology, 35*, 209–213.

Craig, H., Y. Horibe, and T. Sowers (1988), Gravitational separation of gases and isotopes in polar ice caps, *Science*, *242*, 1675-1678.

Cuffey, K.M., and G.D. Clow (1997), Temperature, accumulation, and ice sheet elevation in central Greenland through the last deglacial transition, *Journal of Geophysical Research*, 102:26383-26396.

Curry, W.B. and D.W. Oppo (2005), Glacial water mass geometry and the distribution of $\delta^{13}C$ of SCO2 in the western Atlantic Ocean, *Paleoceanography, 20*, PA1017, doi: 10.1029/2004PA001021.

Cutler, K. B., R. L. Edwards, F. W. Taylor, H. Cheng, J. Adkins, C. D. Gallup, P. M. Cutler, G. S. Burr, and A. L. Bloom (2003), Rapid sea-level fall and deep- ocean temperature change since the last interglacial period, *Earth Planet. Sci. Lett.*, *206*, 253-271.

de Boer, A.M., D.M. Sigman, J.R. Toggweiler, J.L. Russel (2007), Effect of global ocean temperature change on deep ocean ventilation, *Paleoceanography*, *22*, PA2210, doi: 10.1029/2005PA001242.

Dickson, A. (2001), Reference Materials for Oceanic Measurements, *Oceanography 14*(4), 21-22.

Fairbanks, R. (1992), Barbados sea level and Th/U ^{14}C calibration, IGBP PAGES/World Data Center for Paleoclimatology Data Contribution Series #92-020, NOAA/NGDC Paleoclimatology Program, Boulder, CO, USA,.

Francois, R., M.A. Altabet, E.-F. Yu, D.M. Sigman, M.P. Bacon, M. Frank, G. Bohrmann, G. Bareille, and L.D. Labeyrie (1997), Contribution of Southern Ocean surface-water stratification to low atmosphere CO_2 concentrations during the last glacial period, *Nature*, *389*, 929-935.

Galbraith, E.D., S.L. Jaccard, T.F. Pedersen, D.M. Sigman, G.H. Haug, M. Cook, J.R. Southon, R. Francois (2007), Carbon dioxide release from the North Pacific abyss during the last deglaciation, Nature, 449, 890-894.

Grachev, A.M. and J.P. Severinghaus (2003), Determining the thermal diffusion factor for $^{40}Ar/^{36}Ar$ in air to aid paleoreconstruction of abrupt climate change, *Journal of Physical Chemistry A*, *107*, 4636-4642.

Grachev, A.M. and J.P. Severinghaus (2003), Laboratory determination of thermal diffusion constants for $^{29}N_2/^{28}N_2$ in air at temperatures from -60 to 0^{o}C for

reconstruction of magnitudes of abrupt climate changes using the ice core fossil-air paleothermometer, *Geochim. Cosmochim. Acta, 67*, 345-360.

Grachev, A.M. and J.P. Severinghaus (2005), A revised +10±4ºC magnitude of the abrupt change in Greenland temperature at the Younger Dryas termination using published GISP2 gas isotope data and air thermal diffusion constants, Quaternary Science Review, volume 24, 513-519.

Grew, K.E. and T.I. Ibbs, *Thermal Diffusion in Gases*, Cambridge University Press, 1952.

Grootes, P.M., and M. Stuiver (1997), Oxygen 18/16 variability in Greenland snow and ice with 10^3 to 10^5-year time resolution. *Journal of Geophysical Research*, *102*, 26455-26470.

Headly, M.A. and J.P. Severinghaus (2007), A method to measure Kr/N_2 ratios in air bubbles trapped in ice cores and its application in reconstructing past mean ocean temperature, *Journal of Geophysical Research*, *112*, D19105, doi:10.1029/ 2006JD008317.

Jouzel, J., V. Masson-Delmotte, O. Cattani, G. Dreyfus, S. Falourd, G. Hoffmann, B. Minster, J. Nouet, J.M. Barnola, J. Chappellaz, H. Fischer, J.C. Gallet, S. Johnsen, M. Leuenberger, L. Loulergue, D. Luethi, H. Oerter, F. Parrenin, G. Raisbeck, D. Raynaud, A. Schilt, J. Schwander, E. Selmo, R. Souchez, R. Spahni, B. Stauffer, J.P. Steffensen, B. Stenni, T.F. Stocker, J.L. Tison, M. Werner, and E.W. Wolff (2007), Orbital and millennial Antarctic climate variability over the past 800,000 years, *Science*, *317*, 793-797.

Kawamura, K.K., T. Nakazawa, S. Aoki, S. Sugawara, Y. Fuji, O. Wanatabe (2003), Atmospheric CO_2 variations over the last three glacial-interglacial climatic cycles deduced from the Dome Fuji deep ice core, Antarctica using a wet extraction technique, *Tellus*, *55B*, 126-137.

Kawamura, K., J.P. Severinghaus, S. Ishidoya, S. Sugawara, G. Hashida, H. Motoyama, Y. Fujii, S. Aoki, and T. Nakazawa (2006), Convective Mixing of Air in Firn at Four Polar Sites, *Earth Planet Sci. Lett., 244*, 672-682.

Kawamura, K., F. Parrenin, L. Lisiecki, R. Uemura, F. Vimeux, J.P. Severinghaus, M.A. Hutterli, T. Nakazawa, S. Aoki, J. Jouzel, M. Raymo, K. Matsumoto, H. Nakata, H. Motoyama, S. Fujita, K. Goto-Azuma, Y. Fujii, and O. Watanabe (2007), Northern Hemisphere forcing of climatic cycles in Antarctica over the past 360,000 years, *Nature*, *448*, 912-916.

Kawamura, K.K., J.P. Severinghaus, M.R. Albert, Z.R. Courville, M.A. Fahnestock, T. Scambos, J. Shields, C.A. Shuman, Kinetic fractionation of gases by deep air convection in polar firn, *in prep.*

Keeling, R. F., and B. B. Stephens (2001), Antarctic sea ice and the control of Pleistocene climate Instability, *Paleoceanography*, *16*, 112-131.

Kiefer, T. and M. Kienast (2005), Patterns of deglacial warming in the Pacific Ocean: a review with emphasis on the time interval of Heinrich event 1, *Quaternary Science Reviews, 24*, 1063-1081,

Kobashi, T., J.P. Severinghaus, E.J. Brook, J.-M. Barnola, A. Grachev (2007), Precise timing and characterization of abrupt climate change 8,200 years ago from air trapped in polar ice, *Quaternary Science Reviews, 26*, 1212-1222.

Landais, A., J.M. Barnola, K. Kawamura, N. Caillon, M. Delmotte, T. Van Ommen, G. Dreyfus, J. Jouzel, V. Masson-Delmotte, B. Minster, J. Freitag, M. Leuenberger, J. Schwander, C. Huber, D. Etheridge, and V. Morgan (2006), Firn-air $\delta^{15}N$ in modern polar sites and glacial-interglacial ice: a model-data mismatch during glacial periods in Antarctica?, *Quaternary Science Reviews*, *25*(1-2), 49-62.

Levitus, S. (1994), World Ocean Atlas, NOAA, Washington D.C.

Lüthi, D. M. Le Floch, B. Bereiter, T. Blunier, J.-M. Barnola, U. Siegenthaler, D. Raynaud, J. Jouzel, H. Fischer, K. Kawamura, and T.F. Stocker (2008), High-resolution carbon dioxide concentration record 650,000-800-000 years before present, *Nature*, *453*, 379-382.

Marchitto, T.M., J. Lynch-Stieglitz, S.R. Hemming (2005), Deep Pacific $CaCO_3$ compensation and glacial-interglacial atmospheric CO_2, *Earth and Planetary Science Letters*, *231*, 317-336.

Marchitto, T.M., S.J. Lehman, J.D. Ortiz, J. Flückiger, A. van Geen (2007), Marine radiocarbon evidence for the mechanism of deglacial atmospheric CO_2 rise, *Science*, *316*, 1456-1459.

Martin, P. M., D. W. Lea, Y. Rosenthal, N. J. Shackleton, M. Sarnthein, and T. Papenfuss (2002), Quaternary deep sea temperature histories derived from benthic foraminiferal Mg/Ca, *Earth Planet. Sci. Lett.*, *198*, 193-209.

Martin, P., D. Archer, D.W. Lea (2005), Role of deep sea temperature in the carbon cycle during the last glacial, *Paleoceanography*, *20*, PA2015, doi: 10.1029/2003PA000914.

McManus, J.F., R. Francois, J.-M. Gherardi, L.D. Keigwin, and S. Brown-Leger (2004), Collapse and rapid resumption of Atlantic meridional circulation linked to deglacial climate changes, *Nature*, *428*, 834-347.

Monnin, E., A. Indermühle, A. Dällenbach, J. Flückiger, B. Stauffer, T.F. Stocker, D. Raynaud, J.-M. Barnola (2001)., Atmospheric CO_2 concentrations over the last glacial termination, *Science*, *291*(5501), 112-114,

Nemzer, B.V. and J.P. Severinghaus, Thermal diffusion constants of noble gases in air for paleoenvironmental applications, *in prep*.

Parrenin, F**.** and R. Hindmarsh. (2007), Influence of a non-uniform velocity field on isochrone geometry along a steady flowline of an ice sheet, *J. Glaciol., 53*(183), 612-622.

Parrenin, F. J.-M. Barnola, J. Beer, T. Blunier, E. Castellano, J. Chappellaz, G. Dreyfus, H. Fischer, S. Fujita, J. Jouzel, K. Kawamura, B. Lemieux-Dudon, L. Loulergue, V. Masson-Delmotte, B. Narcisi, J.-R. Petit, G. Raisbeck, D. Raynaud, U. Ruth, J. Schwander, M. Severi, R. Spahni, J.P. Steffensen, A. Svensson, R. Udisti, C. Waelbroeck, and E. Wolff (2007), The EDC3 chronology for the EPICA Dome C ice core, *Climate of the Past Discussions*, *3*, 575-606.

Petit, J.R., J. Jouzel, D. Raynaud, N.I. Barkov, J.-M. Barnola, I. Basile, M. Benders, J. Chappellaz, M. Davis, G. Delayque, M. Delmotte, V.M. Kotlyakov, M. Legrand, V.Y. Lipenkov, C. Lorius, L. Pépin, C. Ritz, E. Saltzman, and M. Stievenard (1999), Climate and atmospheric history of the past 420,000 years from the Vostok ice core, Antarctica, *Nature, 399*, 429-436.

Raymo, M.E. (1997), The timing of major climate terminations, *Paleoceanography*, *12*(4), 577-585.

Raynaud, D., J.-M. Barnola, R. Souchez, R. Lorrain, J.-R. Petit, P. Duval, and V.Y. Lipenkov (2005), Paleoclimatology: The record for marine isotopic stage 11, *Nature*, *436*, 39-40.

Sachs, J.P., R.F. Anderson, S.J. Lehman (2001), Glacial surface temperatures of the southeast Atlantic Ocean, *Science*, *293*, 2077-2079.

Schlesinger, W. H. (1997), *Biogeochemistry, An Analysis of Global Change*, 2nd ed., Academic Press, San Diego, CA.

Schrag, D. P., G. Hampt, and D. W. Murray (1996), Pore Fluid Constraints on the Temperature and Oxygen Isotopic Composition of the Glacial Ocean, *Science*, *272*, 1930-1932.

Severinghaus J. P., and M. Battle (2006), Fractionation of gases in polar ice during bubble close-off: new constraints from firn air Ne, Kr, and Xe observations, *Earth Planet. Sci. Lett., 244*, 474-500.

Severinghaus, J.P. and E.J. Brook (1999), Abrupt climate change at the end of the last glacial period inferred from trapped air in polar ice, *Science*, *286*, 930-934.

Severinghaus, J.P., T. Sowers, E.J. Brook, R.B. Alley, M.L. Bender (1998), Timing of abrupt climate change at the end of the Younger Dryas interval from thermally fractionated gases in polar ice, *Nature*, *391*, 141-146.

Severinghaus, J. P., B. Luz, and N. Caillon (2003), A method for precise measurement of argon 40/36 and krypton/argon ratios in trapped air in polar ice with applications to past firn thickness and abrupt climate change in Greenland and at Siple Dome, Antarctica, *Geochim. Cosmochim. Acta*, *67*(3), 325-343.

Siegenthaler, U., T.F. Stocker, E. Monnin, D. Lüthi, J. Schwander, B. Stauffer, D. Raynaud, J.-M. Barnola, H. Fischer, V. Masson-Delmotte, J. Jouzel (2005), Stable carbon cycle-climate relationship during the late Pleistocene, *Science*, *310*(5752), 1313-1317.

Sigman, D.M. and E.A. Boyle (2000), Glacial/interglacial variations in atmospheric carbon dioxide, *Nature, 407*, 859-869.

Sigman, D.M., S.L. Jaccard, G.H. Haug (2004), Polar ocean stratification in a cold climate, *Nature*, *428*, 59-63.

Sigman, D.M., A.M. de Boer, G.H. Haug (2007), Antarctic stratification, atmospheric water vapor, and Heinrich events: a hypothesis for late Pleistocene deglaciations, *Ocean Circulation: Mechanisms and Impacts*, Geophysical Monograph Series 173, 10.1029/172GM21.

Sowers, T. M.L. Bender, D. Raynaud, and Y.S. Korotkevich (1992), $\delta^{15}N$ of N_2 in air trapped in polar ice: A tracer of gas transport in the firn and a possible constraint on ice age-gas age differences, *Journal of Geophysical Research*, *97*, 15,683-15,697.

Sowers, T., M. L. Bender, and D. Raynaud (1989), Elemental and isotopic composition of occluded O_2 and N_2 in polar ice, *J. Geophys. Res.*, *94*, 5137-5150.

Stott, L., A. Timmerman, R. Thunell (2007), Southern Hemisphere and deep-sea warming led deglacial atmospheric CO2 rise and tropical warming, *Science*, *318*, 435-438.

Stuiver, M., P.M. Grootes, and T.F. Braziunas (1995), The GISP2 18O climate record of the past 16,500 years and the role of the sun, ocean and volcanoes, *Quaternary*

Research, 44, 341-354.

Toggweiler, J.R. (1999), Variation of atmospheric CO_2 by ventilation of the ocean's deepest water, *Paleoceanography*, *14*(5), 571-588.

Toggweiler, J.R. and B. Samuels (1995), Effect of drake passage on the global thermohaline circulation, *Deep Sea Research Part I: Oceanographic Research Papers*, *42*(4), 477-500.

Toggweiler, J.R., J.L Russel, and S.R. Carson (2006), Midlatitude westerlies, atmospheric CO_2, and climate change during the ice ages, *Paleoceanography*, *21*, PA2005, doi:10.1029/2005PA001154.

Vidal, L., L. Labeyrie, E. Cortijo, M. Arnold, J.C. Duplessy, E. Michel, S. Becque, and T.C.E. van Weering (1997)., Evidence for changes in North Atlantic Deep Water linked to meltwater surges during the Heinrich events, *Earth and Planetary Science Letters*, *146*(1-2), 13-27.

Waelbroeck, C., L. Labeyrie, E. Michel, J. C. Duplessy, J. F. McManus, K. Lambeck, E. Balbon, and M. Labracherie (2002), Sea-level and deep water temperature changes derived from benthic foraminifera isotopic records, *Quaternary Science Reviews*, *21*, 295-305.

Weiss, R. F. (1970), The solubility of nitrogen, oxygen and argon in water and sea water, *Deep Sea Research*, *17*, 721-735.

Weiss, R.F. and T. K. Kyser (1978), Solubility of krypton in water and seawater, *J. Chem. Eng. Data*, *23*(1), 69-72.

Wolff E. W., H. Fischer, F. Fundel, U. Ruth, B. Twarloh, G. C. Littot, R. Mulvaney, R. Röthlisberger, M. de Angelis, C. F. Boutron, M. Hansson, U. Jonsell, M. A. Hutterli, F. Lambert, P. Kaufmann, B. Stauffer, T. F. Stocker, J. P. Steffensen, M. Bigler, M. L. Siggaard-Andersen, R. Udisti, S. Becagli, E. Castellano, M. Severi, D. Wagenbach, C. Barbante, P. Gabrielli and V. Gaspari (2006), Southern Ocean sea-ice extent, productivity, and iron flux over the past eight glacial cycles, *Nature*, *440*, 491-496.

Wood, D. and R. Caputi (1966), Solubilities of Kr and Xe in fresh and seawater, *Tech. rep.*, U. S. Naval Radiological Defense Laboratory, San Francisco, CA.

Table 3.1. Mass spectrometry information for each measurement made on the Finnigan MAT 252 (δ^{40}Ar, δ^{86}Kr, δKr/Ar, and δXe/Ar). Settings for δ^{86}Kr based on Kawamura et al., in prep.

	# Blocks	# Cycles/ Block	Idle time	Integration time	Internal precision
δ^{40}Ar	5	16	8 sec	16 sec	0.020‰
δ^{86}Kr	6	25	10 sec	16 sec	0.200‰
δKr/Ar	2	2	8 sec	8 sec	N/A
δXe/Ar	2	2	8 sec	8 sec	N/A

Table 3.2. Pier air data used for each set of measurements, measured in reference to working standards.

	Mean	Standard deviation
Vostok glacial inception data		
$\delta Kr/N_2$	60.61‰	± 0.21‰
$\delta Xe/N_2$	77.60‰	± 0.29‰
$\delta^{86}Kr$	1.256‰	± 0.023‰
$\delta^{15}N$	0.002‰	± 0.004‰
$\delta^{40}Ar$	-1.471‰	± 0.014‰
$\delta Kr/Ar$	58.90‰	± 0.22‰
$\delta Xe/Ar$	75.86‰	± 0.28‰
$\delta Ar/N_2$	0.146‰	± 0.043‰
$\delta^{18}O$	0.004‰	± 0.009‰
$\delta O_2/N_2$	0.135‰	± 0.167‰
GISP2 glacial termination data		
$\delta Kr/N_2$	60.61‰	± 0.09‰
$\delta Xe/N_2$	77.24‰	± 0.55‰
$\delta^{86}Kr$	0.0009(day #) + 1.1935	± 0.010‰
$\delta^{15}N$	0.003‰	± 0.002‰
$\delta^{40}Ar$	-1.457‰	± 0.015‰
$\delta Kr/Ar$	59.09‰	± 0.42‰
$\delta Xe/Ar$	75.51‰	± 0.78‰
$\delta Ar/N_2$	0.136‰	± 0.044‰
$\delta^{18}O$	0.004‰	± 0.004‰
$\delta O_2/N_2$	0.174‰	± 0.100

Table 3.3. Thermal diffusion factors used to make the thermal diffusion correction to $\delta Kr/N_2$ and $\delta Xe/N_2$. α_T for $\delta Ar/N_2$ is calculated by multiplying α_T for $\delta^{15}N$ by $^{15}\Omega/^{Ar/N2}\Omega$ (262.3/14.5 = 18.9). Units of firn column temperature (T) are in Kelvin.

	α_T	Ω	Source
$\delta^{15}N$	$8.656/T - 1232/T^2$		Grachev and Severinghaus, 2003a
$\delta^{86}Kr$	$5.05/T - 580/T^2$		Kawamura et al., in prep
$\delta^{40}Ar$	$26.08/T - 3952/T^2$		Grachev and Severinghaus, 2003b
$\delta Kr/Ar$	$60.61/T$		Nemzer and Severinghaus, in prep
$\delta Xe/Ar$	$71.06/T$		Nemzer and Severinghaus, in prep
$\delta Ar/N_2$	$262.4/14.7 * (8.656/T - 1232/T^2)*$	262.4 ±1 per meg per degree at -33ºC	Nemzer and Severinghaus, in prep

Table 3.4. Complete GISP2 deglaciation data. (also plotted in Figure 3.13, with additional δ^{18}Oatm included in this table).

		-------grav therm corr---		-----grav corr----		-----raw data----	
Depth (m)	Age (yr B.P.)	Kr* (‰)	Xe* (‰)	$\delta Kr/N_2$ (‰)	$\delta Xe/N_2$ (‰)	$\delta Kr/N_2$ (‰)	$\delta Xe/N_2$ (´‰)
1798.8	13873	-0.69	1.49	1.42	3.08	26.01	49.16
1806.8	14079	0.61	1.74	2.96	3.52	28.81	51.94
1813.8	14382	-0.17	0.14	2.48	2.14	32.07	57.59
1819.1	14548	1.07	2.06	4.25	4.43	30.80	54.18
1825.8	14771	0.32	-0.69	0.36	-0.57	27.24	49.78
1831.8	14981	0.42	1.87	1.40	2.65	26.88	50.39
1837.8	15303	-0.06	-2.62	-0.22	-2.65	27.02	48.40
1844.8	15541	1.03	0.47	1.85	1.15	27.92	50.01
1850.2	15733	0.04	-1.86	0.47	-1.47	26.28	46.89
1857.8	16024	0.30	0.76	1.15	1.45	25.86	47.77
1863.7	16297	0.23	-0.11	0.62	0.25	25.49	46.84
1869.8	16602	0.11	-0.18	0.40	0.11	25.12	46.43
1876.4	16866	0.03	-0.76	0.40	-0.42	24.91	45.51
1879.7	17105	-0.39	-0.28	-0.78	-0.48	24.66	47.20
1886.2	17404	-0.05	-1.46	0.21	-1.20	24.27	43.88
1894.7	17836	-1.28	-3.91	-2.33	-4.59	24.23	45.18
1899.7	18123	-0.74	-2.44	-0.77	-2.38	24.33	44.64
1906.0	18404	-1.20	-3.82	-1.25	-3.77	24.34	44.18
1911.8	18592	-1.02	-2.89	-0.94	-2.76	23.99	43.96
1916.8	18829	-0.86	-2.27	-0.87	-2.19	23.83	44.09
1921.7	19082	-1.48	-1.70	-1.09	-1.34	22.46	42.78
1926.8	19258	-0.67	-3.19	-1.37	-3.62	23.74	43.43
1930.5	19492	-0.97	-4.24	-1.53	-4.56	24.53	44.27
1936.8	19774	-0.66	-2.16	-0.16	-1.73	23.69	42.97
1942.0	19998	-0.46	-1.60	-0.16	-1.31	24.04	44.04
1946.7	20204	-0.66	-1.67	-0.64	-1.57	23.61	43.86
1954.5	20632	-0.91	-2.99	-1.33	-3.21	24.67	45.52
1961.1	21051	-0.98	-4.02	-1.45	-4.28	24.61	44.54
1964.8	21263	-0.72	-1.75	-0.61	-1.59	23.75	44.06
1968.8	21495	-0.51	-3.41	-0.79	-3.54	24.03	42.97
1972.8	21711	-0.59	-1.13	-0.78	-1.19	23.85	44.95
1977.8	22101	-1.70	-3.94	-2.49	-4.43	24.28	45.73
1982.8	22236	0.07	-1.20	0.10	-1.10	24.16	43.99
1988.1	22529	-1.07	-4.59	-2.15	-5.28	24.06	43.84
1991.8	22653	-1.22	-3.22	-1.97	-3.68	22.66	42.46
1995.8	22862	-1.37	-3.64	-0.93	-3.24	23.71	42.92
2000.2	23156	-1.00	-2.35	-1.04	-2.30	24.47	45.50
2002.8	23386	-0.14	-1.60	1.46	-0.36	27.36	48.17
2007.8	23665	-0.75	-2.32	-1.08	-2.48	23.54	43.66
2012.0	24010	-0.68	-2.69	-1.12	-2.93	22.95	42.16

Table 3.4 (continued)

Depth (m)	Age (yr B.P.)	δ^{40}Ar/4 (‰)	δ^{86}Kr/4 (‰)	δ^{15}N (‰)	δ^{18}Oatm (‰)
1798.8	13873	0.499	0.436	0.509	1.215
1806.8	14079	0.536	0.458	0.54	1.307
1813.8	14382	0.607	0.524	0.617	1.312
1819.1	14548	0.559	0.470	0.581	1.331
1825.8	14771	0.494	0.476	0.475	1.194
1831.8	14981	0.496	0.451	0.484	1.217
1837.8	15303	0.504	0.483	0.474	1.158
1844.8	15541	0.488	0.462	0.489	1.190
1850.2	15733	0.465	0.457	0.47	1.155
1857.8	16024	0.478	0.438	0.466	1.154
1863.7	16297	0.472	0.441	0.452	1.105
1869.8	16602	0.471	0.438	0.446	1.090
1876.4	16866	0.464	0.434	0.445	1.048
1879.7	17105	0.456	0.451	0.434	0.996
1886.2	17404	0.461	0.426	0.433	1.024
1894.7	17836	0.453	0.471	0.43	0.969
1899.7	18123	0.467	0.445	0.441	1.035
1906.0	18404	0.459	0.453	0.449	1.023
1911.8	18592	0.451	0.442	0.442	1.026
1916.8	18829	0.455	0.438	0.435	1.027
1921.7	19082	0.446	0.417	0.429	1.052
1926.8	19258	0.452	0.445	0.417	1.004
1930.5	19492	0.457	0.462	0.439	0.980
1936.8	19774	0.454	0.423	0.438	1.069
1942.0	19998	0.450	0.429	0.437	1.034
1946.7	20204	0.447	0.430	0.428	1.000
1954.5	20632	0.456	0.461	0.443	0.967
1961.1	21051	0.461	0.462	0.442	0.983
1964.8	21263	0.455	0.432	0.433	0.998
1968.8	21495	0.450	0.440	0.427	0.978
1972.8	21711	0.447	0.436	0.427	0.957
1977.8	22101	0.458	0.474	0.443	0.905
1982.8	22236	0.447	0.426	0.425	0.971
1988.1	22529	0.438	0.464	0.423	0.881
1991.8	22653	0.427	0.436	0.407	0.906
1995.8	22862	0.453	0.436	0.45	0.970
2000.2	23156	0.467	0.452	0.448	0.940
2002.8	23386	0.513	0.459	0.514	1.042
2007.8	23665	0.440	0.436	0.422	0.912
2012.0	24010	0.434	0.426	0.408	0.864

Table 3.5. Complete Vostok glacial inception data (as shown in Figure 3.18, with additional δ^{18}Oatm included in this table).

		---grav therm corr---		---grav corr---		----raw data----	
Depth (m)	Age (yr B.P.)	Kr* (‰)	Xe* (‰)	$\delta Kr/N_2$ (‰)	$\delta Xe/N_2$ (‰)	$\delta Kr/N_2$ (‰)	$\delta Xe/N_2$ (‰)
1534.0	105839	-0.21	0.48	0.04	0.76	26.85	50.98
1537.3	106009	0.10	0.30	0.57	0.72	26.75	49.77
1543.0	106247	-0.10	0.20	-0.17	0.23	26.06	49.38
1555.0	106911	-0.56	-0.95	-0.78	-1.03	25.91	48.99
1560.0	107143	-0.22	-0.03	-0.17	0.09	26.06	49.25
1572.2	108012	-0.61	-0.46	-0.74	-0.46	26.79	51.12
1578.4	108613	-0.56	0.16	-0.59	0.23	26.98	51.89
1579.0	108710	-0.38	-0.88	-0.33	-0.76	26.80	50.08
1585.2	109203	-0.79	-1.28	-0.82	-1.22	25.85	48.76
1591.7	109804	0.20	-0.04	0.18	0.04	27.51	51.24
1597.0	110192	-0.05	0.62	-0.17	0.61	27.36	52.19
1598.2	110271	-0.26	1.55	0.17	1.95	26.69	51.65
1603.4	110606	0.09	0.54	0.29	0.77	27.32	51.41
1609.4	111046	0.09	1.72	0.41	2.04	26.58	51.08
1615.0	111461	0.20	0.64	0.74	1.12	26.94	50.22
1621.2	111968	0.32	2.05	0.80	2.48	27.13	51.82
1623.0	112138	0.60	1.37	0.45	1.35	27.57	52.16
1627.0	112501	0.26	3.12	0.68	3.51	27.06	52.94
1633.2	113102	-0.29	1.53	-0.05	1.78	26.23	51.02
1644.8	114158	0.68	1.55	0.40	1.42	26.59	50.51
1646.0	114290	-0.21	2.09	0.45	2.66	25.81	50.17
1650.5	114684	1.23	3.10	1.54	3.40	26.09	49.40
1652.1	114861	2.31	4.57	3.08	5.21	28.40	52.67
1658.2	115376	0.59	3.19	1.21	3.72	26.76	51.59
1665.0	115843	1.55	3.04	2.67	3.95	27.21	49.92
1679.5	117025	0.16	1.18	0.76	1.70	26.51	49.95
1694.3	117992	1.20	3.12	1.49	3.42	28.23	53.52
1709.3	118889	0.21	0.93	-0.19	0.73	28.60	54.67
1725.4	119899	1.21	4.33	1.65	4.74	28.84	55.67
1741.2	120896	1.43	4.68	2.50	5.54	29.29	55.76
1758.0	121956	1.12	3.95	1.30	4.17	28.47	55.09
1774.0	122889	1.59	4.64	1.85	4.92	28.53	54.91

Table 3.5 (continued)

Depth (m)	Age (yr B.P.)	δ^{40}Ar/4 (‰)	δ^{86}Kr/4 (‰)	δ^{15}N (‰)	δ^{18}Oatm (‰)
1534.0	105839	0.494	0.475	0.481	0.614
1537.3	106009	0.488	0.464	0.477	0.603
1543.0	106247	0.472	0.465	0.460	0.515
1555.0	106911	0.486	0.473	0.463	0.563
1560.0	107143	0.487	0.465	0.464	0.578
1572.2	108012	0.501	0.488	0.481	-0.344
1578.4	108613	0.504	0.488	0.485	0.692
1579.0	108710	0.502	0.481	0.480	0.686
1585.2	109203	0.488	0.473	0.469	0.657
1591.7	109804	0.504	0.484	0.481	0.730
1597.0	110192	0.502	0.488	0.481	0.688
1598.2	110271	0.496	0.470	0.482	0.708
1603.4	110606	0.502	0.479	0.483	0.746
1609.4	111046	0.491	0.464	0.472	0.715
1615.0	111461	0.488	0.464	0.480	0.710
1621.2	111968	0.504	0.467	0.480	0.713
1623.0	112138	0.498	0.480	0.473	0.669
1627.0	112501	0.494	0.467	0.479	0.688
1633.2	113102	0.483	0.466	0.471	0.616
1644.8	114158	0.477	0.464	0.452	0.576
1646.0	114290	0.480	0.449	0.469	0.613
1650.5	114684	0.466	0.435	0.443	0.533
1652.1	114861	0.474	0.449	0.472	0.545
1658.2	115376	0.476	0.453	0.471	0.507
1665.0	115843	0.479	0.435	0.470	0.489
1679.5	117025	0.484	0.456	0.474	0.259
1694.3	117992	0.491	0.474	0.481	0.094
1709.3	118889	0.505	0.510	0.494	-0.102
1725.4	119899	0.507	0.482	0.494	-0.175
1741.2	120896	0.516	0.475	0.508	-0.195
1758.0	121956	0.506	0.481	0.485	-0.303
1774.0	122889	0.487	0.473	0.479	-0.375

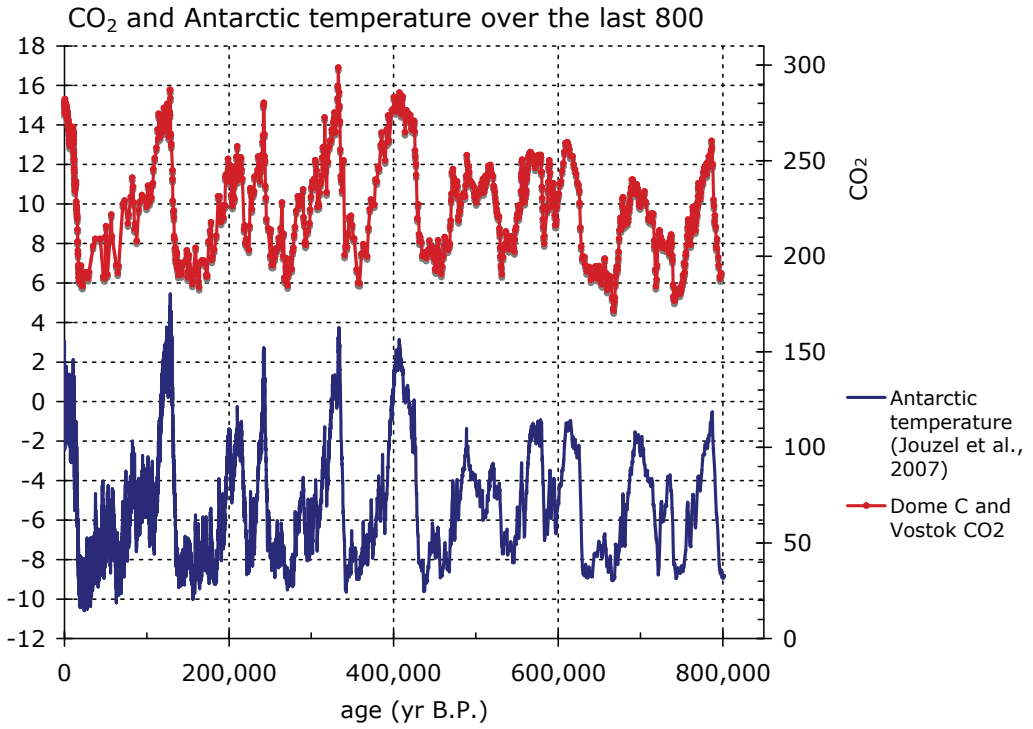

Figure 3.1. CO_2 composite from Lüthi et al., 2008. CO_2 data: 0-22 kyr BP: Dome C (Monnin et al., 2001), 22-393 kyr BP: Vostok (Petit et al., 1999; Pepin et al., 2001; Raynaud et al., 2005), 393-664 kyr BP: Dome C (Siegenthaler et al., 2005), 664-800 kyr BP: Dome C (Lüthi et al., 2008). EPICA Dome C temperature reconstruction from Jouzel et al., 2007.

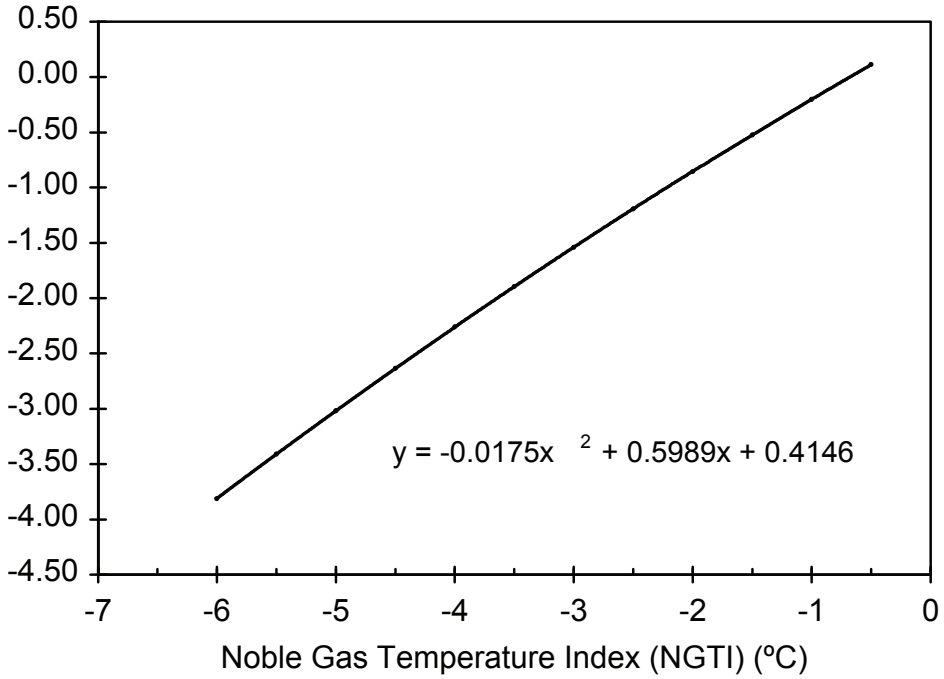

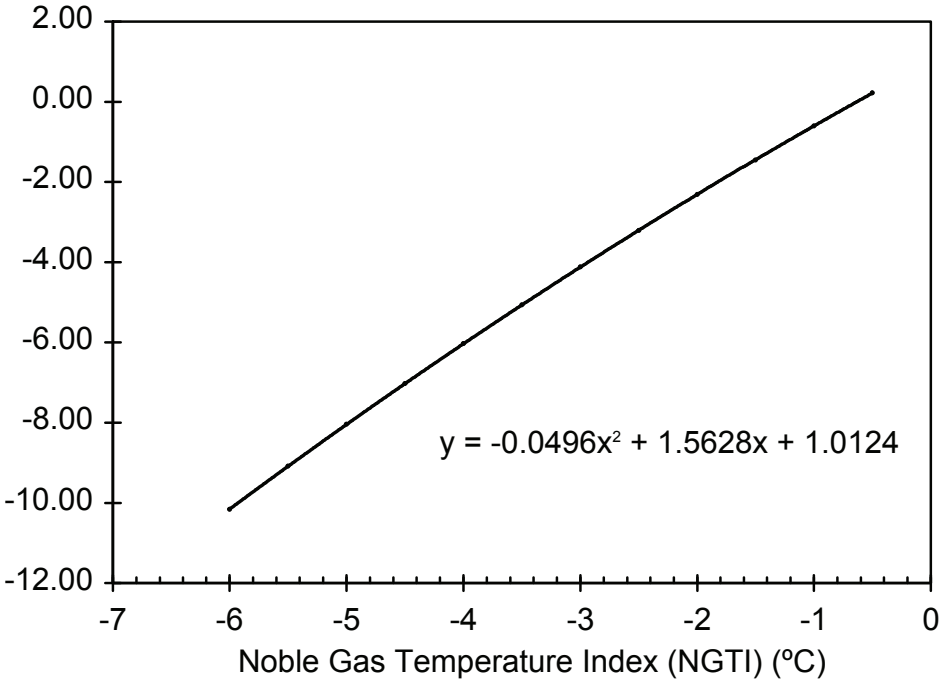

Figure 3.2(a). Model outputs for $\delta Kr/N_2$ and $\delta Xe/N_2$ resulting from ocean temperature change during the deglaciation.

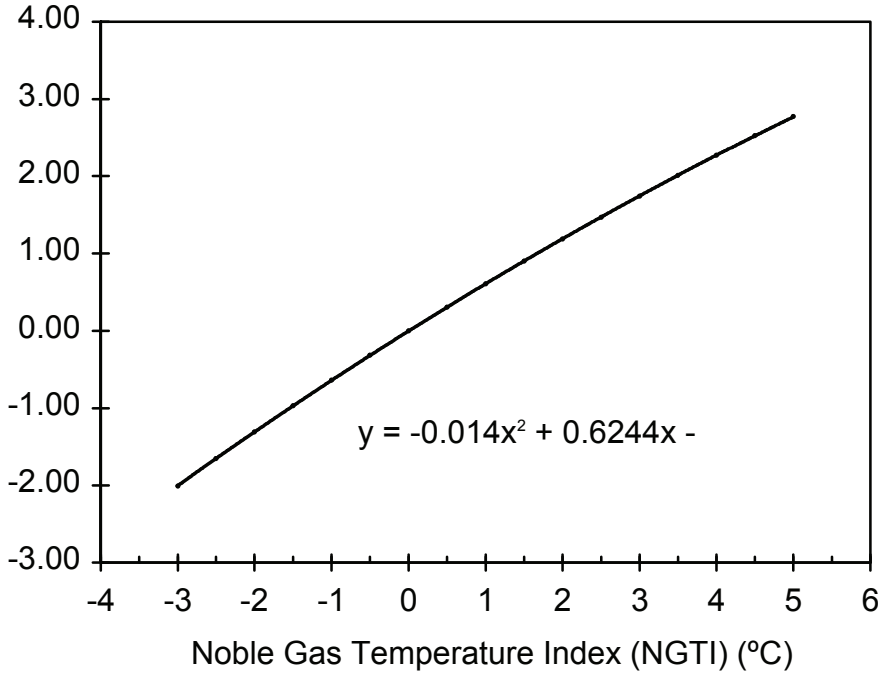

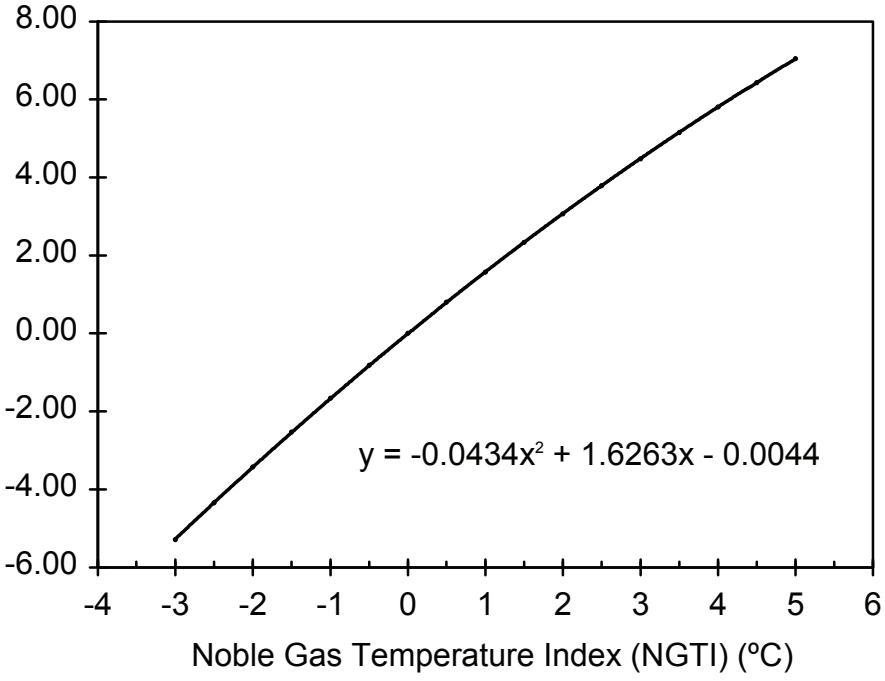

Figure 3.2(b). Model outputs for $\delta Kr/N_2$ and $\delta Xe/N_2$ resulting from ocean temperature change during the glacial inception.

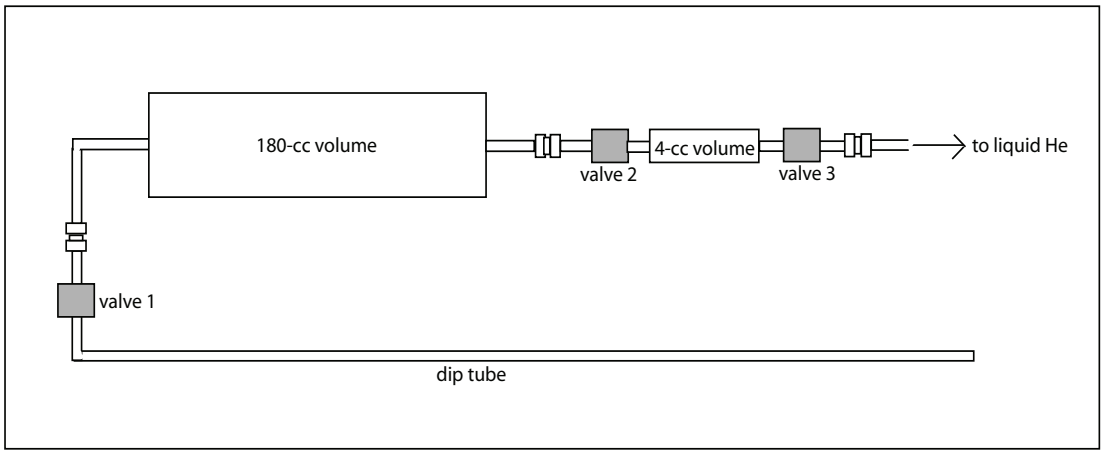

Figure 3.3. Overnight splitting set-up: dip tube, 180-cm^3 volume, and 4-cm^3 volume

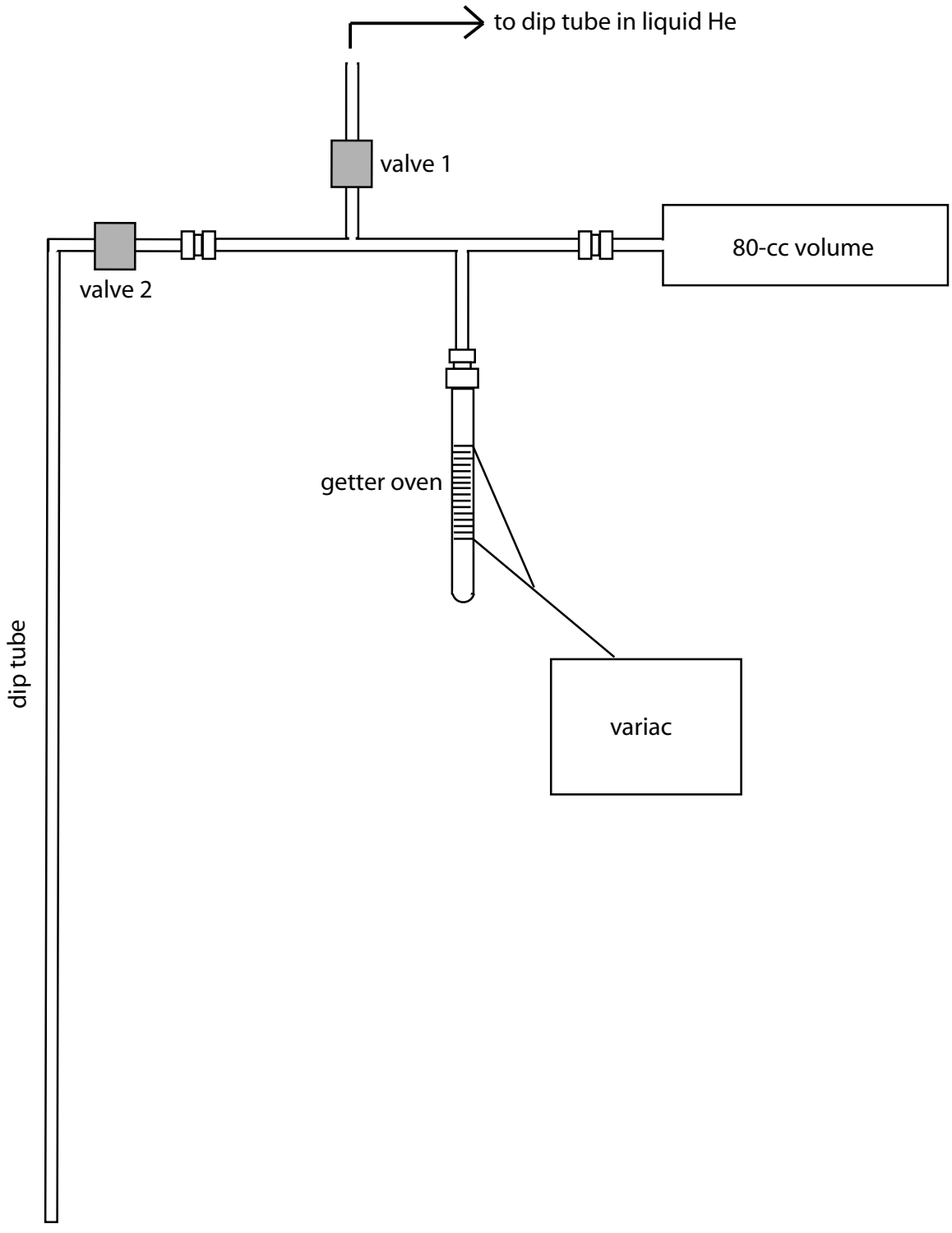

Figure 3.4. Gettering set-up: dip tube, getter oven, 80-cm^3 volume

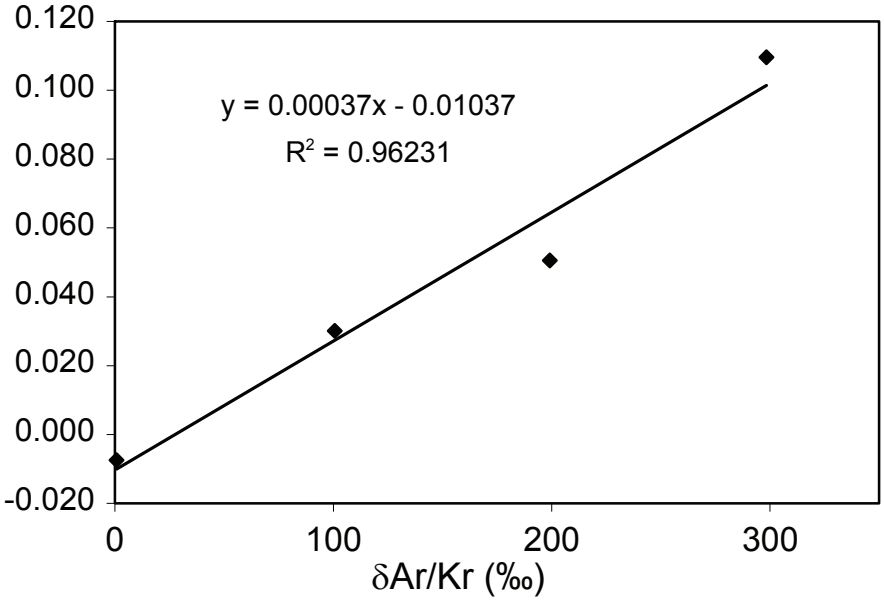

Figure 3.5. Chemical slope: δ^{86}Kr vs. δAr/Kr

Figure 3.6(a)-(d). Pier Air measurements throughout duration of ice core analyses (October, 2007 – March, 2008). Data shown are deviations from a working standard. Blue points are individual measurements. Thick black lines are mean pier air values used to normalize ice core measurements made during those dates. Dashed vertical line separates Vostok (left) from GISP2 (right) measurements. (a) $\delta Kr/N_2$, (b) $\delta Xe/N_2$, (c) $\delta^{86}Kr$ – note a linear trend is used to normalize ice core $\delta^{86}Kr$ measurements during the GISP2 analyses, (d) $\delta^{15}N$. Mean pier air values used to normalize each dataset are listed in Table 3.2.

(a)

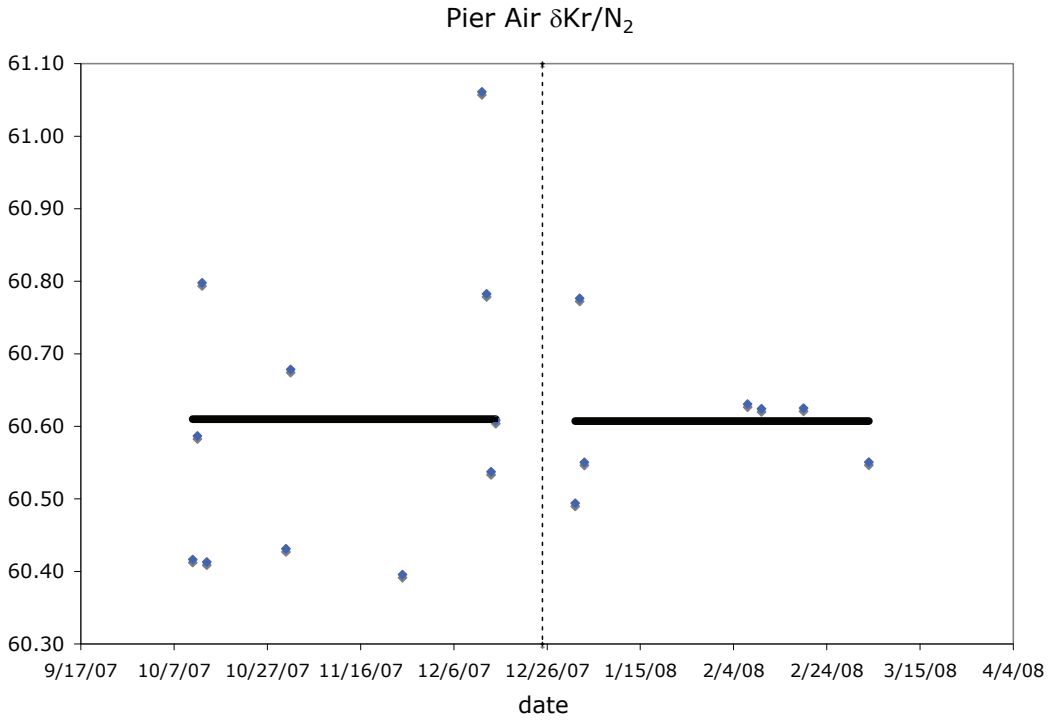
Pier Air δKr/N2
61.10
61.00
60.90
60.80
60.70
60.60
60.50
60.40
60.30
9/17/07
10/7/07
10/27/07
11/16/07
12/6/07
12/26/07
1/15/08
2/4/08
2/24/08
3/15/08
4/4/08
date

(b)

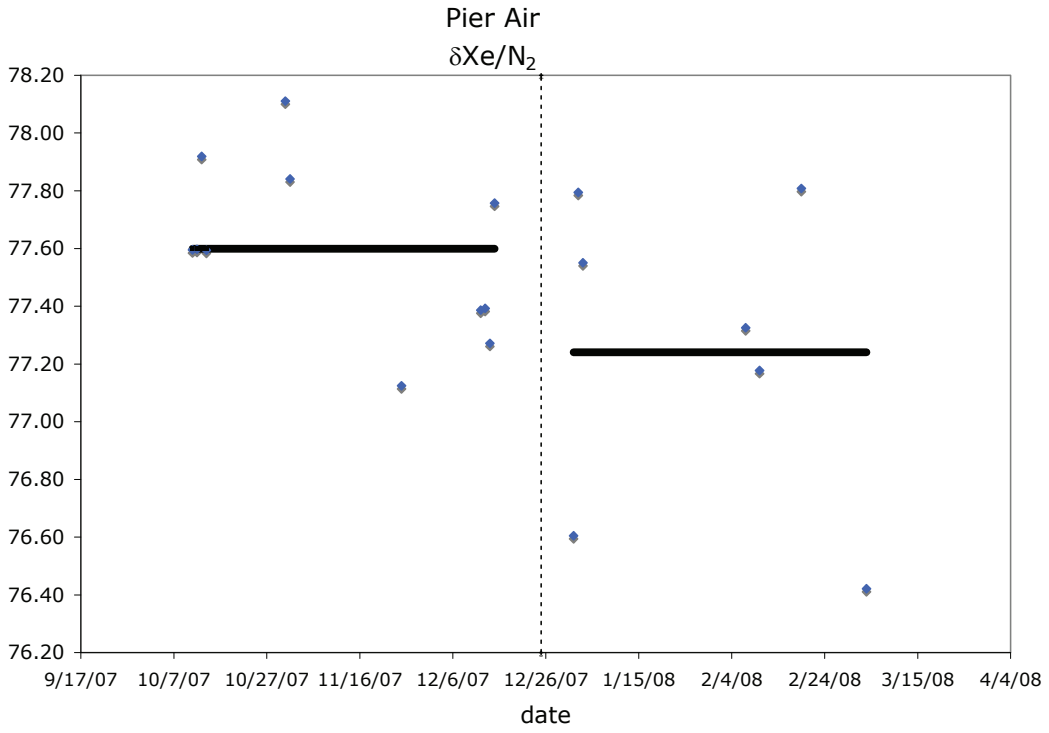
Pier Air
δXe/N2
78.20
78.00
77.80
77.60
77.40
77.20
77.00
76.80
76.60
76.40
76.20
9/17/07
10/7/07
10/27/07
11/16/07
12/6/07
12/26/07
1/15/08
2/4/08
2/24/08
3/15/08
4/4/08
date

(c)

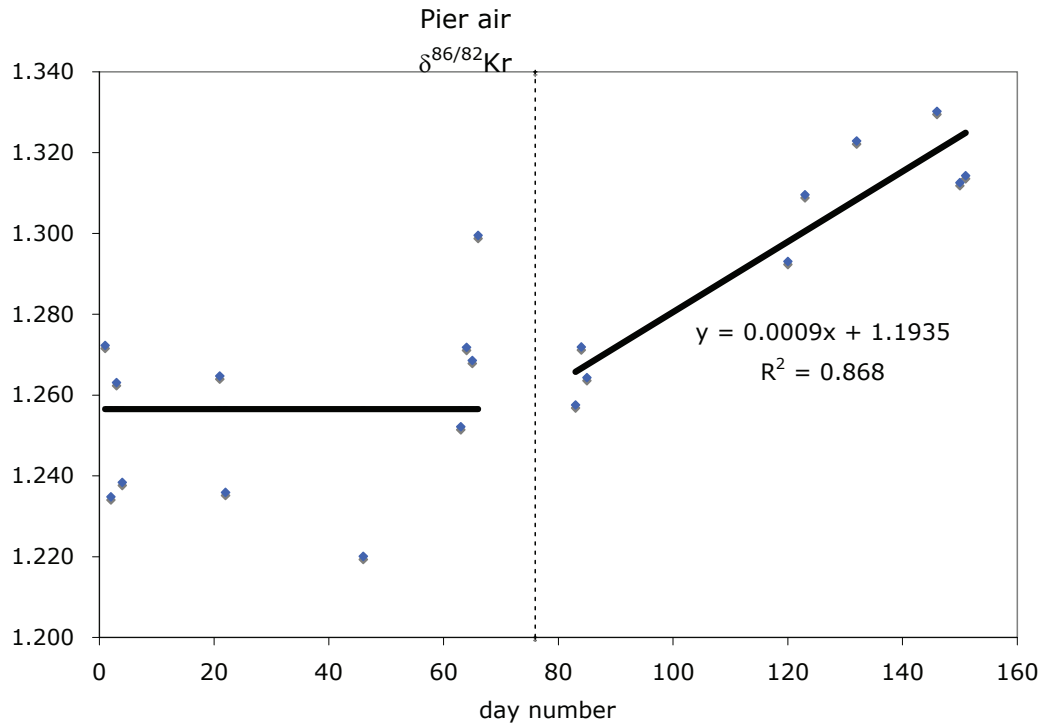

(d)

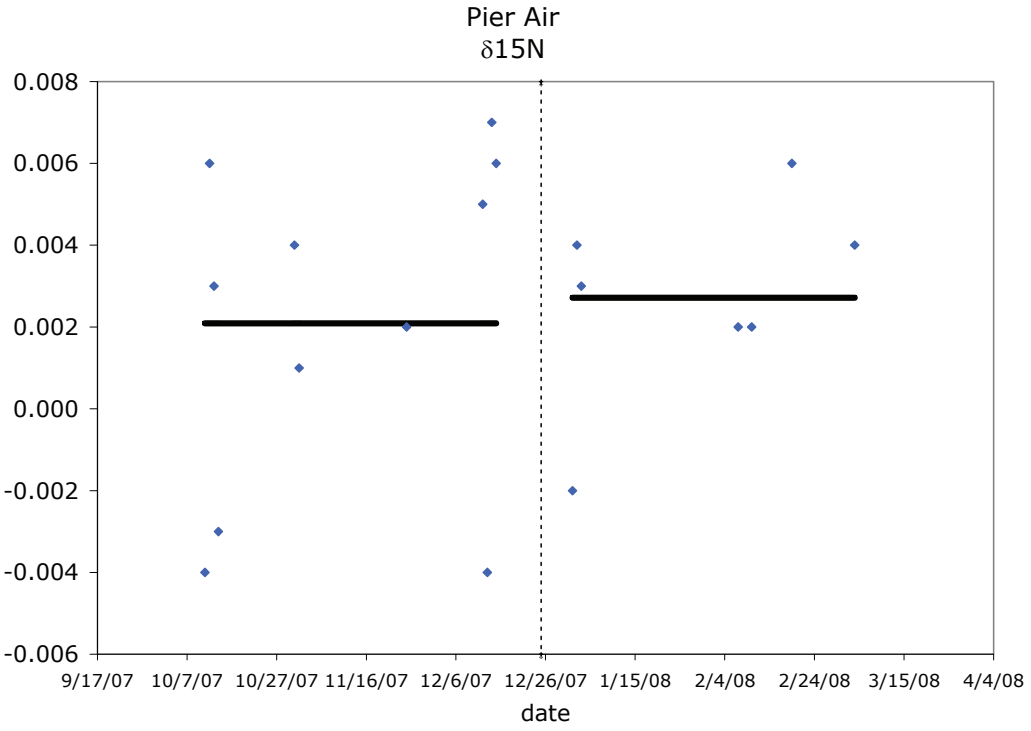

Figure 3.6 continued

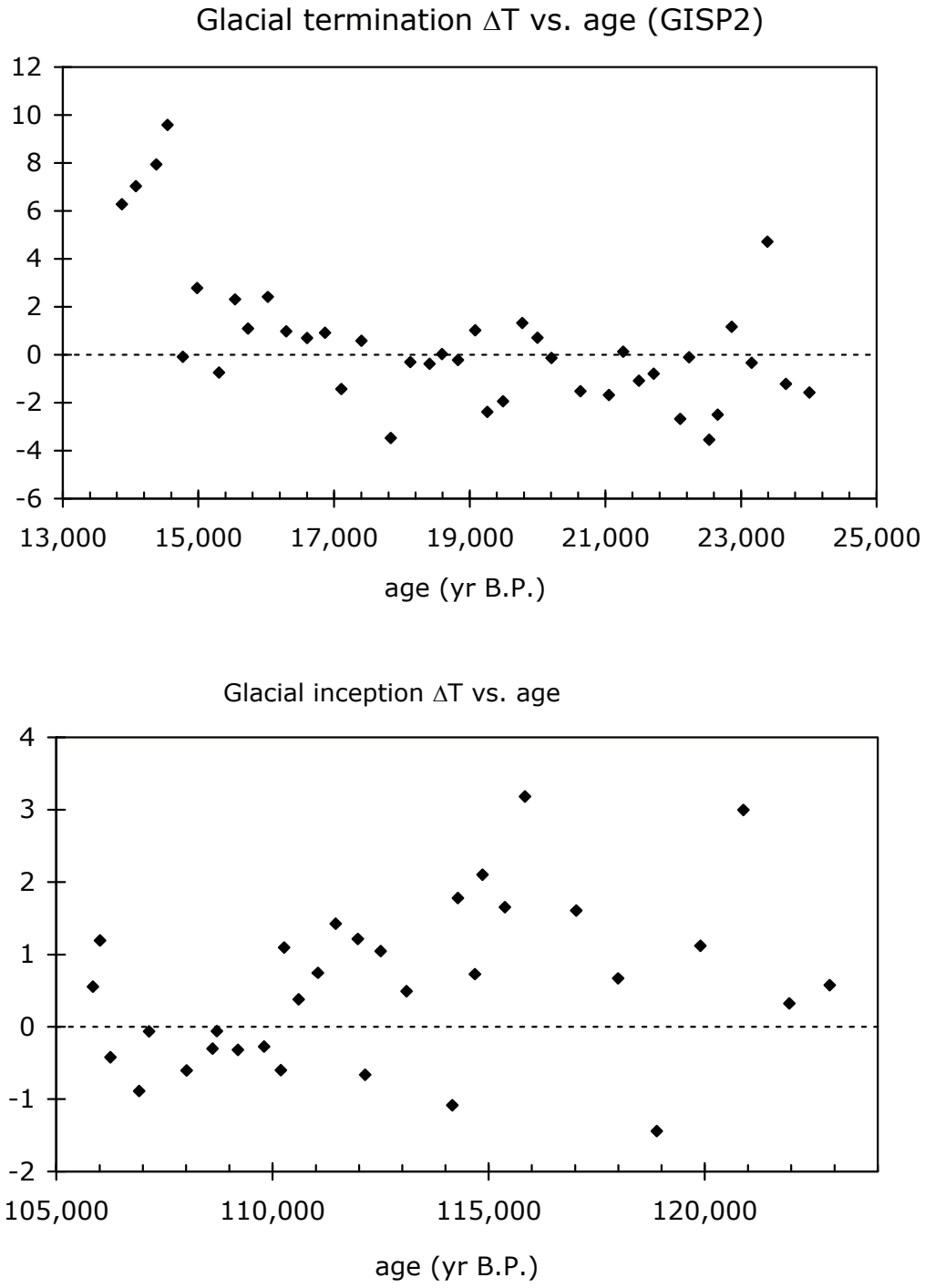

Figure 3.7. ΔT (determined from $\delta^{15}N$ and $\delta^{86}Kr$) used to correct for thermal diffusion in the GISP2 glacial termination data (top) and the Vostok glacial inception data (bottom).

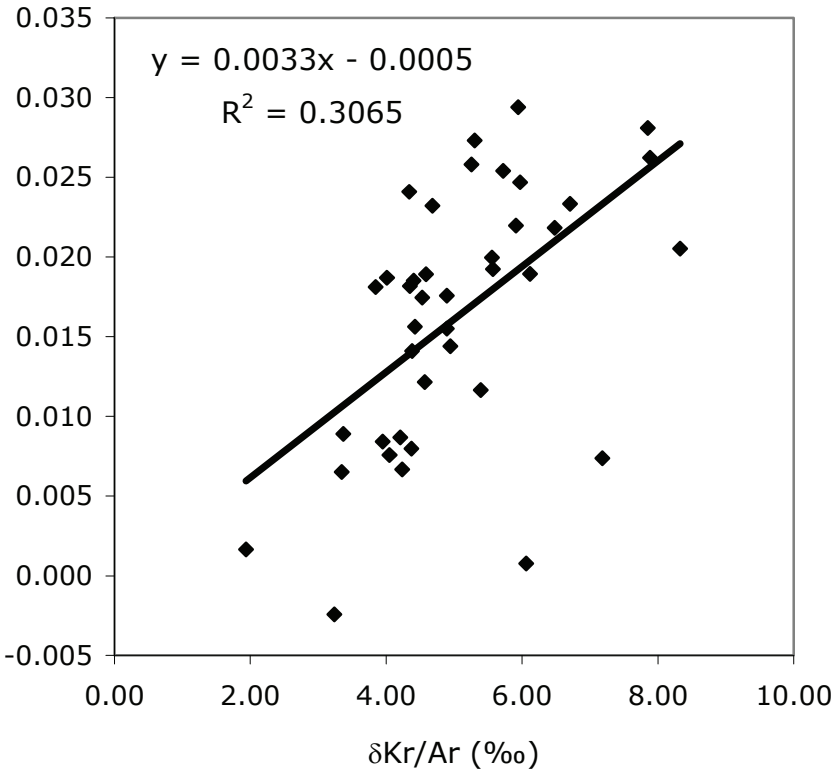

Figure 3.8. $\delta^{40}Ar_{\text{gas loss residual}}$ vs. $\delta Kr/Ar$

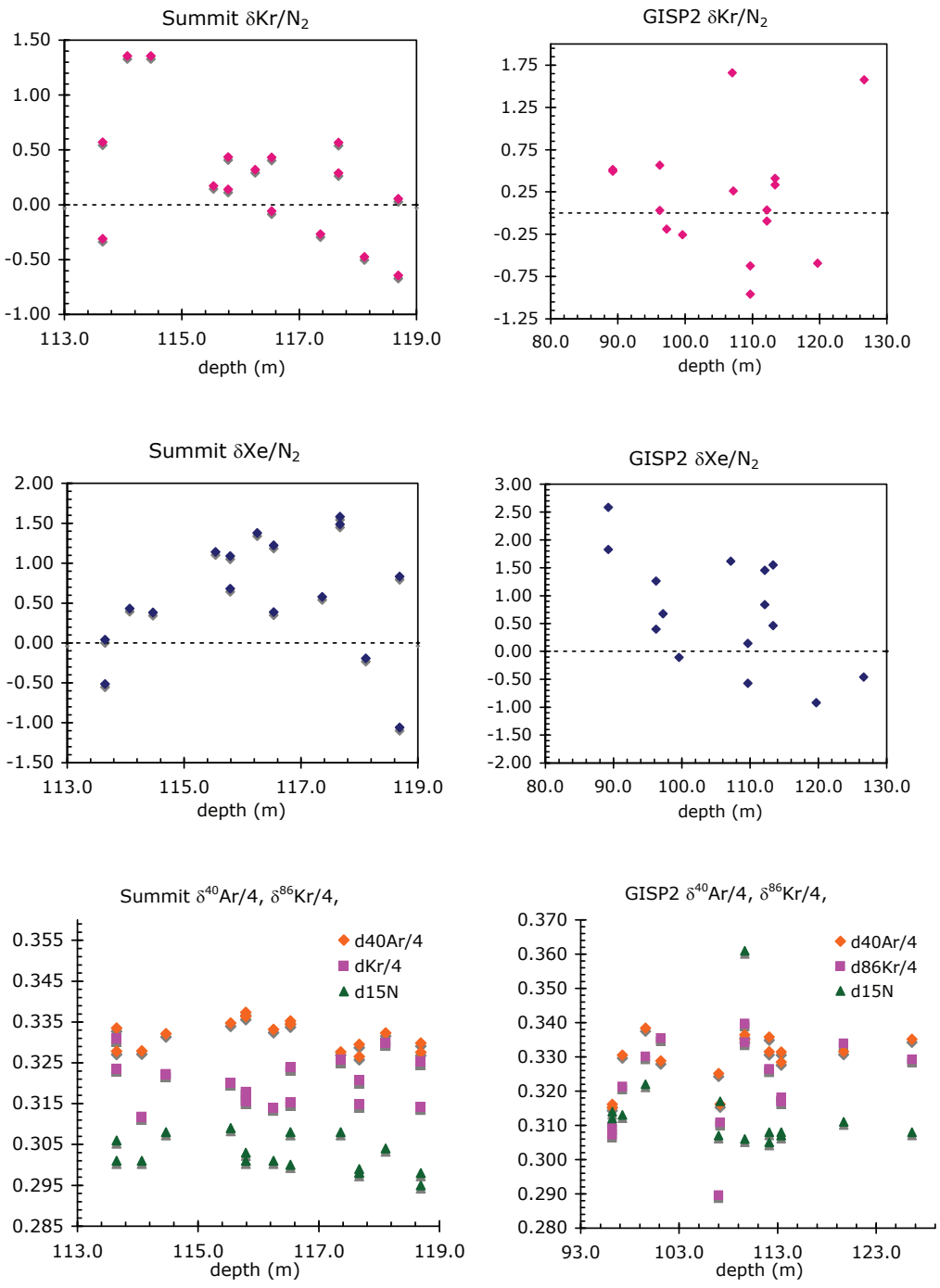

Figure 3.9. Gravitationally corrected $\delta Kr/N_2$, $\delta Xe/N_2$, and isotope ($\delta^{40}Ar/4$, $\delta^{86}Kr/4$, and $\delta^{15}N$) data from the late Holocene measured in the Summit and GISP2 ice cores from Greenland.

(a)

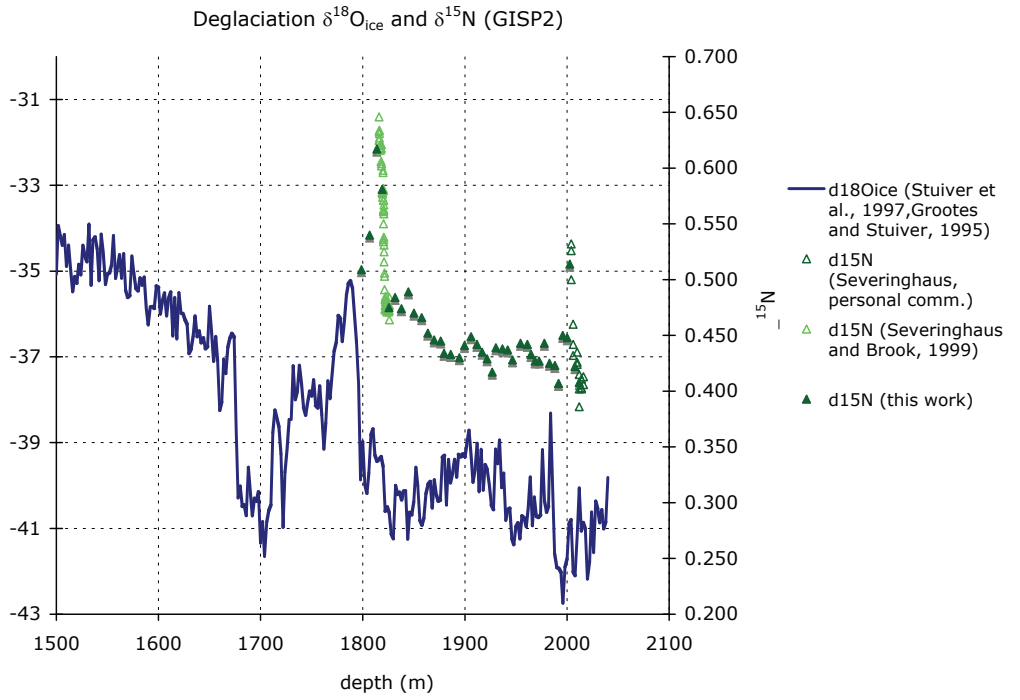

(b)

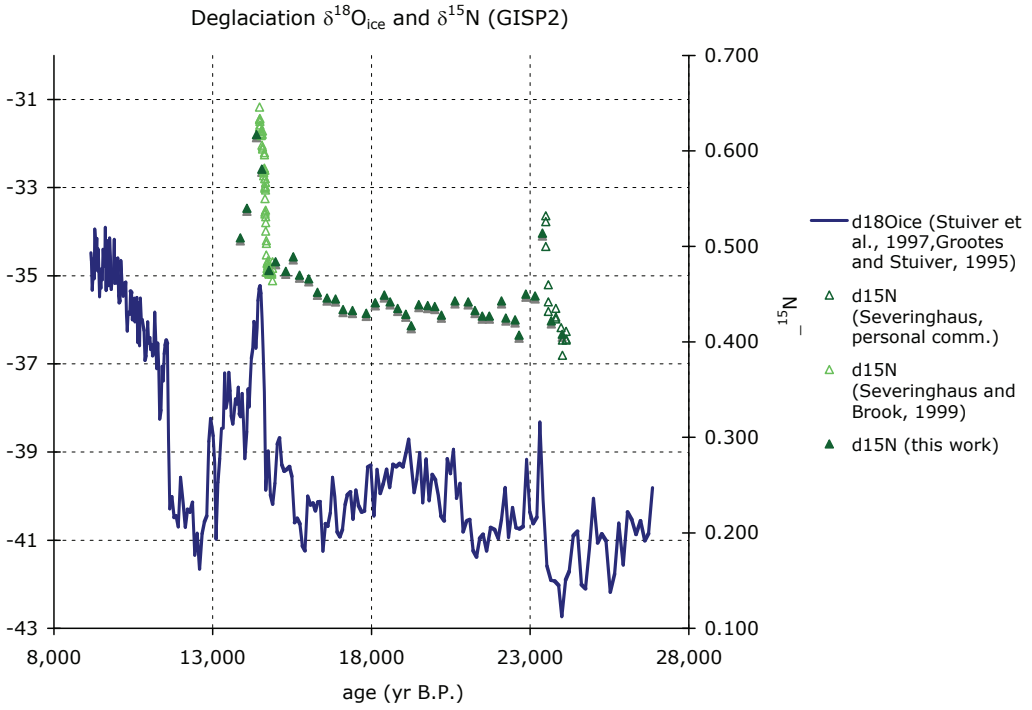

Figure 3.10. $\delta^{15}N$ (this work, Severinghaus and Brook, 1999, Severinghaus, personal communication) and $\delta^{18}O_{ice}$ (Stuiver et al., 1995, Grootes and Stuiver, 1997) during the deglaciation.

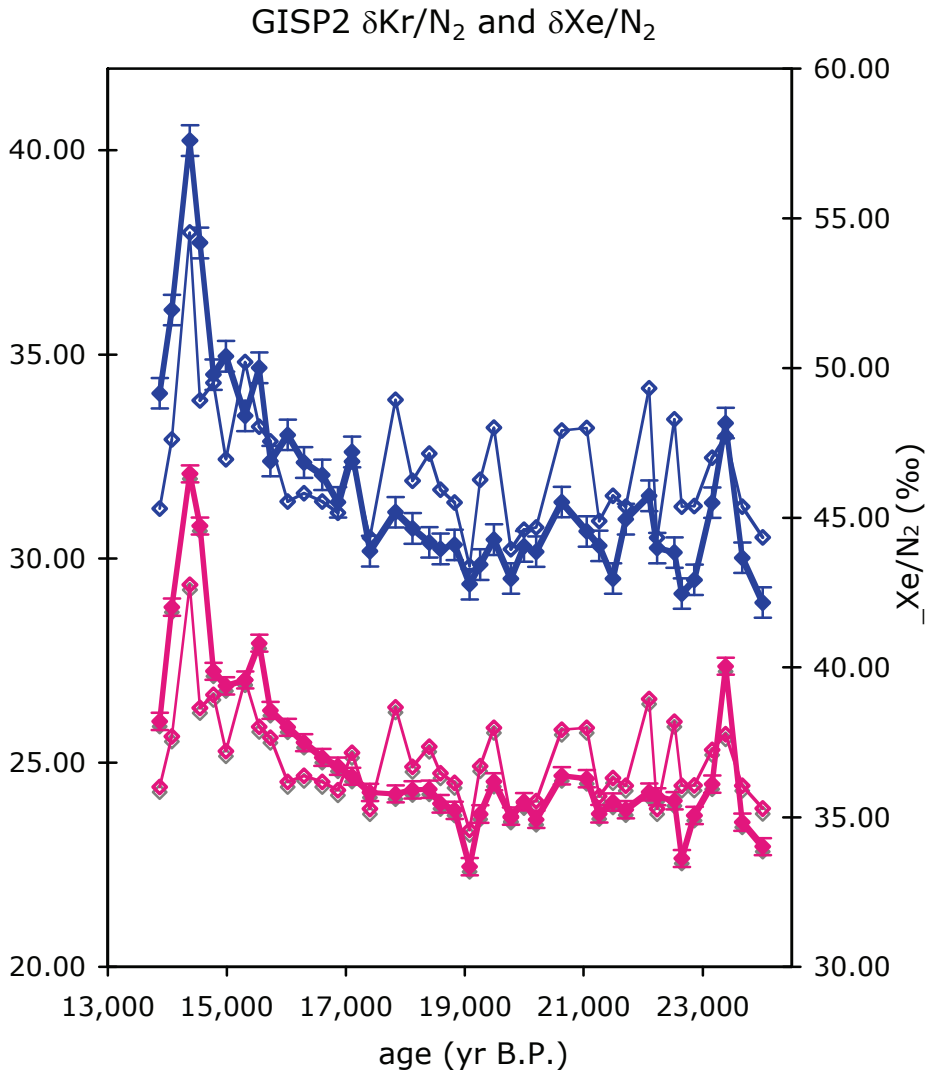

Figure 3.11. Raw data (solid points) and gravity component ($\delta^{86}Kr/4 \times \Delta m$) (hollow points) for $\delta Kr/N_2$ (pink) and $\delta Xe/N_2$ (blue) from the GISP2 deglaciation dataset. Error bars are the standard deviations of the raw $\delta Kr/N_2$ and $\delta Xe/N_2$ (0.21‰ and 0.51‰, respectively) from the Greenland, Summit late Holocene data.

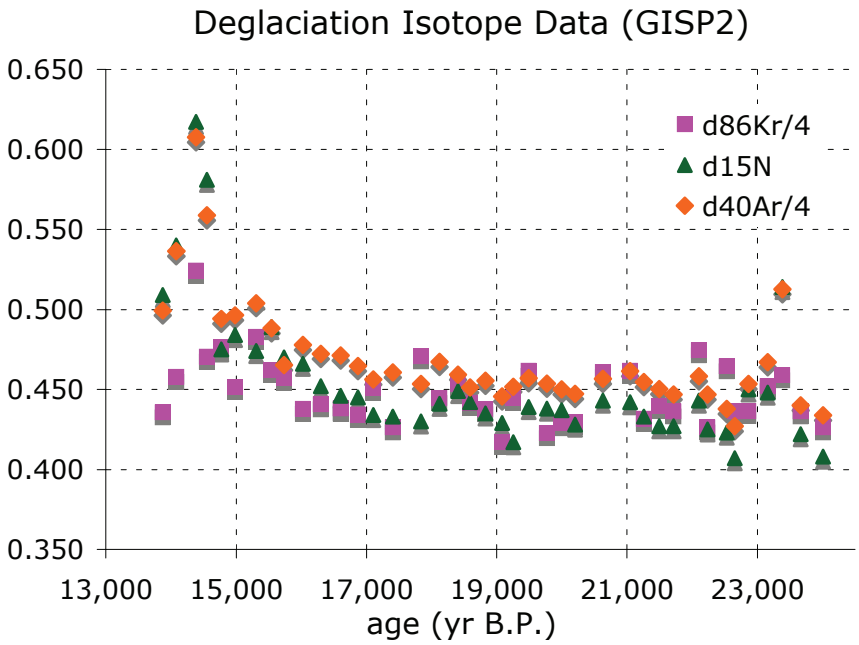

Figure 3.12. GISP2 isotope data ($\delta^{15}N$, $\delta^{40}Ar/4$, $\delta^{86}Kr/4$) from the glacial termination.

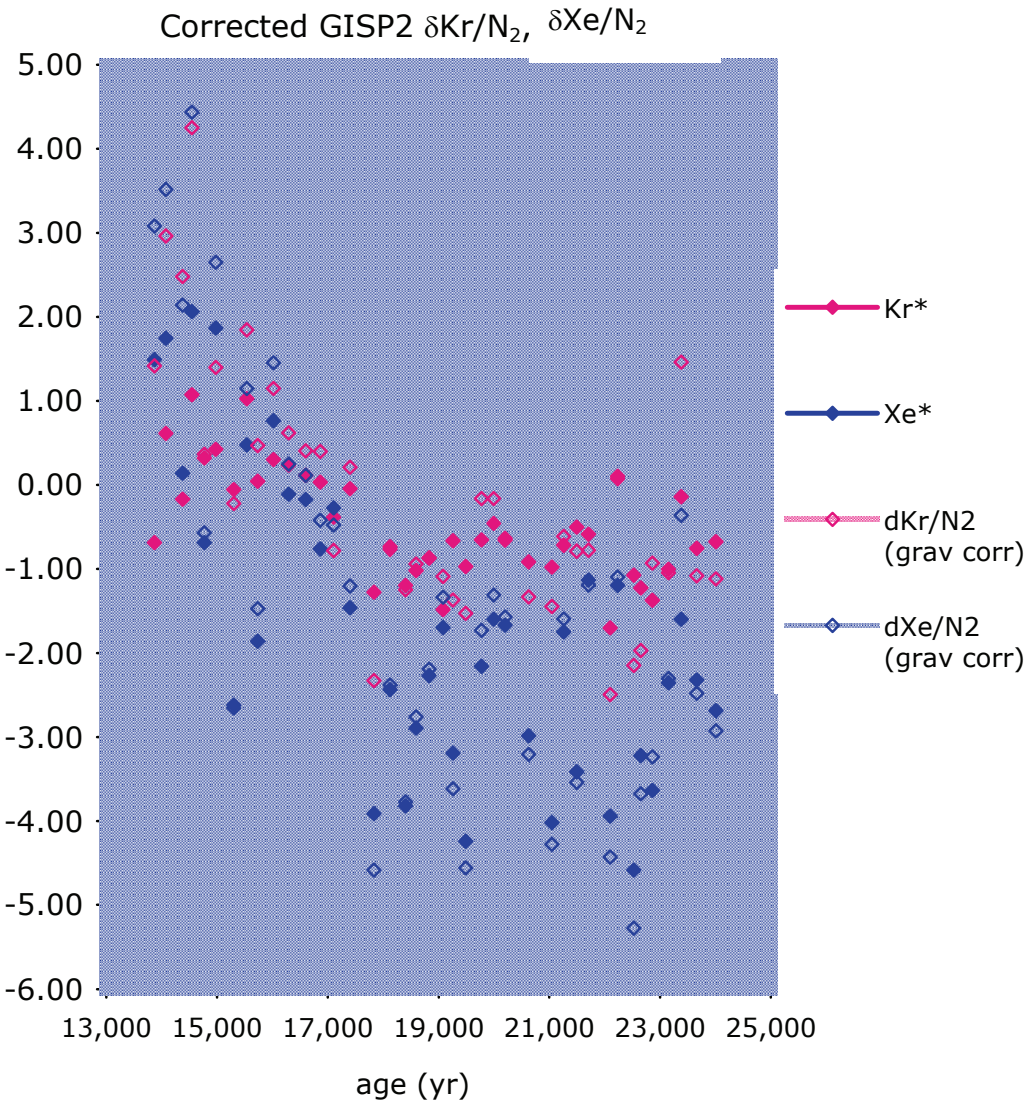

Figure 3.13. Gravitationally corrected $\delta Kr/N_2$ (pink) and $\delta Xe/N_2$ (blue) (hollow points) and Kr* and Xe* (gravitationally and thermally corrected $\delta Kr/N_2$ and $\delta Xe/N_2$) (solid points) from GISP2.

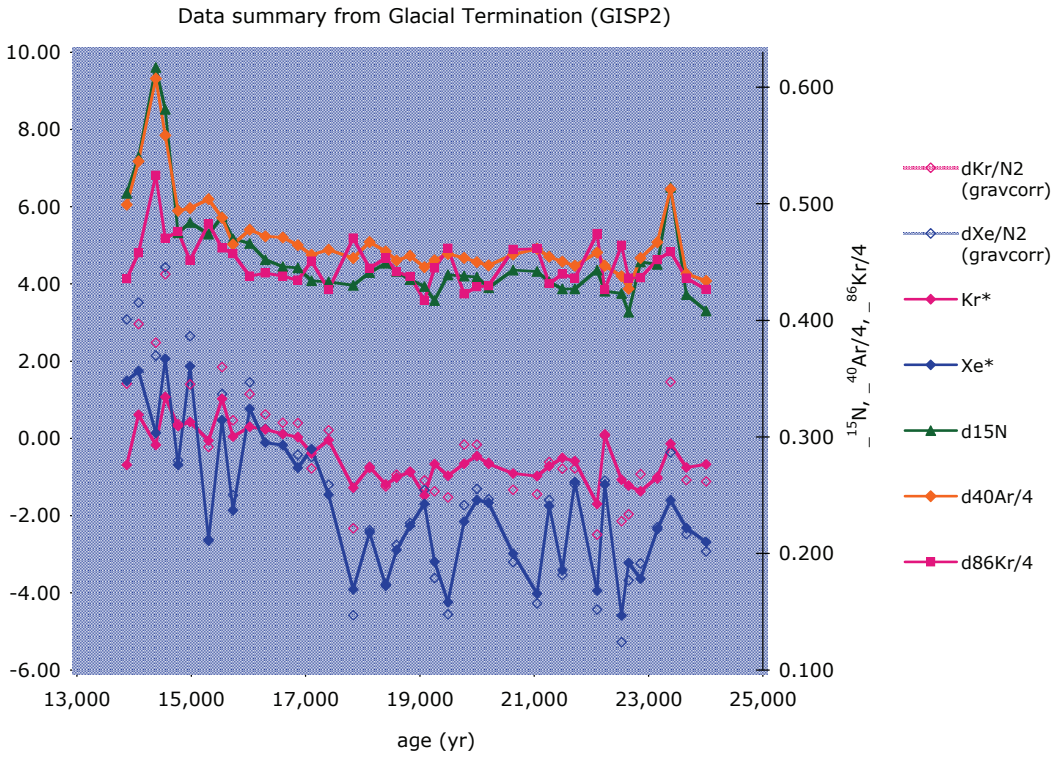

Figure 3.14. Data summary from the GISP2 glacial termination.

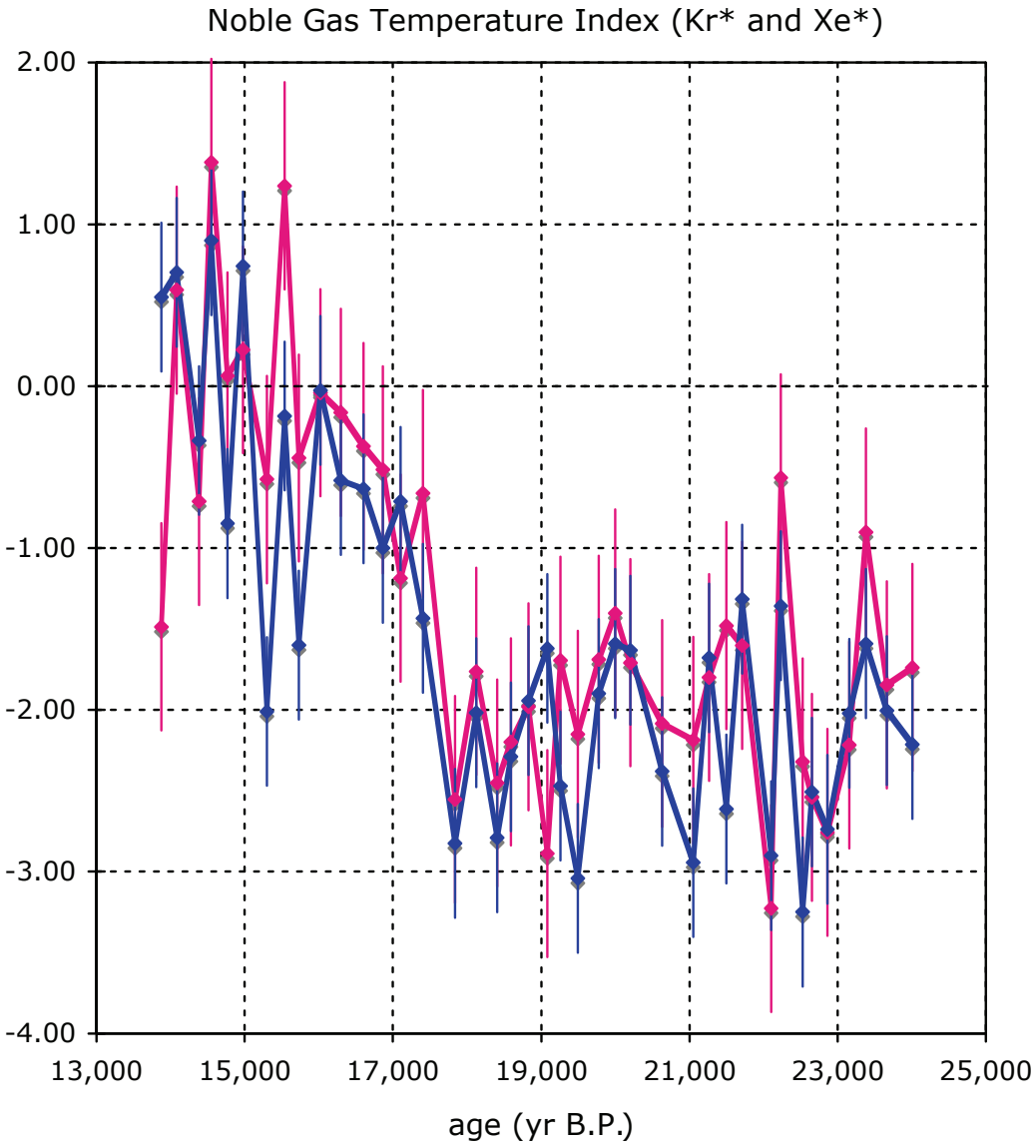

Figure 3.15. Noble Gas Temperature Index (NGTI): solubility-weighted mean ocean temperature change, derived from Kr* (pink) and Xe* (blue).

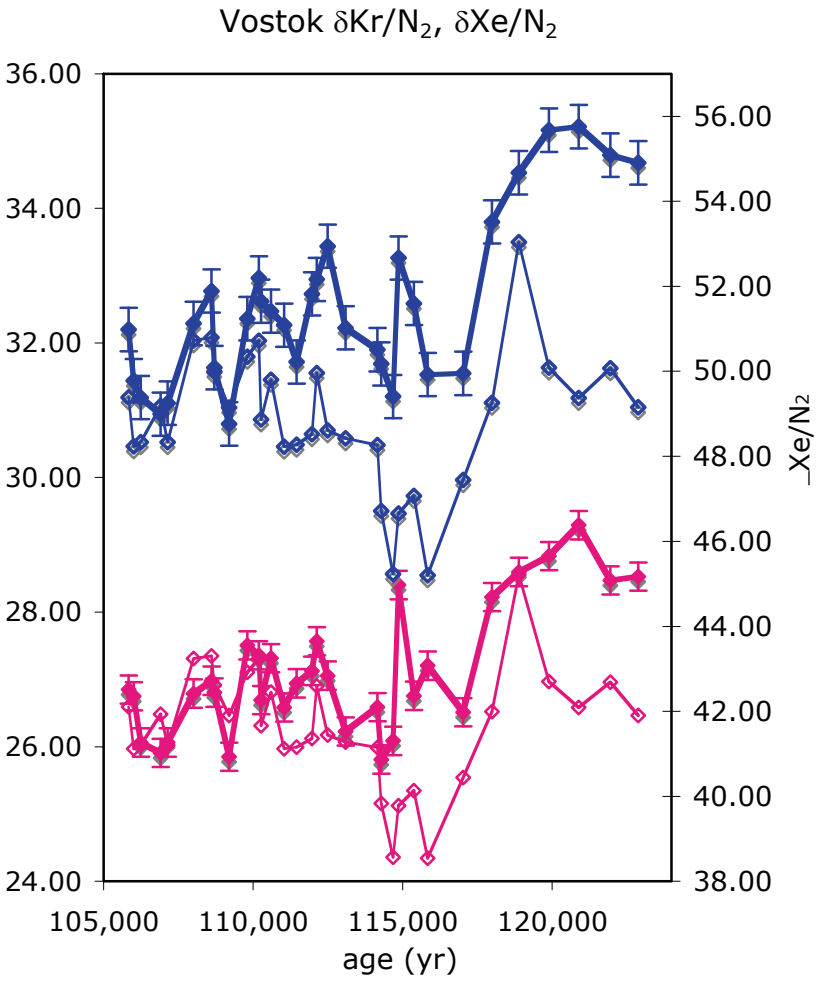

Figure 3.16. Raw data (solid points) and gravity component ($\delta^{86}Kr/4 \times \Delta m$) (hollow points) for δKr/N2 (pink) and $\delta Xe/N_2$ (blue) for the glacial inception as recorded in Vostok. Error bars are the standard deviations of the raw $\delta Kr/N_2$ and $\delta Xe/N_2$ (0.21‰ and 0.51‰, respectively) from the Greenland, Summit late Holocene data.

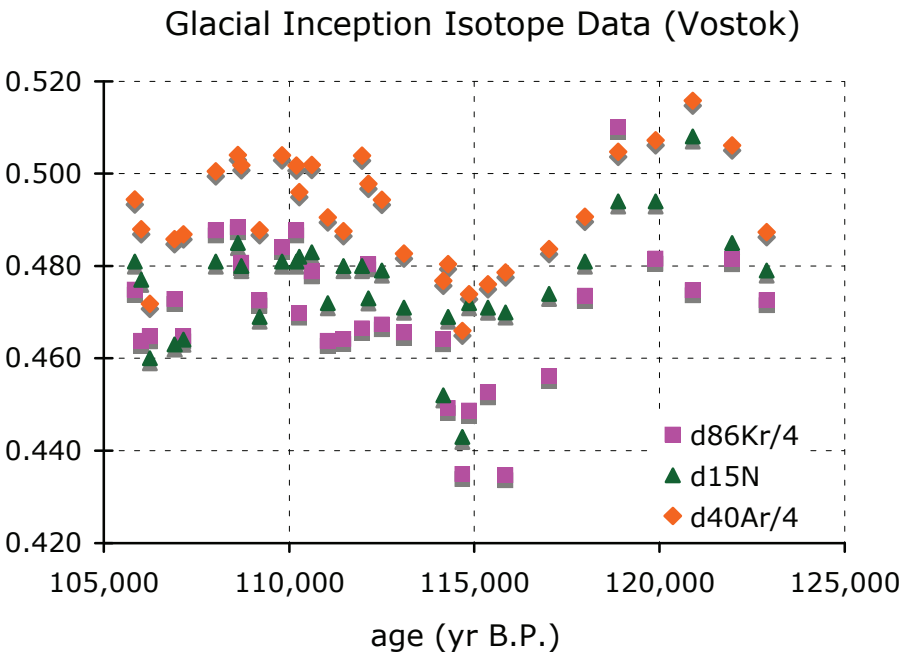

Figure 3.17. Isotope data measured in the Vostok core during the glacial inception (~123,000 – 105,000 years before present).

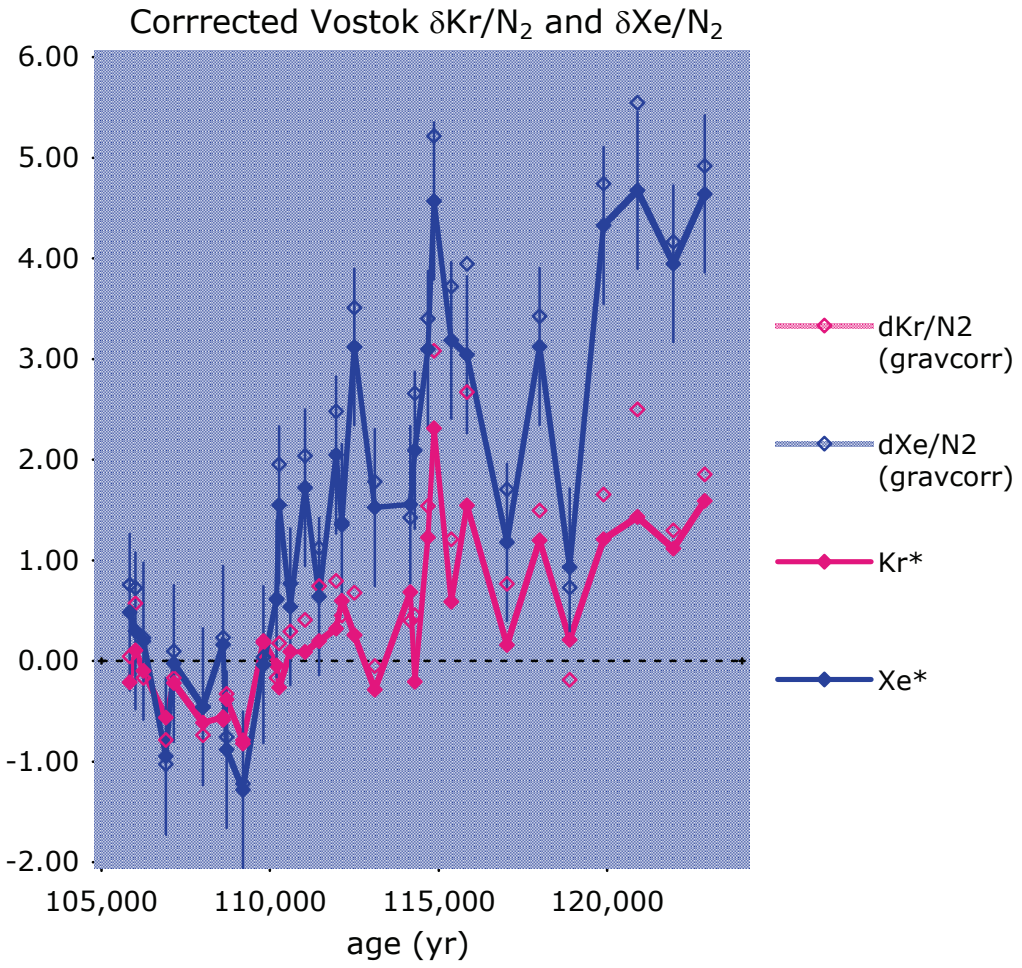

Figure 3.18. Gravitationally-corrected $\delta Kr/N_2$ and $\delta Xe/N_2$ (hollow points) and Kr* and Xe* (gravitationally/thermally-corrected) (solid points) Vostok data.

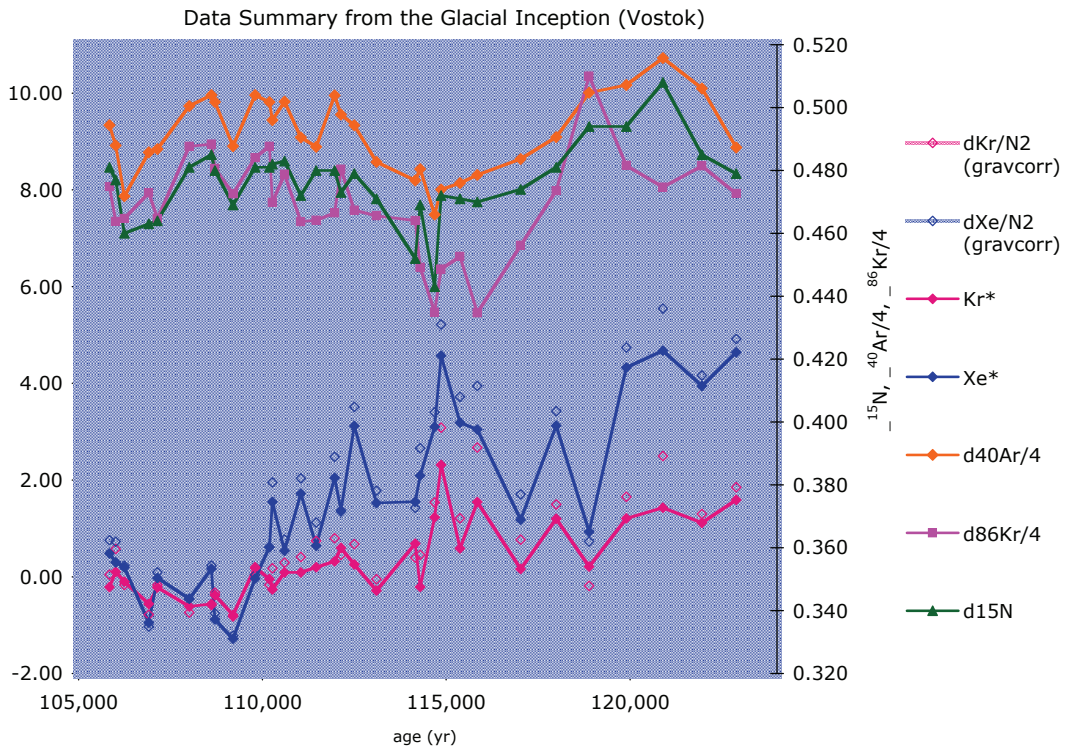

Figure 3.19. Data summary from the Vostok glacial inception (123-104 kyr B.P.).

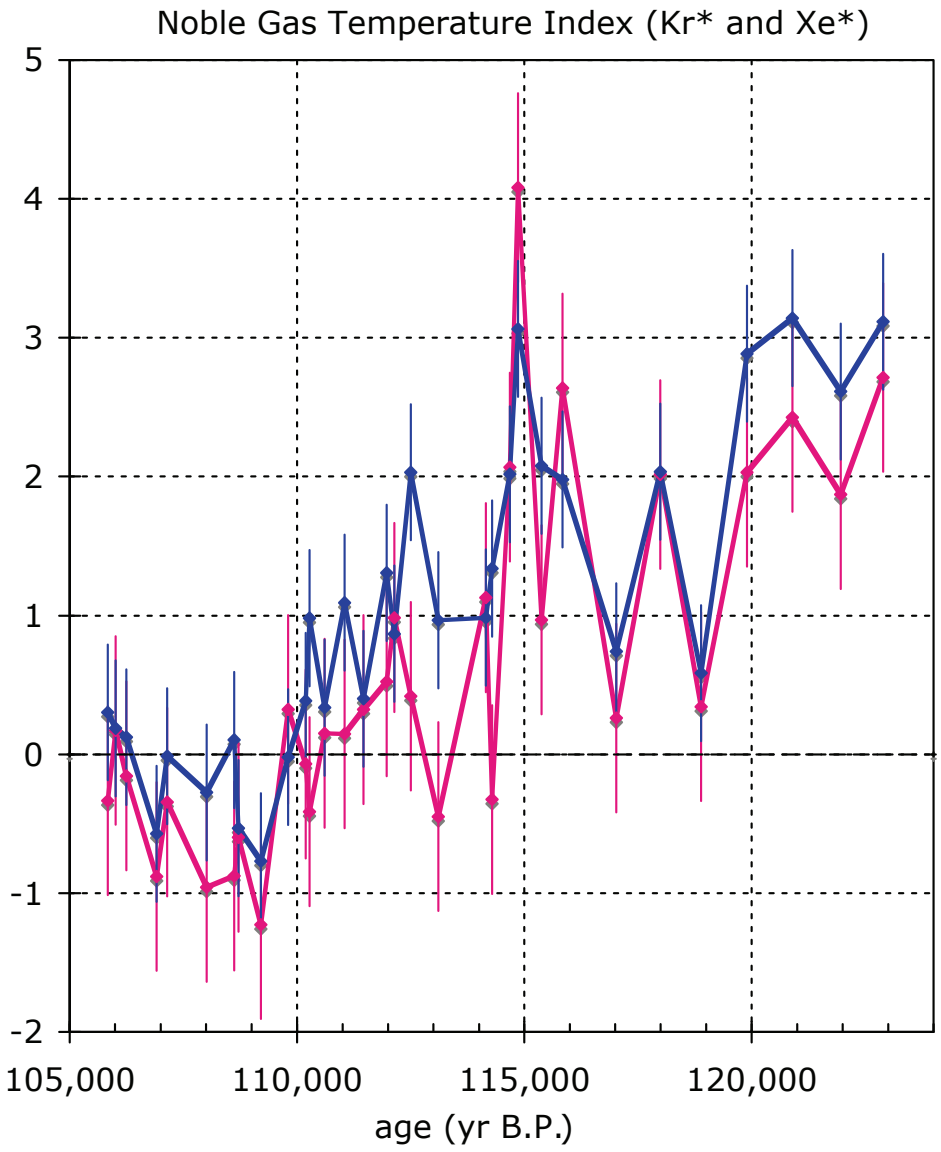

Figure 3.20. Noble Gas Temperature Index (NGTI): solubility-weighted mean ocean temperature change, for the glacial inception, derived from Kr* (pink) and Xe* (blue) from Vostok.

(a)

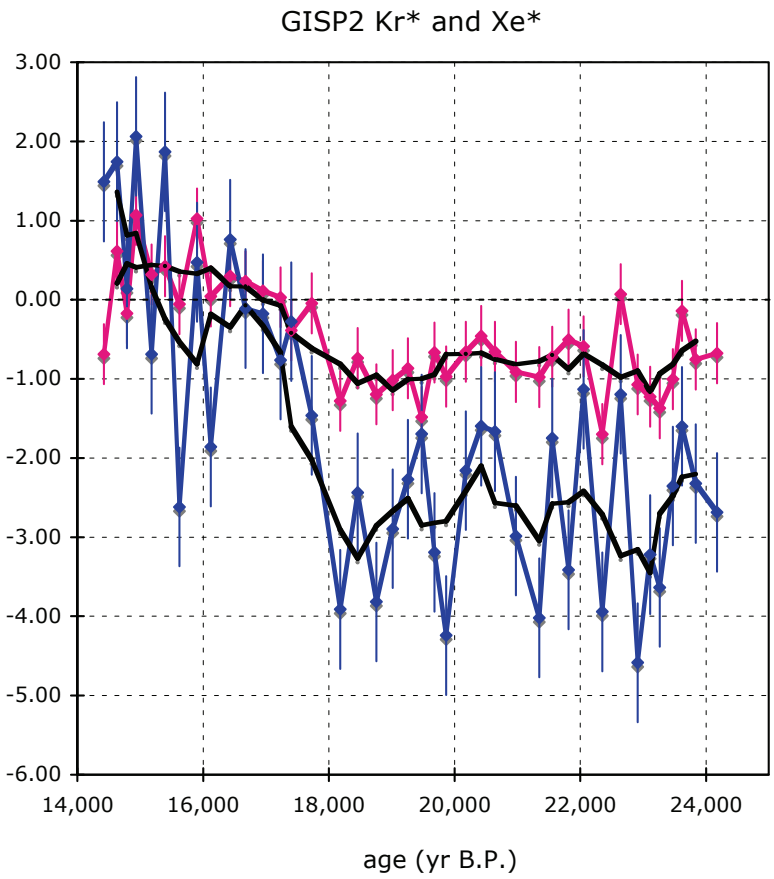

(b)

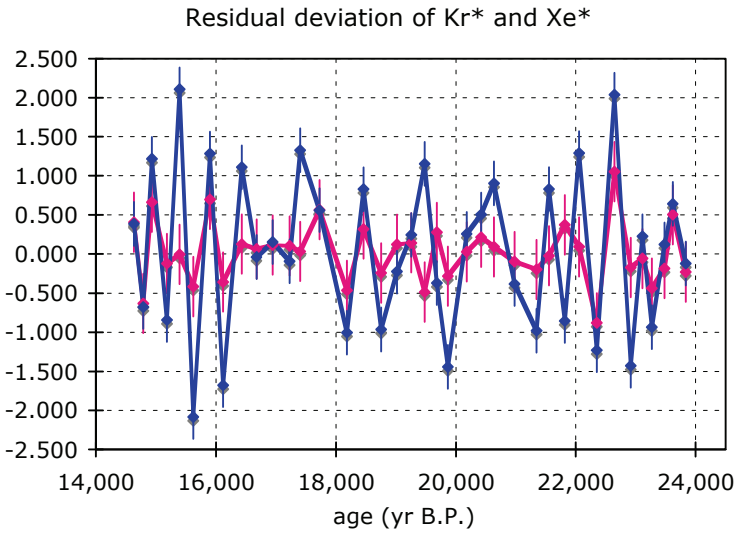

Figure 3.21. (a) GISP2 $\delta Kr/N_2$ and $\delta Xe/N_2$, with overlaying moving average fit (4-point moving average, ~1000 years). (b) Residual deviation of $\delta Kr/N_2$ (pink) and $\delta Xe/N_2$ (blue) from moving average.

(a)

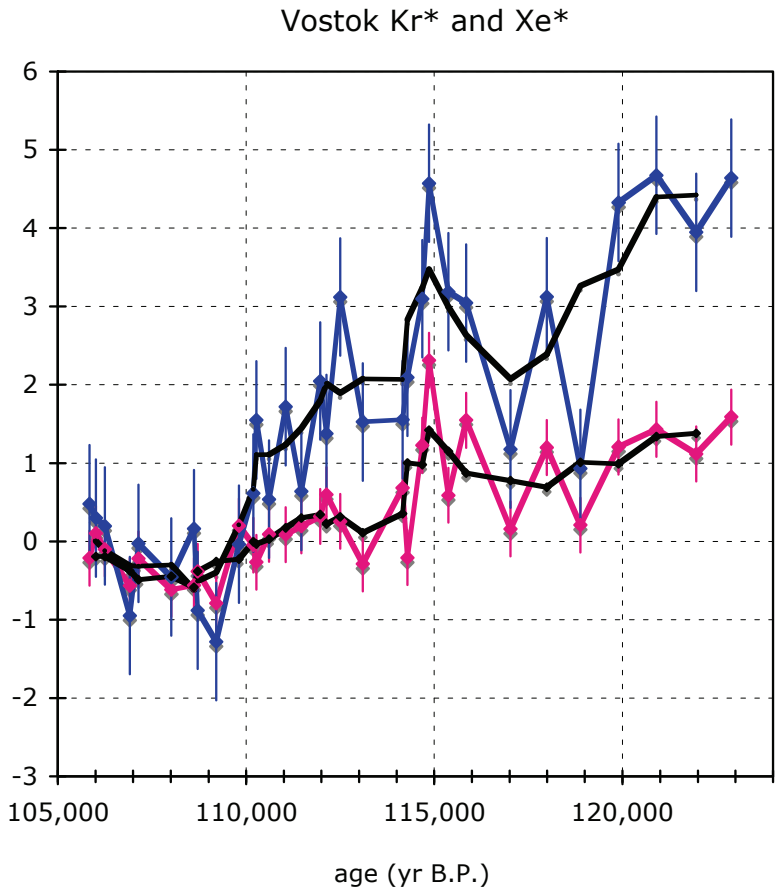

(b)

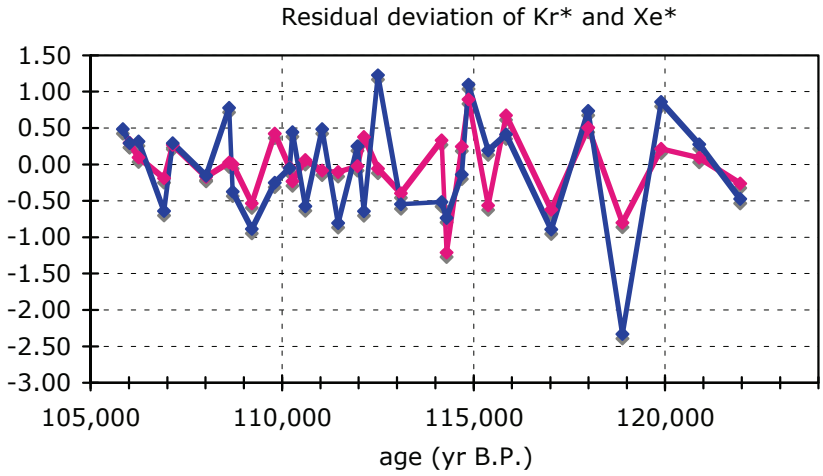

Figure 3.22. (a) Vostok $\delta Kr/N_2$ and $\delta Xe/N_2$, with overlaying moving average fit (4-point moving average, ~1000 years). (b) Residual deviation of $\delta Kr/N_2$ (pink) and $\delta Xe/N_2$ (blue) from moving average.

(a)

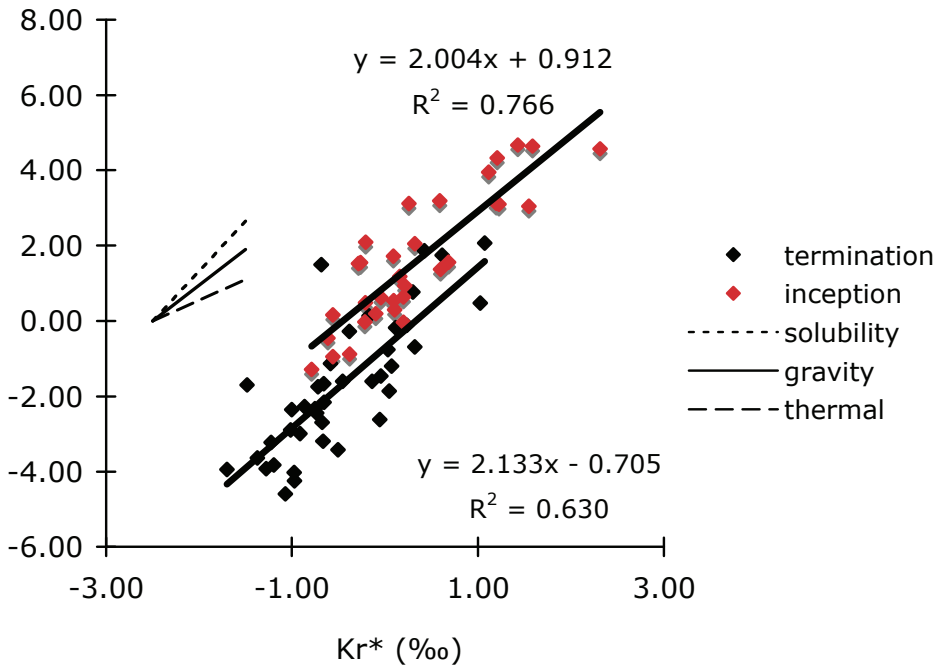

(b)

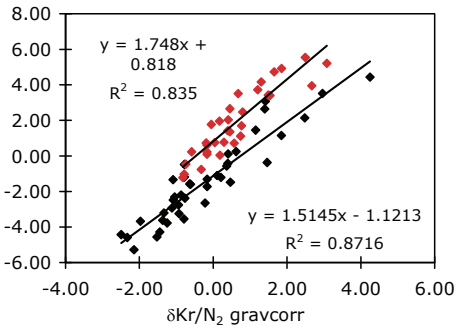

(c)

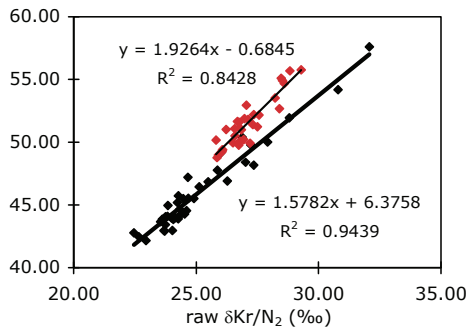

Figure 3.23(a)-(c). (a) Xe* vs. Kr* (gravitationally and thermally corrected $\delta Xe/N_2$ vs. $\delta Kr/N_2$), (b) Gravitationally corrected $\delta Xe/N_2$ vs. $\delta Kr/N_2$, (c) Raw $\delta Xe/N_2$ vs. $\delta Kr/N_2$.

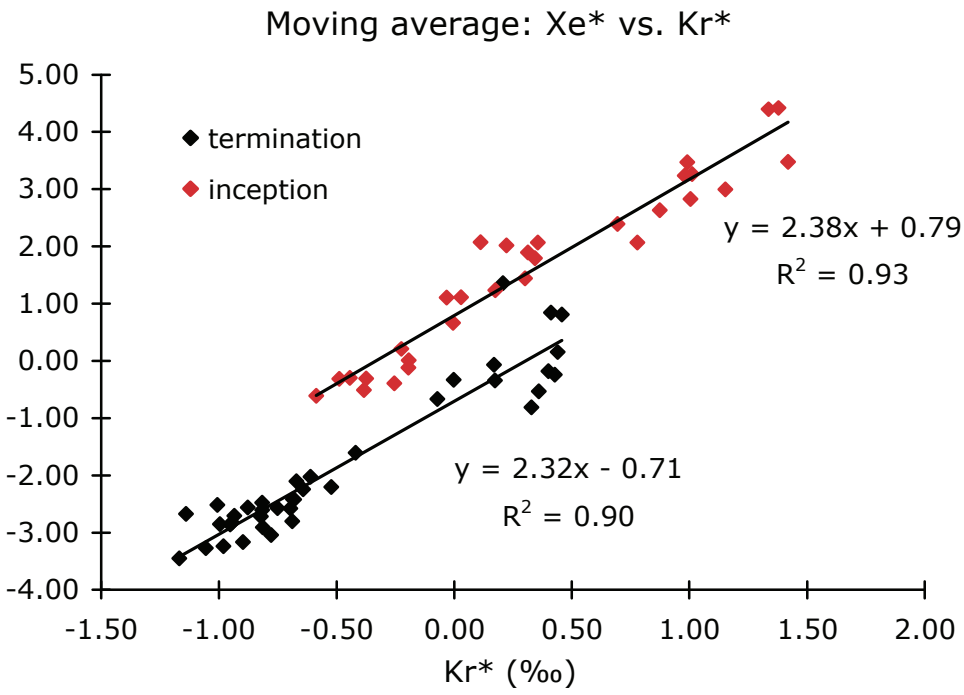

Figure 3.24. Moving average Xe* vs. moving average Kr*

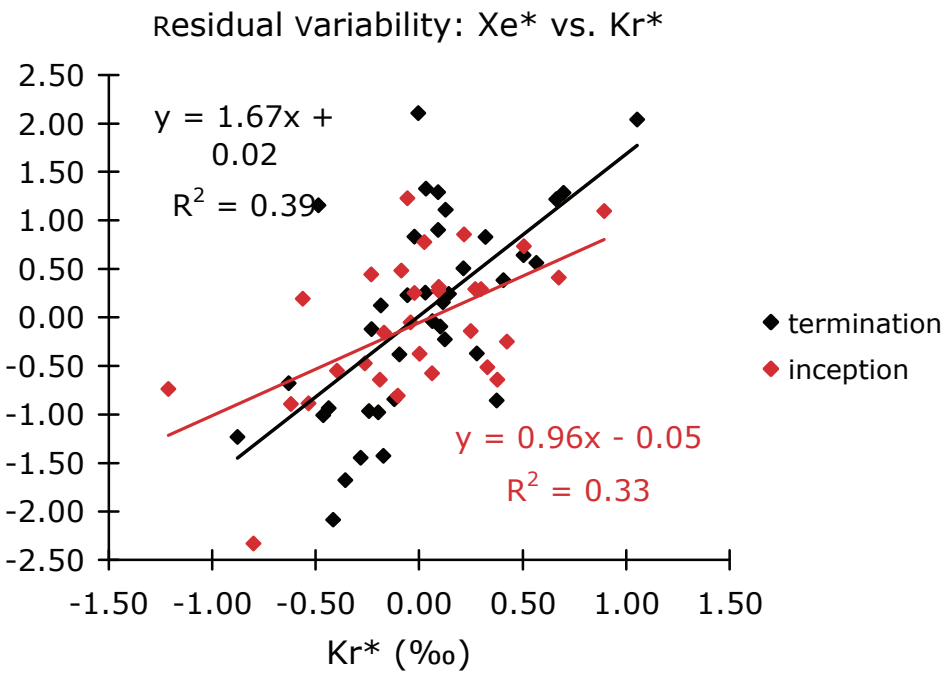

Figure 3.25. Residuals from moving average: Xe* vs. Kr*

(a)

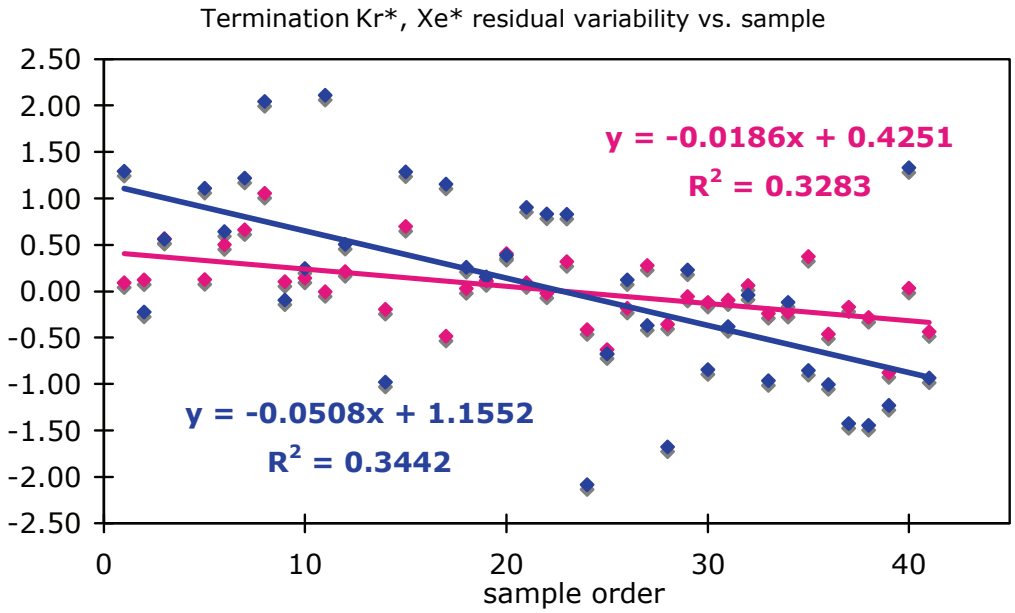

(b)

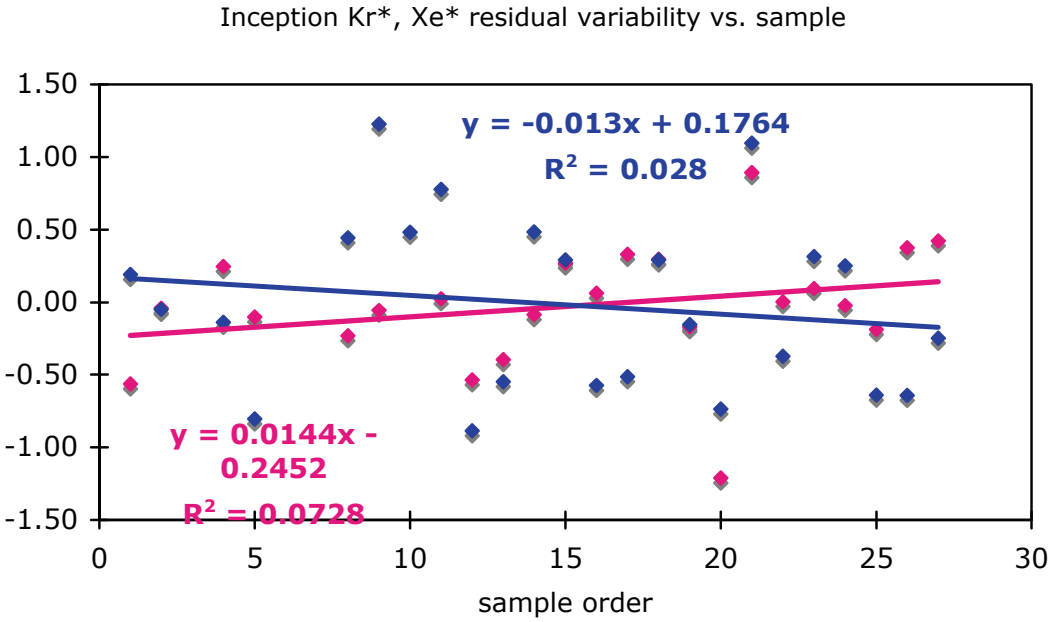

Figure 3.26. Kr* (pink) and Xe* (blue) residual variability from moving average vs. order in which samples were run. (a) GISP2 glacial termination data, (b) Vostok glacial inception data.

(a)

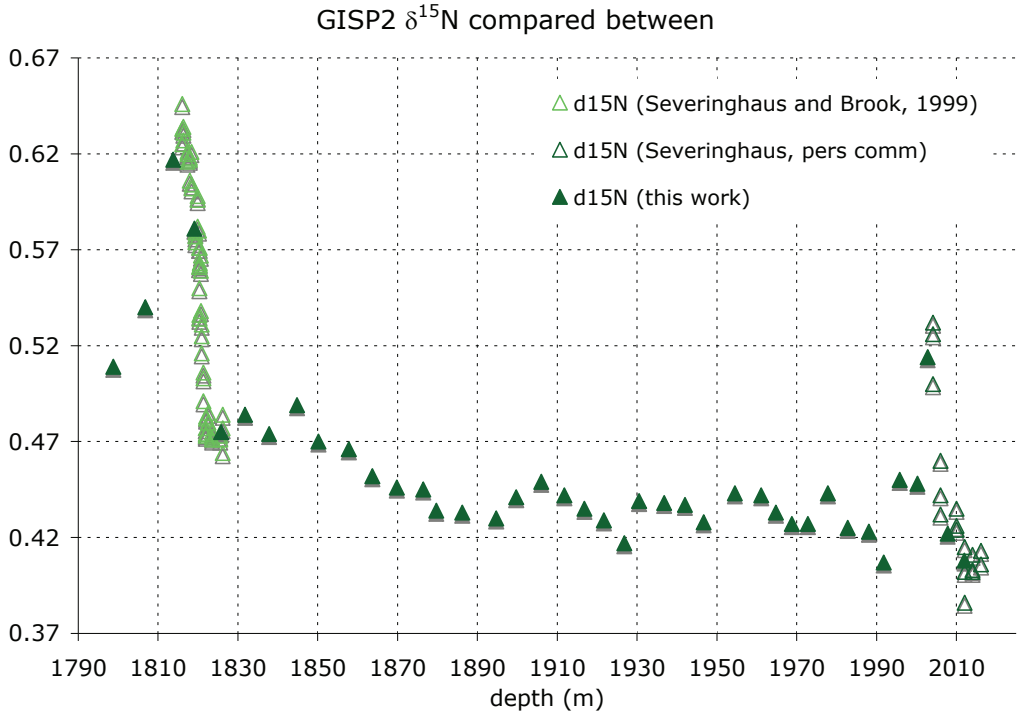

(b)

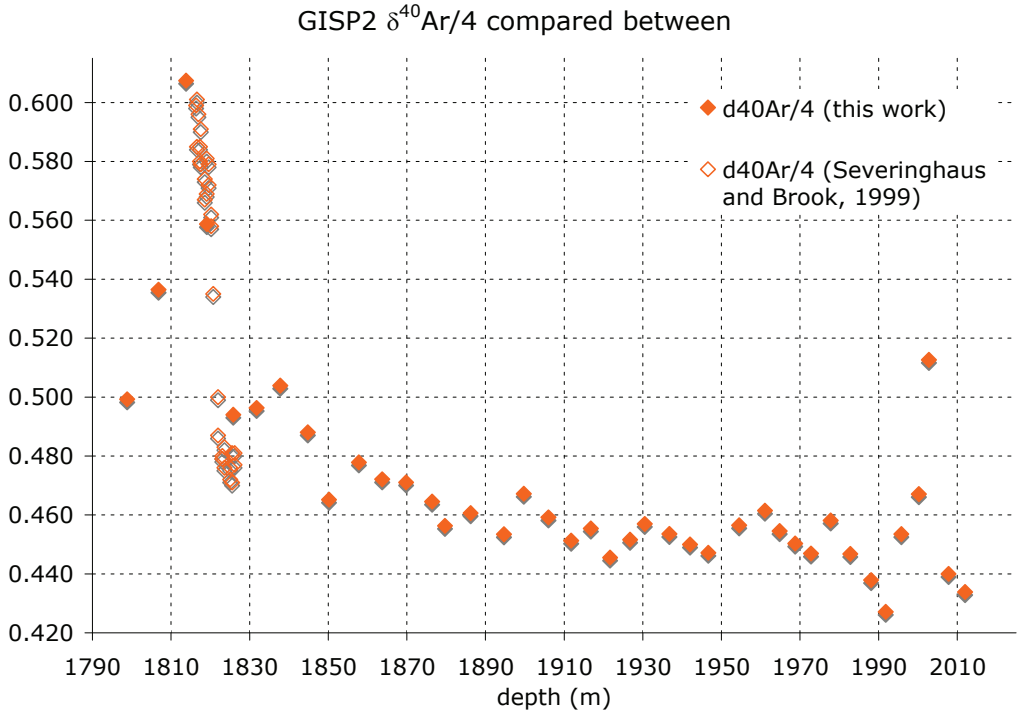

Figure 3.27. Comparison of $\delta^{15}N$ and $\delta^{40}Ar/4$ between the data presented here and earlier studies.

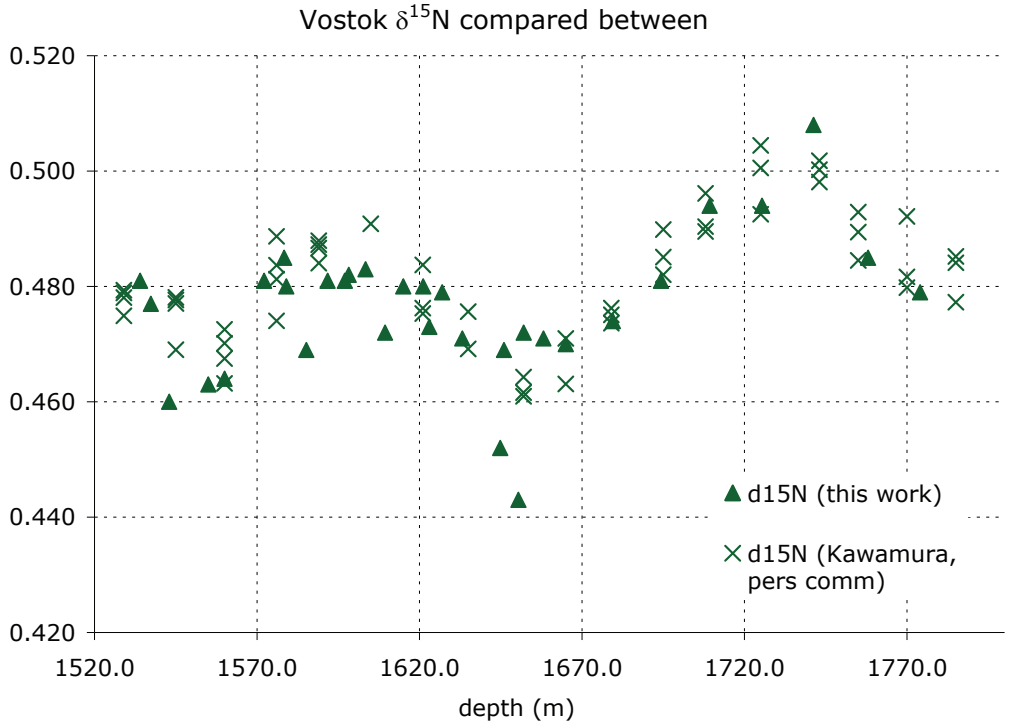

Figure 3.28. Comparison between $\delta^{15}N$ (this work) and $\delta^{15}N$ (Kawamura, personal communication).

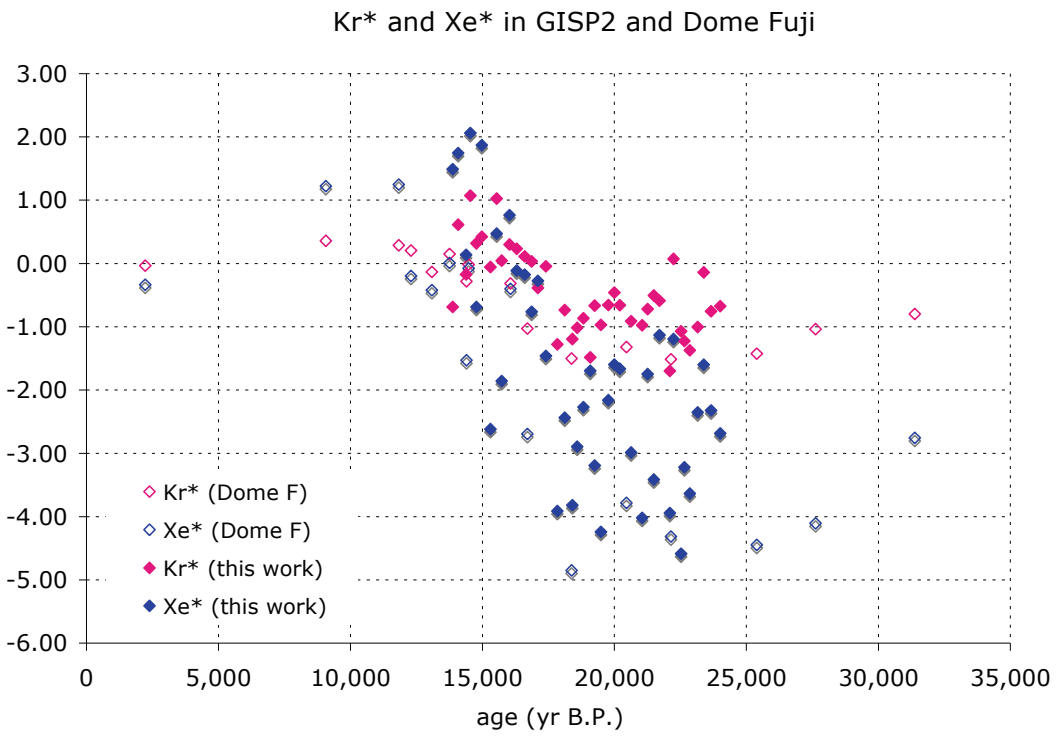

Figure 3.29. Glacial termination Kr* and Xe* from GISP2 (this work) and Dome Fuji (Kawamura, personal communication).

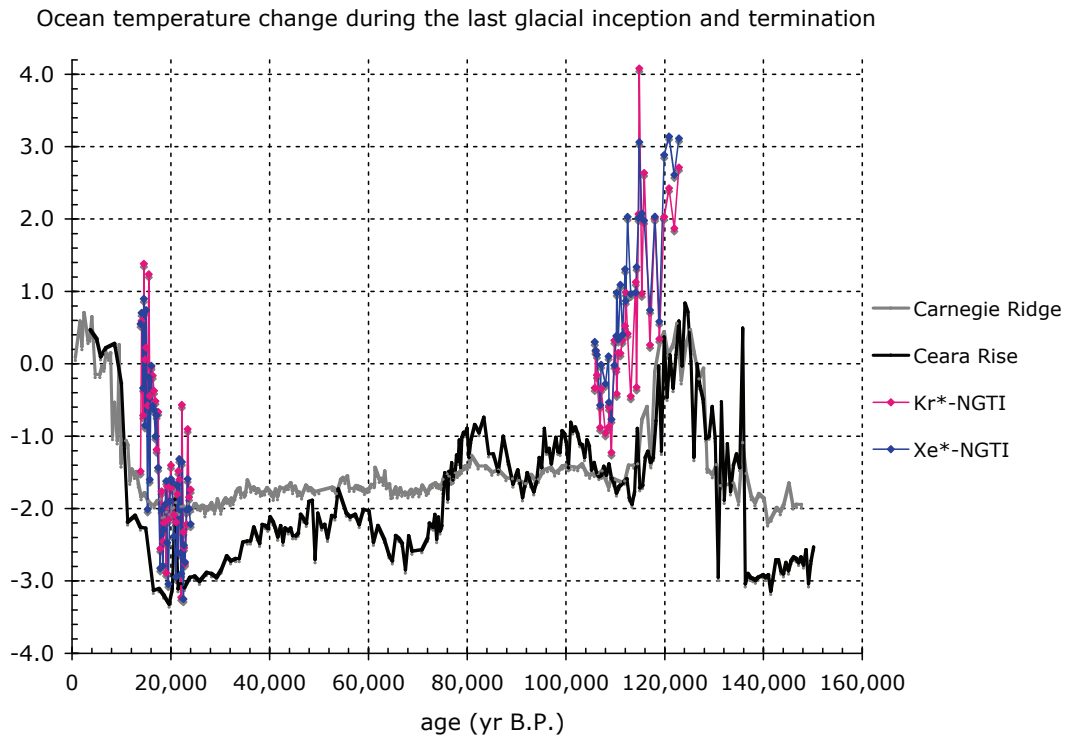

Figure 3.30. Kr*- and Xe*-based Noble Gas Temperature Indices (NGTI's) (in pink and blue, respectively) and the Cutler et al. (2003) deep ocean temperature reconstructions (deep Atlantic: Ceara Rise in black, deep Pacific: Carnegie Ridge in gray).

(a)

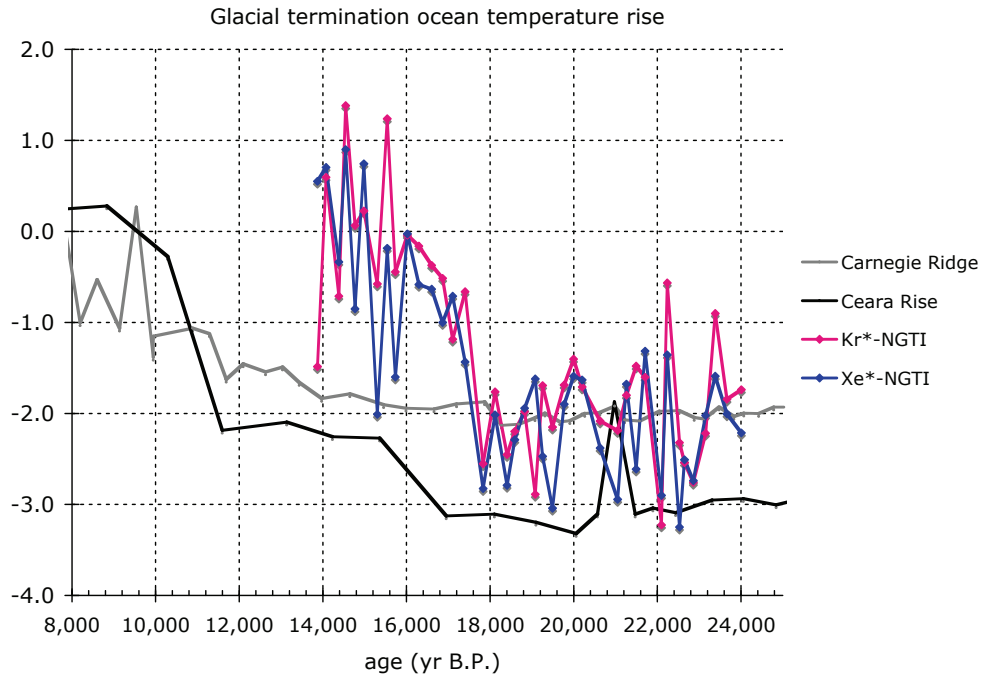

(b)

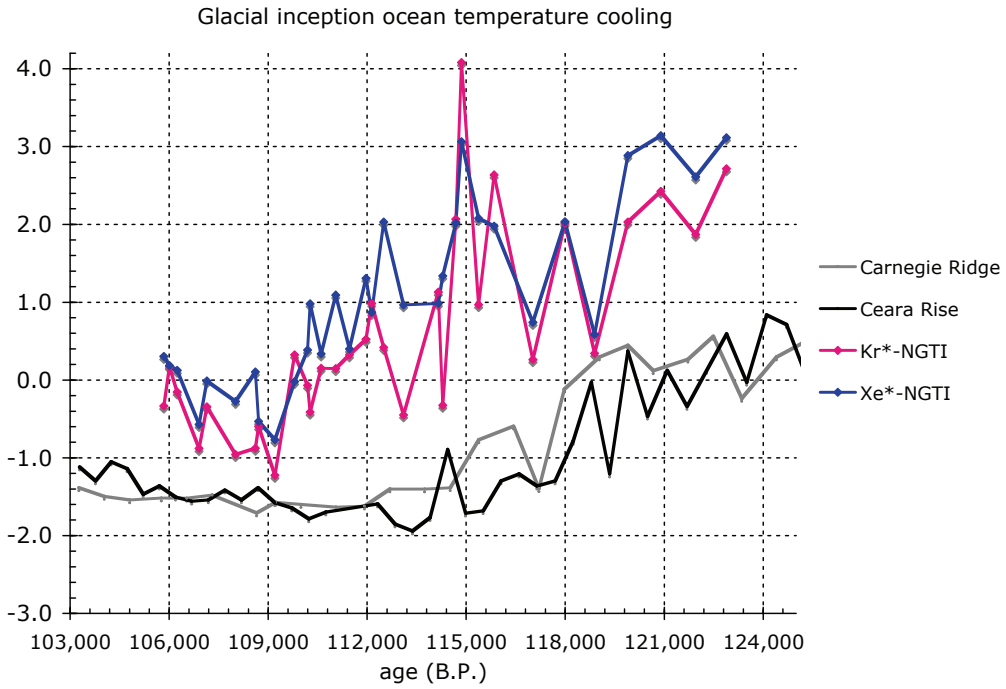

Figure 3.31. Comparison between Kr*- (pink) and Xe*- (blue) based Noble Gas Temperature Indices (NGTI's) and Cutler et al. (2003) deep Atlantic (Ceara Rise, black) and deep Pacific (Carnegie Ridge, gray) during the glacial termination (a) and glacial inception (b).

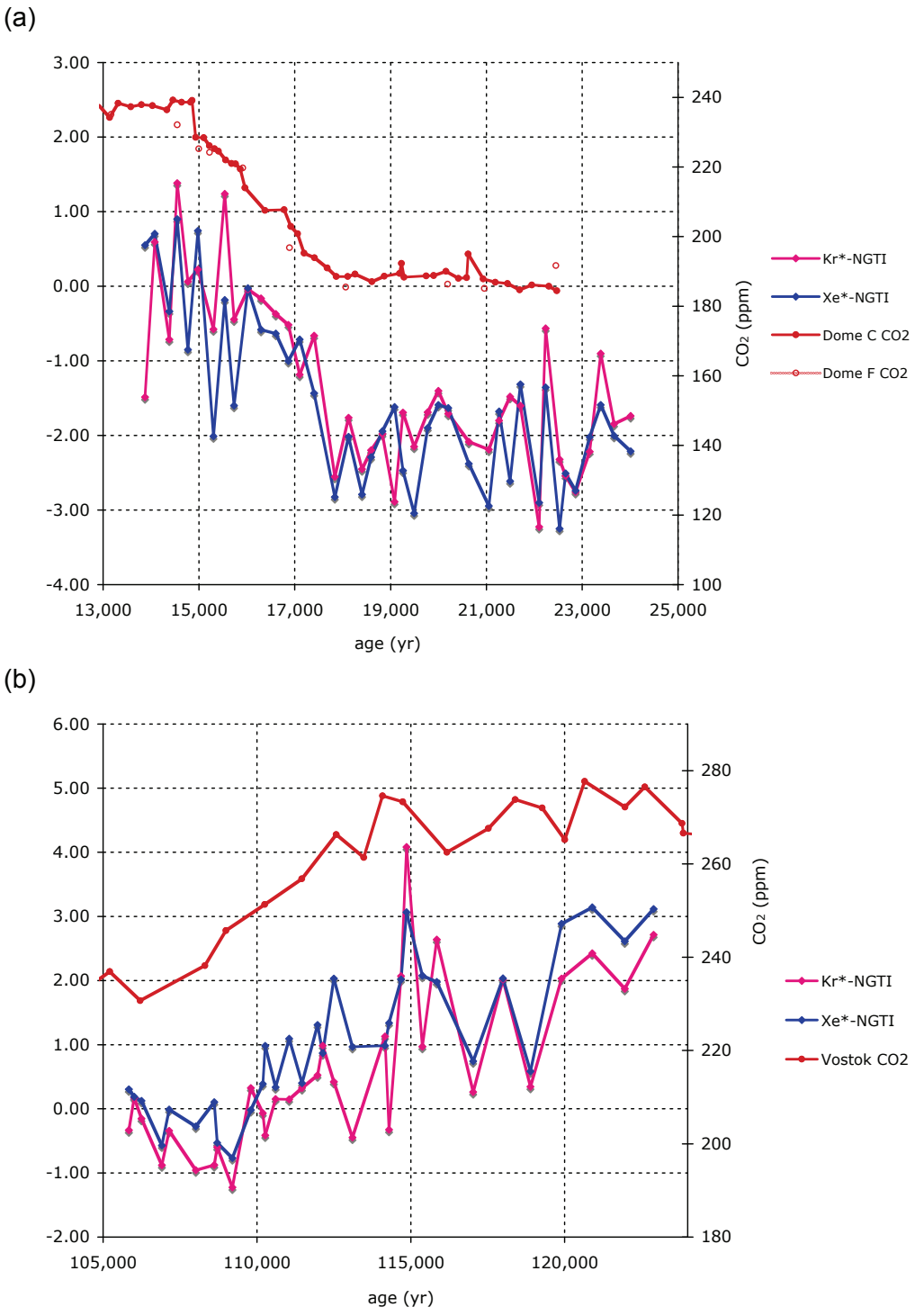

Figure 3.32. Relationship between Kr*-, Xe*-NGTI and CO_2 during (a) the last glacial termination (24-18 kyr B.P.) (CO_2 from Monnin et al., 2001, Kawamura et al., 2007) and (b) the last glacial inception (~123-105 kyr B.P.) (CO_2 from Petit et al., 1999).

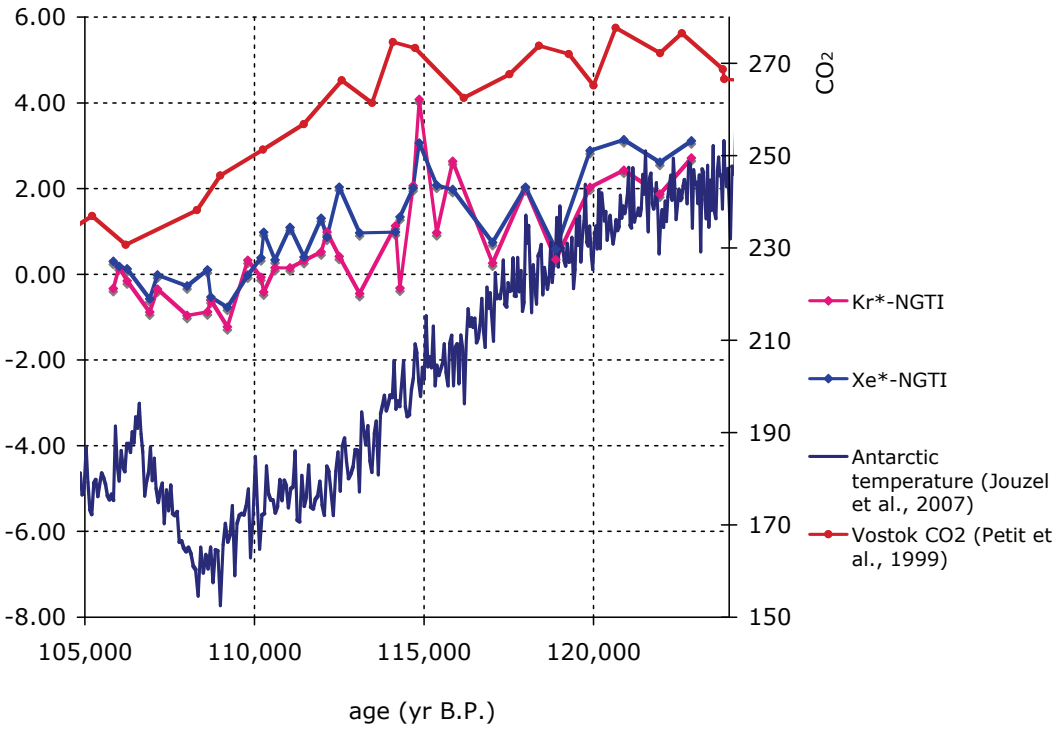

Figure 3.33. Kr*- and Xe*-derived NGTI's, Antarctic temperature (Jouzel et al., 2007), and Vostok CO_2 (Petit et al., 1999) during the glacial inception (123-105 kyr B.P.).

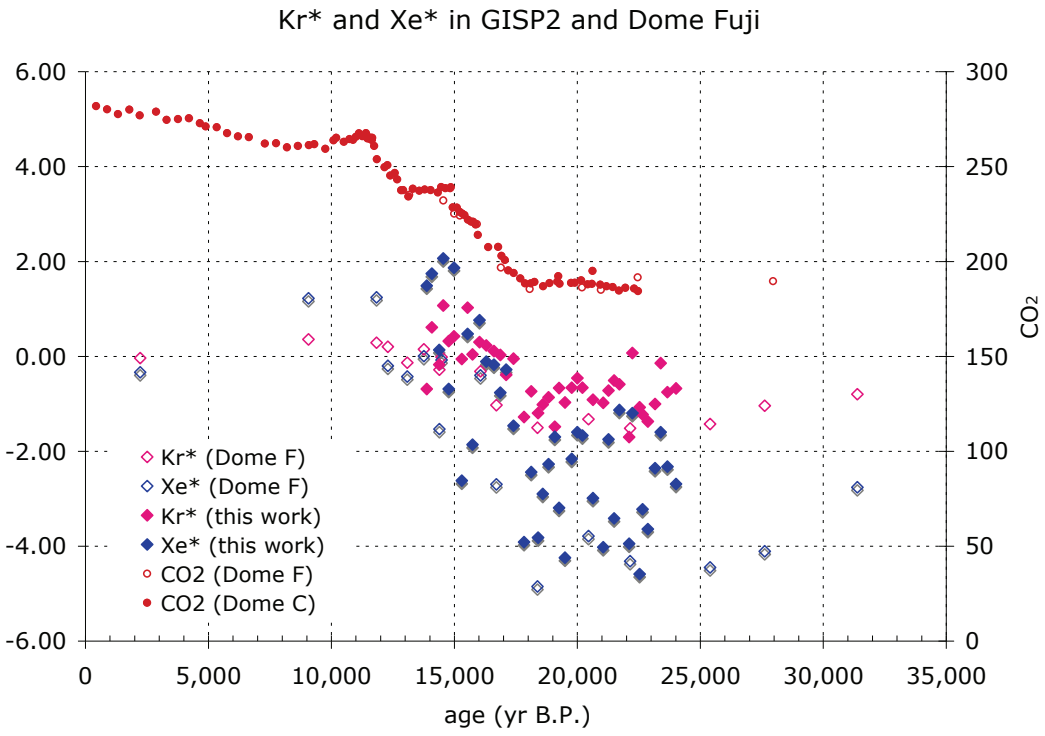

Figure 3.34. Kr* and Xe* (solid points: GISP2, this work, hollow points: Dome Fuji, Kawamura, personal communication), and CO_2 (Dome Fuji: Kawamura et al., 2007, Dome C: Monnin et al., 2001) from ~30 kyr B.P to the present.

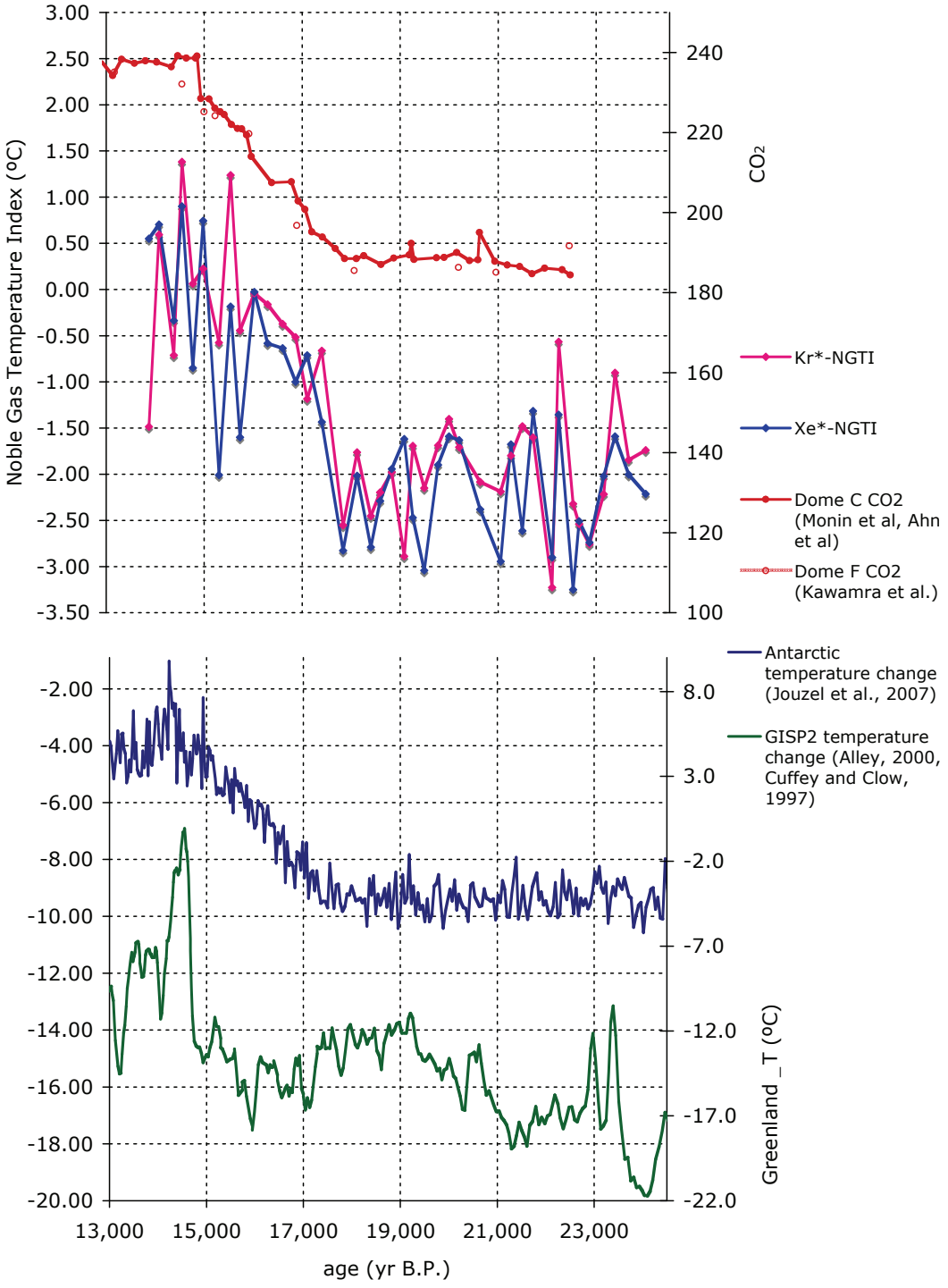

Figure 3.35. From top to bottom: Dome C (Monnin et al., 2001) and Dome F (Kawamura et al., 2007) CO_2 in red, Kr*- and Xe*-derived NGTI (pink and blue, respectively), Antarctic temperature (Jouzel et al., 2007) in blue, and Greenland GISP2 temperature (Alley, 2000, Cuffey and Clow, 1997) in green.

Chapter 4

Kr/Ar and Xe/Ar: indicators of melt layers in ice cores

Abstract

Melt layers are visible in bubbly glacial ice because of their relative dearth of air bubbles, and melt layer frequency has been used as a paleoclimatic indicator of summer temperature. We have measured Kr/Ar and Xe/Ar ratios in visible melt layers in late Holocene ice from the Dye 3 ice core in Greenland. We find that these gas ratios are elevated and distinctly different in melt layers as compared to ice that has not melted and refrozen. Theory predicts that ice should become enriched in Kr and Xe when it equilibrates with the atmosphere as meltwater, and then subsequently refreezes, because Kr and Xe are highly soluble gases in liquid water compared to Ar. Furthermore, the slope of the melt-layer δXe/Ar data vs. δKr/Ar data is approximately double that of non-melted ice, as expected from theory. We have modeled the effects of melt, in addition to gravitational settling and gas loss, on δKr/Ar and δXe/Ar measured in ice. Because of their unique signature in melt layers, δKr/Ar and δXe/Ar measurements in ice cores may be valuable tools for investigating past summer temperatures and changes in seasonality in deep ice cores where bubbles have become clathrates and thus no longer permit visual melt-layer identification. These gases may also aid in the identification of dispersed refrozen melt in bubbly ice where organized melt layers are indistinct or absent, as well as refrozen melt from subglacial water systems.

Introduction

Melt layers in ice sheets typically form during exceptionally warm conditions. Records of melt layers in ice cores can therefore give insight into changes in

seasonality, recording the frequency of anomalously warm summers. Understanding past changes in seasonality may help to explain how and why climate may have changed through time. Recent studies have suggested that changes in seasonality may have played a role in climate change during the last glacial period (Denton et al., 2005, Schaefer et al., 2006).

Melt layers form when air reaches a threshold temperature, causing firn (the porous layer of snow on top of polar ice sheets) at the surface to melt (Zwally and Fiegles, 1994). Das and Alley (2005) have found that observable melt layers in the ice stratigraphy occur when the surface temperatures are 1°C or higher, integrated over a day. When melt water forms at the surface, it percolates down into the firn and settles along thin near-surface crusts (Das and Alley, 2005, Langway and Shoji, 1990, Pfeffer and Humphrey, 1998), subsequently refreezing into a melt layer when air temperatures cool. These crusts do not appear to be limiting factors in the formation of melt layers, as crusts are commonly found in both Greenland and Antarctica (Pfeffer and Humphrey, 1998, Das and Alley, 2005), and can also be found in low-latitude ice cores (Hardy et al., 1998, Stichler et al., 2001).

Melt layers appear in ice cores as horizontal bands of ice with few air bubbles (Das and Alley, 2005). The air bubbles in melt layers tend to be elongated (Alley and Anandakrishnan, 1995). Melt layers are typically 1mm to 100mm thick in Greenland sites (Langway and Shoji, 1990), and thinner (a few mm thick) at sites on the West Antarctic ice sheet (Das and Alley, 2005). Melt layer analyses to date have been limited to these visible melt layers in bubbly ice.

The appearance of melt layers in ice cores has been used to understand past climate. Frequency of melt layers can be used as a climate proxy to estimate summer temperatures (Zwally and Fiegles, 1994; Alley and Anandakrishnan, 1995). The frequency and/or thickness of melt layers in ice cores have been used to investigate summer climate in Greenland (Herron et al., 1981, Langway and Shoji, 1990, Alley and Anadakrishnan, 1995, Kameda et al., 1995, and Rowe et al., 1995), the Agassiz Ice Cap (Koerner and Fisher, 1990), the Devon Ice Cap (Koerner, 1977), and the West Antarctic Ice Sheet (Das, 2003). A time series of melt layer frequency in the Siple Dome ice core has been analyzed through the Holocene, showing an increase in frequency during the last 6600 years (Das and Alley, 2008). Studies have correlated melt layers at different ice core sites (Alley et al., 1997, Kameda et al., 1995), indicating that melt layers may not be limited to local conditions at the ice core site. Rather, they may reflect larger-scale, regional climate conditions. Satellite imaging of recent melt events that extended over much of West Antarctica (Shuman and Stearns, 2001) support this view.

The investigations described above have been limited to visible melt layers. As we explore further back in time using deeper ice, melt layers are harder to identify due to thinning of the layers with depth and air clathrate formation. Air clathrates form when the pressure is sufficient to change the air bubble within the ice into a solid phase, in which the air is surrounded by water molecules, forming a lattice (Miller, 1969). These clathrates are stable at depths at which the pressure is equal to or greater than the dissociation pressure of the air clathrate (~800-1200m) (Miller, 1969). At depths below ~1200m, where the air bubbles have completely changed to air

clathrates, ice appears to be clear and bubble-free, thus precluding visual identification of melt layers.

We have measured Kr/Ar and Xe/Ar ratios in visible melt layers in shallow ice from the Dye 3 ice core in Greenland. These ratios have a distinct signature in melt layers, as compared to ice that has not melted and refrozen. Krypton and xenon are highly soluble in liquid water, and they are more soluble than argon (Figure 4.1). Therefore, Kr/Ar and Xe/Ar ratios are higher in melted and refrozen ice than in air bubbles in ice that has not melted. We show that these noble gas ratios may be used as additional, independent indicators of melt layers in ice cores.

In addition to investigating past changes in seasonality and summer temperatures, melt layer identification in ice cores may prove to be valuable in other types of ice core analyses. Melt layers have been shown to affect other gases measured in ice cores, in addition to the noble gases discussed in this study. For instance, CO_2 measurements are affected by the presence of melt layers (Neftel et al, 1983, Ahn et al., in press). In the Siple Dome ice core, elevated levels of CO_2, Kr/Ar, and Xe/Ar were measured in visible melt layers (Ahn et al., in press). Kr/Ar and Xe/Ar measurements may therefore also provide constraints on the extent of melt that may affect other ice core measurements.

Methods

The ice core samples analyzed in this study were from the Holocene, taken from the Dye 3 and GISP2 ice cores in Greenland. Dye 3 samples were from 115m-, and 143 – 145m-depth, while GISP2 samples were taken from 147 m-, 555 m-, and

637-m-depths. Dye 3 samples from 115 m- and 144 m-depths contained visible melt layers, identified as horizontal bands of ice with few air bubbles, a few mm to a few cm thick (Langway and Shoji, 1990, Alley and Anandakrishnan, 1995, Das and Alley, 2005). The remaining ice samples did not contain visible melt layers, and we refer to them as non-melted ice.

The ice core Kr/Ar and Xe/Ar are measured following the technique outlined by Sowers et al. (1989), Severinghaus et al. (2003), and Headly and Severinghaus (2007). Ice samples are typically 50-60 grams each, measured in duplicate or triplicate for a given depth. The samples are cut using a band saw in a walk-in freezer, kept at –25°C. The ice core sample and two stir bars are placed in a chilled glass vessel. The vessel is then attached to a vacuum line. The ambient air is pumped out of the vessel for 40 minutes, while the sample is kept cold by an ethanol bath around the vessel at –20°C. After 40 minutes, the vessel is sealed from the vacuum line, and the ice is allowed to melt. The air released from the air bubbles in the ice is then transferred through a water trap to a dip tube at 4K. During transfer to the dip tube, the meltwater is agitated by two stir bars to ensure full degassing of the Kr and Xe, which are highly soluble. The gas sample is then gettered to remove the N_2, O_2, and other reactive gases. Gettering is a process in which the sample gas is exposed to Zr/Al sheets at 900˚C. After gettering is complete, the sample is transferred into a dip tube at 4K. Approximately 10 times the sample pressure of ultrahigh purity N_2 is subsequently transferred into the dip tube in order to add bulk to the sample for mass spectrometry. The sample is then analyzed on a Finnigan MAT 252 mass spectrometer to determine the $\delta^{40}Ar/^{36}Ar$, $\delta^{84}Kr/^{36}Ar$, and $\delta^{132}Xe/^{36}Ar$ (hereafter,

δ^{40}Ar, δKr/Ar, and δXe/Ar). Isotopes are measured in dual-collector mode, and elemental ratios are measured by peak-jumping. Results are expressed in delta (δ) notation:

$$\delta \mathrm{Kr/Ar} = \left(\frac{\mathrm{Kr/Ar}_{\mathrm{sample}}}{\mathrm{Kr/Ar}_{\mathrm{standard}}} - 1 \right) \times 1000 \qquad (4.1)$$

The standard used in these measurements is air collected from the Scripps pier in La Jolla, CA. The method used to collect the air is described in Headly and Severinghaus (2007), following that of Severinghaus et al. (2003).

The measured δ^{40}Ar, δKr/Ar, and δXe/Ar are first corrected for any pressure imbalance between the sample and standard gases in the mass spectrometer, following Severinghaus et al. (2003) and Headly and Severinghaus (2007). The pressure-corrected δ^{40}Ar values are then corrected for differences in nitrogen abundance between sample and standard gases. This correction is needed because of ion-molecule reactions in the mass spectrometer source, and is known as a "chemical slope" correction (Severinghaus, et al., 2003, Headly and Severinghaus, 2007).

Results

The δKr/Ar and δXe/Ar measured in Holocene ice from the Dye 3 and GISP2 ice cores are shown in Tables 4.1 and 4.2. In the Dye 3 data, where both melt layers and non-melted samples are found in the same ice core, at similar depths, a comparison between melt layers and non-melted ice is possible. The Dye 3 raw data

are plotted in Figure 4.2. The data show different trends or signatures in melted versus non-melted ice. The δKr/Ar and δXe/Ar in melt layers are clearly enriched, as compared to non-melted ice. The melt layer values (all from Dye 3) range from ~23‰ to 63‰ for δKr/Ar, and 46‰ to 170‰ for δXe/Ar. Non-melted ice from Dye 3, in contrast, had δKr/Ar values of 11.00‰ ± 0.49‰, and δXe/Ar of 22.58‰ ± 1.16‰. Errors are reported as standard error, calculated by dividing the standard deviation of the dataset by the square root of the number of samples, n (in this case, n = 10).

The measured air content in ice samples should also contain information about the abundance of refrozen melt, due to the displacement of air in the pores in the firn by liquid water. For practical reasons, we report relative air content (relative to the mass of ice in each sample, equation 4.2) rather than absolute air content. Plotted in Figures 4.3(a) and 4.3(b) are δKr/Ar and δXe/Ar versus relative air content in Dye 3 and GISP2 samples. We calculate relative air content as follows:

$$\text{Relative air content} = \left(\text{gas pressure of sample} / \text{mass of ice in sample}\right) \times 1000 \qquad (4.2)$$

The gas pressure of the sample used in (4.2) is the pressure measured in the vacuum line after gettering, and the mass of the ice sample in (4.2) is measured by weighing the melted ice after the gas extraction. Figure 4.3 shows that δKr/Ar and δXe/Ar appear to correlate inversely with relative air content, with higher values of Kr and Xe at lower relative air content. Melt layers tend to have fewer air bubbles than non-

melted ice (Das and Alley, 2005, Alley and Anandakrishnan, 1995), so it follows that the relative air content of melt layers should be lower than non-melted ice. One point lies off the trend in Figures 4.3(a) and 4.3(b), which may suggest that relative air content is not always directly indicative of melt extent in an ice core sample.

Another observation from the data is that the slope of δXe/Ar vs. δKr/Ar in melt layers is distinctly different than that of non-melted ice. In ice sampled from melt layers, the δXe/Ar vs. δKr/Ar slope is 3.01, while non-melted ice samples have a slope of 1.77 (Figure 4.4). The value of ~3 is close to that predicted from theory for gases at solubility equilibrium (not including any air bubbles or gases affected by any other processes such as gravitational fractionation), and arises from the fact that Xe is ~4 times, and Kr ~2 times, as soluble as Ar (Wood and Caputi, 1966, Weiss and Kyser, 1978, Weiss, 1970). In concept, this relationship may be seen using the Ar solubility S_{Ar}:

$$\delta \mathrm{Xe/Ar} \equiv \left(\frac{\frac{\mathrm{Xe}}{\mathrm{Ar}}_{aq}}{\frac{\mathrm{Xe}}{\mathrm{Ar}}_{air}} - 1 \right) 1000 \cong \left(\frac{\frac{4S_{\mathrm{Ar}}}{S_{\mathrm{Ar}}} \frac{\mathrm{Xe}}{\mathrm{Ar}}_{air}}{\frac{\mathrm{Xe}}{\mathrm{Ar}}_{air}} - 1 \right) 1000 = 3000‰ \qquad (4.3)$$

$$\delta \mathrm{Kr/Ar} \equiv \left(\frac{\frac{\mathrm{Kr}}{\mathrm{Ar}}_{aq}}{\frac{\mathrm{Kr}}{\mathrm{Ar}}_{air}} - 1 \right) 1000 \cong \left(\frac{\frac{2S_{\mathrm{Ar}}}{S_{\mathrm{Ar}}} \frac{\mathrm{Kr}}{\mathrm{Ar}}_{air}}{\frac{\mathrm{Kr}}{\mathrm{Ar}}_{air}} - 1 \right) 1000 = 1000‰ \qquad (4.4)$$

Therefore, it appears that not only are melt layers enriched in Kr/Ar and Xe/Ar in comparison to non-melted ice, but melt layers also show a unique relationship between δKr/Ar and δXe/Ar.

In non-melted ice, measured Kr/Ar and Xe/Ar are primarily affected by gravitational fractionation. Gravitational fractionation is a process in which heavier isotopes of gases settle farther than the lighter isotopes down into the firn. Gravitational fractionation varies according to mass difference (Craig et al., 1988, equation (4.5)), so δXe/Ar (mass difference of 96) would be twice as affected by gravitational fractionation than δKr/Ar (mass difference of 48). According to Craig et al. (1988), gravitational fractionation is described by the barometric equation modified for a gas pair:

$$R/R_o = \mathrm{e}^{gz\Delta m/RT} \qquad (4.5)$$

where R is the isotope or gas ratio measured, R_o is the same ratio in the free atmosphere, g is the local gravitational acceleration, z is the thickness of the firn, Δm is the mass difference between the two isotopes, R' is the gas constant, and T is the isothermal temperature of the column.

Based on equation (4.5), we expect a δXe/Ar vs. δKr/Ar slope of 2 in non-melted ice. The δKr/Ar and δXe/Ar data from non-melted ice from both Dye 3 and GISP2 reflect this expected relationship, with a slope near 2 (m = 1.77) (Figure 4.4). Our data may show a slope less than 2 due to an incomplete extraction of Xe. Overall,

δKr/Ar and δXe/Ar in melt layers have a distinctly different signature from that of non-melted ice. We investigate the causes of these observations in a melt layer model described in the following section.

Another factor affecting our data is gas loss during air bubble close-off, as well as during ice core storage. Severinghaus and Battle (2006) have studied gas loss during air bubble close-off as ice forms, finding that size-dependent fractionation occurs during this process. They have found that a threshold size exists, in which gas molecules with molecular diameters smaller than N_2 (including Ar), are found to leak out of air bubbles after they form in ice. Kr and Xe, with larger molecular diameters, remain intact in the air bubbles (Severinghaus and Battle, 2006). Bender et al. (1995) have found a similar type of size-dependent fractionation due to gas loss during ice core storage, which they refer to as configurational fractionation. As in the subsequent study by Severinghaus and Battle (2006), Bender and others found a size dependence in configurational fractionation, noting that molecules smaller than N_2 are depleted in ice cores. Both types of gas loss fractionation discussed here would cause air bubbles to be depleted in Ar, due to preferential loss of the smaller Ar gas molecule. This would cause both δKr/Ar and δXe/Ar to be enriched equally due to Ar gas loss.

Modeling a melt layer

In order to understand and quantify the processes affecting our melt layer measurements, we have modeled the effects of the formation of melt layers, as well as gravitational settling and gas loss, on measured δKr/Ar, δXe/Ar, and $\delta^{40}Ar/^{36}Ar$. For simplicity, this model assumes that all the dissolved gas is retained during the

refreezing process. We recognize that this assumption is probably not always valid, but currently we lack any means to quantify the fraction of retained gas. Thus this model should be regarded as a first step, to be improved by future work. Using this model, we are able to invert the three measured parameters (δKr/Ar, δXe/Ar, and $\delta^{40}Ar/^{36}Ar$) for the volume ratio of refrozen liquid water to bubble air at ambient pressure (γ), the amount of gravitational fractionation (expressed as firn diffusive column depth (z)), and the amount of gas loss (F).

We assume the ^{36}Ar, ^{40}Ar, Kr, and Xe in air measured in an ice core sample are affected solely by gravitational fractionation, melt, and gas loss as follows (units are in moles of gas):

$$^{36}Ar_{sample} = {}^{36}Ar_{air\ bubble} + {}^{36}Ar_{dissolve} - {}^{36}Ar_{loss} \qquad (4.6)$$

$$^{40}Ar_{sample} = {}^{40}Ar_{air\ bubble} + {}^{40}Air_{dissolve} - 0.993\left({}^{36}Ar_{loss}\right) \qquad (4.7)$$

$$Kr_{sample} = Kr_{air\ bubble} + Kr_{dissolve} \qquad (4.8)$$

$$Xe_{sample} = Xe_{air\ bubble} + Xe_{dissolve} \qquad (4.9)$$

The "air bubble" terms (e.g. $Kr_{air\ bubble}$) in equations (4.6)-(4.9) represent the abundance of each gas in the air bubble within the ice core. The abundance in the air bubbles reflects both the atmospheric abundance at the time the air bubble formed in the ice, as well as the effect of gravitational fractionation on the gases in the air bubble. The "dissolve" terms reflect the enrichment of these gases due to the presence of melt layers, and thus take into account the solubility of each gas. The $^{36}Ar_{loss}$ term

represents Ar loss due to gas loss from the ice core. Gas loss typically causes $\delta^{40}Ar/^{36}Ar$ in the air that remains in an air bubble to be positively enriched by 0.007‰ per 1‰ δKr/Ar enrichment (Severinghaus et al., 2003). Therefore, ^{40}Ar is slightly less depleted by gas loss than ^{36}Ar (^{40}Ar lost = 0.993(^{36}Ar lost)).

The estimated gas content dissolved in a melt layer (e.g. $Kr_{dissolve}$) assumes that the liquid melt layer is saturated with air at 0˚C and at equilibrium with the atmosphere. As mentioned above, we assume that all gases are retained when the melt layer refreezes. We recognize that this assumption may not be completely valid. Some of the gases may escape during refreezing through diffusion, which may affect each gas differently depending on their diffusion coefficients (Stauffer et al., 1985). Ar has the highest diffusion coefficient in 0ºC water (1.2×10^{-9} m^2s^{-1} (Jähne et al., 1987)), followed by Kr (0.88×10^{-9} m^2s^{-1}) and Xe (0.66×10^{-9} m^2s^{-1}) (Wise and Houghton, 1966). The extent of gas loss during refreezing is primarily dependent on the speed of refreezing (Stauffer et al., 1985).

By using the equations (4.6)-(4.9), as well as the ideal gas law $(pV = nRT)$ and the barometric equation $\left(p = p_o e^{mgz/RT}\right)$, we derive the following system of equations, which can be solved for the firn diffusive column depth (z), fraction of Ar lost due to gas loss (F), and the volume ratio of refrozen liquid water to bubble air at ambient pressure (γ) (all variables are defined in Table 4.3).

$$\left(\frac{\delta^{40}\mathrm{Ar}/^{36}\mathrm{Ar}}{1000}+1\right)_{\text{measured}} = \frac{(1-0.993F)e^{m_{40}gz/RT}/RT + S_{40}\gamma}{(1-F)e^{m_{36}gz/RT}/RT + S_{36}\gamma} \qquad (4.10)$$

$$\left(\frac{\delta \mathrm{Kr}/\mathrm{Ar}}{1000}+1\right)_{\text{measured}} = \frac{\mathrm{e}^{m_{\mathrm{Kr}} gz/RT}/RT + S_{\mathrm{Kr}}\gamma}{(1-F)\mathrm{e}^{m_{36} gz/RT}/RT + S_{36}\gamma} \qquad (4.11)$$

$$\left(\frac{\delta \mathrm{Xe}/\mathrm{Ar}}{1000}+1\right)_{\text{measured}} = \frac{\mathrm{e}^{m_{\mathrm{Xe}} gz/RT}/RT + S_{\mathrm{Xe}}\gamma}{(1-\mathrm{F})\mathrm{e}^{m_{36} gz/RT}/RT + S_{36}\gamma} \qquad (4.12)$$

To solve the system of equations above, we calculate γ, F, and z by iteration using a bisection method (Burden and Faires, 2001). The results from six different melt layer samples from shallow ice from the Dye 3 ice core are shown in Table 4.4. The calculated firn depth, z ~46-49m, agrees with known firn depth at Dye 3 (~50m), so it appears that the model accurately describes the processes that affect gases in a melt layer.

The calculated fraction of ^{36}Ar lost is consistent in all replicates at both depths. F = 0.008 ± 0.002 in Dye 3 samples at 144.20m-depth and F = 0.009 ± 0.002 in those at 144.47m-depth. These results suggest that gas loss may be a fairly constant process at a particular site and depth, and thus may be unaffected by the extent of melt, indicated by γ.

The model results for γ, the volume ratio of refrozen melt water to bubble air, show that the extent of melt is not a spatially uniform parameter in an ice core sample. Rather, there is much variability between replicates at the same depth, as shown by the γ values calculated for two replicates at 144.47m-depth (γ = 0.25 and 0.83 in replicates a and b, respectively). This variability in the amount of refrozen meltwater may help

to explain why a sample at one depth may have very different values of δKr/Ar and δXe/Ar among its replicates (e.g. Dye 3 144.47m).

Discussion

The presence of melt layers in an ice core indicates anomalously warm summer temperatures. Knowing frequency of warm summers through time may give insight into past climate change. Recent studies (Denton et al., 2005, Schaefer et al., 2006) propose that changes in seasonality may have played a role in past abrupt climate change. Denton et al. (2005) suggest that past shifts in seasonality may explain the mismatch between ice core $\delta^{18}O$ records and snowline changes in Greenland during the Younger-Dryas cold period and other abrupt climate changes during the last glacial period. Changes in snowline are usually more sensitive to ablation-season temperatures than winter precipitation, and therefore may be more closely linked to summer temperatures (Oerlemans, 1994). Denton et al. (2005) suggest that the discrepancy between Greenland moraine records and $\delta^{18}O$ in ice may be due to a strong winter influence on the nominally mean-annual ice core $\delta^{18}O$ record (Denton et al., 2005). The cold winters, Denton et al. argue, could be caused by an expansion of sea ice, which would increase the continentality, and hence, seasonality of Greenland and Europe. Denton et al. (2005) propose that these changes in seasonality during the last glacial period may have amplified and propagated abrupt climate change across the Northern Hemisphere.

Schaefer et al. (2006) studied mid-latitude moraines to identify the timing of warming after the last glacial maximum (LGM). They found that the mid-latitudes in

both hemispheres warmed in synchrony, and that the temperature rise was coincident with the rise of both temperature and CO_2 measured in Antarctic ice cores. They propose that warmer summers may have caused the warming following the LGM throughout the mid-latitudes, illustrated by the glacier retreat in both the northern and southern hemisphere mid-latitudes. Following the conclusions of Denton et al. (2005), they suggest that cold winters in the North Atlantic masked the summer warming signal apparent in paleoclimate records outside of the region.

Because δKr/Ar and δXe/Ar in melt layers have a distinct signature (Figures 4.2-4.4), they have the potential to serve as proxies for melt layers, which in turn indicate warm summer temperatures. δKr/Ar and δXe/Ar could therefore be used to identify changes in seasonality, and perhaps constrain climate change hypotheses invoking seasonality (Denton et al., 2005, Shaefer et al., 2006). Using chemical proxies for melt allows for the identification of melt layers in deeper ice when it is no longer possible to visually identify them due to air clathrate formation. This capability to identify melt layers in deeper ice may allow us to investigate the role of seasonality in climate changes further back in time. Das and Alley (2008) have investigated visible melt layer frequency over the Holocene, but there is no record of melt before the Holocene. Using δKr/Ar and δXe/Ar would allow for investigation of melt layer frequency in the ice core record prior to the Holocene. At a relatively warm site such as Dye 3 or Renland, melt layer frequency may serve as an indicator of summer temperature in the early phase of the last deglaciation. δKr/Ar and δXe/Ar could therefore give us insight into the role seasonality may have played in the termination

of the last glacial period, Dansgaard-Oeschger events throughout the last glacial period, and other intriguing climate transitions preceding the Holocene.

We have shown that melt layers can cause elevated Kr and Xe levels in ice cores. Previous studies have found that CO_2, a soluble gas like Kr and Xe, is enriched in melt layers in both Greenland (Neftel et al., 1983, Stauffer et al., 1985) and Antarctica (Ahn et al., in press). Ahn et al. have used Kr/Ar and Xe/Ar measurements in melt layers to constrain the effect of melt on CO_2 concentrations measured in the Siple Dome ice core in Antarctica. Kr/Ar and Xe/Ar can therefore also help to constrain the extent of melt layers that could affect other measured parameters in ice cores.

Finally, bubble-free bands of ice are commonly seen in the margin ice of the Greenland ice sheet, and appear blue in color, and thus are commonly termed "blue bands" (Petrenko et al., 2006). We have measured several samples of "blue band" ice for Kr and Xe, along with the host ice immediately surrounding the blue bands. The δKr/Ar and δXe/Ar in these samples were 423.87‰ ± 0.36‰ and 957.38‰ ± 0.09‰, respectively, displaying a clear solubility signature. In contrast, the δKr/Ar and δXe/Ar in the host ice was 27.82‰ ± 3.81‰ and 52.03‰ ± 11.38‰, respectively. Thus the bubble-free bands appear to have equilibrated with air in a liquid state prior to freezing. This evidence is consistent with the hypothesis that blue bands represent refrozen subglacial meltwater injected into cracks in the ice (Petrenko et al., 2006). These measurements demonstrate the possible utility of noble gas measurements in revealing the genesis of these enigmatic features.

Conclusions

We have demonstrated the potential for δKr/Ar and δXe/Ar to be used to identify melt layers in ice cores. Melt layer frequency is indicative of exceptionally warm summers and changes in seasonality, which may have played a role in past climate change. Using δKr/Ar and δXe/Ar to identify melt layers in ice cores will extend the current record of melt layer frequency, and may also help to constrain current theories about the role seasonality may have played in climate transitions during the last glacial termination.

References

Ahn, J., M.A. Headly, M. Wahlen, E.J. Brook, P.A. Mayewski, and K.C. Taylor, CO_2 diffusion in polar ice: observations from the Siple Dome ice core, Antarctica, *Journal of Glaciology*, *in press*.

Alley, Richard B., and Sridhar Anandakrishnan (1995), Variations in Melt-layer Frequency in the GISP2 Ice Core: Implications for Holocene Summer Temperatures in Central Greenland, *Annals of Glaciology*, *21*, 64-70.

Alley, Richard B., Matthew K. Spencer, and Donald E. Voigt (1997), Visible examination of Siple Dome, West Antarctica, shallow cores, *Antarctic Journal – Review*, 44-45.

Bender, M., T. Sowers, and V. Lipenkov (1995), On Concentrations of O_2, N_2, and Ar in Trapped Gases from Ice Cores, *Journal of Geophysical Research*, *100*, 18,651-18,660.

Burden, Richard L., J. Douglas Faires (2001), *Numerical analysis*, 7th ed., Pacific Grove, CA: Brook/Cole-Thomson Learning.

Das, Sarah B. (2003), West Antarctic Ice Sheet Surface Melting and Holocene Climate Variability, PhD dissertation, The Pennsylvania State University.

Das, Sarah B. and Richard B. Alley (2005), Characterization and formation of melt layers in polar snow: observations and experiments from West Antarctica*, Journal of Glaciology*, *51*(173), 307-312.

Das, S.B. and R. B. Alley (2008), Rise in frequency of surface melting at Siple Dome through the Holocene: Evidence for increasing marine influence on the climate of West Antarctica, *J. Geophys. Res., 113*, D02112, doi:10.1029/2007JD008790.

Denton, George H., Richard B. Alley, Gary C. Comer, Wallace S. Broecker (2005), The Role for Seasonality in Abrupt Climate Change, *Quaternary Science Reviews*, *24*, 1159-1182.

Hardy, D.R., M. Vuille, C. Braun, F. Keimig, R.S. Bradley (1998), Annual and Daily Meteorological Cycles at High Altitude on a Tropical Mountain, *Bulletin of the American Meteorological Society, 79*(9), 1899-1913.

Headly, M. A. and J. P. Severinghaus, A Method to Measure Kr/N_2 Ratios in Air Bubbles Trapped in Ice Cores, and its Application in Reconstructing Past Mean Ocean Temperature*, Journal of Geophysical Research*, *112*, D19105, doi:10.1029/2006JD008317, 2007.

Herron, Michael M., Susan L. Herron, Chester C. Langway, Jr. (1981), Climatic Signal of Ice Melt Features in Southern Greenland, *Nature*, *293*, 389-391.

Jähne, B., G. Heinz, and W. Deitrich (1987), Measurement of the Diffusion Coefficient of Sparingly Soluble Gases in Water, *J. Geophys. Res.*, *92*, 10767-10776.

Kameda, T., H. Narita, H. Shoji, F. Nishio, Y. Fujii, and O. Wanatabe (1995), Melt Features in Ice Cores from Site J, Southern Greenland: Some Implications for Summer Climate Since AD 1550, *Annals of Glaciology*, *21*, 51-58.

Koerner, R. M. (1977), Devon Island Ice Cap: Core Stratigraphy and Paleoclimate, *Science*, *196*(4285), 15-18.

Koerner, R. M., and D.A. Fisher (1990), A Record of Holocene Summer Climate from a Canadian High-Arctic Ice Core, *Nature*, *343*, 630-631.

Langway, Chester C., Jr., and Hitoshi Shoji (1990), Past Temperature Record from the Analysis of Melt Features in the Dye 3, Greenland, Ice Core, *Annals of Glaciology*, *14*, 343-344.

Miller, Stanley L. (1969), Clathrate Hydrates of Air in Antarctic Ice, *Science*, *165*(3892), 489-490.

Oerlemans, J. (1994), Quantifying global warming from the retreat of glaciers, *Science*, *264*, 243-245.

Petrenko, V.V., J.P. Severinghaus, E.J. Brook, N. Reeh, H. Shaefer (2006), Gas records from the west Greenland ice margin covering the last glacial Termination: A horizontal ice core, *Quaternary Science Reviews*, *25*, 865-875.

Pfeffer, W. T. and N. F. Humphrey (1998), Formation of Ice Layers by Infiltration and Refreezing of Meltwater, *Annals of Glaciology*, *26*, 83-91.

Rowe, Clinton M., Mark R. Anderson, Thomas L. Mote, Karl C. Kuivinen (1995), Indications of Melt in Near-Surface Ice-Core Stratigraphy: Comparisons with Passive-Microwave Melt Signals over the Greenland Ice Sheet, *Annals of Glaciology*, *21*, 59-63.

Schaefer, J. M., G. H. Denton, D. J. A. Barrell, S. Ivy-Ochs, P. W. Kubik, B. G. Andersen, F. M. Phillips, T. V. Lowell, and C. Schlüchter (2006), Near-Synchronous Interhemispheric Termination of the Last Glacial Maximum in Mid-Latitudes, *Science*, *312*, 1510-1513.

Severinghaus, J. P, and M. Battle (2006), Fractionation of gases in polar ice during bubble close-off: new constraints from firn air Ne, Kr, and Xe observations, *Earth and Planetary Science Letters*, *244*, 474-500.

Severinghaus, Jeffrey P., Alexi Grachev, Boaz Luz, Nicolas Caillon (2003), A Method for Precise Measurements of Argon 40/36 and Krypton/Argon Ratios in Trapped Air in Polar Ice with Applications to Past Firn Thickness and Abrupt Climate Change in Greenland and Siple Dome, Antarctica, *Geochimica et Cosmochimica Acta*, *67*(3), 325-343.

Severinghaus, J. P., T. Sowers, E. J. Brook, R. B. Alley, M. L. Bender (1998), Timing of abrupt climate change at the end of the Younger Dryas interval from thermally fractionated gases in polar ice, *Science*, *286*, 930-934.

Shuman, C.A. and C.R. Stearns (2001), Decadal-Length Composition Inland West Antarctic Temperature Records, *Journal of Climate*, *14*, 1977-1988.

Stauffer, B., A. Neftel, H. Oeschger, and J. Schwander (1985), CO_2 concentration in air extracted from Greenland ice samples*, Greenland Ice Core: Geophysics, Geochemistry, Environment*, edited by C. C. Langway et al., p. 85-89, AGU, Washington, D.C.

Stichler, W., U. Schotterer, K. Fröhlick, P.Ginot, C. Kull, H. Gäggeler, B. Pouyaud (2001), Influence of sublimation on stable isotope records recovered from high-altitude glaciers in the tropical Andes, *Journal of Geophysical Research*, *106*(D19), 22,613-22,620.

Weiss, R.F. (1970), The solubility of nitrogen, oxygen, and argon in water and seawater, *Deep Sea Res.*, *17*, 721-735.

Weiss, R.F. and T.K. Kyser (1978), Solubility of krypton in water and seawater, *J. Chem Eng. Data*, *23*(1), 69-72.

Wise, D. L. and G. Houghton (1966), The Diffusion Coefficients of Ten Slightly Soluble Gases in Water at 10-60ºC, *Chem. Engineering Sci.*, *21*, 999-1010.

Wood, D. and R. Caputi (1966), Solubilities of Kr and Xe in fresh and seawater, *Tech. rep. USNRDL-TR-988*, U.S. Naval Radiological Defense Laboratory, San Francisco, CA.

Zwally, H. Jay, and Stephen Fiegles (1994), Extent and duration of Antarctic surface melting, *Journal of Glaciology*, *40*(136), 463-476.

Table 4.1. δKr/Ar and δXe/Ar data for Dye 3 ice core samples with visible melt layers from three different depths. Replicates from the same depth are labeled a, b, c, etc. Typical measurement precision (standard deviation) between replicates for δKr/Ar and δXe/Ar in non-melted ice samples is 0.73‰ and 3.48‰, respectively.

Core	Depth (m)	replicate	δKr/Ar (‰)	δXe/Ar (‰)
Dye 3	144.20-144.31	a	30.01	70.72
Dye 3	144.20-144.31	b	49.28	125.49
Dye 3	144.20-144.31	c	38.69	99.09
Dye 3	144.20-144.31	d	49.70	124.70
Dye 3	144.47-144.60	a	31.87	74.32
Dye 3	144.47-144.60	b	63.41	168.55
Dye 3	115.27-115.40	a	30.27	64.14
Dye 3	115.27-115.40	b	23.20	46.01

Table 4.2. δKr/Ar and δXe/Ar data from non-melted ice samples from the Dye 3 and GISP2 ice cores in Greenland. Replicates from the same depth are listed as a, b, c, etc. Also shown are the mean, standard deviation, and standard error (standard deviation/number of data points) for each dataset.

Core	Depth (m)	replicate	δKr/Ar (‰)	δXe/Ar (‰)
Dye 3	143.195-143.315	a	9.31	17.99
Dye 3	143.195-143.315	b	8.95	19.74
Dye 3	143.195-143.315	c	10.15	22.97
Dye 3	143.195-143.315	d	9.11	20.61
Dye 3	143.315-143.415	a	11.78	29.09
Dye 3	143.315-143.415	b	13.16	20.33
Dye 3	143.315-143.415	c	11.96	25.39
Dye 3	143.415-143.52	a	11.99	24.42
Dye 3	143.415-143.52	b	12.70	26.45
Dye 3	143.415-143.52	c	10.89	18.80
	Mean		**11.00**	**22.58**
	standard deviation		1.54	3.67
	standard error		0.49	1.16
GISP2	147.13-147.23	a	18.05	37.88
GISP2	147.13-147.23	b	18.42	35.66
GISP2	147.13-147.23	c	18.03	34.60
GISP2	147.13-147.23	d	18.58	34.26
GISP2	147.13-147.23	e	17.65	35.78
GISP2	554.90 -555.00	a	16.13	32.48
GISP2	554.90 -555.00	b	13.46	27.59
GISP2	554.90 -555.00	c	18.17	35.93
GISP2	637.38 -637.48	a	15.46	24.55
GISP2	637.38 -637.48	b	13.73	28.87
GISP2	637.38 -637.48	c	11.95	20.95
GISP2	637.38 -637.48	d	14.35	29.64
	Mean		**16.16**	**31.52**
	standard deviation		2.32	5.22
	standard error		0.67	1.51

Table 4.3. Definitions of variables used in model.

S =	Solubility, in mol · L^{-1} · Pa^{-1}
γ =	Volume ratio of liquid water to pore air
z =	Depth of diffusive column (m)
R =	Gas constant (8.314 L · kPa · K^{-1} · mol^{-1})
T =	Temperature (250 K)
F =	Fraction of argon lost by gas loss (when Kr and Xe are not being lost)
m =	Mass (kg · mol^{-1})
g =	Gravitational acceleration (m^2 · s^{-1})

Table 4.4. Model results for six Dye 3 ice core samples with visible melt layers at two different depths. Also shown are the mean values and standard deviations of γ, F, and z at each depth

Depth (m)	replicate	Volume fraction, γ	Fraction ^{36}Ar lost, F	Firn depth, z (m)
144.20	a	0.25	0.007	47.37
144.20	b	0.58	0.010	44.74
144.20	c	0.45	0.006	48.79
144.20	d	0.56	0.011	46.09
Mean		**0.45**	**0.008**	**46.75**
St. dev.		0.15	0.002	1.74
144.47	a	0.25	0.008	49.18
144.47	b	0.83	0.011	49.47
Mean		**0.54**	**0.009**	**49.33**
St. dev.		0.40	0.002	0.20

.

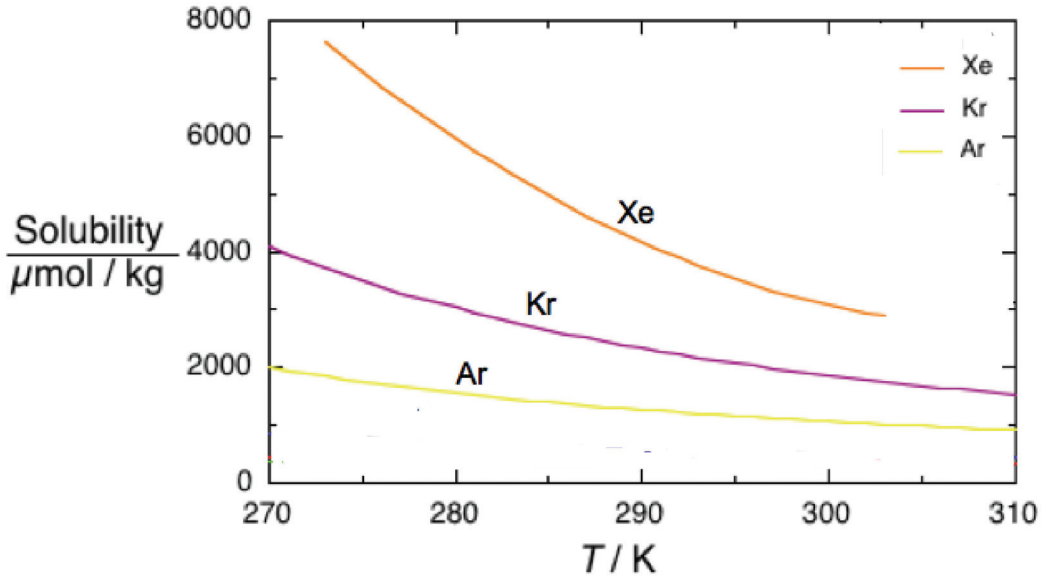

Figure 4.1. Solubility plotted vs. temperature for Xe, Kr, and Ar.

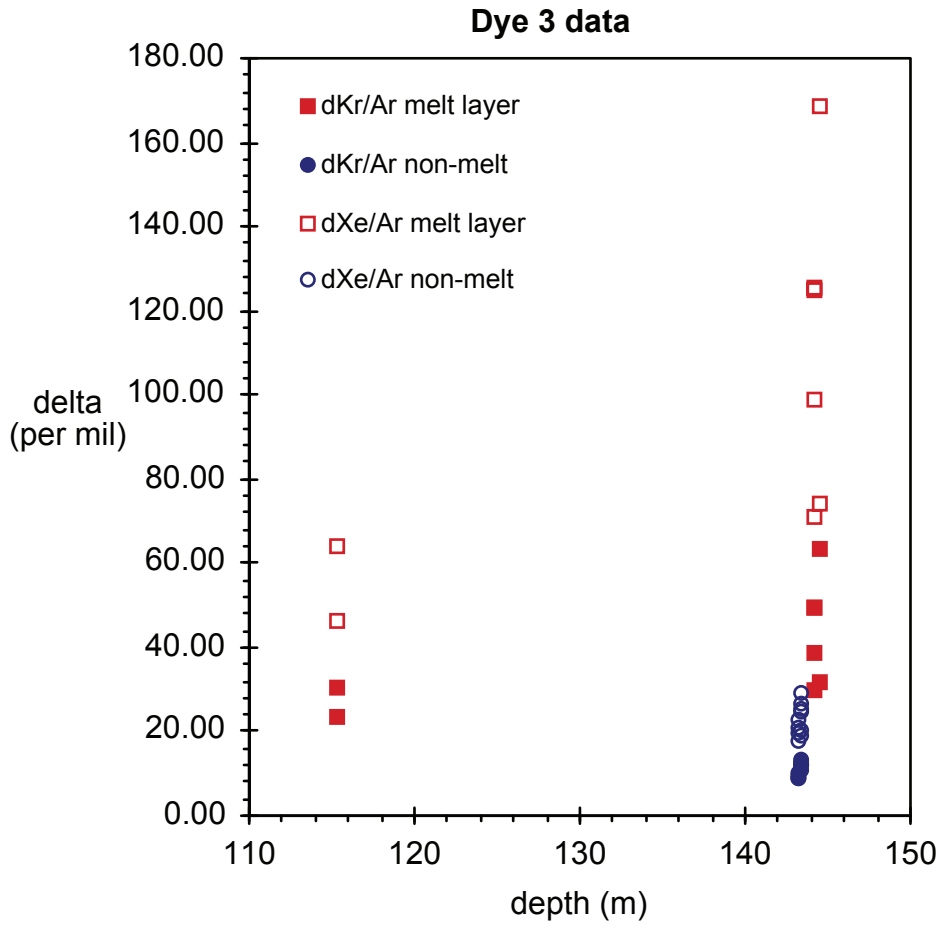

Figure 4.2. δKr/Ar and δXe/Ar measured in Dye 3 melt layers and non-melt samples. Melt layer δKr/Ar and δXe/Ar are shown in solid red squares and open red squares, respectively, while non-melt δKr/Ar and δXe/Ar are shown in solid and open blue circles, respectively. Note the δKr/Ar and δXe/Ar values measured in melt layer samples are higher than those of non-melt samples.

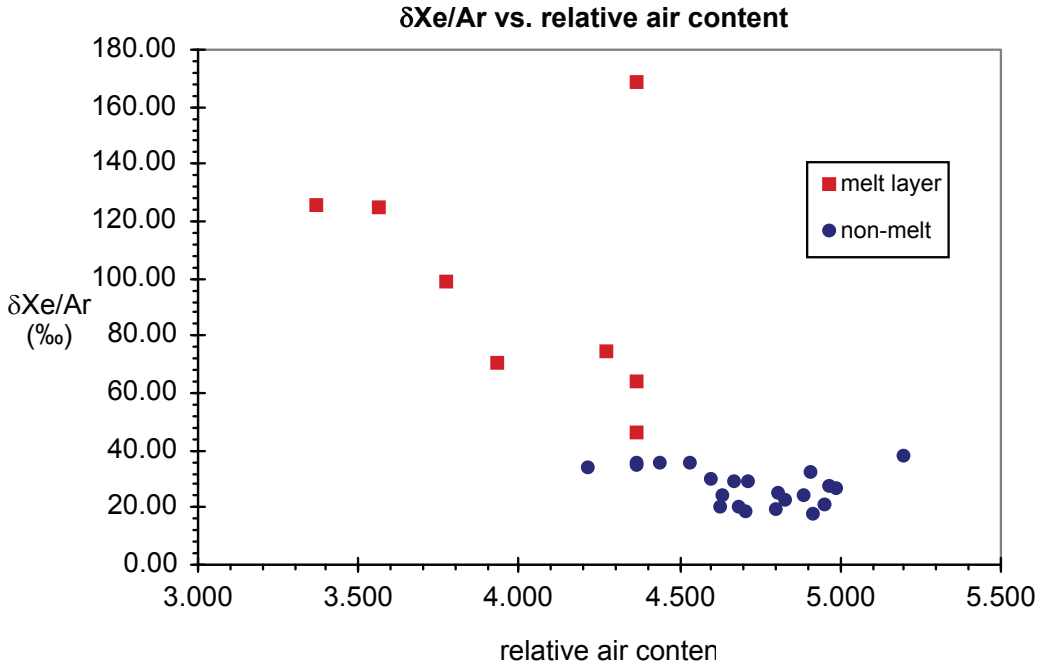

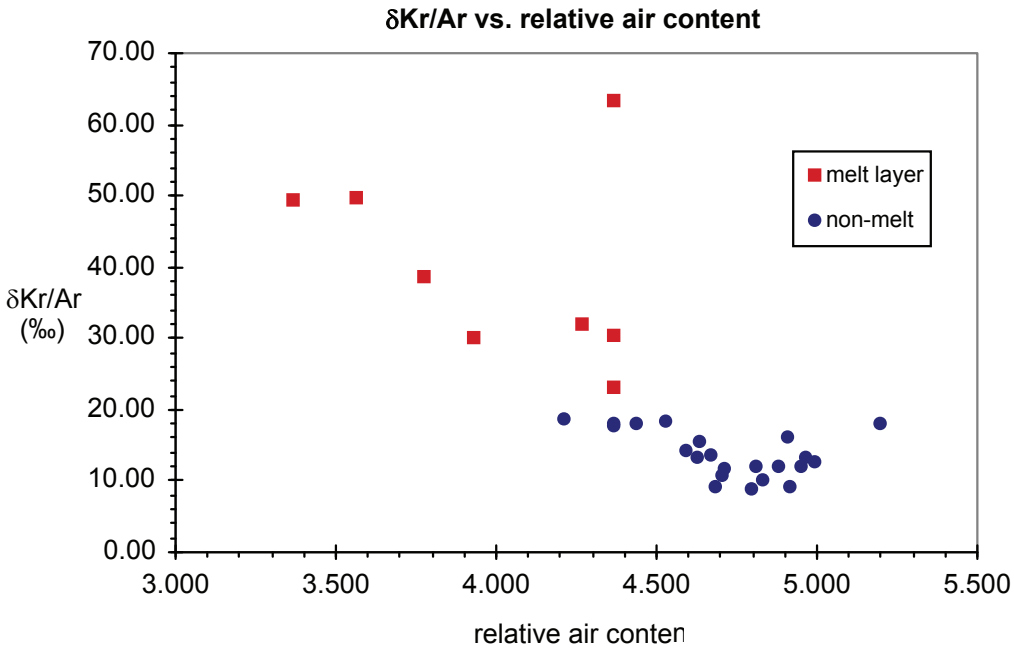

Figure 4.3. δKr/Ar and δXe/Ar plotted vs. relative air content in 3a and 3b, respectively. Red squares represent data from the Dye 3 samples with visible melt layers. Blue circles are non-melted data from GISP2 and Dye 3. With the exception of one melt layer sample, both δKr/Ar and δXe/Ar appear to be inversely proportional to relative air content, with higher levels of δKr/Ar and δXe/Ar associated with lower levels of relative air content.

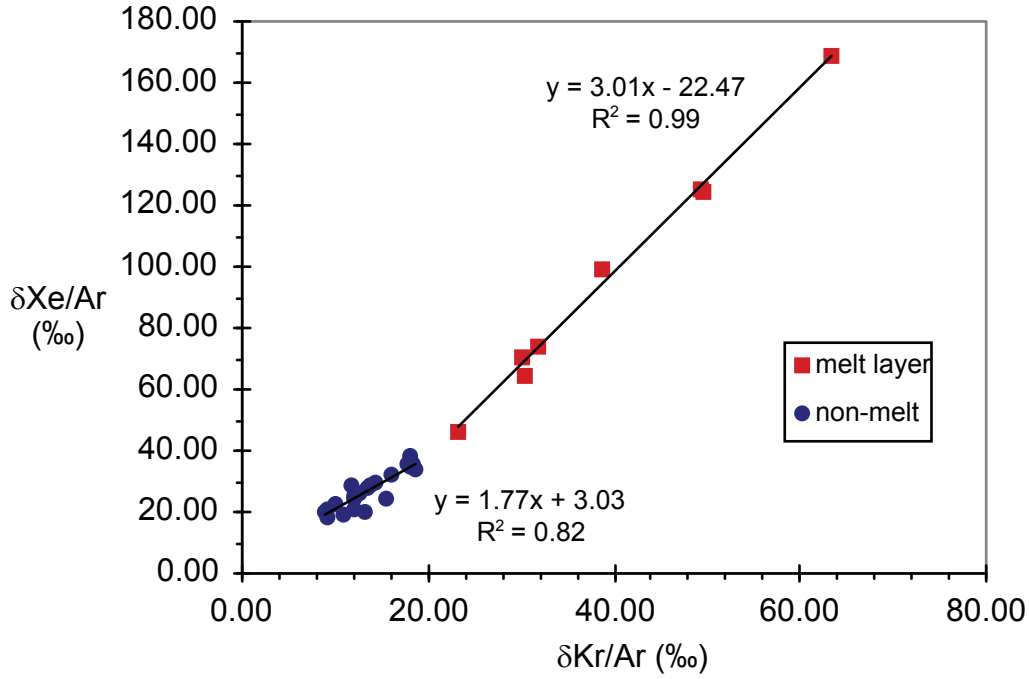

Figure 4.4. δXe/Ar vs. δKr/Ar. Samples with visible melt layers from Dye 3 are represented by red squares, while non-melted samples from Dye 3 and GISP2 are shown in blue. The melt layer samples show a steeper slope (m=3.01) than the non-melted samples (m=1.77).

Chapter 5

Conclusions

The work presented in this thesis contributes to the broader knowledge of paleoclimate by introducing new proxies for past variations in ocean temperature and summer melt frequency. By taking advantage of the solubility properties of krypton and xenon, we have been able to estimate mean ocean temperature change during the last glacial termination and inception. These Kr*- and Xe*-derived solubility-weighted mean ocean temperature reconstructions (Noble Gas Temperature Indices, NGTI's) are the first estimates of the global mean ocean temperature of the past. We have also shown that Kr and Xe, measured as ratios to Ar, may be used to identify the frequency of polar snow melt during warm summers.

In Chapter 2, the first measurements of paleo-atmospheric $\delta Kr/N_2$ and $\delta Xe/N_2$ are presented. These measurements were from air bubbles in ice from the late Holocene and the last glacial maximum (LGM). We used a mass balance model to estimate the average ocean temperature change indicated by a given change in atmospheric $\delta Kr/N_2$ and $\delta Xe/N_2$. The deep ocean temperature during the LGM is relatively well constrained (compared to other times during the last glacial period), so we were able to compare our data with those of other researchers (Schrag et al., 1996, Adkins et al., 2002, Cutler et al., 2003). The $\delta Xe/N_2$ precision was not good enough to use as a measure of past ocean temperature, so we improved upon the measurement method, as described in Chapter 3.

A new method of measurement was presented in Chapter 3, which allowed for improved precision of $\delta Kr/N_2$ and $\delta Xe/N_2$. This improved method also made $\delta^{86}Kr$ measurement possible, which was used to correct for gravitational settling, and may be a better measure of gravitational correction than $\delta^{40}Ar$, which can be affected by gas

loss. Shown in Chapter 3 are the first time series of $\delta Kr/N_2$ and $\delta Xe/N_2$, and their inferred Noble Gas Temperature Indices (NGTI's), during the last glacial termination and inception. These reconstructed NGTI's appear to vary in step with CO_2 during the cooling into the last glacial period (~123-104 kyr B.P.), as well as during the deglaciation (~24-14 kyr B.P.). Identifying mean ocean temperature variations during the last glacial termination and inception can perhaps constrain climate change hypotheses (e.g. Keeling and Stephens, 2001).

Because the $\delta Kr/N_2$ and $\delta Xe/N_2$ data presented in this thesis are the first of their kind, there are many possibilities for future work concerning these measurements. Firstly, it would be useful to extend these measurements in time. In order to better understand that transition from the last glacial period to the Holocene, $\delta Kr/N_2$ and $\delta Xe/N_2$ should be analyzed in ice that spans the remaining portion of the deglaciation (14kyr B.P. – Holocene) to cover the entire warming. This extended deglaciation record could then be compared to the Dome Fuji $\delta Kr/N_2$ and $\delta Xe/N_2$ data (30 kyr – present) shown in Chapter 3, which indicated that the mean ocean temperature may have been warmer than today in the early Holocene. There is a possibility that melt layers are present in ice younger than 14 kyr B.P., so $\delta Xe/Ar$ and $\delta Kr/Ar$ values would need to be closely monitored in this ice. It may also be interesting to measure $\delta Kr/N_2$ and $\delta Xe/N_2$ during Marine Isotope Stage (MIS) 3, as there is some debate as to whether sea level fluctuated during this time (Linsley, 1996, Chappell et al., 1996, Chappell, 2002 Shackleton, 2000). Ocean temperature data during MIS 3 would help to constrain sea level changes. In a broader sense, it would

be informative to measure $\delta Kr/N_2$ and $\delta Xe/N_2$ during the complete duration of the last glacial period, and eventually extending the record further back to cover earlier glacial-interglacial cycles. This expanded mean ocean temperature record would lead to a more robust comparison with other climate parameters that vary on glacial-interglacial timescales.

In addition to extending the record in time, improvements could be made as to the corrections and the measurements themselves. The newer MAT Finnigan 253 mass spectrometers permit Xe isotope measurements, which would allow for a correction for convective mixing within the firn. A correction for convection would result in more accurate estimates of the gravitational and thermal corrections, which would in turn improve the accuracy of the $\delta Kr/N_2$ and $\delta Xe/N_2$ measurements. Furthermore, improvements in mass spectrometry itself (i.e. stronger beam strength) using the newer MAT 253 may allow for more precise measurements of isotopic and elemental ratios.

In Chapter 4, we show that $\delta Kr/Ar$ and $\delta Xe/Ar$ can be used as indicators of melt layers in ice cores, which are used to identify the presence and frequency of warm summers. $\delta Kr/Ar$ and $\delta Xe/Ar$ are elevated in ice that has melted and refrozen, as compared to non-melted ice, and the $\delta Xe/Ar/\delta Kr/Ar$ relationship in melt layers is unique. The addition of these melt layer proxies may be especially useful in deep ice when air bubbles form air clathrates. A robust record of summer seasonality, as provided by visual melt layer identification and $\delta Kr/Ar$ and $\delta Xe/Ar$ measurements, may be useful in supporting and framing explanations of the climate record that

invoke seasonality (Schaefer et al., 2006). Future directions of δKr/Ar and δXe/Ar analyses may include measuring δKr/Ar and δXe/Ar during early the Holocene, when insolation was at a maximum, to strengthen the melt layer record during this time period, and to examine the effect of strong insolation on summer temperatures. δKr/Ar and δXe/Ar should also be measured during the glacial termination to verify theories suggesting strong seasonality during this transition (Schaefer et al., 2006).

By taking advantage of the differential solubilities of Kr and Xe, as compared to less soluble gases, N_2 and Ar, we have developed and presented two new paleoclimate proxies in this thesis. The Kr*- and Xe*-derived NGTI records are a new addition to the paleoclimate literature, and may provide powerful constraints to proposed mechanisms of climate change. Extending the record of $\delta Kr/N_2$ and $\delta Xe/N_2$ to reconstruct mean ocean temperatures during the last several glacial-interglacial cycles will increase our understanding of the causes and mechanisms of climate change.

References

Adkins, J.F., K. McIntyre, D.P. Schrag (2002), The salinity, temperature, and $\delta^{18}O$ of the glacial deep ocean, *Science*, *298*, 1769-1772.

Chappell, J.A., A. Omura, T. Esat, M. McCulloch, J. Pandolfi, Y. Ota, B. Pillans (1996), Reconciliation of late Quaternary sea levels derived from coral terraces at Huon Peninsula with deep sea oxygen isotope records, *Earth and Planetary Science Letters*, *141*, 227-236..

Chappell, J. (2002), Sea level changes forced ice breakouts in the Last Glacial cycle: new results from coral terraces, *Quaternary Science Reviews*, *21*, 1229-1240.

Cutler, K. B., R. L. Edwards, F. W. Taylor, H. Cheng, J. Adkins, C. D. Gallup, P. M. Cutler, G. S. Burr, and A. L. Bloom (2003), Rapid sea-level fall and deep-ocean temperature change since the last interglacial period, *Earth Planet. Sci. Lett.*, *206*, 253-271.

Keeling, R. F., and B. B. Stephens (2001), Antarctic sea ice and the control of Pleistocene climate Instability, *Paleoceanography*, *16*, 112-131.

Linsley, B.K. (1996), Oxygen isotope evidence of sea level and climactic variations in the Sulu Sea over the past 150,000 years, *Nature*, *380*, 234-237.

Shackleton, N.J. (2000), The 100,000-year cycle identified and found to lag temperature, carbon dioxide and orbital eccentricity, *Science*, *289*, 1897-1902.

Schaefer, J. M., G. H. Denton, D. J. A. Barrell, S. Ivy-Ochs, P. W. Kubik, B. G. Andersen, F. M. Phillips, T. V. Lowell, and C. Schlüchter (2006), Near-Synchronous Interhemispheric Termination of the Last Glacial Maximum in Mid-Latitudes, *Science*, *312*, 1510-1513.

Schrag, D. P., G. Hampt, and D. W. Murray (1996), Pore Fluid Constraints on the Temperature and Oxygen Isotopic Composition of the Glacial Ocean, *Science*, *272*, 1930-1932.

Appendix:

CO_2-induced Mass Independent Fractionation of Oxygen Isotopes in Air Measured on a Finnigan Delta XP Mass Spectrometer

Abstract

Fractionation of atmospheric dioxygen isotopes ($^{18}O/^{16}O$ and $^{17}O/^{16}O$) is observed when CO_2 is added to an air sample. Additionally, the oxygen isotopes ($\delta^{17}O$ and $\delta^{18}O$) appear to fractionate in a mass-independent way, with $\delta^{17}O \geq \delta^{18}O$ rather than the typical relationship $\delta^{17}O=0.5(\delta^{18}O)$. The deviation from mass dependence ($\Delta^{17}O$) is found to increase with increasing CO_2 concentration. We repeated this CO_2 addition experiment with a lower electron energy level on the mass spectrometer source to test whether the observed oxygen isotopic fractionation is sensitive to electron energy. We found that both ^{17}O and ^{18}O enrichments slightly decrease with decreasing electron energy. We also repeated the CO_2 addition experiment using ^{13}C-enriched CO_2. The addition of ^{13}C-enriched CO_2 appears to cause $\delta^{17}O$ and $\delta^{18}O$ to decrease, although this effect is much more significant for the $\delta^{18}O$. The cause of the observed oxygen isotopic fractionation is not certain. Furthermore, there may be more than one selection mechanism causing the heavy oxygen isotope enrichment. One possible mechanism involves symmetry, favoring isotopically heterogeneous reactants in the production of O_2^+. It is also possible that resonance, the matching of vibrational levels, plays a role in the observed fractionation. Regardless of the cause, oxygen isotope data should be corrected for variable concentrations of CO_2 in an air sample.

Introduction

We have observed an apparent mass-independent fractionation effect on the isotopes of atmospheric O_2 measured in air samples on a Finnigan Delta Plus XP isotope ratio mass spectrometer. This fractionation effect increases in magnitude as

progressively more CO_2 is added to an air sample, with $\delta^{17}O$ and $\delta^{18}O$ increasing 0.001 and 9×10^{-4} per mil, respectively, for each percent increase in CO_2.

Laboratory use of the Finnigan Delta Plus XP mass spectrometer typically involves the measurement of $\delta^{15}N$ of N_2, $\delta^{18}O$ of O_2, O_2/N_2, and Ar/N_2, as well as H_2O and CO_2 in air trapped in ice cores (Severinghaus, et al., 2003). Because CO_2 is included in the air sample measured, we must correct for the isobaric interference of $^{13}C^{16}O$ (formed when $^{13}CO_2$ dissociates in the mass spectrometer source) with $^{15}N^{14}N$ of N_2, both having a mass of 29 (Sowers, et al., 1989, Bender et al., 1994b, Severinghaus, et al., 2003). We correct for this isobaric interference by measuring the $\delta^{15}N$ of N_2 in an air sample into which incremental amounts of pure CO_2 are added. We call this correction a "chemical slope" correction (Severinghaus, et al., 2003). In making these measurements, we noted an unexpected effect: the $\delta^{18}O$ of O_2 (measured as the mass 34/32 ratio) also appeared to increase as CO_2 was added. Furthermore, the ^{18}O enrichment was twice that of $\delta^{15}N$ when CO_2 was added to the sample (Figure A.1). In addition to an ^{18}O enrichment, we also noted a strong ^{17}O enrichment in the atmospheric O_2 (mass 33/32), with the ^{17}O enrichment deviating from mass-dependence.

In order to investigate the mechanism causing the observed fractionation, we conducted two additional experiments. In the first experiment, we altered the electron energy (E_e) of the mass spectrometer. Variable electron energy has been noted in previous work to cause mass-independent fractionation in oxygen isotopes (Griffith and Gellene, 1992, Yoo and Gellene, 1995). Previous studies have also suggested that

the matching of vibrational levels can cause mass-independent fractionation (Lim, et al., 1999, Bhattacharya et al., 2000). In the second experiment, we added ^{13}C-enriched CO_2 to the air samples instead of the pure CO_2 used in the previous experiments. Because $^{13}CO_2$ has a different mass than the more abundant $^{12}CO_2$, its vibrational energy is different than that of $^{12}CO_2$. By conducting these supplemental experiments, we were able to test whether changing the electron energy and/or the vibrational energy affected the oxygen isotopic fractionation.

Method

The initial CO_2 addition experiments were conducted in August 2003, and repeated in February 2004. A 1-cm^3 aliquot of dry air from a laboratory tank (collected from the Scripps Pier in La Jolla, CA) at approximately 50 psig was transferred through a stainless steel vacuum line into a dip tube. The transfer was accomplished by freezing the sample at 4K into a dip tube that has been lowered into a tank of liquid helium. After the air transfer, we closed the valve to the dip tube, and then added the desired amount of CO_2 to the vacuum line. That CO_2 was then transferred into the sample dip tube in liquid helium. All connections in this experiment and those described subsequently were made using ultratorrs with Viton o-rings. The method used in these CO_2 addition experiments is similar to that of previous studies, where "chemical slope" corrections were made to $\delta^{15}N$ for variable O_2/N_2 ratios (Sowers, et al., 1989, Bender et al., 1994b, Severinghaus, et al., 2003).

In the August 2003 experiment, four dip tubes were prepared for analysis. They consisted of dry La Jolla air samples plus 2, 3, 4, and 10 times the atmospheric

CO_2 concentration. Bone dry grade CO_2 (99.8% pure) was used in this experiment. We collected a small sample of the bone dry grade CO_2 in a 4-cm^3 pipette by flushing the CO_2 through the pipette and a tail of Dekabon tubing for 10 minutes. The tail was used to prevent ambient air from entering the pipette. After 10 minutes of flushing, we waited 5 seconds for gas flow to stop, and then closed the valves on the pipette to collect the CO_2. The CO_2-filled pipette was then attached to the vacuum line, and CO_2 was added to the line directly from the pipette.

In the February 2004 experiment, we used ultra-pure CO_2 (99.999% pure) to verify that the fractionation we observed in the first experiment was due to CO_2, rather than a contaminant in the bone dry grade CO_2. The ultra-pure CO_2 was collected in a pipette by the same procedure used to collect the bone dry CO_2. The samples contained dry La Jolla air from the same laboratory tank used in the August 2003 experiment plus an addition of variable amounts of ultra-pure CO_2. We analyzed eight samples, including a "blank", composed of an aliquot of dry air without added CO_2. We doubled atmospheric CO_2 in two samples, and the others were air samples with 3, 4, 6, 8, and 10 times atmospheric CO_2.

The samples were then analyzed on the Finnigan Delta Plus XP mass spectrometer for $\delta^{15}N$, $\delta^{18}O$, $\delta^{17}O$, $\delta O_2/N_2$, and $\delta Ar/N_2$. The delta (δ) notation indicates the conventional deviation of a ratio from a standard ratio:

$$\delta^{18}O = \left[\left({}^{18}O_{sample} / {}^{16}O_{sample}\right) / \left({}^{18}O_{standard} / {}^{16}O_{standard}\right) - 1\right] \times 1000 \qquad (A.1)$$

To investigate the mechanism responsible for the observed fractionation, we altered two different parameters of the CO_2 addition experiment: the electron energy of the mass spectrometer, and the carbon isotopic composition of the CO_2 added to the air sample.

The electron energy on the mass spectrometer is typically set at its maximum value: 123.9 eV. We lowered the electron energy to 99.7 eV and repeated the CO_2 addition experiment. We measured one "blank" sample, and air samples with 2, 3, 4, and 10 times atmospheric CO_2 concentrations. Ultra-pure CO_2 was used in this experiment, collected in a 4-cm^3 pipette as previously described. We measured these samples on the mass spectrometer against the standard used in all experiments (dry La Jolla air). Decreasing the electron energy and repeating the CO_2 addition experiment allowed us to determine whether the oxygen isotope fractionation is dependent upon changes in electron energy.

We also repeated the CO_2 addition experiment using ^{13}C-enriched CO_2 (99% $^{13}CO_2$, 1% $^{12}CO_2$). The ^{13}C-enriched CO_2 was stored in a glass bulb, which was attached to the vacuum line using an ultratorr with Viton o-rings. We expanded an aliquot of the ^{13}C-enriched CO_2 from the bulb into a small volume in the vacuum line. The desired amount of CO_2 was then added to the vacuum line from that aliquot. As in the electron energy experiment explained above, we measured one blank sample, and air samples with 2, 3, 4, and 10 times atmospheric CO_2 concentrations. We measured each sample at the normal electron energy (123.9eV) and at the lower electron energy (99.7eV).

Results

Results from these four analyses are shown in Tables A.1 and A.2. Initially, we set out to determine the isobaric interference of CO_2 with the $\delta^{15}N$ of N_2, which is apparent in Figure A.1. We also noticed a correlation between $\delta^{18}O$ of O_2 and CO_2. The $\delta^{18}O$ was over twice as enriched as $\delta^{15}N$ when CO_2 was added to the sample. The $\delta^{15}N$ and $\delta^{18}O$ are plotted vs. δCO_2 in Figure A.1. Data in Figure A.1 are from the initial experiment (August 2003) and a subsequent experiment using ultra-pure CO_2 (February 2004).

The addition of CO_2 also appears to have a unique effect on the isotopes of O_2. The $\delta^{18}O$ and $\delta^{17}O$ of atmospheric O_2 are typically fractionated in a "mass-dependent" way, in which fractionation depends on mass difference. Therefore, O_2 is usually twice as enriched in ^{18}O relative to ^{16}O (mass difference of 2) than in ^{17}O relative to ^{16}O (mass difference of 1). Mass dependent fractionation leads to a $\delta^{17}O/\delta^{18}O$ slope of ~0.52 (Hulston and Thode, 1965, Matsuhisa, et al., 1978). In our samples, the $\delta^{17}O$ values were found to be equal to or higher than those of $\delta^{18}O$, with this difference increasing as more CO_2 was added (Figure A.2).

The deviation of $\delta^{17}O$ from mass dependence ($\Delta^{17}O$) can be described by the difference between the measured $\delta^{17}O$ and the $\delta^{17}O$ value that would correspond to mass dependence ($0.52 \times \delta^{18}O$):

$$\Delta^{17}O = \delta^{17}O - 0.52 \times \delta^{18}O \qquad (A.2)$$

The calculated $\Delta^{17}O$ of the August 2003 and February 2004 experiments are plotted in Figure A.3. As more CO_2 is added to the air sample, $\Delta^{17}O$ steadily increases. This deviation from mass dependence is clear in the three-isotope plot for the initial two experiments (Figure A.4), in which the measured $\delta^{17}O$ is plotted vs. $\delta^{18}O$, along with a mass dependent slope of y = 0.52x for comparison. The slopes on this plot are greater than 1, clearly exceeding a mass dependent slope.

When we lowered the electron energy (E_e) by ~30 eV on the mass spectrometer, both $\delta^{17}O$ and $\delta^{18}O$ decreased (Figures A.5 and A.6). Interestingly, the $\delta^{15}N$ was unaffected by lowering the electron energy (Figure A.5). The $\Delta^{17}O/\delta CO_2$ slope decreased slightly at the lower electron energy, while it is impossible to distinguish between the two electron energies in the three-isotope diagram (Figures A.7 and A.8).

Our oxygen isotope measurements also changed when we repeated the CO_2 addition experiment using ^{13}C-enriched CO_2 (99% $^{13}CO_2$, 1% $^{12}CO_2$). In this experiment, the $\delta^{18}O$ values decreased in comparison to earlier experiments using ultra-pure CO_2, yet there was little difference between the $\delta^{18}O$ at the two different electron energies (Figure A.6). $\delta^{17}O$ also decreased when $^{13}CO_2$ was added to the air sample (Figure A.7), but it did not decrease as dramatically as the $\delta^{18}O$. When $^{13}CO_2$ was used, the $\delta^{17}O$ remained sensitive to changes in electron energy, while the $\delta^{18}O$ did not respond to changes in electron energy in this case. The $\delta^{17}O/\delta^{18}O$ slope increased significantly in the three-isotope plot when $^{13}CO_2$ was added to an air sample (Figure A.8). The change in $\Delta^{17}O$ in this experiment was not as clear. When

^{13}C-enriched CO_2 is added to the air sample, $\Delta^{17}O$ values at the higher electron energy increase relative to samples run with "normal" CO_2, while the $\Delta^{17}O$ values at the lower electron energy decrease.

Discussion

The cause of the observed fractionation is still unclear. Possible explanations for the effect include symmetry restrictions, "energy level matching", or a combination of these processes. Within these explanations, there are several possible reactions that could be taking place in the mass spectrometer.

Several explanations of mass-independent fractionation have been proposed in previous work. An early explanation of the observed mass independent enrichments of $\delta^{17}O$ and $\delta^{18}O$ in O_3 attributed the fractionation to self-shielding of the homogeneous $^{16}O^{16}O$ molecule (Thiemens and Heidenreich, 1983). A subsequent study suggested that the mass independent fractionation observed in ozone formation results from symmetry differences between isotopomers of ozone (Heidenreich and Thiemens, 1986). In their study, Heidenreich and Thiemens suggested that because the isotopically heterogeneous ozone reaction intermediate, O_3*, may have a longer lifetime than that of the isotopically homogeneous $^{16}O^{16}O^{16}O$, the heterogeneous ozone intermediate would be more likely to survive to form ozone. Gellene and others have used a permutation-inversion symmetry analysis to show that symmetry differences between isotopomers may favor formation of heterogeneous molecules (e.g. ozone, O_4^+, $(CO_2)_2^+$), causing a mass independent isotopic signature (Gellene, 1992; Griffith and Gellene, 1992; Yoo and Gellene, 1995; Gellene, 1996). Gellene

and others have found that in reactions with homogeneous reactant ions, restrictions are placed on the reaction based on the rotational states of the reactant ion. In contrast, when the reactant ion is heterogeneous, no restrictions are placed on the reaction. Gellene (1992) refers to this fractionation mechanism as a Symmetry Induced Kinetic Isotope Effect (SIKIE). The degree of isotopic fractionation due to symmetry restrictions on an ion may depend on how the ion was ionized, i.e. by electron ionization or charge transfer from another ion. Additionally, the intensity of electron energy seems to have an effect on the extent of fractionation as well (Griffith and Gellene, 1992).

A study of rate coefficients of ozone formation found that asymmetry of the reactant oxygen molecule does not necessarily lead to faster reaction rates (Anderson, et al., 1997). Anderson, et al., found that certain isotopic variants of O_2 and O forming ozone actually contradict the predicted isotopic enrichment based on Gellene's symmetry correlation scheme (Gellene, 1996). Thus, symmetry alone may not be sufficient in explaining the observed oxygen isotopic enrichments.

Others have explained different cases of mass independent fractionation in terms of the crossing of potential energy surfaces and matching of vibrational levels (Lim, et al., 1999; Bhattacharya, et al., 2000). Lim et al. (1999) found anomalously high $O^{37}ClO/O^{35}ClO$, and hypothesized that near-resonance coupling of vibrational levels of the molecules was responsible for the fractionation. The vibrational levels of the $O^{35}ClO$ in an excited state matched those of a less excited state more closely than the vibrational levels of $O^{37}ClO$, giving a pathway of decay for the $O^{35}ClO$ molecule. Therefore, the enhancement in $O^{37}ClO$ was due to slower decay of the $O^{37}ClO$, as

compared to the $O^{35}ClO$. Bhattacharya, et al. (2000) found unusually ^{17}O-enriched O_2 (more than 100‰) in the O_2 product from photolysis of CO_2. They proposed that a similar mechanism as described in Lim et al., the matching of vibrational levels, was responsible for the anomalous ^{17}O enrichment. They tested this hypothesis by repeating the CO_2 photolysis using ^{13}C-enriched CO_2, which has different vibrational levels than $^{12}CO_2$. They found that the nature of oxygen isotopic fractionation changed when the $^{13}CO_2$ was used. Both heavy oxygen isotopes were enriched, with ^{18}O enrichments 100‰ higher than when $^{12}CO_2$ was used. Bhattacharya et al. concluded that the matching of vibrational energy levels might have played a major role in the ^{17}O enrichment in the CO_2 photolysis O_2 product.

There may be more than one mechanism causing the observed oxygen isotopic fractionation presented in this study. One possibility is that symmetry is playing a role in the isotopic enrichments. As proposed by Gellene and others (Gellene, 1992, Griffith and Gellene, 1992, Yoo and Gellene, 1995, Yoo and Gellene, 1996, Gellene, 1996), symmetry restrictions on the homogeneous ion reactant may cause the products to be enriched in isotopically heterogeneous ions. Some form of symmetry restrictions could be present in our study. Another possible mechanism involves the crossing of potential energy surfaces and the matching of vibrational levels as in Lim et al., 1999 and Bhattacharya et al., 2000. This type of resonance could facilitate isotope exchange, or enhance the ionization of oxygen, both of which may fractionate the oxygen isotopes.

Our experiments altering the electron energy and carbon isotopic composition of CO_2 may shed light on mechanism(s) at work here. It is notable in our data that

higher electron energy increases both the $\delta^{17}O$ and $\delta^{18}O$ at a given CO_2 level, but it does not change the partitioning between ^{17}O and ^{18}O (the three-isotope diagram remains unchanged at different E_e's). The addition of ^{13}C-enriched CO_2, on the other hand, significantly changes the partitioning of ^{18}O and ^{17}O, shifting the slope of the three-isotope plot to a higher value, favoring ^{17}O enrichment over that of ^{18}O. Our experiments, therefore, suggest that more than one selection mechanism may be present in this study. It could be that some type of symmetry process favors formation of both heterogeneous O_2^+ ions, and that another mechanism selects for ^{17}O. The addition of CO_2 may act as an intermediate as O_2^+ is ionized, or there may be a transfer of charge from CO_2 to O_2.

Another possibility is that NO_x molecules are being formed in the mass spectrometer source, possibly giving rise to a $^{14}N^{18}O$, $^{15}N^{17}O$, and/or $^{15}N^{18}O$. The former two NO molecules have a mass of 32, which is not found to be enriched in our results. A preferential formation of $^{15}N^{18}O$ would cause an enrichment in mass 33 (also the mass of $^{17}O^{16}O$), which is observed in our data as more CO_2 is added. One possibility is that CO_2 is somehow acting as an intermediary or catalyst for the production of NO. This potential explanation can be tested in the future using mixtures of pure oxygen and CO_2, and omitting N_2.

Although we are not certain of the mechanism causing heavy oxygen isotopes to be enriched in O_2 in air, our observations should be taken into consideration by those measuring oxygen isotopes of O_2 in the presence of CO_2. The linear relationship between δCO_2 and the $\delta^{18}O$ and $\delta^{17}O$ of O_2 allows for a correction to be made to the oxygen isotopes of O_2 in air.

Conclusions

We have shown that the addition of CO_2 to a dry air sample causes a mass independent enrichment of $\delta^{17}O$ and $\delta^{18}O$ of O_2. This enrichment is approximately linear with the addition of CO_2, so measurements of $\delta^{17}O$ and $\delta^{18}O$ of O_2 can be corrected according to changes in CO_2 abundance. The oxygen isotopic enrichment is sensitive to changes in electron energy (E_e), with higher $\delta^{18}O$ and $\delta^{17}O$ at higher electron energy. Changing the carbon isotopic composition of the CO_2 added to the air samples is also observed to affect the oxygen isotopic enrichments measured in O_2. This effect on the oxygen isotopes when $^{13}CO_2$ is added may result from changing the vibrational energy levels of the CO_2 that reacts with O_2. It follows that the matching of vibrational levels may play a role in the observed oxygen isotope fractionation. It is also possible that symmetry plays a role in the isotopic enrichments as well.

References

Anderson, S. M., D. Hulsebusch, K. Mauersberger (1997), Surprising rate coefficients for four isotopic variants of $O+O_2+M$, *Journal of Chemical Physics*, *107*, 14, 5383-5392.

Bhattacharya, S.K., J. Savarino, M.H. Thiemens (2000), A new class of oxygen isotopic fractionation in photodissociation of carbon dioxide: Potential implications for atmospheres of Mars and Earth, *Geophysical Research Letters*, *27*(10), 1459-1462.

Bender, M.L., P.P. Tans, J.T. Ellis, J. Orchardo, K. Habfast (1994b), A high precision isotope ratio mass spectrometry method for measuring the O_2/N_2 ratio of air, *Geochimica et Cosmochimica Acta*, *58*, 4751-4758.

Böhringer, H., M.Durup-Ferguson, D.W. Fahey, F.C. Fehsenfeld, E.E Ferguson, (1983), Collisional relaxation of vibrationally excited O_2^+ ions, *Journal of Chemical Physics*, *79*(9), 4201-4213.

Copp, N.W., M. Hamdan, J.D.C. Jones, K. Birkinshaw, N.D. Twiddy (1982), A selected ion flow tube study of the reactions of the gaseous ion CO_2^+ at 298K, *Chemical Physics Letters*, *88*(5), 508-511.

Derai, R., P.R. Kemper, M.T. Bowers (1985), Effect of reactant ion internal and translational energy on the rate constants of the charge exchange reactions: $CO_2^+ + O_2 \rightarrow O_2^+ + CO_2$ and $O_2^+ + O_2 \rightarrow O_2 + O_2^+$, *Journal of Chemical Physics*, *82*(10), 4517-4523.

Durup-Ferguson, M., H. Böhringer, D.W. Fahey, E.E. Ferguson (1983), Enhancement of charge-transfer reaction rate constants by vibrational excitation at kinetic energies below 1 eV, *Journal of Chemical Physics*, *79*(1), 265-272.

Ferguson, E.E., J.M. Van Doren, A.A. Viggiano, R.A. Morris, J.F. Paulson, J.D. Stewart, L.S. Sunderlin, P.B. Armentrout (1992), Internal and translational energy effects on the charge-transfer reaction of CO_2+ with O_2, *International Journal of Mass Spectrometry and Ion Processes*, *117*, 261-282,.

Gellene, G.I. (1992), Symmetry restrictions in diatom/diatom reactions. I. Group theoretical analysis, *Journal of Chemical Physics*, *96*(6), 4387-4402.

Gellene, G.I. (1996), An Explanation for Symmetry-Induced Isotopic Fractionation in Ozone, *Science*, *274*, 1344-1346.

Glosik, J., A.B. Rakshit, N.D. Twiddy, N.G. Adams, D. Smith (1978), Measurements of the rates of reaction of the ground and metastable excited states of O_2^+, NO^+, and

O^+ with atmospheric gases at thermal energy, *J. Phys. B: Atom. Molec. Phys*., *11*(19), 3365-3379.

Griffith, K.S. and G.I. Gellene (1992), Symmetry restrictions in diatom/diatom reactions. II. Nonmass-dependent isotope effects in the formation of O_4^+, *Journal of Chemical Physics*, *96*(6), 4403-4411.

Heidenreich III, J.E. and M.H. Thiemens (1986), A non-mass dependent oxygen isotope effect in the production of ozone from molecular oxygen: The role of molecular symmetry in isotope chemistry, *Journal of Chemical Physics*, *84*(4), 2129-2136.

Heidenreich III, J.E. and M.H. Thiemens (1985), The non-mass-dependent oxygen isotope effect in the electrodissociation of carbon dioxide: A step toward understanding NoMaD chemistry, *Geochimica et Cosmochimica Acta*, *49,* 1303-1306.

Herzberg, G.H. (1950), *Molecular Spectra and Molecular Structure, I. Spectra of Diatomic Molecules*, D. Van Nostrand Company, Inc.: Princeton, NJ.

Herzberg, G.H. (1966), *Molecular Spectra and Molecular Structure, III. Electronic Spectra and Electronic Structure of Polyatomic Molecules*, D. Van Nostrand Company, Inc.: Princeton, NJ.

Hulston, J.R., and H.G. Thode (1965), Variations in ^{33}S, ^{34}S, and ^{36}S contents of meteorites and their relation to chemical and nuclear effects, *Journal of Geophysical Research*, *70*(14), 3475.

Lim, G., S.M. Lim, S.K. Kim, Y.S. Choi (1999), Unexpectedly large $O^{37}ClO/O^{35}ClO$ intensity ratios of the fluorescence from the low-energy vibrational levels of OClO ($\tilde{A}^2A_2$), *Journal of Chemical Physics*, *111*(2), 456-459.

Lindinger, W., F.C. Fehsenfeld, A.L. Schmeltekopf, E.E. Ferguson (1974), Temperature dependence of some ionospheric ion-neutral reactions from 300°-900°, *Journal of Geophysical Research*, *79*(31), 4753-4756.

Lindinger, W., M. McFarland, F.C. Fehsenfeld, D.L. Albritton, A.L. Schmeltekopf, E.E. Ferguson (1975), Translational and internal energy dependences of some ion-neutral reactions, *Journal of Chemical Physics*, *63*(5), 2175-2181.

Matsuhisa, Y., J.R. Goldsmith, R.N. Clayton (1978), Mechanisms of hydrothermal crystallization of quartz at 250°C and 15 kbar, *Geochimica et Cosmochimica Acta*, *42*, 173-182.

Severinghaus, J.P., B. Luz, and N. Caillon (2003), A method for precise measurement of argon 40/36 and krypton/Argon ratios in trapped air in polar ice with applications to

past firn thickness and abrupt climate change in Greenland and at Siple Dome, Antarctica, *Geochimica Cosmochimica Acta*, *67*(3), 325-343.

Sowers, T, M. Bender, D. Raynaud, Elemental and Isotopic Composition of Occluded O_2 and N_2 in Polar Ice, *Journal of Geophysical Research*, *94*(D4), 5137-5150, 1989.

Thiemens, M.H. and J.E. Heidenreich III (1983), The mass-independent fractionation of oxygen – a novel isotope effect and its possible cosmochemical implications, *Science*, *219*(4588), 1073-1075.

Thiemens, M.H. (1999), Mass-Independent Isotope Effects in Planetary Atmospheres and the Earth Solar System, *Science, 283*, 341-345.

Weston, R.E. Jr. (1999), Anomalous or Mass-Independent Isotope Effects, *Chem. Rev.*, *99*, 2115-2136.

Yoo, R.K. and G.I. Gellene (1995), Symmetry induced kinetic isotope effects in the formation of $(CO_2)_2^+$, *Journal of Chemical Physics*, *102*(8), 3227-3237.

Yoo, R.K. and G.I. Gellene (1996), Symmetry induced kinetic isotope effects in the formation of $Ar{\bullet}CO_2^+$, *Journal of Chemical Physics*, *105*(1), 177-183.

Table A.1. Initial CO_2 slope experiments from August 2003 and February 2004. Bone-dry CO_2 was used in the August 2003 experiment, and ultra-pure CO_2 was used in the February 2004 experiment.

δCO_2 (‰)	$\delta^{15}N$ (‰)	$\delta^{18}O$ (‰)	$\delta^{17}O$ (‰)	$\Delta^{17}O$ (‰)
August 2003				
443.59	0.019	0.055	0.064	0.064
904.18	0.032	0.096	0.128	0.128
1441.73	0.059	0.138	0.231	0.231
4558.84	0.165	0.414	0.675	0.675
February 2004				
377.10	0.014	0.041	-0.346	-0.346
883.32	0.011	0.040	0.080	0.080
1292.75	0.036	0.094	0.139	0.139
4476.27	0.113	0.321	0.428	0.428
908.64	0.037	0.086	0.085	0.085
1897.00	0.064	0.157	0.202	0.202
2774.78	0.085	0.213	0.294	0.294
3642.50	0.106	0.283	0.365	0.365

Table A.2. Data for two experiments: varying the electron energy of the Delta XP mass spectrometer, and using ^{13}C-enriched CO_2 at the normal electron energy and at a lower electron energy. $\delta^{15}N$ in the ^{13}C-enriched CO_2 experiment is exceptionally high due to isobaric interference of $^{13}C^{16}O$ (formed from CO_2 in the source) with $^{15}N^{14}N$, both of mass 29.

Sample ID	Electron energy (eV)	δCO_2 (‰)	$\delta^{15}N$ (‰)	$\delta^{18}O$ (‰)	$\delta^{17}O$ (‰)	$\Delta^{17}O$ (‰)
Change electron energy(5/8/2005)						
Blank	123.9	0.41	-0.004	-0.001	-0.027	-0.026
+300ppm	123.9	356.63	0.018	0.029	0.017	0.002
+600ppm	123.9	854.74	0.036	0.087	0.120	0.075
+900ppm	123.9	1310.38	0.041	0.113	0.168	0.110
+3000ppm	123.9	4190.31	0.146	0.372	0.544	0.352
Blank	99.7	0.41	0.004	-0.003	-0.010	-0.008
+300ppm	99.7	356.63	0.016	0.019	0.040	0.030
+600ppm	99.7	854.74	0.041	0.063	0.076	0.043
+900ppm	99.7	1310.38	0.048	0.101	0.109	0.057
+3000ppm	99.7	4190.31	0.145	0.301	0.468	0.313
^{13}C-enriched CO_2, change electron energy (6/22/2005)						
Blank	123.9	-*	0.008	0.007	-0.015	-0.019
+300ppm	123.9	-	2.898	0.014	0.012	0.005
+600ppm	123.9	-	7.072	0.016	0.063	0.055
+900ppm	123.9	-	10.481	0.041	0.143	0.122
+3000ppm	123.9	-	35.319	0.093	0.416	0.368
Blank	99.7	-	--	--	--	--
+300ppm	99.7	-	--	--	--	--
+600ppm	99.7	-	7.603	0.011	0.050	0.044
+900ppm	99.7	-	11.279	0.038	0.104	0.084
+3000ppm	99.7	-	38.005	0.083	0.299	0.256

-* CO_2 not shown because mass spectrometer not equipped to measure $^{13}CO_2$
-- no data available for these samples

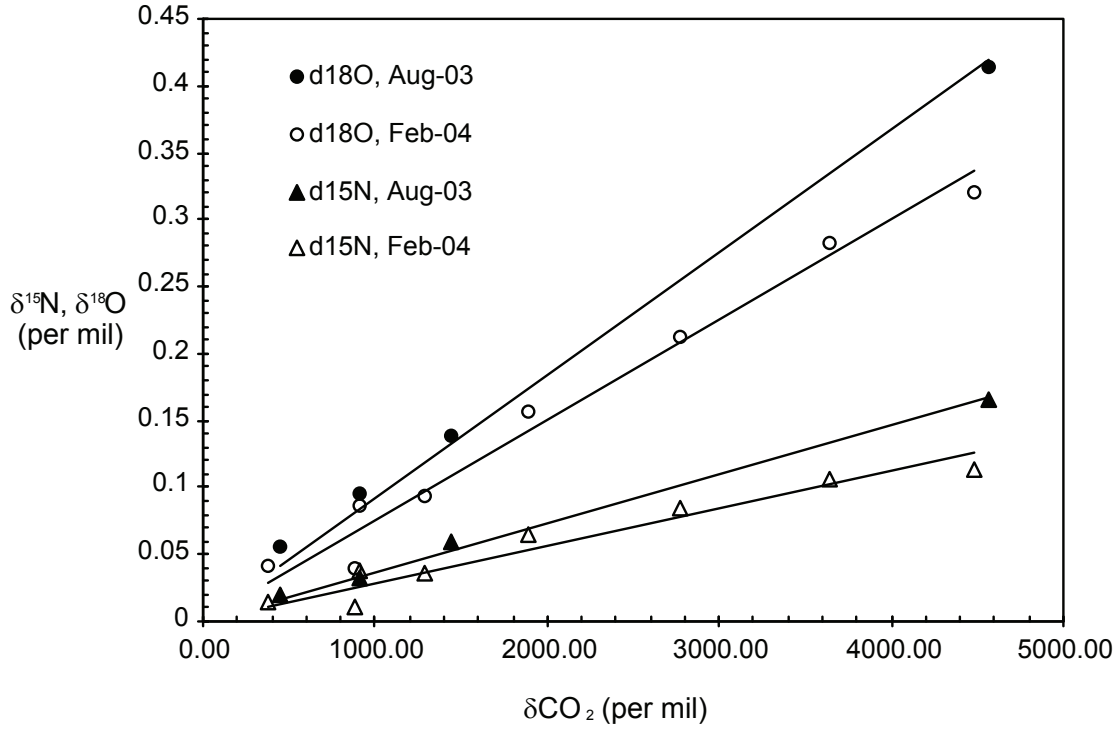

Figure A.1. $\delta^{15}N$ and $\delta^{18}O$ from the initial experiments in August 2003 and February 2004. Slopes and correlation coefficients for $\delta^{15}N$ from August 2003: y = 4e-5x, R^2 = 0.9961; $\delta^{15}N$ from February 2004: y = 3e-5x, R^2 = 0.9396 y = 9e-5x, R^2 = 0.9946; $\delta^{18}O$ from August 2003: y = 9e-5x, R^2 = 0.9946; $\delta^{18}O$ from February 2004: y = 8e-5x, R^2 = 0.9789.

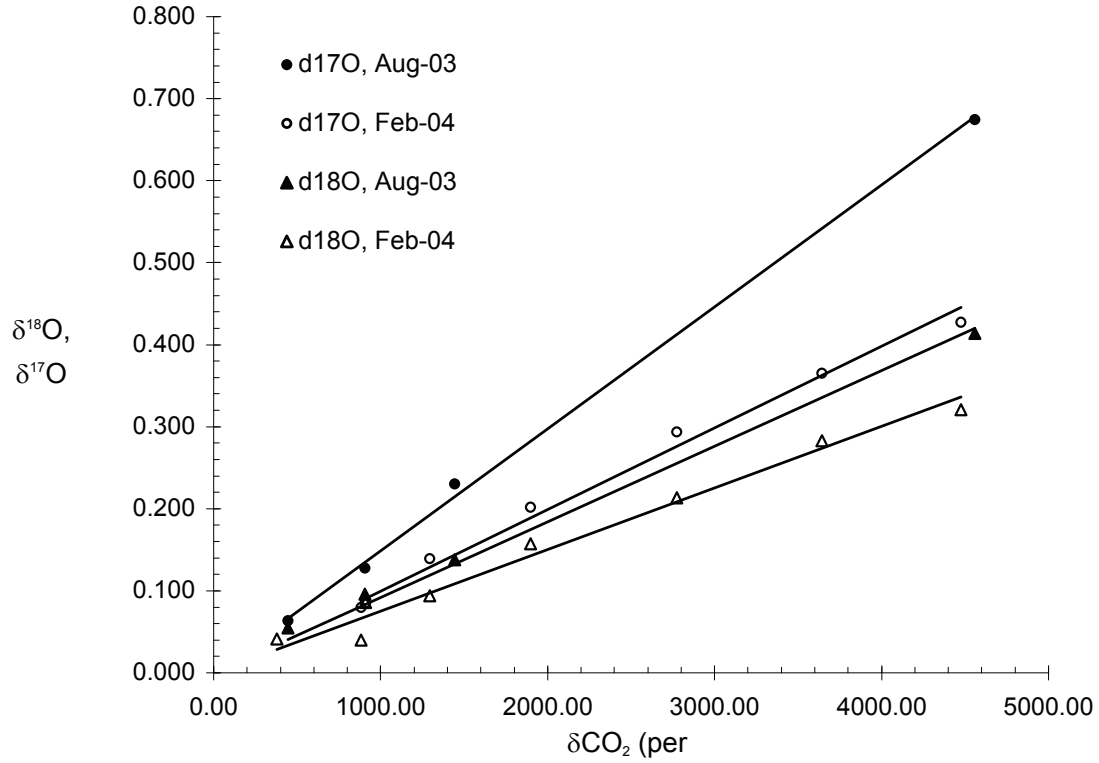

Figure A.2. $\delta^{17}O$ and $\delta^{18}O$ from the initial experiments in August 2003 and February 2004. Slopes and correlation coefficients for $\delta^{17}O$ from August 2003: $y = 0.0001x$, $R^2 = 0.9986$; $\delta^{17}O$ from February 2004: $y = 0.0001x$, $R^2 = 0.9910$; $\delta^{18}O$ from August 2003: $y = 9e\text{-}5x$, $R^2 = 0.9946$; $\delta^{18}O$ from Feb 2004: $y = 8e\text{-}5x$, $R^2 = 0.9789$.

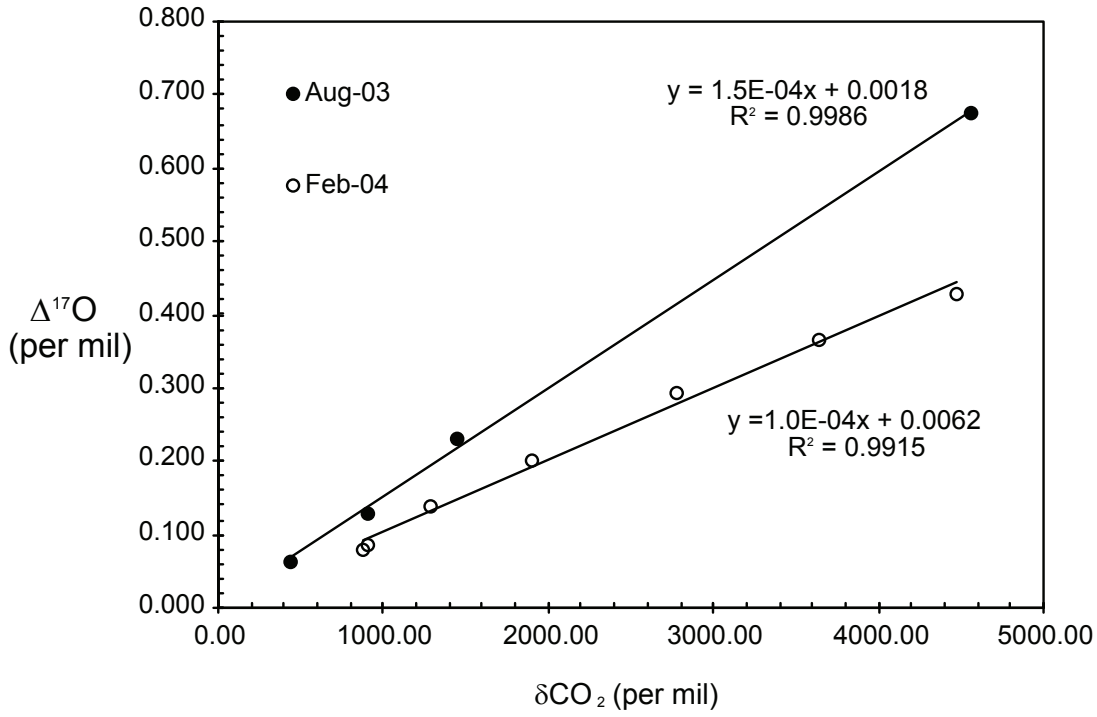

Figure A.3. $\Delta^{17}O$ vs. δCO_2 for the August 2003 and February 2004 experiments. Note that $\Delta^{17}O$ ($\delta^{17}O - 0.52 \times \delta^{18}O$) increases with increasing δCO_2.

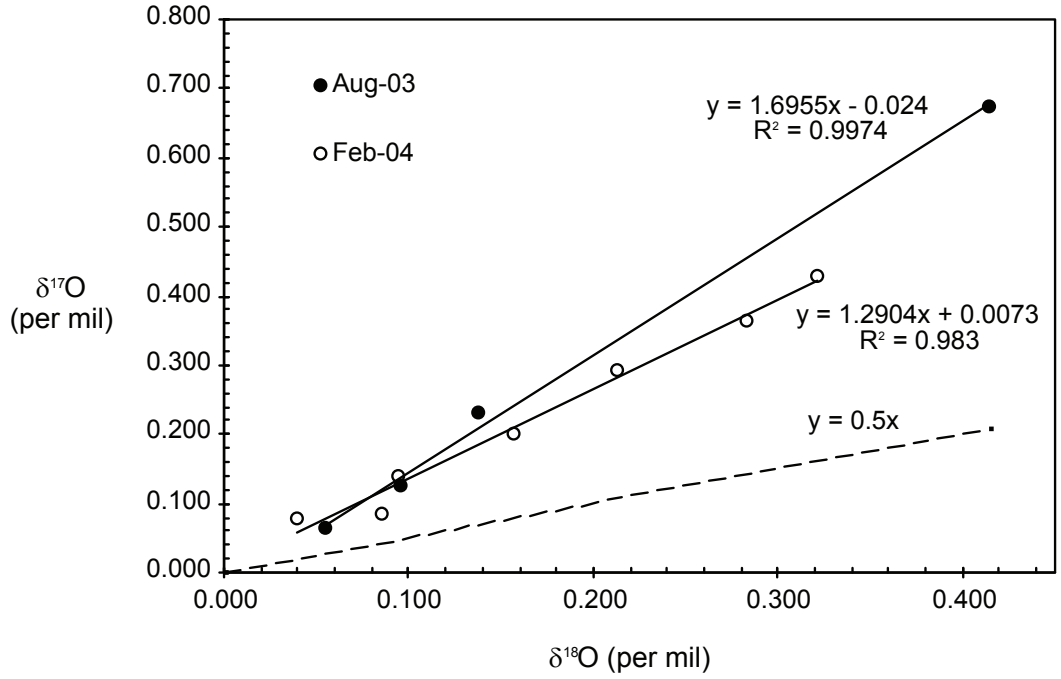

Figure 4. Three-isotope plot: $\delta^{17}O$ vs. $\delta^{18}O$ for the August 2003 and February 2004 experiments. Note the deviation from a mass dependent relationship (y = 0.5x).

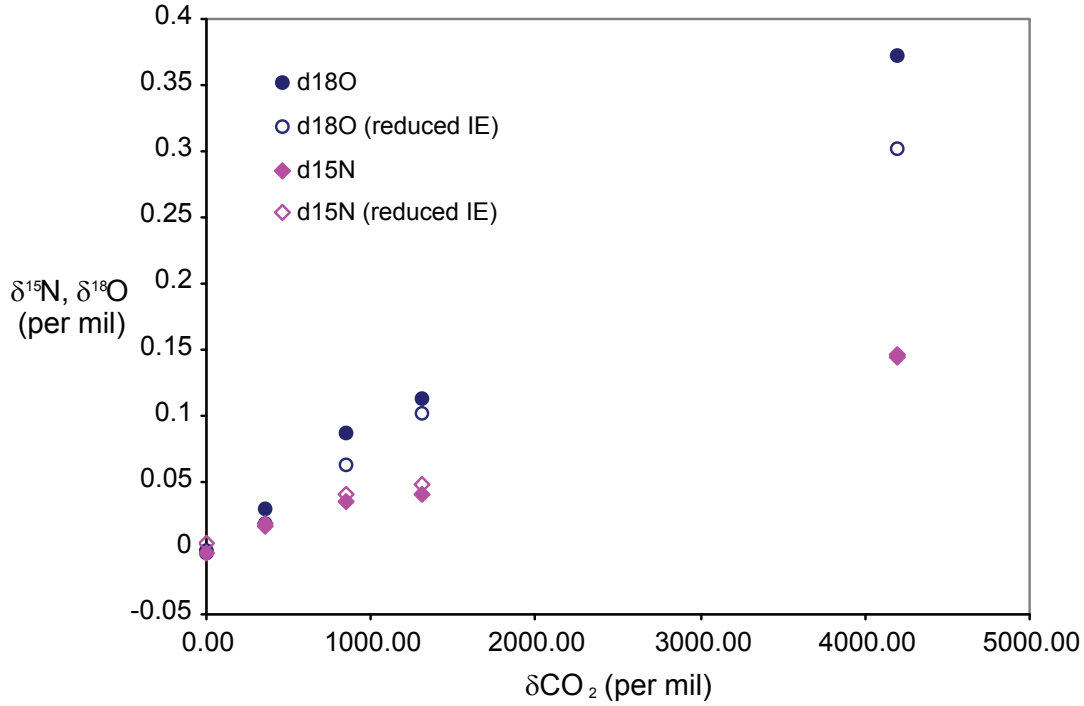

Figure A.5. $\delta^{15}N$ and $\delta^{18}O$ vs. δCO_2 at normal (123.9 eV) and reduced (99.7 eV) electron energies. The $\delta^{18}O$ measured values change when the electron energy is reduced, while those of $\delta^{15}N$ do not appear to be affected by changing the electron energy of the mass spectrometer.

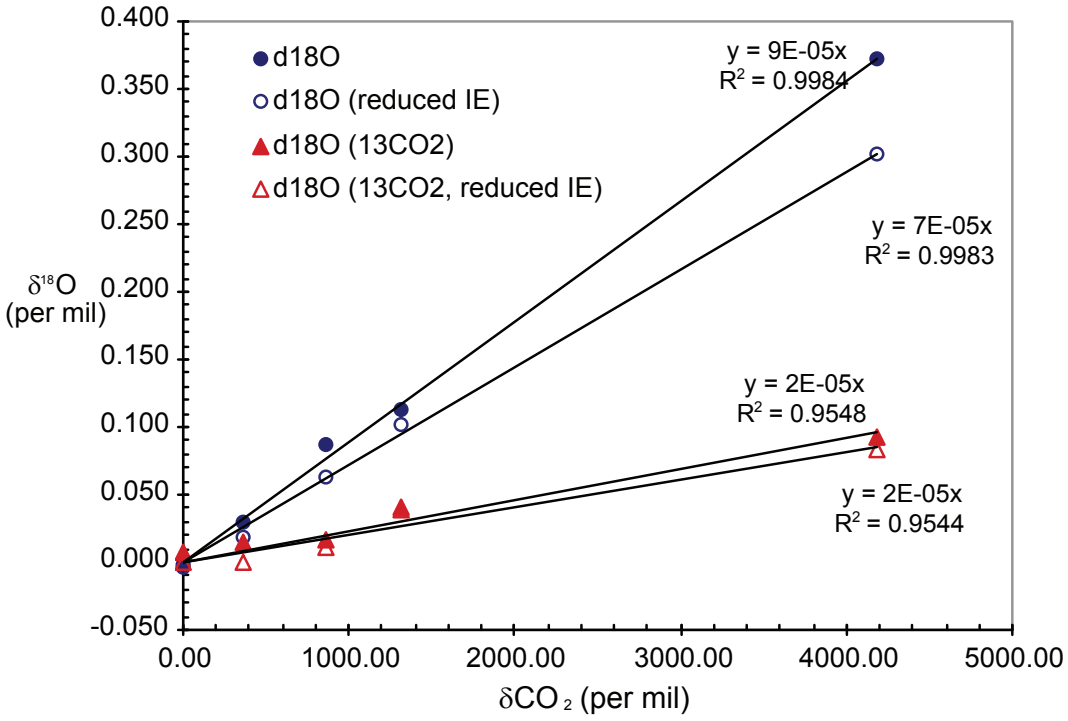

Figure A.6. $\delta^{18}O$ vs. δCO_2 for two sets of experiments: (1) normal and reduced electron energy (blue circles), and (2) normal and reduced electron using when ^{13}C-enriched CO_2 is added to the sample (red triangles). When ^{13}C-enriched CO_2 is used, $\delta^{18}O$ values are reduced, but they appear to be unaffected by changes in electron energy.

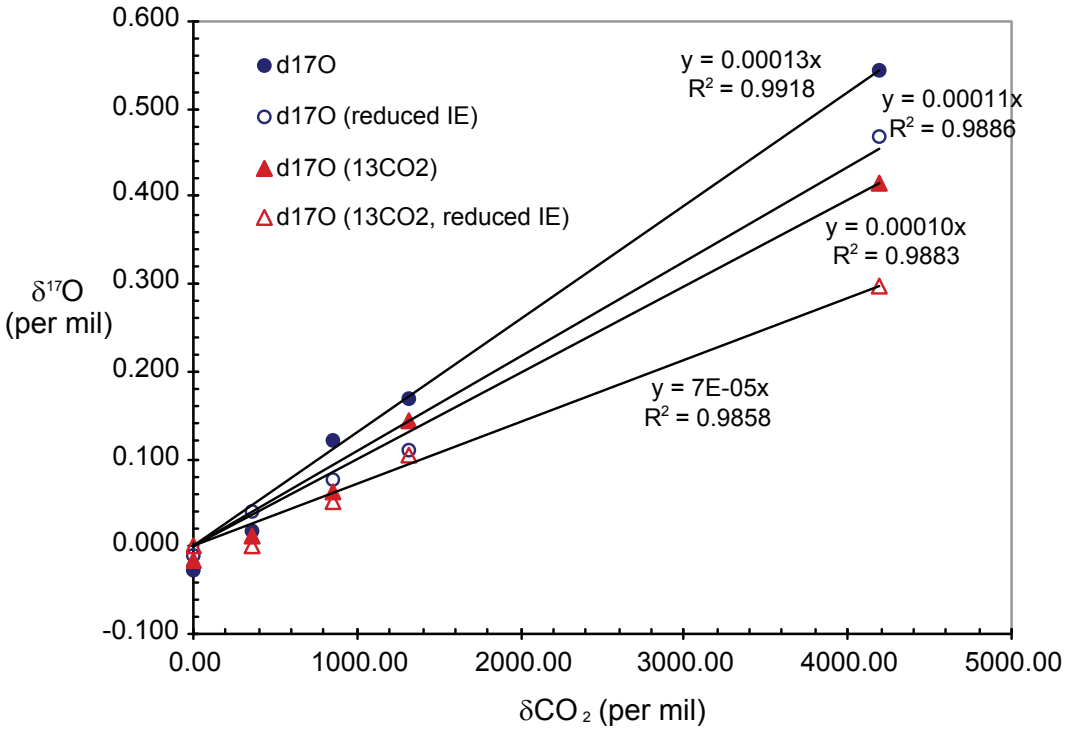

Figure A.7. $\delta^{17}O$ vs. δCO_2 for two sets of experiments: (1) normal and reduced electron energy (blue circles), and (2) normal and reduced electron energy using ^{13}C-enriched CO_2 (red triangles). When ^{13}C-enriched CO_2 is added, $\delta^{17}O$ values decrease, with the samples with reduced electron energy lower than those with normal electron energy.

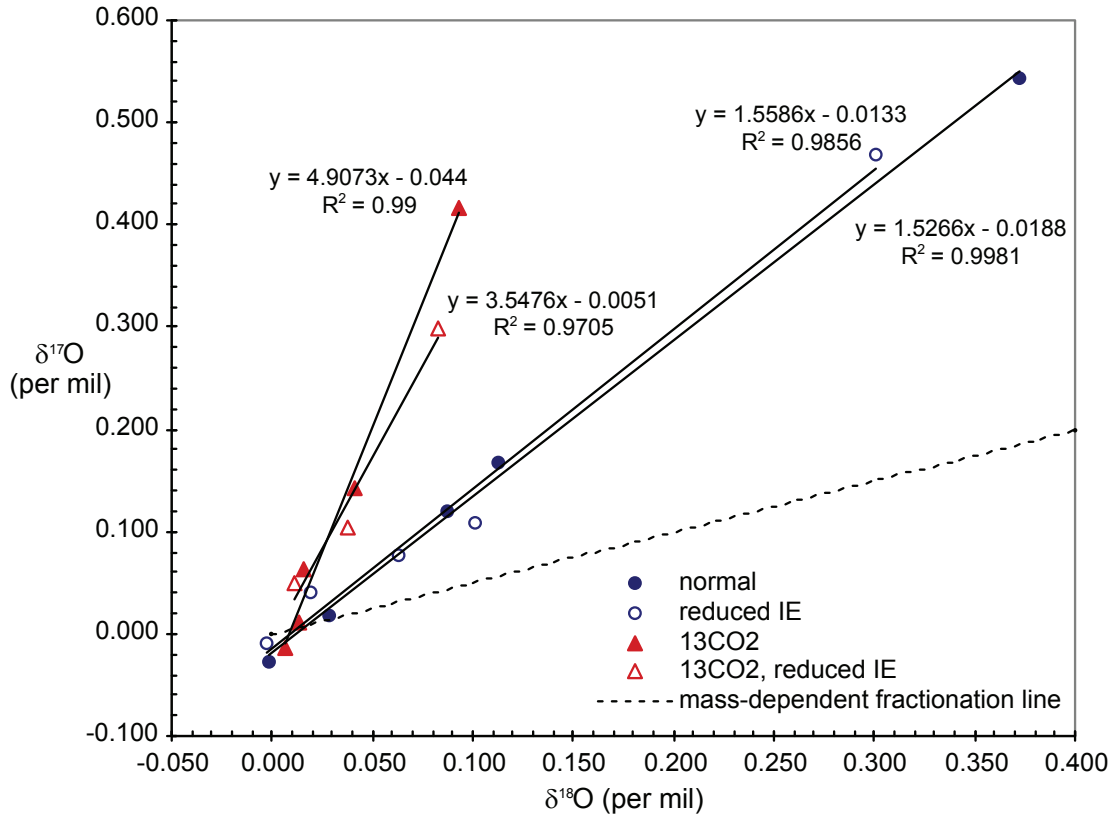

Figure A.8. Three-isotope plot: $\delta^{17}O$ vs. $\delta^{18}O$. As in Figures 6 and 7, data is plotted from two experiments: (1) normal and reduced electron energy (blue circles), (2) normal and reduced electron energy when ^{13}C-enriched CO_2 is added (red triangles). Also included is the mass-dependent fractionation line (y = 0.5x). Adding ^{13}C-enriched CO_2 to the air sample significantly increased the $\delta^{17}O/\delta^{18}O$ slope, as compared to the samples using ultra-pure CO_2. For each experiment (using ultra-pure CO_2 or ^{13}C-enriched CO_2), there is little difference between samples run at different electron energies.

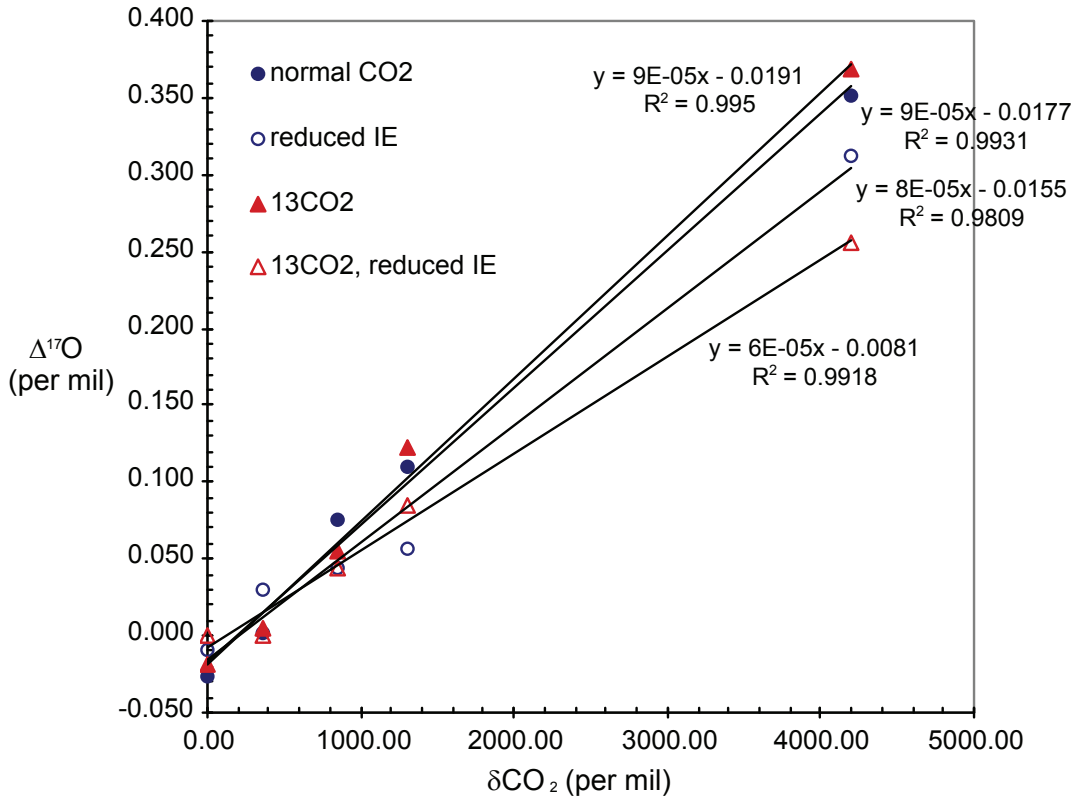

Figure A.9. $\Delta^{17}O$ vs. δCO_2 from two experiments: (1) normal and reduced electron energy (blue circles), (2) normal and reduced electron energy when ^{13}C-enriched CO_2 is added (red triangles).